85th ARFTG Microwave Measurement Conference

Measurements and Techniques for 5G Applications

May 22, 2015
Hyatt Regency
Phoenix, Arizona

IEEE Catalog Number: CFP15ARF-USB
ISBN: 978-1-4799-8886-0

85th ARFTG Conference Organizers

General Chair	**David Blackham**
Technical Program Chairs	**Nick Ridler**

85th ARFTG Technical Program Committee

Nick Ridler, *NPL*

Mitch Wallis, *NIST*

Peter Aaen, *University of Surrey*

Gayle Collins, *MaXentric Technologies*

Leonard Hayden, *Qorvo Inc.*

Karel Hoffmann, *Czech Technical University in Prague*

Jon Martens, *Anritsu*

Joe Gering, *Qorvo*

Masahiro Horibe, *NMIJ*

Martin Salter, *NPL*

Roland Clarke, *University of Leeds*

Andrej Rumiantsev, *Brandenburg University*

J. Apolinar Reynoso-Hernandez, *CICESE*

Patrick Roblin, *The Ohio State University*

Dominique Schreurs, *KU Leuven*

Ken Wong, *Keysight Technologies*

John Wood, *Maxim Integrated Products*

Jörgen Stenarson, *Chalmers University Technology*

Martin Salter, *NPL*

The 2015 ARFTG Executive Committee (ExCom)

President	**Mohamed Sayed**, MMS
Vice President	**Jon Martens,** Anritsu
Secretary	**Dominique Schreurs**, K.U.Leuven
Treasurer and Standards	**Ronald Ginley**, NIST
Nonlinear Network Analyzers and Publicity	**Jean-Pierre Teyssier**, Keysight Technologies
Electronic Communications	**Mitch Wallis**, NIST
Education and Workshops	**Patrick Roblin**, Ohio State University
Publications	**David Blackham**, Keysight Technologies
Sponsorship & Exhibits	**Joe Gering**, RFMD
Technical Coordination and Planning	**John Wood,** Maxim Integrated Products
Membership and Standards	**Ken Wong**, Keysight Technologies
Publicity & Exhibits	**Gayle Collins**, MaXentric Technologies
Technical Coordination and Planning	**Nick Ridler**, NPL
Electronic Publicity	**Peter Aaen**, University of Surrey
MTT-S Liaison and Awards	**Leonard Hayden**, Qorvo Inc.

Ex-Officio

Executive Secretary	**John Cable**

Session A: Nonlinear Measurements and Models

Chair: Jon Martens, Anritsu

Measurements for Millimeter-wave 5G Wireless Systems: Increased Frequency, Increased Bandwidth, Increased Calibration (Invited)

K. Remley, National Institute of Standards and Technology, Lafayette, United States

Comparison of Sampler and VNA based Large Signal Measurement Systems (LSNA) Under CW and Pulsed Operation

M. A. Casbon, P. J. Tasker, Cardiff University, Cardiff, United Kingdom

Towards a Denser Frequency Grid in Phase Measurements using Mixer-based Receivers

D. C. Ribeiro, P. M. Cruz, N. B. Carvalho, Universidade de Aveiro - IT, Aveiro, Portugal

A Compact Millimeter-wave Comb Generator for Calibrating Broadband Vector Receivers

P. D. Hale[1], K. A. Remley[1], D. F. Williams[1], J. A. Jargon[1], J. C. Wang[2], [1]National Institute of Standards and Technology, Boulder, United States, [2]Standards and Technology, Boulder, United States

Session B: Calibration and Verification

Chair: Leonard Hayden, Qorovo

Design and Analysis of a Verification Device for the Nonlinear Vector Network Analyzer

M. Rajabi[1], D. H. Humphreys[2], T. Nielsen[3], P. Barmuta[1,4], D. Schreurs[1], [1]KU Leuven, Leuven, Belgium, [2]National Physical Laboratory, Teddington, United Kingdom, [3]Keysight Technologies, Aalborg East, Denmark, [4]Warsaw University of Technology, Warsaw, Poland

Calibration of channel mismatch in time-interleaved real-time digital oscilloscopes

C. Cho[1], J. Lee[1], P. Hale[2], J. Jargon[2], P. Jeavons[2], J. Schlager[2], A. Dienstfrey[2], [1]Korean Research Institute of Standards and Science, Daejeon, Republic of Korea, [2]National Institute of Standards and Technology, Boulder, United States

Multiline TRL revisited

Y. Rolain, M. Ishteva, E. Van Nechel, F. Ferranti, VUB, Brussels, Belgium

Analyzing Uncertainty Matrices Associated with Multiple S-parameter Measurements

N. Ridler, M. Salter, National Physical Laboratory, Teddington, United Kingdom

Session C: 5G Communications

Chair: Peter Aaen, University of Surrey

Measuring 5G: Business as usual or time for a rethink? (Invited)

M. Rumney, Keysight Technologies, Wokingham, United Kingdom

Complex LO waveforms for wideband systems: some frequency-converter measurement implications

J. Martens, Anritsu, Morgan Hill, United States

A comparison of MIMO antenna efficiency measurements performed in Anechoic Chamber and Reverberation Chamber

T. Loh[1], W. Qi[2], [1]National Physical Laboratory, Teddington, United Kingdom, [2]Beijing Institute of Radio Metrology and Measurement, Beijing, China

Automated Wideband Test System, Measurement Uncertainty, and Design of On-chip Six-Port Reflectometers for 5G Applications

B. Hur, W. R. Eisenstadt, University of Florida, Gainesville, United States

Session D: Other Topics

Chair: Mitch Wallis, NIST

Rectangular-Waveguide Impedance

D. F. Williams[1], J. Jargon[1], U. Arz[2], P. D. Hale[1], [1]NIST, Boulder, United States, [2]PTB, Braunschweig, Germany

Power Control for S-parameters and Large Signal Characterization at (sub)-mmWave frequencies

L. Galatro, S. Galbano, A. Santaniello, M. Spirito, Delft University of Technology, Delft, Netherlands

Full-Wave Electromagnetic Modeling of Sub-millimeter Wave HEMT Parasitics

Y. Karisan, C. Caglayan, G. C. Trichopoulos, K. Sertel, The Ohio State University ElectroScience Laboratory, Columbus, United States

An Automatized Time-Domain Set-up for On-Wafer Characterization, Doherty Oriented, of High Power GaN HEMTs

L. Ayari[1], M. Ayad[2], E. Byk[2], M. Camiade[2], G. Neveux[1], D. Barataud[1], [1]XLIM, Limoges, France, [2]UMS, Villebon sur yvette, France

Interactive Forum

Chair: Ken Wong, Keysight Technologies

Physical Models for 2.4 mm and 3.5 mm Coaxial VNA Calibration Kits Developed within the NIST Microwave Uncertainty Framework

J. A. Jargon[1], C. Cho[2], D. F. Williams[1], P. D. Hale[1], [1]NIST, Boulder, United States, [2]KRISS, Daejeon, Republic of Korea

Transient Temperature Measurement of Microwave Devices

D. Kendig[1], K. Yazawa[1,2], A. Shakouri[2], [1]Microsanj, LLC, Santa Clara, United States, [2]Purdue University, West Lafayette, United States

Novel Components for a Fully Automated PIM and S-Parameter Test System

M. Grassl, W. Zissler, Spinner GmbH, Feldkirchen-Westerham, Germany

On the Implementation of the LZZ Calibration Technique in the S-Parameters Measurement of Devices Mounted in Test Fixtures

M. A. Pulido-Gaytan[1], J. A. Reynoso-Hernandez[1], M. d. Maya-Sanchez[1], A. Zarate-de Landa[2], J. R. Loo-Yau[3], [1]CICESE Research Center, Ensenada, Mexico, [2]Peregrine Semiconductor, San Diego, United States, [3]CINVESTAV Research Center, Zapopan, Mexico

De-embedding differential noise figure using the correlation of output noise waves

Y. Andee[1,2], C. Arnaud[1,2], F. Graux[3], F. Danneville[4], [1]Univ. Grenoble Alpes, Grenoble, France, [2]CEA, Grenoble, France, [3]Rohde&Schwarz, Meudon-la-Forêt, France, [4]IEMN, Villeneuve d'Ascq , France

A Simple Adaptive Method of Antenna Frequency Parameters Measurements with Local Reflections

A. A. Savin[1], V. G. Guba[2], [1]Tomsk State University of Control System and Radioelectronics, Tomsk, Russian Federation, [2]NPK Tair, Tomsk, Russian Federation

Measurement Setup for X-Parameter Characterization of BAW Resonators

W. Akstaller[1], A. Tag[1], C. Musolff[1], R. Weigel[1], A. Hagelauer[1], [1]Friedrich-Alexander Universitaet Erlangen-Nuernberg, Erlangen, Germany, [2]Erlangen, United States

Effects of the effective efficiency of the thermistor mount with WR-22(33 to 50 GHz) microcalorimeter

C. Ma, X. Cui, W. Yuan, Y. Li, National Institute of Metrology of China, Beijing, China

Microstrip Open - Problematic Calibration Standard

M. Haase, K. Hoffmann, Z. Skvor, Czech Technical Univeristy in Prague, Praha 6, Czech Republic

Consideration of Error Model with Cable Flexure Influences on Waveguides Vector Network Analyzers at submillimeter-wave frequency

M. Horibe[1], R. Kishikawa[1], Y. Kato[1], Y. Tsukahara[2], [1]National Institute of Advanced Industrial Science and Technology , Tsukuba, Japan, [2]Junkosha Inc., Kasama, Japan

Investigating Scattering Parameters Measurements for 50GHz High-speed Printed Circuit Boards (PCBs)

H. Huang[1,1], D. Liu[2,2], T. Guan[3,3], M. X. Liu[4,4], [1]National Institute of Metrology,China, Beijing, China, [2]Keysight Technologies Co,China, Beijing, China, [3]Huawei Technologies Co,Ltd,China, Shenzhen, China, [4]National Institute of Metrology,China, Beijing, China

A simplified calibration procedure for on-wafer power leveled S-parameter measurements at mm-wave

S. Galbano, L. Galatro, M. Spirito, TU Delft, Delft, Netherlands

Repeatability Performance of Non-Contact Probes in the 500-750 GHz Band

C. Caglayan, G. C. Trichopoulos, K. Sertel, ElectroScience Laboratory, Columbus, United States

Impedance Renormalization in CMOS-based Single-Element Electronic De-embedding

J. Chien, A. M. Niknejad, University of California, Berkeley, Berkeley, United States

V- and W-band waveguide microcalorimeters for millimeter-wave power standards

J. Kwon, Y. Hong, D. Lee, T. Kang, Korea Research Institute of Standards and Science, Daejeon, Republic of Korea

A 500 MHz Portable Evaluation Platform for Digital Pre-Distortion and Envelope Tracking Power Amplifiers

J. J. Yan, T. Nakatani, P. Theilmann, D. F. Kimball, MaXentric Technologies, La Jolla, United States

Comparison of Sampler and VNA based Large Signal Measurement Systems (LSNA) Under CW and Pulsed Operation

M.A. Casbon, P.J. Tasker.

Centre for High Frequency Engineering, School of Engineering, Cardiff University, Wales

Abstract — Here we present a comparison of the Large Signal Measurements provided by both a VNA based and a sampler based LSNA system. In this study, in order to achieve a robust and reliable relative phase calibration a dual frequency phase differential method was used. Significantly this work compares measurements performed under both CW and pulse mode operation. Very similar RF I-V waveforms are achieved in both cases, verifying that both architectures can provide comparable measurements not only in CW but also under pulsed operation. The test device was a GaN on silicon carbide HFET.

Index Terms — Waveform Engineering, fully active harmonic load-pull, power amplifiers.

I. Introduction

It has previously been shown that measuring and manipulating the harmonic behavior of transistors can lead to better circuit designs and enable improvements in process understanding [1]. As these "Waveform Engineering" techniques come into common use the expectations of LSNA measurement accuracy continue to rise, and as the advantages of gathering data during pulsed operation become recognized then the need for a robust and accurate method of LSNA phase calibration and verification under pulsed operation becomes more pressing. Here we demonstrate the accurate measurement of RF I-V waveforms under pulsed conditions by comparing those achieved using both a Vector Network Analyzer based system [2], and a sampler based system [3].

The highly stable performance of modern DDS synthesizers allows relative phase calibration and verification using two tones, by a dual frequency phase differential method [2]. A fundamental (f_0) signal and a signal at each harmonic in turn (f_n) are fed through the measurement path, and the measured phase relationship can be directly compared with that reported by an oscilloscope or other phase meter attached to the output [2]. In this investigation a Tektronix DSA8200 with 80E09 sampling heads is used as the phase standard, and an Agilent 8487A sensor is used as the power standard.

Measurements are made on wafer, to avoid possible de-embedding errors. The device used was a Win Semiconductor Corp. 10 x 125um GaN HFET on a silicon carbide substrate, the drain bias voltage was set at 18V, which avoids stressing the device and consequent aging effects or failure.

II. The Measurement Systems

Two Large Signal (LSNA) system architectures are compared in this study. The VNA based architecture uses a Rohde & Schwarz ZVA 67 analyzer, while the sampler based architecture uses a VTD SWAP-X402 based system. The external modulator set ups for pulsing (RF and DC drain bias) are essentially the same for both systems. High speed RF switches modulate the RF while a high side FET switch modulates the drain DC bias [3]. In both cases the RF and drain bias can be independently switched between pulse and CW, enabling three different measurement conditions without making any changes to the sampling regime, therefore any measured changes can safely be ascribed to the device under test. The drain bias current is measured using a high side series resistor, monitored by a LT2940 IC driving an Agilent U2531A high speed ADC, an arrangement which can measure true DC and pulsed currents, allowing precise calibration against resistive standards. Placing the sense element before the switch removes the large common mode signal and greatly improves settling time (2µs typical). The timing of the DC sample can be adjusted to ensure it is taken at a representative time in the pulse.

The main difference between these LSNA systems is the method of measuring the RF waveforms. The time domain based VTD SWAP assembles a continuous record from a number of samples [4], while the frequency domain based ZVA takes a complete record in a single pulse. In order to shorten the sampling period to fit within the specified RF pulse length the ZVA measurement bandwidth must be increased, with a consequent impact on the dynamic range, however much of the lost performance can be recovered by averaging a large number of measurements, at the expense of speed. For a 10µs pulse the bandwidth must be more than 200KHz, compared to the 100Hz or even 10Hz which could be used for CW operation. It is important for optimum accuracy that calibration is performed at the bandwidth to be used for the measurements. The VTD method lends itself well to pulse operation, a sampling window as narrow as 0.5µs can be positioned anywhere in the pulse, allowing pulse profiling if required [5].

978-1-4799-8887-7/15/$31.00 ©2015 IEEE

The ZVA system was built around a Cascade Summit 12000 probe station, whereas the VTD uses a Signatone station, Cascade Z probes were used on both.

III. Phase Calibration

Phase calibration and verification was carried out on both systems using a dual frequency phase differential method. This approach involves combining an f_0 reference with a harmonic signal, f_n, and passing it through the LSNA measurement path [2] into the sampling oscilloscope. In this way the relative phase of the two signals can be measured by both the LSNA and the sampling oscilloscope. When measuring on wafer it is not possible to attach the oscilloscope directly at the measurement plane, so any dispersion in the output half of the measurement path must be corrected, this is simply done with routine passive network measurements.

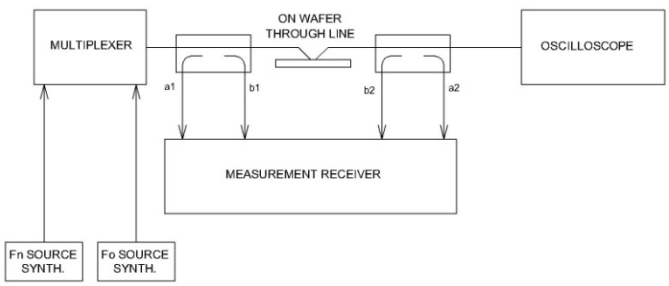

Fig. 1 The dual signal phase calibration setup.

IV. Measurements

Initially to compare the systems a set of load-pull measurements was taken on both, in this case those consistent with performing basic device analysis. The fundamental and harmonic load impedance was varied along the real axis of the Smith chart on each system, both in pulse and CW. The second and third harmonic output loads were held at the same reflection coefficient as the fundamental, over the range -0.5 to +0.5 in 0.1 steps, permitting the plotting of "fan diagrams" of the load-lines as well as examination of the waveforms. The higher harmonics were passively terminated in 50 Ohms, as were the input impedances

In figure 2 we can see the fan diagrams for the device measured in CW mode on the two systems, which are in close agreement. Since different RF measurement couplers and multiplexers were used on the two systems the variation in the nominal harmonic loads result in slight differences in the higher harmonic waves, giving the impression that the loadlines approach the vertical axis more closely when measured with the ZVA.

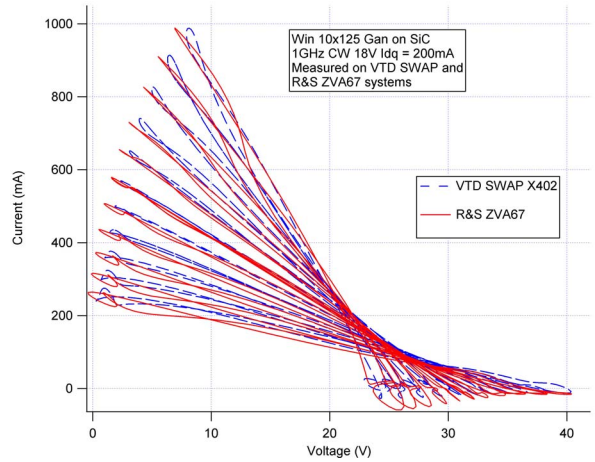

Fig. 2 Dynamic loadlines measured in CW on both systems

It can be seen from fig. 4, which compares the output waveforms from both systems in CW at 50 Ohms, that this is not due to the fundamental wave. The waveforms are aligned by the f_0 input voltage phase, showing good consistency between systems. Fig 4 also compares the sampling oscilloscope waveform with the measured waves, demonstrating that accurate relative phase calibration has been achieved with both systems.

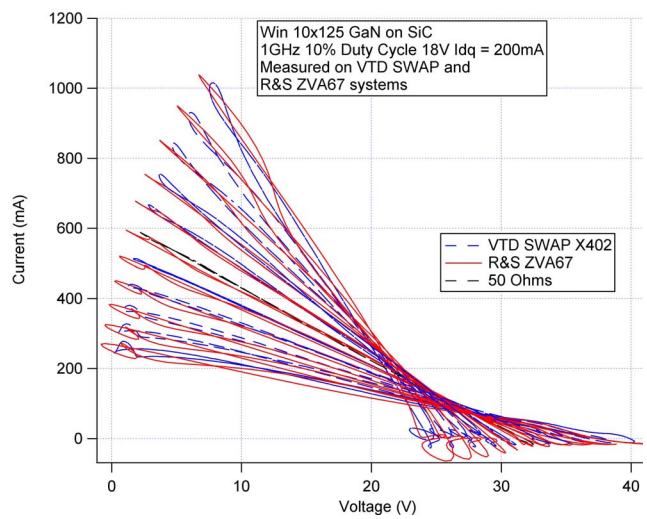

Fig. 3 Dynamic loadlines measured in pulse on both systems

In fig. 3 we see the loadlines measured in pulse operation, once again there is good agreement, with only small differences in the harmonic loops, as shown in fig. 5. There is a small improvement in the device performance under pulse operation, which is seen in both sets of measurements.

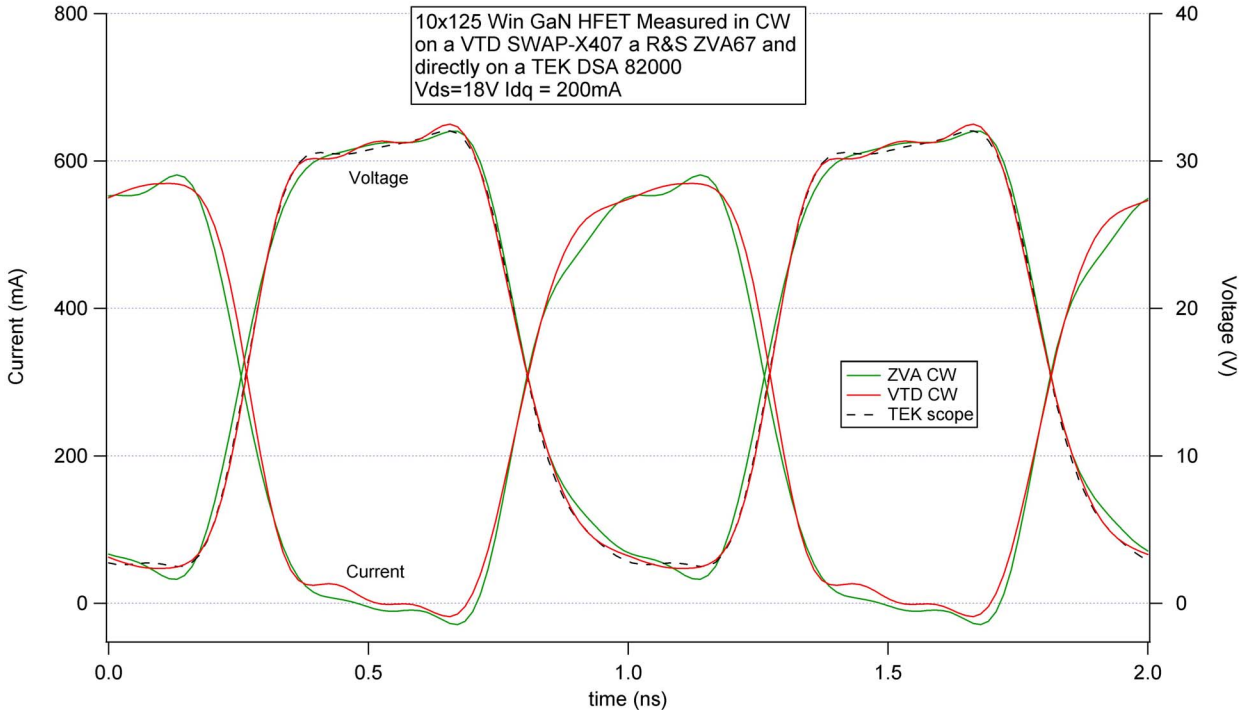

Fig. 4 Waveforms into 50 Ohms on the VTD-SWAP and R&S ZVA67 based systems, and directly on the Tektronix scope.

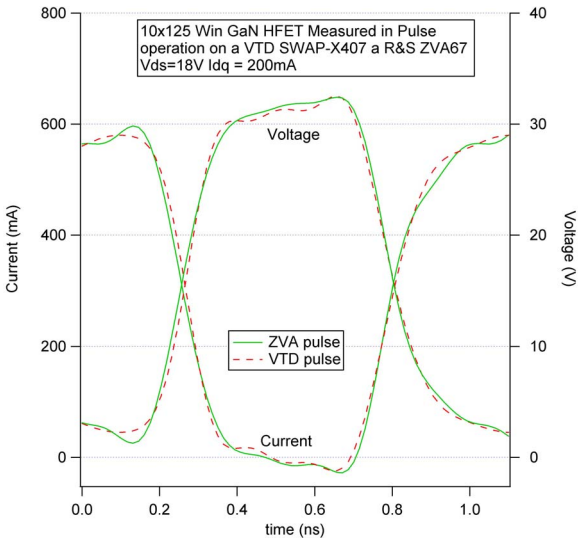

Fig. 5 Waveforms in pulse operation into 50 Ohms on the VTD-SWAP and R&S ZVA67 based systems

V. Conclusion

It has been demonstrated that information for waveform engineering can be collected in pulse mode as well as CW, using either a broadband sampling receiver or a narrow band VNA receiver. The systems are precise enough to allow accurate analysis of device behavior.

Acknowledgement

The authors wish to acknowledge the assistance and support of Win semiconductor corp.

References

[1] Tasker P.J. "Practical Waveform Engineering", Microwave Magazine, IEEE, Volume 10, Issue 7, pp 65-76, December 2009.

[2] A. Aldoumani et al, "Operation and calibration of VNA-based Large Signal RF I-V waveform measurements system without using a harmonic phase reference standard.", 81st ARFTG microwave measurement conf., June 2013, pp 151-154.

[3] M.A. Casbon, P.J. Tasker and J Benedikt, "Waveform Engineering beyond the Safe Operating Region" *IEEE CSIC Symp. Dig.*, Hawaii, HI, Oct 16-19, 2011, pp. 37-40.

[4] Fabien De Groote, Olivier Jardel, Tibault Reveyrand, Jean-Pierre Teyssier, and Raymond Quéré, "Very small duty cycles for time domain transistor characterization," Proceedings of Euma, Vol. 4, No. 2 2008.

[5] J. Faraj, F. De Groote, J.-P. Teyssier, J. Verspecht, R. Quéré and R. Aubry, "Pulse profiling for AlGaN/GaN HEMTs large signal characterization," *Proc. 38th EuMC*, Amsterdam, The Netherlands, Oct. 2008, pp. 757-760

Towards a Denser Frequency Grid in Phase Measurements using Mixer-based Receivers

Diogo C. Ribeiro
dcribeiro@ua.pt

Pedro M. Cruz
pcruz@av.it.pt

Nuno Borges Carvalho
nbcarvalho@ua.pt

Universidade de Aveiro, DETI - Instituto de Telecomunicações

***Abstract*—In this paper a new method to achieve a dense frequency grid in synchronous phase measurements is presented. This technique is suitable to use with instruments that employ a mixer-based internal architecture.**

Contrary to other works, the grid density is not being enhanced through the increase of the comb-generator (CG) output tone density, nor through the use of successive multi-sine waveforms. The technique proposed uses the same reference signals for any band measurable by the instrument. Besides, the power of each CG output tone is also kept at a high level. The tradeoff is the requirement for wide-band receivers, which are already commonly present in modern instrumentation.

Multi-sine phase measurements performed with a nonlinear vector network analyzer (NVNA) will be compared with results obtained using the new technique (and performed by commercial mixer-based receivers). The comparisons will be used to validate the suggested method.

***Index Terms*—nonlinear measurements, phase measurements, multi-sine measurements, comb-generator.**

I. Introduction

In order to achieve high dynamic range measurements, mixer-based instruments are nowadays the work-horse of the test and measurement industry.

However, mixer-based instruments suffer from a fundamental downside, since they do not measure the entire spectrum at the same time (they split the whole spectrum into pieces) the phase information of each frequency of interest will not be correlated with the surrounding ones.

The basic way to phase correlate these measurements is by the use of a phase reference artifact, traditionally a comb-generator (CG). This artifact will produce a comb of frequency tones equally spaced by a specific reference frequency. Additionally through the careful characterization of the CG, it may also serve as a calibration standard, as described in [1]. The calibration step is a fundamental one to achieve traceability between measurements performed at different sites.

Nowadays, commercially available CGs allow the user to define a frequency grid as low as 625 kHz, for measurements up to 67 GHz [2], [3]. However, the power of each tone at the output of the phase reference artifact (CG), is already very low. This limits the lowest frequency spacing achievable.

A denser frequency grid, with a frequency spacing below 100 kHz is very important for a variety of applications, such as the measurement of multi-sine waveforms used to mimic the stimulus effects of modulated signals for characterization and verification purposes, [4]. Moreover, in the characterization of mixed-signal devices a dense frequency grid is also a fundamental key point to obtain reliable and broader models.

The traditional method to achieve a denser frequency grid is to reduce the frequency of the fundamental reference frequency (which dictates the tone separation at the output of the CG) by a division factor (N_{div}). However, with the increment of N_{div} the power of each tone at the CG output will be reduced, following the expression:

$$\text{Power Drop}(dB) = 20\,log_{10}(N_{\text{div}}) \tag{1}$$

To effectively achieve a denser frequency grid it is mandatory to be able to maintain the CG output power, while doing so.

In order to accomplish this goal, several contributions have already been made during the last few years. One approach is to concentrate the output power of the CG around the frequencies of interest, this work was initialized with [5] and has evolved to become what was presented in [6] and in [7].

This kind of approaches focus its research on the artifact itself. While this has some advantages, because it keeps the measurement complexity at low levels, it is not suitable for a broader usage. Since the CG configuration has to be changed when the measurement definitions change, there is no guaranty that the phase characteristic at the output of the CG will remain the same. Thus, traceable measurements cannot be assured.

Another approaches are based on the generation of different phase reference signals, such as multi-sines [8], that may or may not be up-converted. Then, a superposition of tones is used to keep the continuous relation over frequency, [9]. Nevertheless, these techniques require additional hardware to be performed, they may need to use high speed arbitrary waveform generators (AWGs) or vector signal generators (VSGs). Moreover, with these techniques the phase characteristics of the reference signal cannot once more be easily guaranteed. Therefore, traceability is once again hard to ensure.

The main goal of this work is to develop a method that can increase the frequency grid density (diminish the frequency grid spacing). This is to be accomplished, while maintaining the same reference signals, no matter what is the spectrum band of interest (therefore, maintaining the configuration of the phase reference artifact), and without reducing the power of each reference tone. For this purpose, investigation focus will be given to another element of the measurement apparatus, the instrument receiver.

978-1-4799-8887-7/15/$31.00 ©2015 IEEE

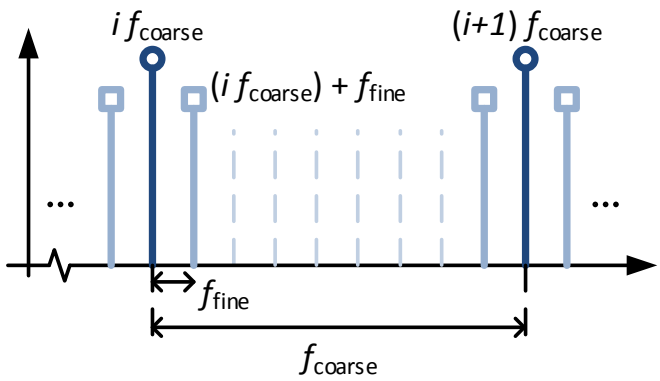

Fig. 1. Example of the assumptions made relatively to the position of the phase reference frequency tones position.

Contrary to other works published so far, our focus will not be in trying to develop new phase reference artifacts or architectures or even configurations. Instead, we will explore the advantages of modern wide-bandwidth instrument receivers. Taking into account this characteristic, a new method will be developed to compute the phase of each tone across frequency for a denser grid.

This paper is organized as follows: in the next section some assumptions and requirements will be made, so that the presented method may function properly. Next a description of the method itself and a description of the phase reference signals will be made. After, multi-sine phase measurements will be presented to validate the proposed method. Finally, some conclusions will be written.

II. The New Method

Modern mixer-based instruments, like the nonlinear vector network analyzer (NVNA) and other multi-port vector network analyzers (VNAs) or instrument receivers have wide instantaneous bandwidths, in the order of tens of MHz [10]–[12]. Due to advances in the design of analog-to-digital converters (ADCs) an high sampling rate (in the order of hundreds of MSPS) is now achievable. At the same time, an high number of resolution bits can be kept, which is a key factor to achieve high dynamic range.

The method presented in this work will try exploit this characteristic in order to enhance the measurement frequency grid density. For that purpose some assumptions and requirements need to be fulfilled.

First of all, it is assumed that there is available a reference signal producing an equally spaced frequency grid with a coarse step frequency (f_{coarse}). This coarse grid will from now on be referred as coarse frequency grid (CFG). It will also be assumed that additional reference tones exist at an offset frequency (f_{fine}) of the previously mentioned CFG (at the upper and lower side of the CFG). An example of these assumptions is depicted in Fig. 1.

The first requirement is that the instantaneous bandwidth of the instrument receiver has to be larger than f_{coarse}, which means that the internal ADC of the receiver has to have a sampling rate higher than $2 \times f_{\text{coarse}}$.

Furthermore, f_{fine} must follow:

$$f_{\text{fine}} = \frac{f_{\text{coarse}}}{N_{\text{div}}} \tag{2}$$

where N_{div} is a positive integer. N_{div} corresponds to the division factor by which the CFG will be reduced. Therefore, the objective is to create an equally spaced frequency grid with a step frequency of f_{fine}. This denser frequency grid will from now on be mentioned as fine frequency grid (FFG).

A. Description

The biggest challenge to perform phase related measurements with mixer-based receivers is to get rid of the local oscillator (LO) phase impairments from measure to measure. The traditional method employed in this situation uses a reference comb signal that needs to be followed in order to cancel the mentioned LO impairment. However, in order for that to stand true, the reference signal must present a frequency tone at the same frequency of the tone that is required to be measured from the RF input.

In the proposed case this is not valid, therefore a different procedure must be used.

To accomplish that, it will be considered that the frequency to be measured, corresponding to f_{wanted} is a tone between $i f_{\text{coarse}}$ and $(i+1) f_{\text{coarse}}$, and it is a multiple of f_{fine}, so that the following stands true:

$$f_{\text{wanted}} = i f_{\text{coarse}} + k f_{\text{fine}} \tag{3}$$

with k being an integer value that can vary from 0 to $N_{\text{div}} - 1$. This means that f_{wanted} is a frequency present on the FFG.

Then, taking into account the two reference signals described previously, the following phase definitions can be considered:

- $\theta_{\text{IN}} \rightarrow$ phase of the signal to be measured in a frequency point corresponding to f_{wanted}, at the input of the receiver.
- $\theta_{i\ \text{coarse}} \rightarrow$ phase of the coarse reference signal in a frequency point corresponding to $i f_{\text{coarse}}$, at the input of the receiver.
- $\theta_{i\ \text{fine (upper)}} \rightarrow$ phase of the fine (modulated) reference signal in a frequency point corresponding to $i f_{\text{coarse}} + f_{\text{fine}}$, at the input of the receiver.
- $\theta_{\text{LO}} \rightarrow$ phase of the LO.

Considering ideal down-converters, the following θ' definitions can be established as the phases read by the receivers and therefore affected by the down-conversion process:

$$\theta'_{\text{IN}} = \theta_{\text{IN}} + \theta_{\text{LO}} \tag{4}$$

$$\theta'_{i\ \text{coarse}} = \theta_{i\ \text{coarse}} + \theta_{\text{LO}} \tag{5}$$

$$\theta'_{i\ \text{fine (upper)}} = \theta_{i\ \text{fine (upper)}} + \theta_{\text{LO}} \tag{6}$$

Since, in an opposite way to the traditional method, a reference tone is not available at the frequency f_{wanted}, the

purpose of this work is to find a way to compute it using the phase information presented before. For that, the following phase quantity needs to be determined:

$$\theta_{\text{REF eq}} = \theta_{i\ \text{coarse}} + k\,\theta_{\text{fine}} \tag{7}$$

where $\theta_{\text{REF eq}}$ is the equivalent phase quantity of a reference signal at the frequency f_{wanted}.

Using $\theta_{\text{REF eq}}$, the phase of the input wanted signal in relation to a known reference, or by other words, the corrected phase value can be computed directly as:

$$\theta_{\text{IN corrected}} = \theta_{\text{IN}} - \theta_{\text{REF eq}} \tag{8}$$

For simplification of our explanation, f_{wanted} will be limited to the first half of the considered frequency interval, so that $k \leq \frac{\text{div factor}}{2}$.

Taking this into account the phase, θ_{fine}, of the low frequency modulation signal (f_{fine}), can be computed as follows:

$$\theta'_{i\ \text{fine (upper)}} - \theta'_{i\ \text{coarse}} = \theta_{i\ \text{fine (upper)}} - \theta_{i\ \text{coarse}} = \boldsymbol{\theta_{\text{fine}}} \tag{9}$$

We are now at half-way to be able to compute $\theta_{\text{REF eq}}$, for that purpose, the following relation can be used:

$$\theta'_{\text{IN}} - \theta'_{i\ \text{coarse}} = \theta_{\text{IN}} - \theta_{i\ \text{coarse}} \tag{10}$$

Now, by using (9) together with (10), the corrected input phase quantity can be finally computed as:

$$(\theta_{\text{IN}} - \theta_{i\ \text{coarse}}) - k\,\theta_{\text{fine}} = \theta_{\text{IN}} - \theta_{\text{REF eq}} = \boldsymbol{\theta_{\text{IN corrected}}} \tag{11}$$

As can be noticed from (11), there is a drawback with the presented method. Since the computed value of θ_{fine} needs to be multiplied by the position index k, the phase error associated with the determination of θ_{fine} will be amplified. The worst case scenario will be for tone frequencies right in the middle of the interval defined by $i f_{\text{coarse}}$ and $(i+1) f_{\text{coarse}}$, where the k value is larger. Furthermore, for higher division factors the value of k will also reach higher values, thus the measured phase error will increase with the increase of N_{div}.

B. Reference signal(s)

In this work two reference signals were used to generate the tones at the required frequencies.

The first was a traditional CG signal with a repetition rate equal to f_{coarse}, it will be mentioned as the coarse CG. The second is an amplitude modulation of the first signal with the a square signal of frequency f_{fine}, this reference signal will be mentioned as the modulated CG. The conceptual representation of both signals is shown in Fig. 2.

An AWG was used to generate these reference signals, in this case a Tektronix AWG70002A. In Fig. 3 the spectral power at some frequencies of interest is compared with the power of the traditional CG output. It has to be referred that in the implemented measurement setup, all the three signals had the same peak-to-peak voltage excursion, which in this case was 500 mV.

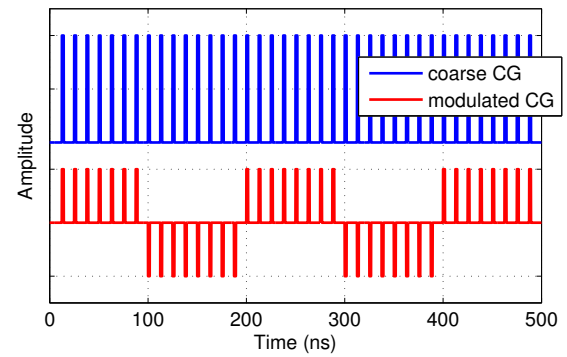

Fig. 2. Conceptual output of both phase reference signals. Coarse frequency of 80 MHz and fine (modulation) frequency of 10 MHz, division factor of 8.

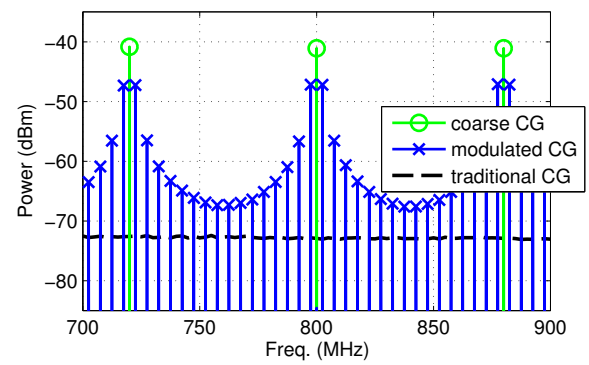

Fig. 3. Measured spectra of the signals used as CG's outputs. These signals were generated using an AWG and have 500 mVpp each.

It is worth to mention that the use of two signals was employed only for simplification reasons. A single reference signal with all the necessary tones could be used instead, but the time and effort required to its design would have to be expended. For example, using the work developed in [7] the single wanted signal may be achieved, with the additional benefit of being a signal with only two levels (which means it can be generated by a logic gate).

III. Obtained Results

An absolute characterization of any of the used CGs was not available, and performing such a characterization is a time-consuming and demanding task, as explained in [1]. Thus, a relative comparison was used instead to validate the proposed method. In order to validate the proposed approach the phases of two different multi-sines were measured using the new technique, and compared against measurements performed using the traditional approach in a NVNA (Keysight PNA-X N5242A). For all the measurements the Keysight U9391C CG [3] was used as a relative phase reference standard.

To implement the new method a National Instruments (NI) PXI system was used together with three NI 5792R Flex RIO receivers. This system was chosen due to its high flexibility, which is a crucial factor in our work. The equivalent IF bandwidth used in each of the PXI system receivers was 1 kHz

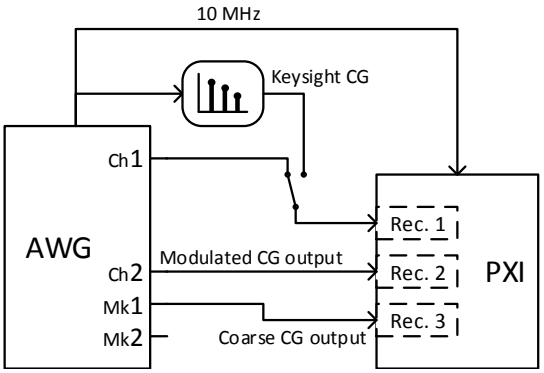

Fig. 4. Block diagram of the measurement setup employed during the phase measurements using the new method.

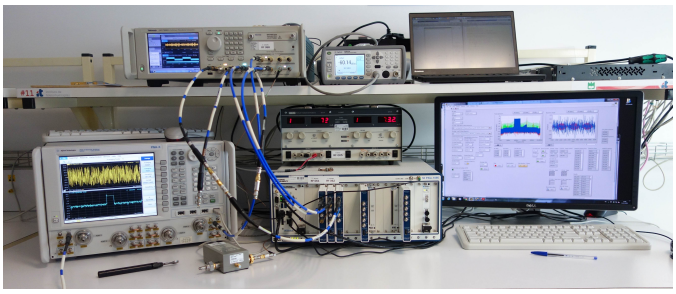

Fig. 5. Photo of the measurement setup.

and 100 averages were performed. While, in the NVNA the IF bandwidth was set to 20 Hz and were also used 100 averages (note that the NVNA was the golden reference in the results presented next).

A block diagram of the measurement setup employed to perform the new technique is shown in Fig. 4. In Fig. 5 a photo of the entire measurement setup is also included.

The characteristics of the two multi-sines to be measured were as follows: the first was a 16-tone, starting at 800 MHz and with a tone spacing of 2.5 MHz. The second was a 64-tone, starting also at 800 MHz and with a tone spacing of 625 kHz. Both multi-sines were generated with random phases for each tone and using the same AWG that was used for the reference signals.

The coarse reference frequency was fixed in both cases to 80 MHz. This means that in the first case a division factor of 32 was required to achieve an equivalent fine frequency spacing of 2.5 MHz. In the second case a division factor of 128 was required and a fine frequency spacing of 625 kHz was achieved.

The phase error over the frequency band of interest for each case is presented in Fig. 6.

In the first case, with a division factor of 32, the error obtained was between $\pm 0.5°$. Which revealed a good result, for an already relatively high division factor. Consecutive measurements have revealed similar phase error results.

In the second case, with a division factor of 128, the phase error increased to $\pm 2°$, but it was still within acceptable values. Especially considering that the division factor (128)

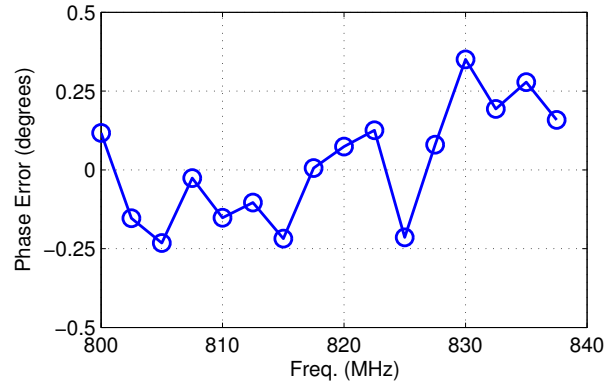

(a) 2500 kHz $\rightarrow$ $N_{\text{div}} = 32$

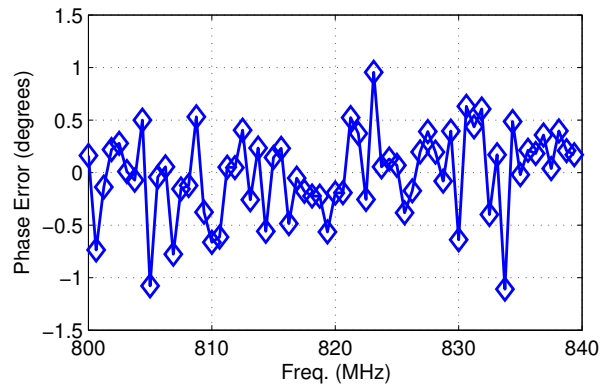

(b) 625 kHz $\rightarrow$ $N_{\text{div}} = 128$

Fig. 6. Measured phase error of the proposed method relatively to the reference measurement performed in a NVNA. Results for two different multi-sines, between 800 MHz and 840 MHz, with different frequency spacing achieved by different division factors (N_{div}).

is already very high. Once again, consecutive measurements have revealed similar results.

As shown the measured phase error stood at acceptable values even for large division factor values which proves the validity and the applicability of the developed method.

It should be mentioned that the minimum f_{fine} of 625 kHz was limited by the commercial CG used for comparison. Since a direct comparison was required for validity of the method, lower f_{fine} values could not be tested. Furthermore, the value of f_{coarse} was chosen so that an high division factor would be employed. Finally, the multi-sines start and stop frequencies were chosen so that half of an entire coarse interval (between $i f_{\text{coarse}}$ and $(i+1) f_{\text{coarse}}$) had been covered and thus the effects of error amplification were noted from the best case point up to the worst case point.

IV. Conclusion

In this paper a new method to achieve phase referenced measurements across frequency for mixer-based receivers has been presented. The proposed method allows to keep the power of each tone of the phase reference signal(s), when the grid is made thinner, contrary to what happens with other approaches.

The tradeoffs of this new presented method are: 1) a requirement for wide-bandwidth receivers in the instrument to be used and 2) a linear increase of the phase error with the decrease of the frequency grid spacing. Nevertheless, it can be a valid solution to enable sub 100 kHz frequency grid phase measurements.

Besides, in this work the method was described and successfully validated by real measurements. However, calibration of the measurement apparatus still need some additional work before this method can be broadly used by the community.

ACKNOWLEDGMENT

The authors would like to thank National Instruments, especially Dr. Marc Vanden Bossche, for the support given to this work.

This work was supported by the Fundação para a Ciência e a Tecnologia (FCT) under the projects: PEst-OE/EEI/LA0008/2013, UID/EEA/50008/2013 and EXCL/EEI-TEL/0067/2012 (CREaTION). The work of the first and second authors was supported by the PhD grant SFRH/BD/92746/2013 and Post-doc grant SFRH/BPD/92452/2013, respectively.

REFERENCES

[1] H. Reader, D. Williams, P. Hale, and T. Clement, "Comb-generator characterization," *IEEE Trans. Microw. Theory Techn.*, vol. 56, no. 2, pp. 515–521, Feb 2008.

[2] W. Van Moer and L. Gomme, "NVNA versus LSNA: enemies or friends?" *IEEE Microw. Mag.*, vol. 11, no. 1, pp. 97–103, Feb 2010.

[3] Keysight Technologies, "U9391C/F/G Comb Generators," Technical Overview 5989-7619EN, August 2014. Available: http://literature.cdn.keysight.com/litweb/pdf/5989-7619EN.pdf

[4] J. Pedro and N. Carvalho, "Designing multisine excitations for nonlinear model testing," *IEEE Trans. Microw. Theory Techn.*, vol. 53, no. 1, pp. 45–54, Jan 2005.

[5] L. Gomme and Y. Rolain, "A reference signal for a dense frequency grid phase calibration," in *IEEE Instrumentation and Measurement Technology Conf. (IMTC) Proc.*, May 2008, pp. 49–53.

[6] F. Verbeyst, M. Bossche, and G. Paillonc y, "Next-generation comb generators for accurate modulated measurements," in *81st ARFTG Microwave Measurement Conf.*, June 2013, pp. 1–4.

[7] P. Barrnuta, F. Verbeyst, A. Lewandowski, and D. Schreurs, "Optimization of a next-generation comb generator for accurate large-signal measurements on a user-defined frequency grid," in *Int. Workshop on Integrated Nonlinear Microwave and Millimetre-wave Circuits (INMMiC)*, April 2014, pp. 1–3.

[8] Y. Zhang, Z. He, H. Li, and M. Nie, "Dense spectral grid nvna phase measurements using vector signal generators," *IEEE Trans. Instrum. Meas.*, vol. 63, no. 12, pp. 2983–2992, Dec 2014.

[9] M. Mirra, M. Marchetti, F. Tessitore, M. Spirito, L. de Vreede, and L. Betts, "A multi-step phase calibration procedure for closely spaced multi-tone signals," in *75th ARFTG Microwave Measurements Conf.*, May 2010, pp. 1–5.

[10] Keysight Technologies, "Active-Device Characterization in Pulsed Operation Using the PNA-X," Application Note 1408-21, Aug 2014, pp. 10. Available: http://literature.cdn.keysight.com/litweb/pdf/5990-7781EN.pdf

[11] Rohde & Schwarz, "R&S® ZVA Vector Network Analyzer," Product Brochure, July 2014. Available: http://cdn.rohde-schwarz.com/pws/dl_downloads/dl_common_library/dl_brochures_and_datasheets/pdf_1/ZVA_bro_en_5213-5680-12_v1100.pdf

[12] National Instruments, "NI 5792R - User Manual and Specifications," Tech. Rep., May 2013. Available: http://www.ni.com/pdf/manuals/373947b.pdf

A Compact Millimeter-wave Comb Generator for Calibrating Broadband Vector Receivers

Paul D. Hale, Kate A. Remley, Dylan F. Williams, Jeffrey A. Jargon, and C. M. Jack Wang

National Institute of Standards and Technology, Boulder, CO, 80305 USA
e-mail: hale@boulder.nist.gov

***Abstract*—We propose a compact and low-cost waveform source that can be used to calibrate the magnitude and phase response of vector receivers over a bandwidth as large as a few gigahertz. The generator consists of a broadband comb generator followed by a filter and amplifier. As a demonstration, we constructed and calibrated a source suitable for calibrating vector signal analyzers operating between 43 GHz and 46.5 GHz. We then used the source to characterize the response of a commercially available vector signal analyzer. We compared the result with calibrations performed with a general-purpose source.**

***Index Terms*—Calibration, comb generator, oscilloscope, vector signal analyzer, vector signal generator.**

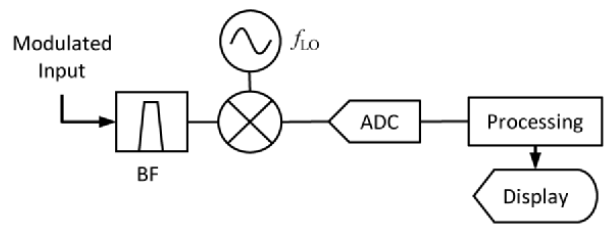

Fig. 1. Simplified schematic of a typical vector signal analayzer consisting of an optional bandpass filter (BF), a downconverter (mixer) and an analog-to-digital converter (ADC). The output of the ADC is digitally processed to form, for example, a constellation diagram or a plot of magnitude and phase verses frequency.

I. Introduction

BROADBAND vector receivers are used to characterize signals that are modulated in phase as well as amplitude such as quadrature amplitude modulation (QAM). A simplified schematic of a vector signal analyzer (VSA, a type of vector receiver) is shown in Fig. 1. The VSA consists of an optional bandpass filter, a downconverter and an analog-to-digital converter. These components cause linear and nonlinear distortion in the signal measurement as demonstrated in, *e.g.*, [1] and [2]. Assuming the instrument is operated in a linear voltage regime, linear distortion dominates the measurement and can be quite significant [1], [2]. If the distortion can be characterized, then digital processing can be used in the VSA to compensate/calibrate the measurement system.

VSA calibration at microwave frequencies is often accomplished by internal calibration routines, however at millimeter-wave frequencies, calibration can be more of an issue. In this work we propose and demonstrate a compact, low-cost waveform generator that can be used to calibrate the response of vector receivers operating in the millimeter-wave frequency regime.

A modulated signal source can be used to calibrate a VSA by assuming that the response of the source is ideal. However, modulated sources can exhibit significant phase errors that increase with modulation bandwidth, as in eg., [3]-[6]. Alternatively the source can be calibrated by use of a sampling oscilloscope and then used to calibrate the vector receiver [5]. However, most currently available general-purpose modulated sources are based on arbitrary waveform generators and frequency converters. These are typically large, expensive, and susceptible to temperature changes and mechanical shock, making them impractical for field applications such as self-calibration of a VSA.

Comb generators are often used for calibrating large-signal network analyzers (LSNAs). Since they can be based on a variety of nonlinear circuits, they are relatively simple, compact, and inexpensive, but are not as versatile as arbitrary waveform generator-based multisine sources. Some comb generators are based on step-recovery diodes and are sensitive to changes in drive power [7], [8] and temperature [9]. Recently, more stable comb generators have been demonstrated, e.g. [8], [10]. These generators produce impulse-like periodic pulses with a broad spectrum.

Because the energy in a train of impulse-like pulses is localized in a very short time interval, the power P_k in the kth tone of the comb is quite low for a given peak voltage V_p. For example, if the pulse repetition frequency is f_0 and the pulse is approximated as rectangular with duration Δ, P_k is given by

$$\begin{aligned} P_k &= \frac{V_p^2 f_0^2}{50\ \Omega}\left(\int_{-\Delta/2}^{\Delta/2}\cos(2\pi k f_0 t)dt\right)^2 \\ &\leq \frac{(V_p f_0 \Delta)^2}{50\ \Omega} \end{aligned}$$

so that $P_k \leq -81$ dBm for typical parameters $V_p = 0.1$ V, $f_0 = 10$ MHz, and $\Delta = 20$ ps. The noise background of a typical VSA is on the order of -100 dBm or more, giving only a 20 dB dynamic range without averaging. (A dynamic range on the order of 40 dB is required to obtain

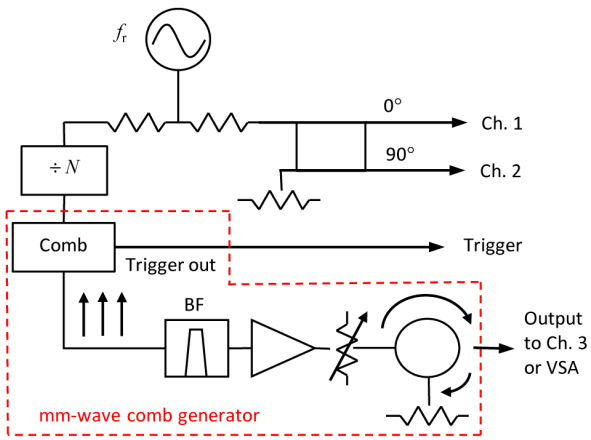

Fig. 2. Schematic drawing of the portable millimeter-wave comb generator and system used to characterize its output with known accuracy. Ports labeled Ch. 1, 2, and trigger refer to connections to a calibrated sampling oscilloscope that is used to calibrate the output of the generator, measured on channel 3. Channels 1 and 2 measure sine waves that are used by the NIST TBC algorithm [13] to correct the oscilloscope timebase. Once calibrated, the comb generator's output can be used to calibrate the linear response of a VSA.

error vector magnitude measurements that are accurate at the $\sim 1\%$ level.) If the pulse duration could be increased, by use of band limiting and/or dispersive elements, while keeping the peak voltage fixed, the power in each tone would be increased, thus improving the signal-to-noise ratio when characterizing a vector receiver. Such an approach was hinted at in [10] and [5]. A source that was designed for a similar application over the 100 MHz to 2 GHz band was described in [11]. In this work we demonstrate a comb-generator-based source, with band-limiting filter, operating between 43 GHz and 46.5 GHz. With this source, other bands up to 67 GHz are realizable.

II. Comb Generator System For millimeter-wave Applications

Our comb-generator system and the apparatus used to characterize its output are shown schematically in Fig. 2. We use commercially available components everywhere in the system. The box labeled "Comb" is a comb generator that is similar to that described in [8] but has been modified to have higher bandwidth and a 1.85 mm coaxial output connector. The output of the comb generator is filtered and temporally broadened by a 43 GHz to 46.5 GHz bandpass filter. Amplification and further filtering are provided by a 20 dB gain amplifier. An optional variable attenuator can be included for studying behavior of the vector receiver under test with respect to the signal power. The isolator is included to make the system source mismatch small and relatively constant when the reflection of the attenuator changes.

Different operating frequency ranges can be chosen by use of different filter/amplifier combinations. The highest useful frequency of our system, 67 GHz, is determined by the bandwidth and coaxial connector of the commercially available comb generator. Higher signal-to-noise ratios can be achieved by higher amplification and/or choosing a narrower bandwidth or a more dispersive filter, such as an all-pass filter [11].

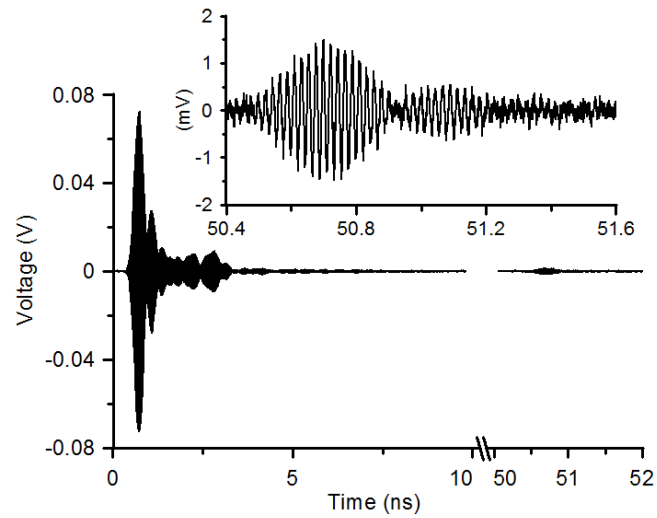

Fig. 3. Measured comb generator waveform.

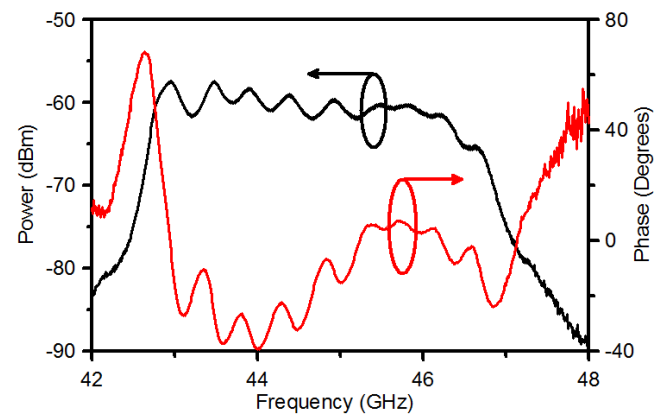

Fig. 4. Frequency domain view of comb generator waveform.

III. Calibration of the Comb Generator System

Calibration of the comb generator system is performed with a calibrated sampling oscilloscope [12] and by using procedures similar to those described in [3], [7], [13]. The system in Fig. 2 and our measurement procedures utilize the publicly available NIST timebase correction algorithm [13], [14]. The signal generator produces sine waves with frequency f_r on the order of 10 GHz used for timebase distortion correction and as the reference for the trigger. The prescaler ($\div N$ block) produces a fast transition that triggers the comb generator, which is measured on channel 3 simultaneously with the sinusoid measurements on channels 1 and 2. Because all of the samplers in the oscilloscope are activated by the same trigger pulse, the timing errors in all the channels in the oscilloscope are nearly identical [14]. The timebase correction algorithm fits the sinusoids measured on channels 1 and 2 and estimates the timing error in their measurement. This estimate is then used to correct the timing error in the measurement of the comb generator.

Portions of a waveform with repetition frequency $f_0 = 10$ MHz are shown in Fig 3. It is important to measure a full period of the waveform because temporally windowing will

cause errors if energy is present away from the main pulse, as is the case in our comb generator system (as shown in Fig. 3). In our case, this extra pulse causes ripple in the spectrum with period of 20 MHz and approximately 0.4 dB peak-to-peak magnitude variation (not resolved in Fig. 4) and 0.3 degree peak-to-peak phase variation.

A typical single waveform measurement is timebase corrected by use of the sequential timebase correction algorithm described in [13]. To facilitate further processing steps that use discrete Fourier transforms, the timebase corrected waveform is interpolated onto an evenly spaced temporal grid over an epoch equal to the period of the comb, that is, $1/f_0$. Measurements of the comb are time consuming and subject to temperature drift. The drift error is efficiently corrected by first Fourier transforming the data and then using the phase-alignment algorithm of [15]. After drift correction, the waveforms are transformed back to the time domain and averaged. In our measurements the rms noise of a single waveform is approximately 1 mV and is reduced to 0.1 mV by averaging 100 measurements. Finally, the averaged measurements are corrected for the response of the oscilloscope and impedance mismatch, as described in [16], to obtain the response of the comb generator. Note that, while the samplers are calibrated by electro-optic sampling techniques through a National Metrology Institute, all other steps described above may be implemented by users.

IV. Calibration of a VSA and Comparison With Results Obtained with Other Sources

We used our comb generator system to calibrate the response of a commercially available VSA over a bandwidth of 120 MHz centered at 45 GHz. For comparison, we also synthesized two different multisines with 10 MHz tone spacing centered at 45 GHz [4]. These multisines were calibrated with the oscilloscope in the same way as with the comb generator system and had peak voltages that were comparable to that of the comb generator system. The first multisine had a (nominally) constant phase with respect to frequency and the second had Schroeder phase [17] characteristic.

The VSA was configured to acquire an integer number of cycles of the comb [18]. The input range was set about 4 dB below saturation. Multiple measurements of all signals were acquired, aligned using the technique of [15] and then averaged. Measurements of the comb generator system were aligned to a constant phase of zero.

Results of the measurements are shown in Fig. 5. The phase of the VSA measurements were compared to those measured by the calibrated oscilloscope. Agreement in the characterization of the VSA's phase error indicates that the portable comb system is performing on par with the rack of equipment that constitutes the AWG-based source. To quantify this, we used a paired t-test [19] to compare the mean measured phase $\overline{\phi}_{\mathrm{MS}}(f_j) = (\phi_{\mathrm{C}}(f_j) + \phi_{\mathrm{S}}(f_j))/2$ of the two multisine signals with the comb phase $\phi_{\mathrm{comb}}(f_j)$. The difference $d_j = \overline{\phi}_{\mathrm{MS}}(f_j) - \phi_{\mathrm{comb}}(f_j)$ averaged over the 13 frequencies is $\overline{d} = 3 \times 10^{-5}$ and its standard deviation is $s_{\overline{d}} = 0.042$. The test statistic $\overline{d}/s_{\overline{d}} = 7.5 \times 10^{-4}$ produces

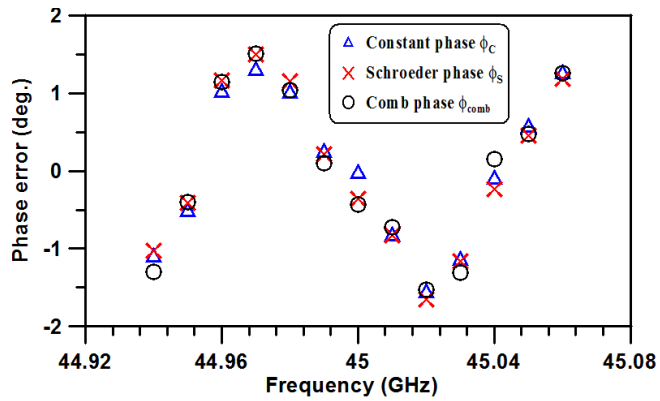

Fig. 5. Difference between phase measured with oscilloscope and phase measured with VSA based on measurements with the comb (○) and multisines with fixed phase (△) and Schroeder phase (×).

a p-value of 0.999. Therefore, based on the data, we find no significant difference between the multisine- and comb generator-based calibrations.

V. Conclusion

We presented a straightforward measurement technique for calibrating vector signal analyzers at millimeter-wave frequencies by use of a calibrated comb generator. The method uses off-the-shelf parts and is portable, allowing users to conduct these calibrations in their own labs, without use of cumbersome, expensive AWG-based sources. The results presented here demonstrate that our prototype millimeter-wave comb generator can be used for calibrating VSAs without a significant degradation in the calibration of the phase response.

VI. Acknowledgements

This work was partially supported by the Defense Advanced Research Projects Agency's Efficient Linearized All-Silicon Transmitter ICs (ELASTx) Program. The views, opinions, and/or findings contained in this article are those of the authors and should not be interpreted as representing the official views or policies, either expressed or implied, of the Defense Advanced Research Projects Agency or the U.S. Department of Defense.

References

[1] C. J. Clark, A. A. Moulthrop, M. S. Muha, and C. P. Silva, "Transmission response measurements of frequency-translating devices using a vector network analyzer", *IEEE Trans. Microw. Theory Tech.*, vol. 44, no. 12, pp.2724 -2737, Dec. 1996.

[2] D. F. Williams, H Khenissi, F. Ndagijimana, K. A. Remley, J. P. Dunsmore, P. D. Hale, C. M. Wang, and T. S. Clement, "Sampling-oscilloscope measurement of a microwave mixer with single-digit phase accuracy," *IEEE Trans. Microwave Theory Tech.*, Vol. 54, pp. 1210-1217, Mar. 2006.

[3] K. A. Remley, P.D. Hale, D.I. Bergman, D. Keenan,"Comparison of multisine measurements from instrumentation capable of nonlinear system characterization," *66th ARFTG Conf. Dig.*, Dec. 2005, pp. 34-43.

[4] K. A. Remley, P. D. Hale,D. F. Williams, J. Wang, "A precision millimeter-wave modulated-signal source", *2013 IEEE MTT-S Int. Microwave Symp.*, 2013.

[5] D. A. Humphreys, M. R. Harper, and M. Salter, "Traceable calibration of vector signal analyzers", *75th ARFTG Microwave Meas. Conf.*, 2010.

[6] D. Rabijns, W. Van Moer, and G. Vandersteen, "Using multisines to measure state-of-the-art analog-to-digital converters," *IEEE Trans. Instrum. Meas.*, vol. 56, no. 3, pp. 1012-1017, June 2006.

[7] H. C. Reader, D. F. Williams, P. D. Hale, and T. S. Clement, "Characterization of a 50 GHz comb generator," *IEEE Trans. Microwave Theory Tech.*, vol. 56, no. 2, pp. 515-521, Feb. 2008.

[8] D. Gunyan and Y.-P. Teoh, "Characterization of active harmonic phase standard with improved characteristics for nonlinear vector network analyzer calibration," *2008 IEEE MTT-S Int. Microwave Symp.*, pp. 73-79, 2008.

[9] J. A Jargon, J. D. Splett, D. F. Vecchia, and D. C. DeGroot, "An empirical model for the warm-up drift of a commercial harmonic phase standard," *IEEE Trans. Instrum. Meas.*, vol. 56, no. 3, pp. 931-937, June 2007.

[10] D. B. Gunyan and J. B. Scott, U.S. Patent No. 7,423,470 B2, Sept. 9, 2008.

[11] T. Van der Broeck, R. Pintelon, and A. Barel, "Design of a microwave multisine source using allpass functions estimated in the Richards domain," *IEEE Trans. Instrum. Meas.*, vol. 43, no. 5, pp. 753-757, Oct. 1994.

[12] T. S. Clement, P. D. Hale, D. F. Williams, C. M. Wang, A. Dienstfrey, and D. A. Keenan, "Calibration of sampling oscilloscopes with high-speed photodiodes," *IEEE Trans. Microwave Theory Tech.*, vol. 54, pp. 3173-3181 (Aug. 2006).

[13] C. M. Wang, P. D. Hale, J. A. Jargon, D. F. Williams, and K. A. Remley, "Sequential estimation of timebase corrections for an arbitrarily long waveform," *IEEE Trans. Instrum. Meas.*, vol. 61, no. 10, pp. 2689-2694, Oct. 2012.

[14] P. D. Hale, C. M. Wang, D. F. Williams, K. A. Remley, and J. Wepman, "Compensation of random and systematic timing errors in sampling oscilloscopes," *IEEE Trans. Instrum. Meas.*, vol. 55, no. 6, pp. 2146-2154, Dec. 2006.

[15] K. A. Remley, D. F. Williams, D. Schreurs, G. Loglio, and A. Cidronali, "Phase detrending for measured multisine signals, *61st ARFTG Conf. Dig.*, June 2003, pp. 73-83.

[16] D. F. Williams, T. S. Clement, P. D. Hale, and A. Dienstfrey,"Terminology for High-Speed Sampling-Oscilloscope Calibration," *68th ARFTG Conference Digest, Boulder, CO, Nov. 30-Dec. 1, 2006*.

[17] R. Pintelon and J. Schoukens, *System Identification: A Frequency Domain Approach*, New York, NY: IEEE Press, 2001.

[18] M. D. McKinley, K. A. Remley, M. Myslinski, and J. S. Kenney,"Eliminating FFT artifacts in vector signal analyzer spectra," *Microwave Journal*, vol. 49, no. 10, pp. 156-164, Oct. 2006.

[19] Peter W. M. John, *Statistical Methods in Engineering and Quality Assurance*, John Wiley & Sons, 1990.

Design and Analysis of a Verification Device for the Nonlinear Vector Network Analyzer

Mohammad Rajabi*, David A. Humphreys†, Troels Nielsen‡,
Paweł Barmuta*§, Dominique Schreurs*
*Department of Electrical Engineering, KU Leuven, B-3001 Leuven, Belgium
†National Physical Laboratory, Hampton Road, Teddington, Middlesex, TW11 0LW, U.K.
‡Keysight Technologies, Alfred Nobels Vej 21D, 9220 Aalborg East, Denmark
§Institute of Electronic Systems, Warsaw University of Technology, 00-665 Warsaw, Poland

***Abstract*—We propose a verification device to validate the calibration of a nonlinear vector measurement instruments such as Nonlinear Vector Network Analyzer (NVNA). The verification device is a two-port device that has two operating modes, namely linear and nonlinear. The designed circuit's response is almost insensitive to small harmonic mismatches of the instrument ports ($|\Gamma| < 0.1$). Since neither an amplifier nor a circulator is used, the traceability procedure of the device to Electro-Optical Sampling (EOS) is less complicated compared to earlier prototypes.**

***Index Terms*—Verification device, Network analyzer, NVNA, LSNA, Verification of calibration, Traceability.**

I. Introduction

Our objective is to develop a nonlinear verification device to confirm the quality of the calibration of a Nonlinear Vector Network Analyzer (NVNA) in the same way that a linear verification device is used to verify the calibration of a linear VNA [1]. The basic differences between the linear and nonlinear calibration are explained in [2]. Calibration of an NVNA requires absolute vector voltage and therefore Radio Frequency (RF) power and phase standards are needed in addition to the traditional impedance and transmission standards. Harmonic comb generators are commonly used as the "phase standard". Although our main goal is to design a reference device to validate the calibration in NVNA measurement system, the verification device can also be used to verify the calibration of a Large Signal Network Analyzer (LSNA) as well. The LSNA and NVNA are respectively based on the sampler-based methodology and the mixer-based methodology [3] to convert the RF bandwidth to the IF bandwidth.

The verification device should allow the user to verify both the linear and the nonlinear calibrations of the NVNA with a single-connection of the device to the NVNA. The user measures the device on the NVNA and by comparing the measurement results with the traceable data delivered with the verification device, the user can evaluate the calibration of the instrument. The verification device should have the following properties:

1) It should be a two-port device;
2) It should operate in two modes: linear and nonlinear;
3) In the linear mode, the linear calibration of the NVNA can be verified;
4) In the nonlinear mode, the aim is to verify the power and phase calibrations of the NVNA;
5) In the nonlinear mode, the fundamental frequency is 2 GHz and the number of harmonics is five;
6) The behaviour of the device in the nonlinear mode should be insensitive to small load harmonic mismatches of the instrument ($|\Gamma| < 0.1$).

The last property is essential since mismatch characteristics of instruments are different even when comparing two NVNAs from the same manufacturer.

So far, related research has been limited to a verification device working only in the nonlinear mode. The first attempt was presented in [4]. In [5], a method was proposed based on manipulating the behavioral model of the device to predict the output signal as a function of the load impedance. If the measured signal is different from the predicted signal then this indicates a poor calibration of the NVNA. The method did not work very well, because the device was not insensitive enough to harmonic load mismatches. In [6] and [7], nonlinear verification devices are described that use an amplifier as the nonlinear block. To make the circuit insensitive to the output mismatch in [6] and [7], the waves going in and out are controlled by a feedback system, so the circuit behaviour remains the same and the waves remain almost the same (independent of the load and source mismatches). Although the results are good, the circuit's traceability procedure is complicated.

In our design of verification device, we have avoided the use of an amplifier in the nonlinear block and the use of a circulator or amplifier in the Mismatch Compensation Block (MCB) in order to make the traceability of the device to Electro-Optical Sampling (EOS) [8] as simple and accurate as possible. Instead we have used diodes in the nonlinear block to generate harmonics and coupled lines in the MCB to equalise the amplitudes of the harmonics and to make the circuit less sensitive to mismatch at the output. Our main focus was on the effect of load mismatch as in [6] and [7]. We found that source mismatch, unlike load mismatch, does not have a great impact on the performance of the verification device. We tried to design the device to be applicable in linear mode as well as in nonlinear mode. The diodes are placed in such a configuration that, when the diodes are reverse biased, the device becomes passive and can be used as linear verification device without any physical replacement. In Section II, we describe the design approach adopted, and then in Section III,

978-1-4799-8887-7/15/$31.00 ©2015 IEEE

the measurement setup and results are explained.

II. Verification Device Design

Fig 1a shows the schematic of the proposed verification device. The nonlinear block generates the fundamental and harmonics power. The objective of the Mismatch Compensator Block (MCB) is to reduce the sensitivity of the verification device to output mismatches.

The nonlinear block is an IC that consists of four diodes in limiter configuration (Fig 1a). These diodes are capable of handling high drive levels without degrading frequency performance [9]. The IC can be readily integrated into microwave design. One of the features of this IC compared to its counterpart in [6], [7] and [10] is that it just acts as a transmission line if it is reversed biased and the input excitation is smaller than $-20\,\mathrm{dBm}$. Single-layer capacitors are used as bypass capacitor in the biasing configuration of the IC.

The MCB consists of two cascaded coupled lines. By using two-stage coupled lines and using the isolated ports of the coupled lines, an isolator and a high-pass filter function are achieved. By connecting the nonlinear block to the MCB, the harmonics have a similar power level as the fundamental, so the uncertainty of their measurement will be smaller. Moreover, the fundamental frequency signal that has the dominant power at the output of IC (point M in Fig 1a) sees a large mismatch due to high pass filter characteristics of the MCB, thus the reflected wave will drive the diodes into more nonlinear condition and harmonics will be more powerful. A high-quality RF PCB material was used for the MCB to facilitate comparison with the simulation results. The substrate properties are as follows: relative dielectric constant=9.8, substrate thickness =1.27 mm, top cladding = 17.5 um.

The simulation is conducted in ADS 2014. The purpose of the simulation is to find out the effect of the MCB design on the insensitivity level. We do not know the pattern or statistic variation of the port impedances of NVNA instrument to another NVNA instrument. Therefore, in Monte Carlo analysis, the impedance at each harmonic frequency is independently and randomly with an "uniform distribution" changed in the circle ($|\Gamma| < 0.1$).

The reduced load sensitivity comes at the price of lower output power e.g., the MCB insertion loss is 50 dB at 2 GHz and 10 dB at 10 GHz. The output power starts to decrease above 12 GHz (Fig 1b) so we do not advise to use the device above 10 GHz. To better quantify the effect of the MCB, a "Figure of Merit" (FOM) is defined.

The FOM expression based on the waves for R different load conditions at $\mathrm{n_{th}}$ harmonic is defined as follows [6]:

$$\mathrm{FOM} = \left[\frac{1}{R} \frac{\sum_{r=1}^{R} |\widetilde{\mathrm{B2}}(\mathrm{n}\omega, \Gamma_\mathrm{r}) - \overline{\mathrm{B2}}(\mathrm{n}\omega)|^2}{|\overline{\mathrm{B2}}(\mathrm{n}\omega)|^2} \right]^{\frac{1}{2}} \times 100 \qquad (1)$$

	2 GHz	4 GHz	6 GHz	8 GHz	10 GHz
Without MCB	0.51	6.51	7.18	18.18	16.97
With MCB	0.32	0.83	0.76	1.24	1.04

(a) Only the output impedances are varying

	2 GHz	4 GHz	6 GHz	8 GHz	10 GHz
Without MCB	2.16	9.27	7.99	26.62	24.46
With MCB	1.80	4.09	1.93	33.24	7.04

(b) Input and output impedances are varying

Table I: Calculated FOM of the proposed design

Γ_r corresponds to R_{th} load condition and n_{th} harmonic. The B2 waves are first phase aligned based on Equation (2). The new $\widetilde{\mathrm{B2}}$ are calculated as follows [6]:

$$\begin{aligned} \angle \widetilde{B2}(n\omega, \Gamma_r) &= \angle \mathrm{B2}(n\omega, \Gamma_\mathrm{r}) - n\angle \mathrm{A1}(\omega, \Gamma_r) \qquad (2) \\ |\widetilde{\mathrm{B2}}(n\omega, \Gamma_r)| &= |\mathrm{B2}(n\omega, \Gamma_r)| \end{aligned}$$

In simulation, the 50 Ω load are known so the $\overline{\mathrm{B2}}(n\omega)$ is the situation with 50 Ω load in simulation. In measurement, we choose $\overline{\mathrm{B2}}(n\omega)$ as

$$\overline{\mathrm{B2}}(n\omega) = \frac{1}{R} \sum_{r=1}^{R} \widetilde{\mathrm{B2}}(\mathrm{n}\omega, \Gamma_\mathrm{r}) \qquad (3)$$

The smaller the measured FOM is in these measurements, the more insensitive the device is towards load and source impedances. The calculated FOM using Equation (1) is shown in Table Ia. To show the influence of the mismatch compensator block, the FOM is shown for the case without mismatch compensator block as well.

To understand more about the mismatch effect of the instruments' ports, the source mismatch is considered in Monte Carlo analysis in simulation. Considering whether only load impedance is changing or load and source impedances are changing has an impact on the FOM that is shown in Table Ib. When both load and source impedances are changing the FOM at 8 GHz increases dramatically. By changing the load and source impedances in this design, there are plenty of possible situations that result in resonant frequencies. Those frequencies that undergo such behavior will have FOM's performance decrement. Moreover, we conclude that the MCB has not a significant effect on source mismatch unlike the load mismatch, because source mismatch changes the delivered power to the IC. Since the nonlinear behavior of the IC is completely input power dependent, the variation of input power changes fundamentally the behavior of the IC. By using only a simple passive component such as MCB, controlling the delivered power is not possible. Therefore, using a MCB again in the input will not increase the performance.

III. Experimental Results

The realized circuit is shown in Fig 2. The measurement of the nonlinear verification device was done by an NVNA. The same device can be used to verify calibration in LSNA as well. The nonlinear verification device was measured with an input RF power of -20 dBm (linear mode) and 10 dBm (nonlinear

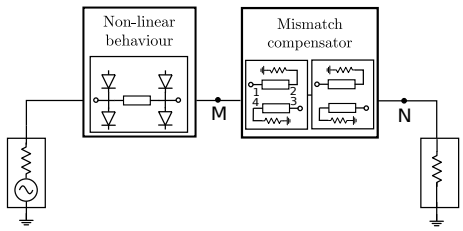

(a) Simplified block diagram consisting of a nonlinear block to generate a train of harmonics and another block to improve the performance of the total circuit with respect to output mismatch

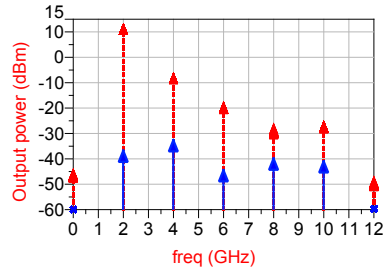

(b) (Red) The power spectrum at point N in Fig 1a when the point M is short circuited to the point N. . (Blue) The power spectrum at point N in Fig 1a when the MCB is placed between the point M and N

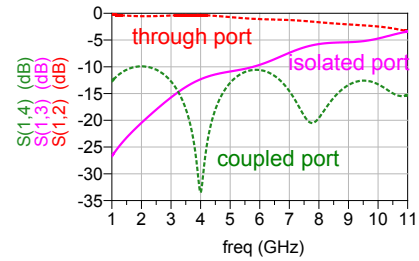

(c) S-Parameters magnitudes versus frequency of one stage coupled-lines of MCB

Figure 1: Proposed verification device design

mode). We used the measurement setup that is shown in Fig 3. This configuration allows to change the load after calibration from $50\,\Omega$ to any desired value.

Non-Linear mode

After the calibration we put loads consisting of [0, 6, 10, 16, 20] dB attenuator plus short/ open/ load standards to provide a range of different loads to the DUT. The averaging number in NVNA was 100 and the IF bandwidth was 30 Hz for each measurement. The FOM corresponding to those measurements that have $|\Gamma| < 0.1$ is shown in Table II. The higher values correspond to higher frequencies, where the isolation of the nonlinear devices is lower. By increasing the mismatch (specially $|\Gamma| > 0.3$) at the output of the DUT, the FOM increases (Fig 4).

In [10], the performance over the bandwidth of interest with condition of $|\Gamma| < 0.2$ is reported as quadratic mean of the FOM as 1.5%. If the bandwidth is considered From 2 GHz to 8 GHz, our FOM is 2.1% that is acceptable compared to its amplifier-based counterpart [10].

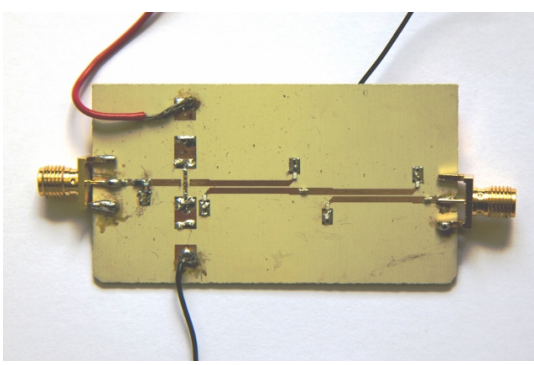

Figure 2: Physical realization of the proposed design

Linear mode

We used the same measurement setup like in Fig 3 with the fixed load as $50\,\Omega$. In order to make the device work in the linear mode as explained in Section II, the device should

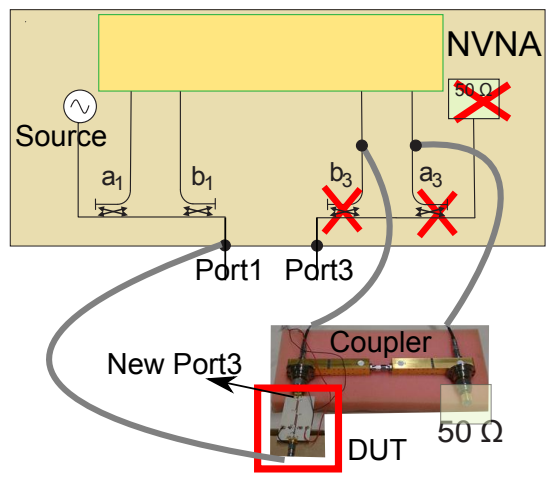

Figure 3: Measurement setup to change the load after calibration from $50\,\Omega$ to any desired value. (the simplified diagram of NVNA is from [3])

	2 GHz	4 GHz	6 GHz	8 GHz	10 GHz
Simulation (With MCB)	0.32	0.83	0.76	1.24	1.04
Measurement	1.2	3.2	2.4	2.3	12.8

Table II: FOM comparison between measurements and simulations

be reverse-biased with 2 V and the excitation should be -20 dBm. We have to be sure that harmonics are not generated by these specifics.

To check the linear mode performance, the circuit is reverse-biased and excited with two values of -10 dBm and -20 dBm. The output is measured and showed in Fig 5. When the device is excited with -20 dBm and -10 dBm, the difference between the fundamental and the harmonics respectively is about 30 dB and 20 dB. Since the device excited by -20 dBm operates in the linear mode, the verification device can be used as linear verification device as well.

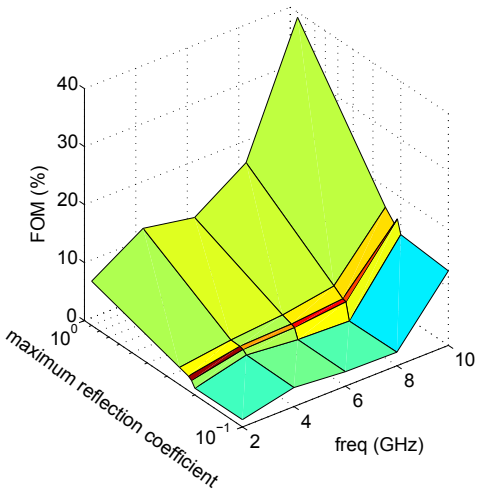

Figure 4: FOM versus frequency and the mismatch at the output

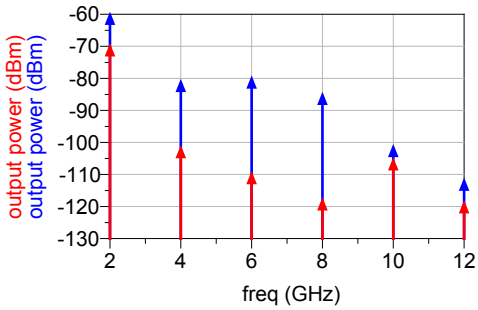

Figure 5: Power spectrum of the output is shown to evaluate the performance of the device in linear mode. (blue) input power is -10 dBm (red) input power is -20 dBm

IV. Conclusions

In this work, a verification device to check nonlinear vectorial calibrations and linear calibration has been built and tested. The device has two modes. When the device is biased in the desired operating point, it acts in nonlinear mode. The device mode is linear when the device is reverse biased and the excitation signal is small signal. By operating the device in small-signal and reverse biasing the nonlinear block, the linear calibration can be verified. The nonlinear mode is performed by doing a large signal excitation. The input power level should be about 10 dBm to drive the nonlinear block into nonlinear behavior. The output harmonics have similar power level as the fundamental. so the uncertainty of their measurement will be close.

All measurements are frequency-based measurements. No impedance mismatch corrections have been applied to the results. The achieved average Figure of Merit (FOM) over frequency of the output wave is 2.1% (if the FOM corresponding to10 GHz is considered then the average FOM would be 4.3%) with minimum value of 1.2%. The device is insensitive to $|\Gamma| < 0.1$ mismatch. The device becomes more mismatch sensitive above $10\,\mathrm{GHz}$ even when $|\Gamma| < 0.1$. The design is not using any amplifier or circulator or any vague system that would make the traceability less certain and more complicated. The price of not using amplifier or usual isolator is “a device without traceability procedure complexity” that was our goal.

V. Acknowledgments

The work has been supported by the EMRP joint research project ”SIB62 HF Circuits”. The EMRP is jointly funded by the EMRP participating countries within EURAMET and the European Union. Moreover, the authors like to thank Dr. Ken Wong from Keysight Technologies for the fruitful discussions.

References

[1] R. Ginley, “Confidence in VNA measurements,” *IEEE Microwave Magazine*, vol. 8, no. 4, pp. 54–58, Aug 2007.

[2] W. Van Moer and Y. Rolain, “A large-signal network analyzer: Why is it needed?” *IEEE Microwave Magazine*, vol. 7, no. 6, pp. 46 –62, December 2006.

[3] W. Van Moer and L. Gomme, “NVNA versus LSNA: enemies or friends?” *IEEE Microwave Magazine*, vol. 11, no. 1, pp. 97 –103, feb. 2010.

[4] U. Lott, “Measurement of magnitude and phase of harmonics generated in nonlinear microwave two-ports,” *IEEE Transactions on Microwave Theory and Techniques*, vol. 37, no. 10, pp. 1506–1511, Oct 1989.

[5] Y. Rolain, W. Van Moer, C. Gaquière, D. Ducateau, M. Fernandez Barciela, D. Schreurs, M. Vanden Bossche, and F. Verbeyst, “A round-robin benchmark for the large signal network analyzer,” in *26th Benelux Meeting on Systems and Control*, Lommel, Belgium, March 2007, p. 82.

[6] K. Wang, S. Adhikari, A. Ghiotto, and K. Wu, “Multiharmonic generator for large-signal-network-analyzer verification,” *IEEE Microwave Magazine*, vol. 15, no. 1, pp. 120–128, Jan 2014.

[7] S. Adhikari, A. Ghiotto, K. Wang, and K. Wu, “Development of a large-signal-network-analyzer round-robin artifact,” *IEEE Microwave Magazine*, vol. 14, no. 1, pp. 140–145, Jan 2013.

[8] D. Humphreys, M. Harper, J. Miall, and D. Schreurs, “Characterization and behavior of comb phase-standards,” in *Microwave Conference (EuMC), 2011 41st European*, Oct 2011, pp. 926–929.

[9] E. R. Ehlers, S. W. Johnsen, and D. A. Gray, “Extending millimiter-wave diode operation to 110 GHz,” *Hewlett-Packard Journal*, vol. 37, no. 11, pp. 10–14, November 1986.

[10] H. Jang, Y. Ko, and P. Roblin, “Development of multiharmonic verification artifact for the LSNA and NVNA (MTT-11),” *IEEE Microwave Magazine*, vol. 14, no. 1, pp. 134–139, Jan 2013.

Calibration of channel mismatch in time-interleaved real-time digital oscilloscopes

Chihyun Cho[1], Joo-Gwang Lee[1], Paul D. Hale[2], Jeffrey A. Jargon[2], Peter Jeavons[2], John Schlager[2], and Andrew Dienstfrey[2]

[1]Center for Electromagnetic Wave, Korean Research Institute of Standards and Science, Daejeon, Korea
[2]National Institute of Standards and Technology, 325 Broadway, M/S 815.01, Boulder, CO 80305 USA
Email: chihyun.cho@kriss.re.kr

Abstract — A novel method is proposed for the calibration of channel mismatch in a time-interleaved real-time digital oscilloscope (RTDO). A simple simultaneous equation is derived from the Fourier transform of the time-interleaved signals. Thus, it only requires a transfer function of time-interleaved ADCs (TIADCs), while most of previous works have employed additional filters. A measurement method for the transfer function of a commercial RTDO is also proposed. The accuracy of the calibration method is determined by the noise produced after the interleaving process. To validate the proposed method, we measure two-tone signals using a commercial RTDO. The calibrated results clearly show signals at spurious frequencies are substantially reduced.

Index Terms — Oscilloscope, channel mismatch, calibration, time interleaved, TIADC.

I. Introduction

Impairments of time-interleaved analog-to-digital converters (TIADCs) include gain, sampling time, and offset mismatch terms [1]. Correction methods for the errors of TIADCs have been extensively discussed in the literature [2-4]. At higher frequencies, the defects in components, such as sample and hold (S/H) circuits and pre-amplifiers (or attenuators) are critical since fabricating identical components is extremely difficult. In addition, the system responses of these RF components vary as a function of frequency.

Thus, to comprehensively calibrate the systematic errors in time-interleaved real-time digital oscilloscopes (RTDO), a novel calibration method is required for handling frequency-dependent channel mismatch terms.

Recently lots of research has been reported for the calibration of the frequency response mismatch [5-8]. Most of these works are concerned with calibrating the channel mismatch by applying FIR type filters on each channel. As a result, the accuracy of the calibration is greatly dependent on the design of the filter. In [6], the calibration is performed in the frequency domain. The method separates the frequency regions depending on the number of channel, and determines the multiplying coefficients. As the number of channels increases, the complexity of the formula is drastically increased.

In this paper, we have derived a simple simultaneous equation for the time-interleaved signals in the frequency domain. Thus, the input and the output signals of the RTDO can be represented as a matrix form with a transfer function of the scope, and the measured signal can be easily calibrated by the inverse of the matrix. Also we have developed a novel calibration procedure for the commercial RTDO, and the proposed method and procedure have been validated.

II. Calibration Method

The basic diagram of an RTDO employing TIADCs is shown in Fig. 1(a). The input signal is divided into M channels and amplified (or sometimes attenuated). Each signal passes through an S/H circuit, and then an ADC converts the analog signal to a digital signal. This process can be equivalently represented as a sum of transfer functions $H_k(f)$ and DC offsets as shown in Fig. 1(b).

To calibrate the transfer functions $H_k(f)$, the measured data should be separated according to the channel as shown in Fig. 2. The output of the TIADC system $y(t)$ is a convolution of the input signal $x(t)$ and the transfer function $h(t)$:

$$y(t) = (x * h)(t) \tag{1}$$

To separate data sets for each channel, we first define a uniform time mesh $\vec{t}$:

$$\vec{t} = [t_1,\ t_2,\ \cdots,\ t_N]^T \in \mathbb{R}^{N\times 1},\ t_i = t_1 + iT_s,\ i \in \{2,\ 3,\ \cdots,N\} \tag{2}$$

, where T_s is a sampling time interval. On this time mesh the sampled, discrete, output of the TIADC system is a vector $\vec{y} \in \mathbb{R}^{N\times 1}$. The ith entry of this output vector is given by:

$$\vec{y}[i] = y(t_i) = \sum_{j=1}^{N} x(t_i - t_j)h(t_j),\ i \in \{1,\ 2,\ \cdots,\ N\}. \tag{3}$$

We next subsample the output into M vectors that each contain data of a single channel or ADC. The vector $\vec{y}_k$ represents the data collected by the kth channel. The $\vec{y}_k$ vector will have (N/M) entries, $\vec{y}_k \in \mathbb{R}^{(N/M)\times 1}$, and the ith component is given as:

$$\vec{y}_k[i] = \vec{y}[(i-1)M + k],\ i \in \{1,\ 2,\ \cdots,\ N/M\}. \tag{4}$$

The Fourier transform of $\vec{y}_k$ is:

$$Y_k(f) = \frac{1}{MT_s}\sum_{m=-\infty}^{\infty} X(f - \frac{m}{MT_s})H_k(f - \frac{m}{MT_s})e^{-j2\pi k\frac{m}{M}}. \tag{5}$$

978-1-4799-8887-7/15/$31.00 ©2015 IEEE

The sampling time interval of the separated data set $y_k(t)$ is increased from T_s to MT_s. Thus the under-sampled signal produces an aliasing M times with $e^{-j2\pi km/M}$ rotation vectors [5, 6].

Eq. (5) is graphically represented in Fig. 3 for M=4 and k=1. Fig. 3(a) shows the spectrum of the signal $X(f)H_1(f)$, which is produced when the signal is fully sampled. The signal is assumed band-limited (BW < $F_s/2$, $F_s=1/T_s$), thus the hashed triangle refers to the image frequency spectrum. Generally, TIADCs perform under-sampling, and aliasing is produced. If we consider the signal spectrum as four parts ($iF_s/M < f < (i+1)F_s/M$: i=0, ···, M-1), each spectrum can be represented as Fig. 3(b) – (e). The signal spectrum (m=0) is the same as the fully sampled signal spectrum as shown in Fig. 3(a), and the aliasing spectra (m=1, 2, 3) are rotated by $e^{-j\pi m/2}$ since the response is channel 1 (or k=1). Thus the total spectrum (or under-sampled spectrum) through channel 1 is the sum of Fig. 3(b) to Fig. 3(e), and can be represented as:

$$Y_1(f)=\frac{1}{M}\Bigg((X(f)H_1(f)+X(f-\frac{F_s}{M})H_1(f-\frac{F_s}{M})e^{-j2\pi 3\frac{1}{M}}+ X(f-2\frac{F_s}{M})H_1(f-2\frac{F_s}{M})e^{-j2\pi 2\frac{1}{M}}+ X(f-3\frac{F_s}{M})H_1(f-3\frac{F_s}{M})e^{-j2\pi 1\frac{1}{M}}\Bigg) \quad (6).$$

Eq. (6) can be formulated in a more general matrix form as:

$$\begin{bmatrix} Y_0(f) \\ \vdots \\ Y_{k-1}(f) \end{bmatrix}=\frac{1}{M}\begin{bmatrix} H_0(f)e^{-j2\pi(M-0)\frac{0}{M}} & \cdots & H_0(f-\frac{mF_s}{M})e^{-j2\pi(M-m)\frac{0}{M}} \\ \vdots & \ddots & \vdots \\ H_{k-1}(f)e^{-j2\pi(M-0)\frac{k-1}{M}} & \cdots & H_{k-1}(f-\frac{mF_s}{M})e^{-j2\pi(M-m)\frac{k-1}{M}} \end{bmatrix}\begin{bmatrix} X(f) \\ \vdots \\ X(f-\frac{mF_s}{M}) \end{bmatrix} \quad (7)$$

Finally, the calibration of the channel mismatch in an RTDO can be regarded as a linear algebra problem. The input signal $X(f)$ can be reconstructed from the transfer function $H(f)$ and the measured data set $Y(f)$ using (7).

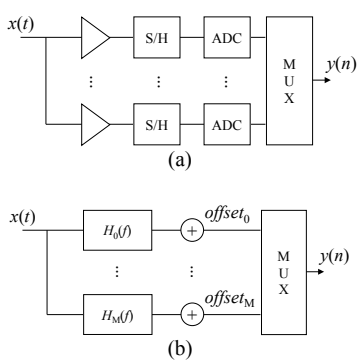

Fig. 1. Block diagram of RTDO with TIADCs structure (a) actual system (b) equivalent block diagram.

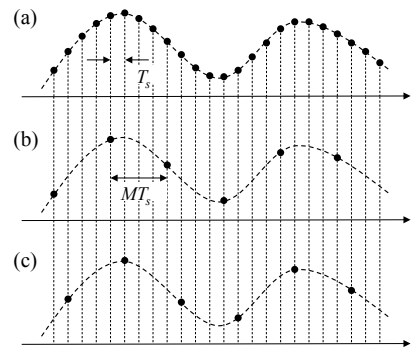

Fig. 2. Separated data set depending on each channel. Four channels (M=4) is assumed. (a) raw measurement (b) $y_0(t)$ (c) $y_1(t)$.

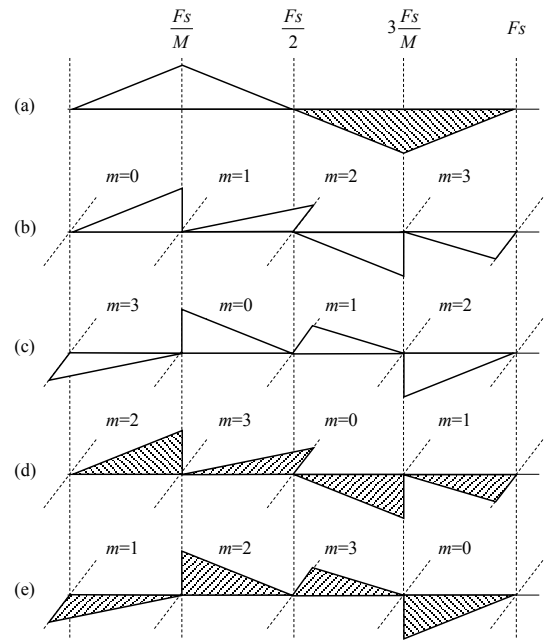

Fig. 3. Frequency spectrum (a) $X(f)H_1(f)$, (b)$Y_1(f)$ where $0<f<F_s/M$, (c) $Y_1(f)$ where $F_s/M<f<F_s/2$, (d) $Y_1(f)$ where $F_s/2<f<3F_s/M$, (e) $Y_1(f)$ where $3F_s/M<f<F_s$. Here, M is chosen to be 4 for our example.

III. Simulations

The proposed calibration method is confirmed using a simulation. Here, we choose the number of channels to be 4, with transfer functions $H_k(f)$ shown in Fig. 4. As the frequency is changed from DC to $F_s/2$, the magnitudes of $H_k(f)$ are varied linearly from 1 to 0.9, 1 to 0.8, 1 to 0.5, and 1 to 1.1, and the phases are varied linearly from 0 to 0.3, 0 to -0.1, 0 to -0.3, and 0 to 0.15, respectively. The measured signal $y(t)$ is calculated using a Fourier transform coefficient as follows:

$$y_k(t)=\sum_{f=0}^{Fs}\left|H_k(f)\right|\left|X(f)\right|\cos\left(2\pi ft+\arg\left(X(f)\right)+\arg\left(H(f)\right)\right) \quad (8)$$

Then, $y(t)$ is obtained by an interleaving process (product of pulse trains like Fig. 2 from $y_0(t)$ ~ $y_3(t)$. Fig. 5(a) shows the

frequency spectrum of the input signal $X(f)$, the output signal $Y(f)$ through TIADCs, and the calibrated output signal. $Y(f)$ is greatly distorted due to the largely different transfer function among channels. However, the difference between the calibrated signal and the input signal is only -250 dB (see Fig. 5 (b) without noise). This indicates the proposed method can be used to reconstruct the input signal with negligible error. The error produced by the limitations of floating point numbers on a computer is all that remains. In addition, the proposed method does not require any information about the input signal except for the band limited condition.

Next, the effect of noise on the calibration is simulated. A random Gaussian noise of -75 dB is added before and after the time interleaving process. The output signals are also obtained using (5), and are then calibrated by applying the proposed method. The difference between the input and calibrated signals are shown in Fig. 5(b). The result of 'before interleaving' shows the same result as the absence of noise, while 'after interleaving' is increased to about -75 dB. Fig. 5(b) indicates that the noise produced after time-interleaving process is not calibrated out by the proposed method, as expected.

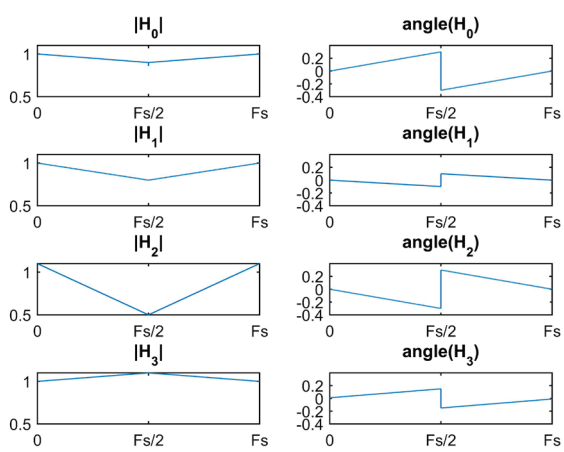

Fig. 4. Transfer function $H(f)$ used in the simulation

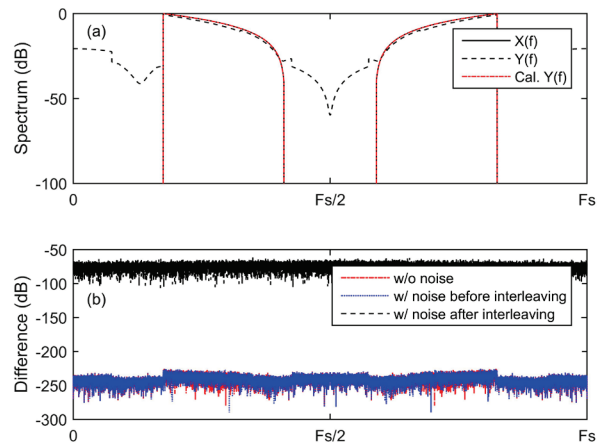

Fig. 5. Simulation results (a) frequency spectrum of input, output, and calibrated signals (b) difference between input and calibrated signals.

IV. Measurements

The proposed method is confirmed by measurements using a commercial RTDO. Fig. 6 shows the flow chart of the proposed measurement procedure. The measurement method for the transfer function of the RTDO is explained in subsection *A*, and the measured result is discussed in subsection *B*. The number of ADCs (or channels) is found by applying DC voltages to the RTDO. The different DC offset values produce M spurious signals at frequency spacing of nF_s/M frequency where n=0, ···, M-1 [4]. In this measurement, 32 spurious peaks are observed on the frequency spectrum, which means 32 ADCs are used in the RTDO.

A. Measurement of transfer function H(f)

The proposed method requires the transfer function $H(f)$ of the RTDO to be known in order to fully calibrate the measurement result. The measurement of *absolute* $H(f)$ is quite involved. It requires prior knowledge of the source, and careful consideration of the impedance mismatch between the source and the RTDO. In this paper, *relative* $H(f)$ is used to focus on the confirmation of the proposed method, and can be obtained by using a CW source and normalization of mean values:

$$H_m(f) = \frac{A_m(f)}{\overline{A}(f)} e^{j\left(\phi_m(f) - \overline{\phi}(f)\right)} \tag{9}$$

, where the over-line "$\overline{}$" denotes the mean value over the M ADCs. However, most commercial RTDOs start making measurements with a random ADC during its sampling sequence. It means that sequences of $H_m(f_1)$ and $H_m(f_2)$ typically do not align with each other by using only the CW source since the starting point of ADCs is changed every measurement. Thus an additional CW source is

simultaneously used as a reference to properly assign $H_k(f)$ to its corresponding ADC. The measured signal $y_m(t)$ can be represented as

$$y_m(t) = A_m(f)\cos(2\pi ft + \phi_m(f)) + A_m(f_{ref})\cos(2\pi f_{ref}t + \phi_m(f_{ref})) + offset_m + n(t) \quad (10)$$

, where $n(t)$ is a random noise. If we assume $n(t)$ is a normal distribution with zero mean, each parameter $A_m(f)$, $\phi_m(f)$, $A_m(f_{ref})$, $\phi_m(f_{ref})$, and $offset_m$ can be estimated using a least-square fitting. The sequences at different frequencies are aligned by comparing the reference parameters $A_m(f_{ref})$ and $\phi_m(f_{ref})$. The reference frequency should be carefully chosen not to occur at a spurious frequency that is produced due to the channel mismatch [5]. The measurement is performed multiple times, and the averaged $H(f)$ is shown in Fig. 7. The measured RTDO consists of 4 banks of 8 ADCS, and each channel has similar frequency characteristics, and unique offset values. As the frequency is increased, the channel mismatch is increased. This clearly shows the channel mismatch should be dealt with as a function of frequency in the calibration of the RTDO.

B. Calibration of channel mismatch

After measuring the *relative* transfer function $H(f)$, we apply two-tone signals (1.656 GHz and 3.007 GHz) to the RTDO as shown in Fig. 8(a). Many spurious signals are observed due to the channel mismatch. The spectra of the input signal and the spurious signals are about -40 dB and -80 dB, respectively. As a result, spurious free dynamic range (SFDR) is about 40 dB when the DC component is excluded. Fig. 8(b) shows the calibrated result using our proposed method. The offset values are first subtracted from the measurement, and then the calibrated result is obtained by solving (7). This shows that most spurious signals are removed from the measurement, and SFDR is increased by about 20 dB. Some spurious signals are still observed near the noise floor due to the non-linearity of the RTDO and harmonics of the source. Some of the spurious signals may be removed by applying the non-linearity terms in eq. (7).

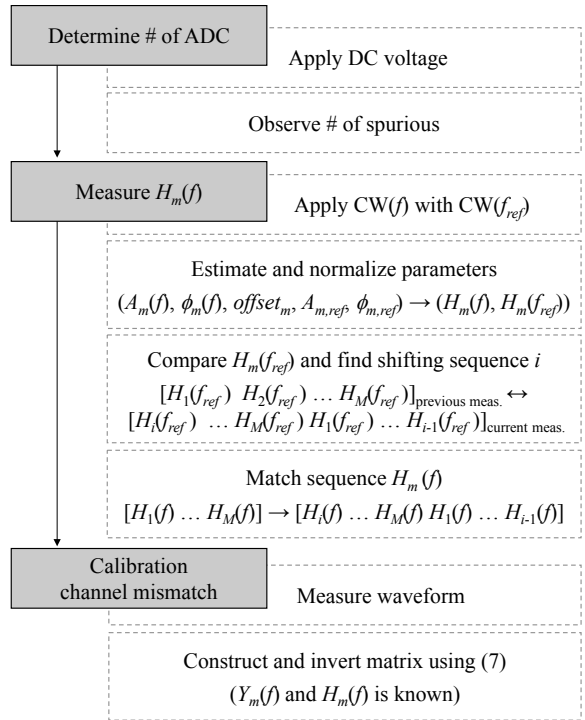

Fig. 6. Flow chart of the measurement procedure

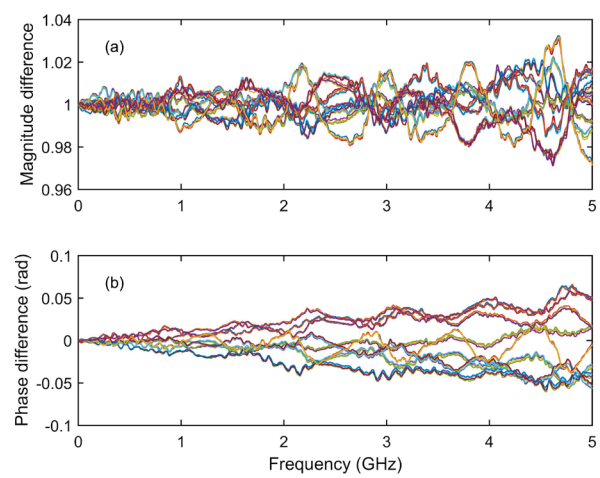

Fig. 7. TIADCs channel mismatch (a) relative magnitude difference, (b) relative phase difference.

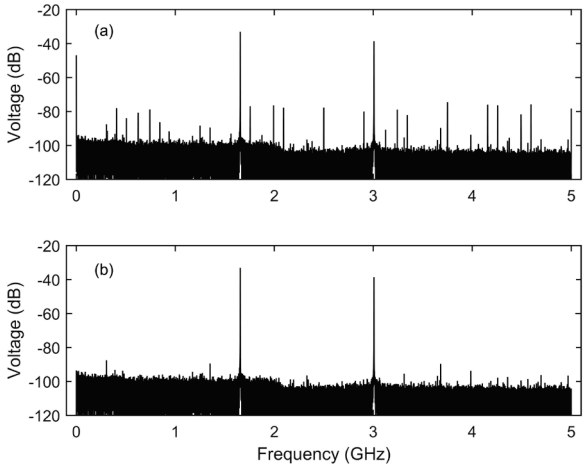

Fig. 8. Measurement result (a) before calibration (b) after calibration

V. Conclusions

In this paper, we explained our method for calibrating channel mismatches in time-interleaving ADCs. Our proposed method can be more effectively applied when the channel mismatch terms vary as a function of frequency. To confirm our proposed method, we performed simple simulations where the RTDO had 4 different channels. Here, the output signal was strongly distorted, whereas the calibrated output signal was identical to the input signal except for additional noise due to the interleaving process. Finally, we measured a signal using a commercial RTDO, and calibrated it. Only small spurious signals remained due to non-linearities in the RTDO.

Acknowledgement

This work was partially supported by the U.S. Department of Commerce, and is not subject to U.S. copyright. Also it was partially supported by the Korea Research Institute of Standards and Science under the project 'Development of Technologies for Next-generation Electromagnetic Wave Measurement Standard,' grant 15011014.

References

[1] W.C. Black and D. Hodges, "Time interleaved converter arrays," *IEEE J. Solid-State Circuits*, vol. 15, no. 6, pp. 1022–1029, Dec. 1980.

[2] A. Petraglia and S. K. Mitra, "Analysis of mismatch effects among A/D converters in a time-interleaved waveform digitizer," *IEEE Trans. Instrum. Meas.,* vol. 40, no. 5, pp. 831–835, Oct. 1991.

[3] N. Kurosawa, H. Kobayashi, K. Maruyama, H. Sugawara, and K. Kobayashi, "Explicit analysis of channel mismatch effects in time-interleaved ADC systems," *IEEE Trans. Circuits Syst. I : Fundam. Theory Appl*, vol. 48, no. 3, pp. 261–271, Mar. 2001.

[4] V. Divi and G. W. Wornell, "Blind Calibration of Timing Skew in Time-Interleaved Analog-to-Digital Converters," *IEEE J. Sel. Topics Signal Process.*, vol. 3, no. 3, pp. 509–522, Jun. 2009.

[5] M. Seo, M. J. W. Rodwell, and U. Madhow, "Comprehensive digital correction of mismatch errors for a 400-msamples/s 80-dB SFDR time-interleaved analog-to-digital converter," *IEEE Trans. Microw. Theory Tech.*, vol. 53, no. 3, pp. 1072–1082, Mar. 2005.

[6] K. Asami, "Technique to improve the performance of time-interleaved A-D converters," *in Proc. IEEE Int. Conf. Test*, Nov. 2005, pp. 851–857.

[7] C. Vogel and S. Mendel, "A Flexible and Scalable Structure to Compensate Frequency Response Mismatches in Time-Interleaved ADCs," *IEEE Trans. Circuits Syst. I, Regular Papers*, vol. 56, no. 11, pp. 2463–2475, Nov. 2009.

[8] Y. C. Lim, Y.-X. Zou, J. W. Lee, and S.-C. Chan, "Time-Interleaved Analog-to-Digital-Converter Compensation Using Multichannel Filters," *IEEE Trans. Circuits Syst. I, Regular Papers*, vol. 56, no. 10, pp. 2234–2247, Oct. 2009.

[9] L. P. Rao, N. Sitthimahachaikul, and P. J. Hurst, "Correcting the Effects of Mismatches in Time-Interleaved Analog Adaptive FIR Equalizers," *IEEE Trans. Circuits Syst. I: Reg. Papers*, vol. 59, no. 11, pp. 2529–2542, Nov. 2012

Multi-Line TRL Revisited

Yves Rolain, Mariya Ishteva, Evi Van Nechel and Francesco Ferranti
VUB dept ELEC Pleinlaan,2 1050 Brussels, Belgium

***Abstract*—An alternative is proposed for the line pairing process that underspans the multi-line Thru-Reflect-Load (M-TRL) calibration. The tensor decomposition based method shows a potential to further improve the calibration accuracy.**

I. Introduction

The multiline TRL (MTRL) calibration is one of the most accurate and widely used calibration methods for the measurement of S-parameters [2]. As a consequence, there is an extensive literature available on the subject, see for example [2], [4], [5], [6], [7]. The core concept of MTRL boils down to the fundamental knowledge that any section of an infinite, homogeneous transmission line can be perfectly described by its characteristic impedance, $Z_c(\omega)$, its propagation factor $\gamma(\omega)$, and its physical length l_0. When the reference impedance used to define the waves is set to match the characteristic impedance of the line, the associated S matrix becomes an antidiagonal matrix with elements $e^{-\gamma l}$.

Unfortunately, the behavior of a practical transmission line does not fully match this idealized situation. The transition between the coaxial field pattern in a probe or a cable and the reference standard line perturbes the wave propagation, hereby destroying the theoretic relation described above. To get around this problem, the elegant solution proposed by MTRL conceptually considers lines of different lengths to consist of a launcher section at both ends and a homogenous part in the middle of the line. If now more than one line of different length is measured, the difference in behavior between the lines is caused by a homogeneous, nearly ideal line section alone [2].

To practically remove the effect of the launcher, the state of the art methods pick an arbitrary reference line [2], [4], [5], [6], [7]. The response of the homogeneous ideal line section is then obtained as the product of the cascade T matrix of the line and the inverse T matrix of the reference line. This procedure is repeated $N-1$ times if N line standards are available.

Extensions to the original work cover the (sometimes tedious) selection of the propagation constant of the line [6], the modeling of the propagation constant over the frequency [6], or the estimation of the compensation coefficients [5]. To our knowledge, the fundamental step that consists in taking the lines in a pair-wise arrangement was never questioned up to now. This is peculiar in the sense that the selected reference line will appear in every line pair, therefore its influence on the result is expected to be emphasized w.r.t. the other lines.

In this paper, we propose to process the T-matrices of all the reference lines simultaneously rather than pair-wise. This avoids the selection of a reference line completely. Additionaly it circumvents the sometimes tedious inversion of the cascade matrix and imposes the equality of the laucher response over all lines simultaneously and by construction.

II. The line calibration workbench

For the convenience of the reader, the assumptions used for the measurements and the definitions are summarized below.

A. The measurement setup

Consider a non-ideal, repeatable, linear time-invariant 2-port Vector Network Analyzer (VNA). The instrument measures a set of N transmission lines of different, known length l_i that share the same transmission line parameters (same geometry apart from their length l_i, same material properites, same connection type). The N transmission lines share access networks X and Y. They are described by their cascade wave matrix $\mathbf{T}_X(\omega)$ and $\mathbf{T}_Y(\omega) \in \mathbb{C}^{2\times 2}$. The cascade matrix of line i is obtained as

$$\mathbf{T}_{l_i}(\omega) = \mathbf{X}(\omega)\,\mathbf{E}_{l_i}(\omega)\,\mathbf{Y}(\omega)$$

where $\mathbf{E}_{l_i}$ is a diagonal matrix as below

$$\mathbf{E}_{l_i} = \begin{bmatrix} e^{\gamma(\omega)l_i} & 0 \\ 0 & e^{-\gamma(\omega)l_i} \end{bmatrix}$$

B. Measured quantities and their uncertainty

In the M-TRL calibration, the measurement of the lines is the main part of the calibration procedure. The cascade matrix measured by the VNA is considered to be equal to the cascade matrix $\mathbf{T}_{m_i}$of each line. Because the lines are identical except for their length up to the non-idealities of the VNA, it is safe to assume that the measured cascade matrix can be written as:

$$\mathbf{T}_{m_i} = \mathbf{X}_{m_i}\mathbf{E}_{m_i}\mathbf{Y}_{m_I} = \mathbf{T}_{l_i} + \mathbf{N}_{m_i}$$

where a suffix $_m$ denotes a measured quantity. This statement holds under the equality of the geometry of the lines, under mild assumptions for the measurement noise on the $\mathbf{S}$-parameters, and for a sufficiently high signal-to-noise ratio. Then, the measurement noise on the $\mathbf{T}$ matrix can be assumed to be additive, circular normal distributed and independent over the frequency. For the model errors that account for the non-idealities in the behavior of the line, a similar assumption is used and its influence is also contained in $\mathbf{N}_{\mathbf{m_i}}$.

978-1-4799-8887-7/15/$31.00 ©2015 IEEE

C. A tensor formalism top process all lines simultaneously

To avoid the selection of a reference line, we propose to stack the measured $\mathbf{T}$ matrices at each frequency in a 3-dimensional tensor. When N reference lines are used in the calibration, this object contains N planes of 2×2 $\mathbf{T}$ parameter entries. Such a tensor can be decomposed in a number of elementary, rank 1 basis elements [1]. Put in a nutshell, this decomposition is a generalization of the well-known singular value decomposition to higher dimensional matrices. The CPD decomposition method is now well established in the linear algebra community, and there are different methods/algorithms to compute it. Software that allows to use the algorithm in the Matlab environment is freely available on the web [1]. For each separate line, the obtained decomposition yields a matrix triplet as follows

$$\mathbf{T}_{m_i} \approx \hat{\mathbf{X}}\hat{\mathbf{E}}_i\hat{\mathbf{Y}}$$

Note that a single pair of matrices $\hat{\mathbf{X}}$ and $\hat{\mathbf{Y}}$ is obtained for all the lines simultaneously. The matrices are calculated during the simulataneous decomposition of the lines performed by CPD. This result is clearly different from the classical approach of paired lines, where a different set of matrices $\hat{\mathbf{X}}, \hat{\mathbf{Y}}$ is obtained for each line pair. The question now arises whether or not this will lead to different values for the propagation factor γ of the line(s) and the calibration coefficients of MTRL.

III. Comparing CPD and line pairing

A. The considered line set

To compare both approaches we consider a set of microstrip lines whose response is simulated in Keysight Momentum. The simulator parameters are set to have a maximum accuracy for all lines. A simulation is considered here to allow for a measurement noise free context that allows to compare the accuracy of the methods rather than their noise sensitivity.

The substrate parameters are selected as follows: the dielectric material has a relative permittivity $\varepsilon_r = 3.55$, a loss tangent $\tan\delta = 0.0022$, and a height $h = 1.524\,\mathrm{mm}$. The copper conductors have a thickness $t = 35\ \mu\mathrm{m}$, and a conductivity $\sigma = 5.8\mathrm{E}7$. The transmission line geometry is defined by a width $W = 3.4\,\mathrm{mm}$. The eight lines have the randomly selected length l of 21.9, 42.6, 78.8, 99.1, 111.5, 121.2, 144.7, and 167.1 mm. The lines are simulated in a frequency range starting at 500 MHz and ending at 5 GHz with a frequency resolution of 50 MHz. The results proposed here are obtained at the lowest frequency of 500 MHz.

B. Comparing the propagation constants γ

The results obtained by CPD are compared to the classical pairing method. The shortest line is selected as a reference line for the pairing method. For the CPD case, the ratio of the propagation factors $\frac{\gamma_i}{\gamma_1}$ obtained from $\hat{\mathbf{E}}_i$is displayed, as CPD does not need to evaluate this ratio. Results are displayed in figures 1 and 2 for the absolute value of the real and imaginary part of γ. Note the close match that is obtained between both approaches. This clearly shows that CPD is indeed decomposing the set of matrices as is predicted by the theory.

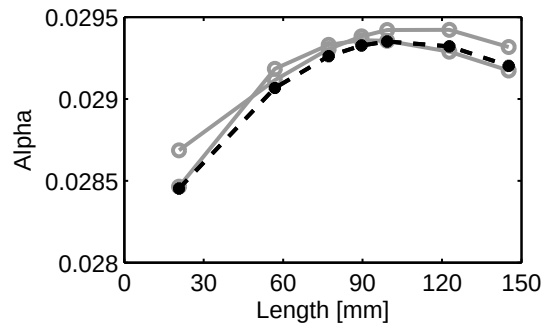

Figure 1. Real part of the propagation constant for the line pairs. (Classical in black, CPD in gray)

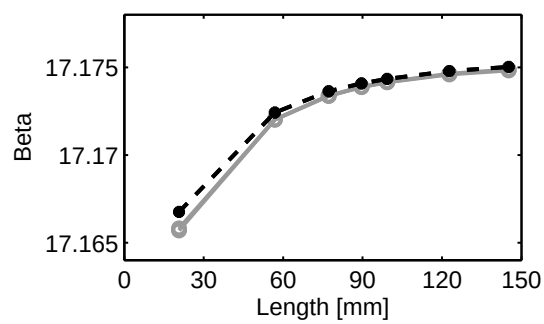

Figure 2. Imaginary part of the propagation constant for the line pairs. (Classical in black, CPD in gray)

Note also that the CPD method produces two distinct values for propagation factors while the classical approach produces two equal values. This is perfectly normal, as the symmetry between the eigenvalues is not imposed for CPD while it is imposed for the classical approach. This freedom is an advantage for CPD, as it is then used by CPD to include the small non-symmetric imperfections in the construction of the line. Imposing a symmetry that is not perfectly obeyed as in the classical method can lead to the appearance of a small bias term, both in the propagation factors and the estimated eigenvectors in $\hat{\mathbf{X}}$ and $\hat{\mathbf{Y}}$. This bias is to appear in the final calibration too.

To show that both methods do indeed extract the properties of the line, the effective permittivity and the loss tangent are calculated using the γ values as obtained before. The mean value and the standard deviation over the line pairs is summarized in table I. Their agreement for the two alternatives is extremely good and complies with the expectation. The comparison to the values obtained from the data sheet of the material for the loss tangent and from the data sheet and the linecalc utility of ADS for the effective permittivity show underestimation of roughly 3% for the relative permittivity and 25% for the loss tangent. The latter difference is somewhat higher than expected and deserves further attention. Note however that the value in the table is obtained at 2.5 GHz, while the test frequency is only 0.5 GHz.

	CPD	class	data sheet + ADS
ε_{eff}	2.6892	2.6893	2.75
σ_ε	0.001	0.001	
$\tan\delta$	0.001700	0.001696	0.0022 @ 2.5 GHz
$\sigma_{\tan\delta}$	0.00002	0.00002	

Table I
MEAN γ FOR THE LINE PAIRS AND THEIR STANDARD DEVIATION

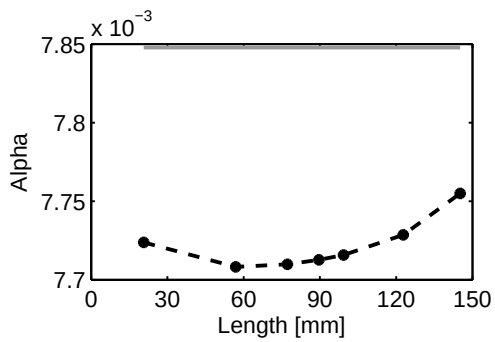

Figure 3. Real part of ratio_1 . (dashed line = classical, full grey line near the top = CPD)

C. Comparing the calibration coefficients

The situation for the eigenvectors is different, as $N-1$ sets of eigenvectors are estimated for N lines in the classical method while one single set is obtained form CPD. Remember that the ratio of the elements of these eigenvectors convey the calibration information that is used in the seminal TRL papers [3]. We label this quantity as ratio_i for the ith line pair.

The ratio_i obtained by CPD and the pairing method are compared next. The real and the imaginary part of that ratio for the two eigenvectors is shown in the figures 3, 4, 5, and 6. Note that all the ratios do indeed vary significantly for the classical method, while the CPD method obtains a constant value by construction. A preliminary study of the quantification of this variation on the accuracy of the final calibration tends to indicate that this variation is indeed significant. For the imaginary part of the ratios, one could argue that taking the mean value of the individual ratio's over the line pairs will result in a result that is similar to CPD. However, for the real part this is no longer true. For ratio_1, the real part obtained by CPD is significantly larger (close to the top of the figure) while for ratio_2 the CPD value is smaller (close to the bottom of the plot). This points towards the presence of a (small) bias, as was expected and explained above.

IV. CONCLUSION

An alternative approach is proposed for the line pairing procedure that is at the basis of the multiline TRL method. The method decomposes the T-matrices of the lines simulataneously using a numerical procedure that was orignally designed for tensor decomposition. The method is illustrated to retrieve accurately the propagation factor of the lines and one set of eigenvectors for all matrices simultaneously. As these eigenvectors are used in the calibration to determine the calibration coefficients, an increased accuracy for the overall calibration is expected.

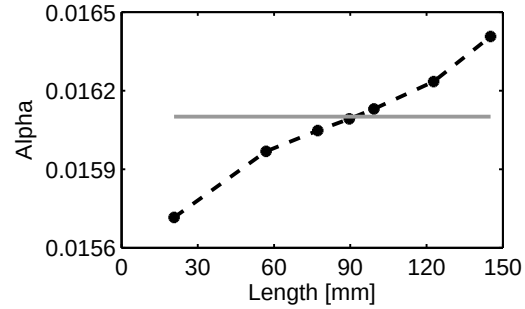

Figure 4. Imaginary part of ratio_1 . (dashed line = classical, full grey line = CPD)

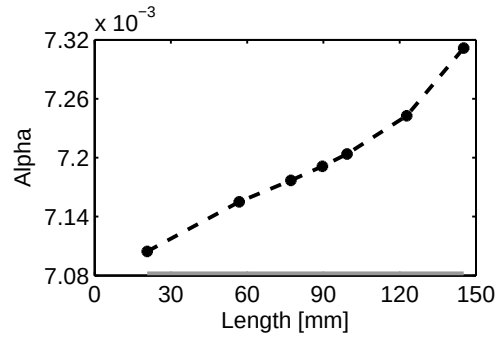

Figure 5. Real part of ratio_2 . (dashed line = classical, full grey line near the bottom = CPD)

REFERENCES

[1] L. Sorber, M. Van Barel and L. De Lathauwer; *'Tensorlab v2.0'*, Available online, January 2014. URL: http://www.tensorlab.net/.

[2] R. B. Marks, "A multiline method of network analyzer calibration," MTT IEEE Trans., vol. 39, no. 7, pp. 1205–1215, 1991.

[3] G. F. Engen and C. A. Hoer, "Thru-Reflect-Line: An Improved Technique for Calibrating the Dual Six-Port Automatic Network Analyzer," MTT. IEEE Trans., vol. 27, no. 12, pp. 987–993, 1979.

[4] D. C. DeGroot, J. Jargon, and R. B. Marks, "Multiline TRL revealed," in 60th ARFTG, 2002, 2002, pp. 131–155.

[5] K. Andersson and C. Fager, "Statistical estimation of the propagation constant in multiline calibrations", 2006 67th ARFTG, 2006, pp. 133–136.

[6] D. C. DeGroot, Y. Rolain, R. Pintelon, and J. Schoukens, *"Corrections for Nonlinear Vector Network Analyzer Measurements Using a Stochastic Multi-Line Reflect Method"*, in MTT-S, 2004, pp. 1735–1738.

[7] D. F. Williams, C. M. Wang, and U. Arz, *"An optimal multiline TRL calibration algorithm",* IEEE MTT-S, 2003, vol. 3, pp. 1819 – 1822.

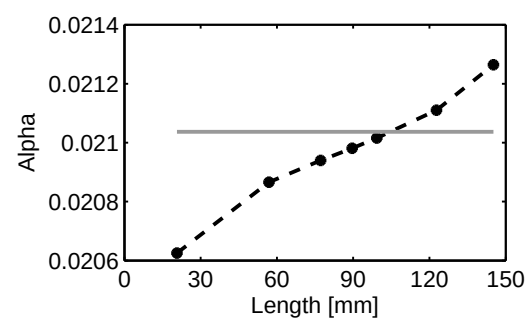

Figure 6. Imaginary part of ratio_2 . (dashed line = classical, full grey line = CPD)

Analyzing Uncertainty Matrices Associated with Multiple *S*-parameter Measurements

Nick M. Ridler, *Fellow, IEEE*, and Martin J. Salter, *Member, IEEE*

National Physical Laboratory, Teddington, UK nick.ridler@npl.co.uk

Abstract — This paper presents a detailed analysis of uncertainty matrices (i.e. measurement covariance matrices) associated with multiple complex-valued microwave scattering (*S*-) parameter measurements. The analysis is based on forming combinations of (2 × 2) sub-matrices from selected elements in the uncertainty matrix and using these sub-matrices to define uncertainty ellipses in two-dimensional measurement planes. These uncertainty ellipses can be used to assess the quality, accuracy and validity of the measurements. A simple example is given using measurements made on a waveguide mismatched line section at frequencies from 75 GHz to 110 GHz. The analysis is also useful when multiple *S*-parameter measurements are used as input quantities for measurement models used to determine other measurement quantities (i.e. as output quantities).

Index terms — S-parameters, uncertainty of measurement, uncertainty matrices, measurement covariance matrices, multivariate measurands.

I. Introduction

Since the publication, in 1993, of the ISO "Guide to the Expression of Uncertainty in Measurement" (GUM) [1], much work has been undertaken, in many areas of science and technology, to implement the general techniques outlined in the GUM.[1] In the area of high-frequency electromagnetic metrology, a key issue with implementing the techniques given in the GUM has been that many of the measurands that are encountered are complex-valued quantities, i.e. the measurand has both a Magnitude and Phase, or, equivalently, a Real and Imaginary component.

A procedure for dealing with the uncertainty in a complex-valued measurand has been described in [3, 4], where the uncertainties in the Real and Imaginary components of the measurand were analysed in terms of a (2 × 2) covariance matrix. The examples given in [3, 4] were of *S*-parameter measurements that occur in microwave metrology. The matrix formulation that was used enabled the correlation between the uncertainties in the Real and Imaginary components of the complex-valued measurand to be included in the overall expression of uncertainty. This led to the use of the correlation coefficient to describe the interrelationship between the two components of the measurand.

More recently, the procedures outlined in the GUM [1, 2] have been extended to deal with measurement situations where there are multiple output quantities (i.e. where there is more than one measurand) [5]. This extended procedure enables the interactions between all the measurands to be taken into account when establishing the uncertainty in the multiple output quantities. Correlation coefficients can be established between suitable pairs of output quantities selected from the complete set of output quantities. This leads to a correlation matrix which has the same number of elements as the uncertainty matrix. The elements in the correlation matrix are the correlation coefficients that describe all possible correlations between pairs of output quantities.

This paper applies the techniques given in [5] to the situation where there are multiple complex-valued output quantities. The techniques given in [3, 4] that accounted for the interactions between the Real and Imaginary components of an individual complex-valued *S*-parameter are extended to take account of interactions between the components of all the complex-valued *S*-parameters. This includes interactions between components of different *S*-parameters – i.e. the interaction between a component of one *S*-parameter and a component of a different *S*-parameter. For example, the interaction between the real (or imaginary) component of S_{11} and the real (or imaginary) component of, say, S_{21}, and so on.

Accounting for interactions between different *S*-parameters can be important especially in situations when the behavior of one *S*-parameter is physically related to the behavior of other *S*-parameters. For example, a measurement device that contains a significant mismatch will generate both an increase in reflection and a decrease in transmission, compared to the matched condition. The relationship between the amount of energy reflected and the amount of energy transmitted is governed by the law of conservation of energy – i.e. energy that is reflected cannot at the same time be transmitted, so, in this situation, there is clearly a strong physical relationship between reflection and transmission. For an *n*-port device (where $n > 1$) containing significant mismatch, there is expected to be correlation between the reflection coefficients, S_{ii}, ($i = 1, \ldots, n$) and the transmission coefficients, S_{ij} ($i = 1, \ldots, n$; $j = 1, \ldots, n$; $i \neq j$).

[1] Since 1993, there have been several minor revisions/updates to the GUM. The most recent edition was published in 2008 [2]. This edition can be downloaded from www.bipm.org/en/publications/guides.

978-1-4799-8887-7/15/$31.00 ©2015 European Union

In general, for measurements of multi-port devices, there may be many possible combinations of pairs of components of different *S*-parameters. However, in this paper, the investigation is restriced to measurements of two-port devices, as this is sufficient to illustrate the necessary concepts.[2] A simple example is given showing measurements made on a mismatched waveguide line in the WR-10 waveguide size, developed by OML, Inc. As mentioned above, the mismatch in this device should give rise to significant interactions between the reflection and transmission coefficients. This is investigated in terms of the interactions between the various combinations of the components of these complex-valued coefficients.

II. Concept

The *S*-parameters for a two-port device can be represented using the following scattering matrix:

$$[S] \equiv \begin{bmatrix} S_{11} & S_{21} \\ S_{12} & S_{22} \end{bmatrix} \tag{1}$$

The uncertainty for each of the four complex-valued *S*-parameters in (1) can be represented by a (2 × 2) uncertainty matrix[3]. For example, the uncertainty matrix for S_{11} is:

$$\begin{pmatrix} u^2(S_{11_R}) & u(S_{11_R}, S_{11_I}) \\ u(S_{11_I}, S_{11_R}) & u^2(S_{11_I}) \end{pmatrix} \tag{2}$$

where the sub-subscripts R and I are used to indicate the Real and Imaginary components, respectively, of an *S*-parameter, S_{ij} (i = 1, 2; j = 1, 2). This matrix represents the uncertainties in the Real and Imaginary components of S_{11}, including the interaction between these components, using the off-diagonal element $u(S_{11_R}, S_{11_I})$, or, equivalently $u(S_{11_I}, S_{11_R})$. Similar (2 × 2) matrices are used to represent the uncertainties in, and interactions between, the Real and Imaginary components of S_{21}, S_{12} and S_{22}.

In addition, other uncertainty terms are needed to represent interactions between components of different *S*-parameters. This results in an (8 × 8) uncertainty matrix being used to represent all the uncertainty information for the four *S*-parameter measurements of a two-port device, where the off-diagonal elements are used to represent all the interactions between the components of these four *S*-parameters. The elements of this (8 × 8) uncertainty matrix are listed in Table 1.

The shaded regions in Table 1 indicate the four (2 × 2) sub-matrices that represent the uncertainty associated with each of the four *S*-parameters, independent of any interactions between other *S*-parameters.

Without loss of generality, this investigation is further restricted to consider measurement of two-port devices that exhibit both reciprocity (i.e. $S_{21} = S_{12}$) and symmetry ($S_{11} = S_{22}$), as this will simplify the analysis but will still be sufficient to illustrate the necessary concepts.[4] Under these conditions, only the *S*-parameters, S_{11} and S_{21}, need to be considered. The (8 × 8) uncertainty matrix described in Table 1 can therefore be reduced to include only terms involving uncertainty in S_{11} (Real and Imaginary), or S_{21} (Real and Imaginary), or a combination of both S_{11} and S_{21} (Real and Imaginary). The (8 × 8) uncertainty matrix therefore reduces to the following (4 × 4) uncertainty matrix:

$$\begin{pmatrix} u^2(S_{11_R}) & u(S_{11_R}, S_{11_I}) & u(S_{11_R}, S_{21_R}) & u(S_{11_R}, S_{21_I}) \\ u(S_{11_I}, S_{11_R}) & u^2(S_{11_I}) & u(S_{11_I}, S_{21_R}) & u(S_{11_I}, S_{21_I}) \\ u(S_{21_R}, S_{11_R}) & u(S_{21_R}, S_{11_I}) & u^2(S_{21_R}) & u(S_{21_R}, S_{21_I}) \\ u(S_{21_I}, S_{11_R}) & u(S_{21_I}, S_{11_I}) & u(S_{21_I}, S_{21_R}) & u^2(S_{21_I}) \end{pmatrix} \tag{3}$$

This reduction process results in six sub-matrices representing the interactions between the Real and Imaginary components of S_{11} and S_{21}. Two of these sub-matrices are the usual uncertainty matrices for S_{11} and S_{21} – i.e. the S_{11} sub-matrix:

$$\begin{pmatrix} u^2(S_{11_R}) & u(S_{11_R}, S_{11_I}) \\ u(S_{11_I}, S_{11_R}) & u^2(S_{11_I}) \end{pmatrix} \tag{4}$$

relates to the Real and Imaginary components of S_{11} and describes the uncertainty associated with a measurement coordinate (S_{11_R}, S_{11_I}) in the S_{11} two-dimensional complex plane.

Similarly, the S_{21} sub-matrix:

$$\begin{pmatrix} u^2(S_{21_R}) & u(S_{21_R}, S_{21_I}) \\ u(S_{21_I}, S_{21_R}) & u^2(S_{21_I}) \end{pmatrix} \tag{5}$$

relates to the Real and Imaginary components of S_{21} and describes the uncertainty associated with a measurement coordinate (S_{21_R}, S_{21_I}) in the S_{21} two-dimensional complex plane.

However, the other four sub-matrices are uncertainty matrices that represent the uncertainties in, and interactions between, a component of one *S*-parameter and a component of a different *S*-parameter. For example, for the Real component of S_{11} and the Real component of S_{21}, the sub-matrix:

[2] It is relatively straight-forward to extend these concepts to devices with more than two ports.

[3] The term "uncertainty matrix" is as used in [6]. The same type of matrix is referred to as a "measurement covariance matrix" in [5].

[4] Again, it is relatively straight-forward to extend these concepts to devices that are either non-reciprocal, non-symmetric, or both.

Table 1: Elements of the (8 × 8) uncertainty matrix associated with the S-parameter matrix in (1)

		S_{11}		S_{21}		S_{12}		S_{22}	
		Real	Imag	Real	Imag	Real	Imag	Real	Imag
S_{11}	Real	$u^2(S_{11_R})$	$u(S_{11_R}, S_{11_I})$	$u(S_{11_R}, S_{21_R})$	$u(S_{11_R}, S_{21_I})$	$u(S_{11_R}, S_{12_R})$	$u(S_{11_R}, S_{12_I})$	$u(S_{11_R}, S_{22_R})$	$u(S_{11_R}, S_{22_I})$
	Imag	$u(S_{11_I}, S_{11_R})$	$u^2(S_{11_I})$	$u(S_{11_I}, S_{21_R})$	$u(S_{11_I}, S_{21_I})$	$u(S_{11_I}, S_{12_R})$	$u(S_{11_I}, S_{12_I})$	$u(S_{11_I}, S_{22_R})$	$u(S_{11_I}, S_{22_I})$
S_{21}	Real	$u(S_{21_R}, S_{11_R})$	$u(S_{21_R}, S_{11_I})$	$u^2(S_{21_R})$	$u(S_{21_R}, S_{21_I})$	$u(S_{21_R}, S_{12_R})$	$u(S_{21_R}, S_{12_I})$	$u(S_{21_R}, S_{22_R})$	$u(S_{21_R}, S_{22_I})$
	Imag	$u(S_{21_I}, S_{11_R})$	$u(S_{21_I}, S_{11_I})$	$u(S_{21_I}, S_{21_R})$	$u^2(S_{21_I})$	$u(S_{21_I}, S_{12_R})$	$u(S_{21_I}, S_{12_I})$	$u(S_{21_I}, S_{22_R})$	$u(S_{21_I}, S_{22_I})$
S_{12}	Real	$u(S_{12_R}, S_{11_R})$	$u(S_{12_R}, S_{11_I})$	$u(S_{12_R}, S_{21_R})$	$u(S_{12_R}, S_{21_I})$	$u^2(S_{12_R})$	$u(S_{12_R}, S_{12_I})$	$u(S_{12_R}, S_{22_R})$	$u(S_{12_R}, S_{22_I})$
	Imag	$u(S_{12_I}, S_{11_R})$	$u(S_{12_I}, S_{11_I})$	$u(S_{12_I}, S_{21_R})$	$u(S_{12_I}, S_{21_I})$	$u(S_{12_I}, S_{12_R})$	$u^2(S_{12_I})$	$u(S_{12_I}, S_{22_R})$	$u(S_{12_I}, S_{22_I})$
S_{22}	Real	$u(S_{22_R}, S_{11_R})$	$u(S_{22_R}, S_{11_I})$	$u(S_{22_R}, S_{21_R})$	$u(S_{22_R}, S_{21_I})$	$u(S_{22_R}, S_{12_R})$	$u(S_{22_R}, S_{12_I})$	$u^2(S_{22_R})$	$u(S_{22_R}, S_{22_I})$
	Imag	$u(S_{22_I}, S_{11_R})$	$u(S_{22_I}, S_{11_I})$	$u(S_{22_I}, S_{21_R})$	$u(S_{22_I}, S_{21_I})$	$u(S_{22_I}, S_{12_R})$	$u(S_{22_I}, S_{12_I})$	$u(S_{22_I}, S_{22_R})$	$u^2(S_{22_I})$

$$\begin{pmatrix} u^2(S_{11_R}) & u(S_{11_R}, S_{21_R}) \\ u(S_{21_R}, S_{11_R}) & u^2(S_{21_R}) \end{pmatrix} \tag{6}$$

describes the uncertainty associated with a measurement coordinate (S_{11_R}, S_{21_R}) in a two-dimensional plane with the Real component of S_{11} as one axis and the Real component of S_{21} as the other axis. This is not a conventional *S*-parameter. Instead, it is a two-dimensional quantity based on a combination of two components coming from two different complex-valued *S*-parameters.

In the same way, for the Real component of S_{11} and the Imaginary component of S_{21}, the sub-matrix:

$$\begin{pmatrix} u^2(S_{11_R}) & u(S_{11_R}, S_{21_I}) \\ u(S_{21_I}, S_{11_R}) & u^2(S_{21_I}) \end{pmatrix} \tag{7}$$

describes the uncertainty associated with a measurement coordinate (S_{11_R}, S_{21_I}) in a two-dimensional plane with the Real component of S_{11} as one axis and the Imaginary component of S_{21} as the other axis.

For the Imaginary component of S_{11} and the Real component of S_{21}, the sub-matrix:

$$\begin{pmatrix} u^2(S_{11_I}) & u(S_{11_I}, S_{21_R}) \\ u(S_{21_R}, S_{11_I}) & u^2(S_{21_R}) \end{pmatrix} \tag{8}$$

describes the uncertainty associated with a measurement coordinate (S_{11_I}, S_{21_R}) in a two-dimensional plane with the Imaginary component of S_{11} as one axis and the Real component of S_{21} as the other axis.

Finally, for the Imaginary component of S_{11} and the Imaginary component of S_{21}, the sub-matrix:

$$\begin{pmatrix} u^2(S_{11_I}) & u(S_{11_I}, S_{21_I}) \\ u(S_{21_I}, S_{11_I}) & u^2(S_{21_I}) \end{pmatrix} \tag{9}$$

describes the uncertainty associated with a measurement coordinate (S_{11_I}, S_{21_I}) in a two-dimensional plane with the Imaginary component of S_{11} as one axis and the Imaginary component of S_{21} as the other axis.

III. Example

To illustrate the above concepts, measurements were made on a mismatched waveguide component designed and developed by OML, Inc. The waveguide size for this device is WR-10 and so measurements were made at frequencies from 75 GHz to 110 GHz. These measurements are used to present the data shown in Figures 1 to 3.

Figure 1 shows the magnitudes of S_{11} and S_{21}. These are the conventional *S*-parameters for such a device. The magnitudes of these *S*-parameters show the characteristic undulation in response due to interacting mismatches inside the device. Maximum reflection (and minimum transmission) occurs at approximately 78 GHz, 87 GHz, 95 GHz and 104 GHz. Minimum reflection (and maximum transmission) occurs at approximately 75 GHz, 83 GHz, 91 GHz, 100 GHz and 109 GHz. As mentioned previously, the strong relationship between the behavior of the reflection and the transmission is due to energy conservation – i.e. signal that is reflected cannot be transmitted, and vice versa.

The strong relationship, shown in Figure 1, between the value of S_{11} and S_{21} at any given frequency can be investigated further by examining the behavior of combinations of components of both S_{11} and S_{21} – these combinations are shown in Figures 2 and 3. In Figure 2, the magnitude of the vectors (S_{11_R}, S_{21_R}) and (S_{11_I}, S_{21_I}) are plotted as a function of frequency, and in Figure 3, the magnitude of the vectors (S_{11_R}, S_{21_I}) and (S_{11_I}, S_{21_R}) are plotted as a function of frequency. The choice of which vector to plot on which of these graphs is not important – however, the choice made here does indicate a strong relationship between combinations of the components of S_{11} and S_{21}. (In principle, the magnitudes of all six voltage ratios could be plotted on the same graph, but having this amount of data displayed on the same graph might make it difficult to interpret.)

At each frequency, in Figures 1, 2 and 3, the uncertainty in the six vectors, (S_{11_R}, S_{11_I}), (S_{21_R}, S_{21_I}), (S_{11_R}, S_{21_R}), (S_{11_R}, S_{21_I}), (S_{11_I}, S_{21_R}) and (S_{11_I}, S_{21_I}), can be represented by the (2 × 2) uncertainty matrices shown in (4) to (9), respectively.

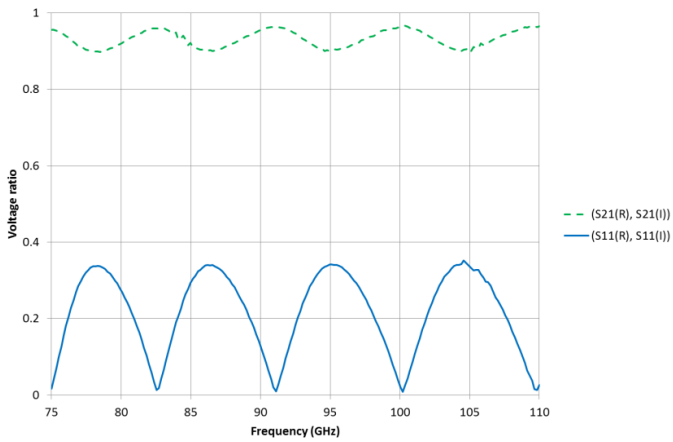

Figure 1: Magnitude of S_{11} and S_{21}, derived from the S-parameter measurements

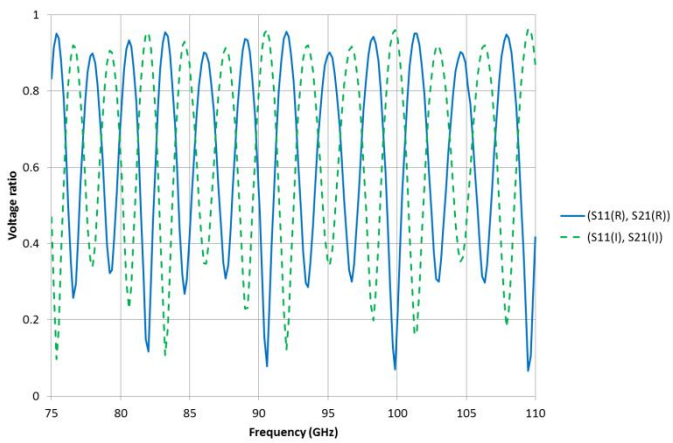

Figure 2: Magnitude of the vectors (S_{11_R}, S_{21_R}) and (S_{11_I}, S_{21_I}), derived from the S-parameter measurements

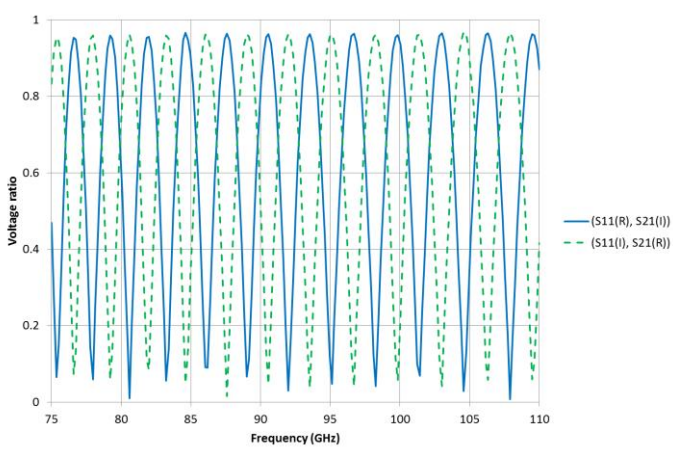

Figure 3: Magnitude of the vectors (S_{11_R}, S_{21_I}) and (S_{11_I}, S_{21_R}), derived from the S-parameter measurements

IV. Uncertainty ellipses

If $S = (x, y)^{\mathrm{T}}$ denotes a variable point in the measurement plane[5], $\bar{S} = (\bar{x}, \bar{y})^{\mathrm{T}}$ denotes the measured value of the two-dimensional vector-valued measurand at a particular frequency and

$$V = \begin{pmatrix} s^2(\bar{x}) & s(\bar{x}, \bar{y}) \\ s(\bar{y}, \bar{x}) & s^2(\bar{y}) \end{pmatrix} \tag{10}$$

denotes the uncertainty matrix (covariance matrix) associated with the measured value, then the following equation represents an ellipse that bounds a region of uncertainty in the measurement plane associated with the measured value

$$(S - \bar{S})^{\mathrm{T}} V^{-1} (S - \bar{S}) = k^2 \tag{11}$$

where k is a "coverage factor" [2].[6]

It has been shown elsewhere [7] that the elements of a (2 × 2) covariance matrix can be used to construct an ellipse in a two-dimensional plane used to depict a two-dimensional vector measurand. For an (2 × 2) uncertainty matrix, this ellipse represents a region of uncertainty associated with the measured value of the two-dimensional measurand.

On this occasion, the measurement procedure for the WR-10 mismatch waveguide line included making a series of 12 replicate measurements of the device, in order to assess the repeatability of the measurements. These replicate measurements were used to establish the elements in the uncertainty matrices described in (4) to (9).[7] This procedure was applied at each measurement frequency. In addition, uncertainty ellipses were constructed using these uncertainty matrices, (4) to (9), for each of the six two-dimensional vectors described in the previous section. Sets of six ellipses were generated at each measurement frequency. As an example, the six ellipses that were produced at 75 GHz are shown in Figures 4 to 6. In all these Figures, a large coverage (i.e. multiplying) factor, k, has been used (k = 500) to enable the ellipses to be seen easily. The red dashed circle in each of the plots is the "unit circle" centred on the origin of the plane.

[5] The use of a superscript "T" here indicates the transpose of a vector.
[6] Note that in equation (11), superscript "-1" indicates the inverse of a matrix.
[7] These uncertainty matrices therefore do not contain information concerning all uncertainty contributions to these measurements. However, these matrices are considered sufficient to demonstrate the concepts described in this paper.

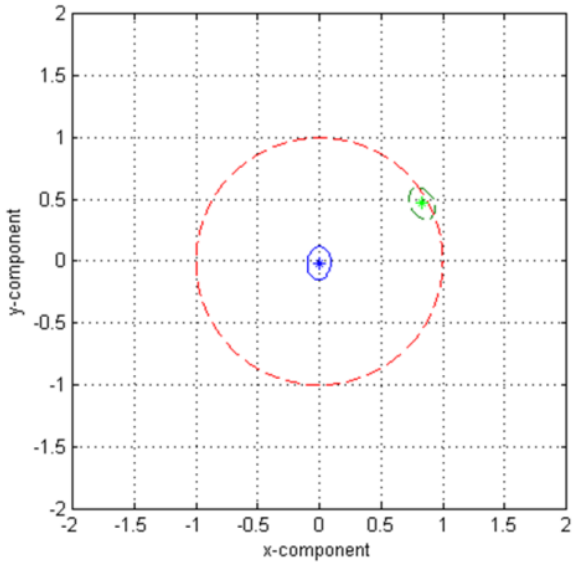

Figure 4: Uncertainty ellipses at 75 GHz. The solid blue ellipse is for the vector (S_{11_R}, S_{11_I}) and the dashed green ellipse is for the vector (S_{21_R}, S_{21_I})

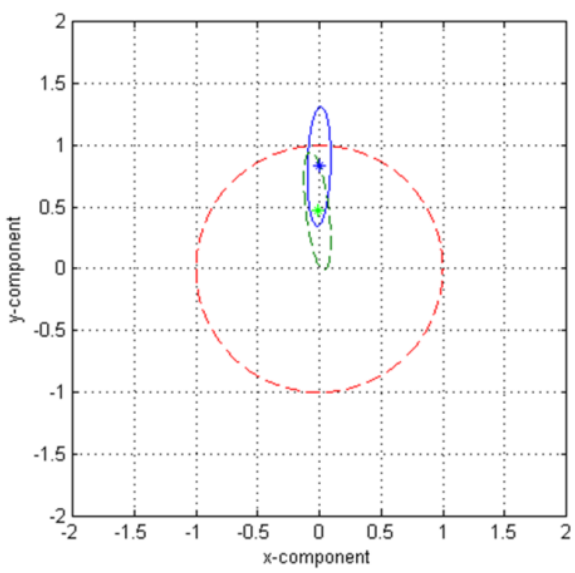

Figure 5: Uncertainty ellipses at 75 GHz. The solid blue ellipse is for the vector (S_{11_R}, S_{21_R}) and the dashed green ellipse is for the vector (S_{11_I}, S_{21_I})

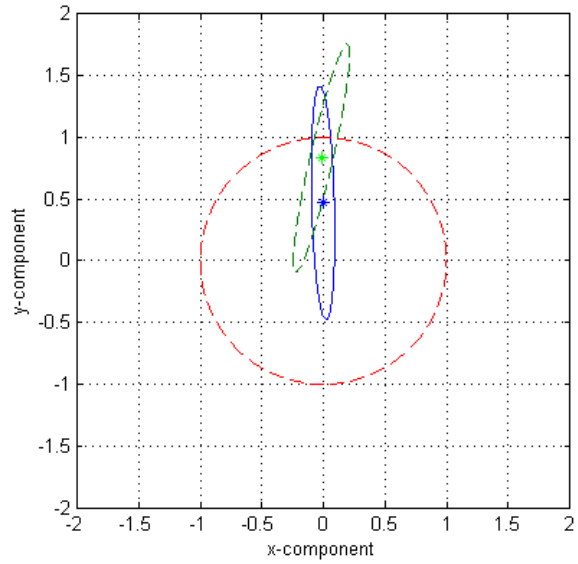

Figure 6: Uncertainty ellipses at 75 GHz. The solid blue ellipse is for the vector (S_{11_R}, S_{21_I}) and the dashed green ellipse is for the vector (S_{11_I}, S_{21_R})

V. Discussion

The uncertainty ellipses shown in Figures 4 to 6 provide a visual representation of the interactions between the components of the measured *S*-parameters. Figure 4 relates directly to S_{11} and S_{21}, respectively, whereas Figures 5 and 6 show the interactions between a component of S_{11} (either Real or Imaginary) and a component of S_{21} (either Real or Imaginary).

These uncertainty ellipses can be used to assess the quality of the measurement results in terms of accuracy – i.e. relatively large ellipses suggest relatively poor measurement quality, and vice versa. The uncertainty ellipses can also be used to verify measurements by comparison with other sets of measurement data (see, for example, [8]). A detailed and rigorous verification procedure for multiple *S*-parameter measurement data is beyond the scope of this paper, and so this will form the subject of a subsequent paper.

VI. Conclusion

A procedure has been presented for the detailed analysis of the uncertainty associated with measurements of multiple complex-valued *S*-parameters. The procedure follows recommendations, outlined in Supplement 2 to the GUM [5], for the treatment of uncertainty for any number of output quantities (i.e. measurands). The procedure quantifies the uncertainty for each individual *S*-parameter using a (2 × 2) uncertainty matrix (i.e. a measurement covariance matrix). Additional (2 × 2) matrices are then used to quantify the interactions between components of different *S*-parameters.

All these (2 × 2) uncertainty matrices are effectively sub-matrices drawn from a 'parent' uncertainty matrix which contains all uncertainty information for the multiple *S*-parameter measurements. For a two-port device, this parent matrix is a fully populated (8 × 8) uncertainty matrix – more generally, for an *n*-port device, the parent matrix will be a $(2n^2 \times 2n^2)$ uncertainty matrix.

For a reciprocal, symmetric, two-port device (as presented in this paper), six ellipses are needed, at each measurement frequency, to describe all the interactions between the uncertainty components for the two *S*-parameters, S_{11} and S_{21}. For a non-reciprocal, non-symmetric, two-port device, a total of 28 ellipses would be needed to describe all interactions between the uncertainty components for all the four *S*-parameters, S_{11}, S_{21}, S_{12} and S_{22}.

The analysis presented in this paper can also be applied to the situation where measurements of multiple *S*-parameters are used as inputs to the determination of other subsequent measurement quantities. The use of fully populated $(2n^2 \times 2n^2)$ uncertainty matrices for measurements of *n*-port devices enables the effects due to all interactions between the components of the *S*-parameters to be taken into account, in terms of their effects on these subsequent measurement quantities.

ACKNOWLEDGEMENT

The authors would like to thank Dr Yuenie Lau (OML, Inc) for the loan of the mismatched waveguide line that was used for the experimental results presented in this work. The work described in this paper was jointly funded by the European Metrology Research Programme (EMRP) Project SIB62 'HF-Circuits', and, the National Measurement System Directorate of the UK government's Department for Business, Innovation and Skills. The EMRP is jointly funded by the EMRP participating countries within EURAMET and the European Union.

REFERENCES

[1] "Guide to the Expression of Uncertainty in Measurement", International Organization for Standardization, 1st edition, ISBN 92-67-10188-9, 1993.

[2] JCGM 100:2008, "Evaluation of measurement data – Guide to the expression of uncertainty in measurement".

[3] N M Ridler and M J Salter, "Evaluating and expressing uncertainty in complex S-parameter measurements", *Proc. 56th ARFTG Microwave Measurement conference*, Boulder, CO, USA, November 2000.

[4] N M Ridler and M J Salter, "An approach to the treatment of uncertainty in complex *S*-parameter measurements", *Metrologia*, Vol 39, No 3, pp 295-302, June 2002.

[5] JCGM 102:2011, "Evaluation of measurement data – Supplement 2 to the 'Guide to the expression of uncertainty in measurement' – Extension to any number of output quantities".

[6] JCGM 101:2008, "Evaluation of measurement data – Supplement 1 to the 'Guide to the expression of uncertainty in measurement' – Propagation of distributions using a Monte Carlo method".

[7] N M Ridler and P R Young, "Investigating the random error distribution of vector network analyser measurements", *Proc. 29th ARMMS Conference Digest*, pp 26-34, Bracknell, UK, April 1999.

[8] K Kuhlmann and R Judaschke, "Reduction technique for Measurement Comparisons with Complex-valued Measurands", *Proc. Conference on Precision Electromagnetic Measurements (CPEM)*, Rio de Janeiro, Brazil, August 2014.

Complex LO waveforms for wideband systems: some frequency-converter measurement implications

J. Martens

Anritsu Company, 490 Jarvis Drive, Morgan Hill, CA 95037 US

Abstract — Systems containing frequency-conversion stages using complex Local Oscillator (LO) waveforms, sometimes under the heading of compressive sampling, have been proposed for general wideband communications, 5G applications (large-scale MIMO), signal intelligence and for other purposes. The characterization of the converters used in those applications can be critical for link budgets but those measurements can be complicated by the LO spectral distribution. Aside from the expected waveform dependence of linearity, image response complications and converter operating state questions can lead to multiple dB (or even 10s of dB) variations in the more small-signal-esque conversion efficiency and noise power measurements when taking into account only average or peak power.

Index Terms — mixer measurement, frequency converter, compressive sampling, mixer noise figure.

I. Introduction

In recent years, there has been work on a number of communications and receiver systems where non-traditional LO waveforms are instrumental. One type of system (e.g., [1]-[4]) uses a sub-sampling receiver for widely dispersed, but individually narrowband, frequency swaths. A receiver using a number of pseudo-random LOs can compress the signal space into a relatively small baseband bandwidth that can be digitized efficiently and then the information decoded in post-processing using knowledge of the LO waveforms (often called 'compressive sampling' techniques). A different type of system (e.g., [5]-[6]) may instead want to make more efficient use of RF bandwidth by taking multiple baseband signals and using varied LOs to transfer that information to a bandlimited RF zone. The receiver in that system uses similar LO structures to recover the various baseband signals.

Similar to both types of systems is the use of a complex LO waveform. Because the details of those waveforms are critical to information control, certain common frequency converter structures could become problematic: strong limiting LO paths, wave sharpening LO structures, etc. As a result, passive mixers are often discussed in the context of these systems (e.g., [1]). At any rate, the measurement of these frequency converters also raises some questions:

- How much is conversion efficiency a function of waveform details?
- Noise figure definitions can be problematic even for simple converters (e.g., [7]) so what is appropriate here? How will the more complex image situation affect the noise measurements?

From power amplifier work, it would be expected that dependencies will be present. While a complete analysis would seem to require a fairly sophisticated nonlinear model, there is some desire to explore basic component measurements in this domain if, for no other reason, to get an estimate of link budgets (e.g., [1]). This paper will then start to look at some of these measurement questions, semi-heuristically, particularly for conversion efficiency and noise figure/noise power. The spectral flow-through for a simple class of frequency converters will be examined, both for multisine (e.g., [8]) and more elaborate pseudo-random LO waveforms, to elucidate hardware and analysis points. Measurements at microwave and millimeter-wave frequencies will serve to help explore these behaviors.

II. System structures and the implications

A simplified diagram of a complex-LO-based system is shown in Fig. 1. In one incarnation, the input represents band-limited signals somewhere in a wide RF bandwidth (but perhaps not known where). With a series of properly encoded LO waveforms [1], these band-limited input signals are converted to a baseband signal that can be decoded after digitization. In this situation, the input signal is sent to each converter and the multitude of output waveforms are used to recover the information in post-processing.

While many LO waveforms are possible, commonly used ones (e.g., [4]) are fast-period digital signals as might be realized by using different taps from a fast shift register (see Fig. 2). The spectrum of the LO is thus DC-centered but with a very wide comb-line extent. Certain other variations (for wideband systems centered in different parts of the spectrum) use upconverted variations of that type of digital waveform. For our purposes here, a pseudo-random sequence (upconverted or not) may serve as a useful proxy to explore some dependencies. As a starting point in some of the measurements, multisine signals (e.g., [8]-[9]) will be used as proxies to look at some mechanisms as they often have been

978-1-4799-8887-7/15/$31.00 ©2015 IEEE

used to replace more complex signals in other situations. It should be emphasized that many aspects of characterization (particularly linearity) will be local to a particular LO waveform so generalizations will be approached cautiously.

In another variation, the input may be a series of different communications signals at baseband and the output becomes a spectrally efficient combination of those signals at RF that can be recovered later. In this case, each separate baseband signal may be applied to a different converter for transmission.

Either way, the behavior of the individual converters needs to be characterized in terms of the usual conversion efficiencies, noise figure and linearity for purposes of assessing link budgets and other system variables.

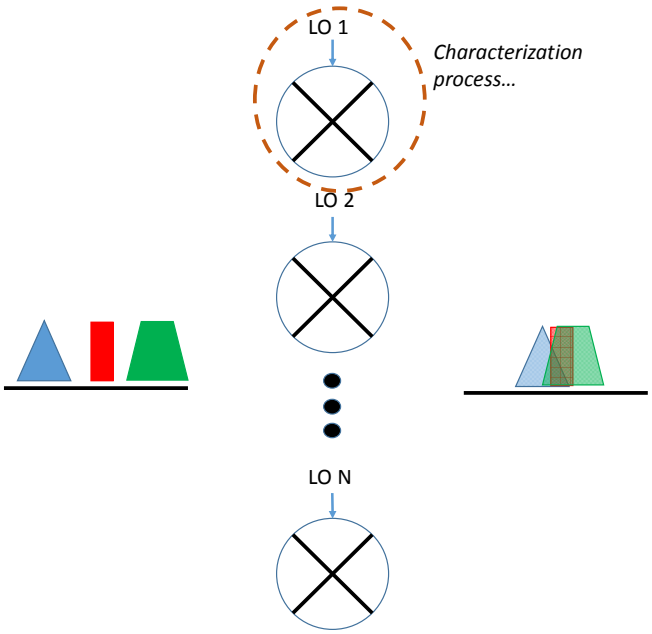

Fig. 1. A simplified conversion scheme characteristic of the wideband compressing systems discussed in this paper is shown here.

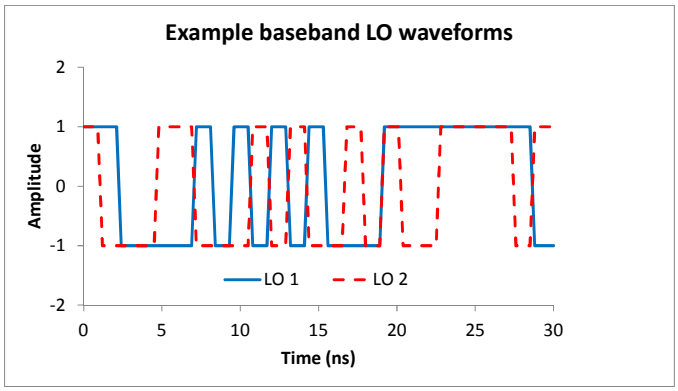

Fig. 2. An example pair of LO waveforms are illustrated here that may be used in the applications discussed.

As would be expected, spurious generation with a complex LO is generous and highly amplitude-dependent. It is not within the scope of this paper to analyze this process but, for purposes of illustration, a two-sine LO (spacing 90 MHz) was used at various levels on a passive mixer. A single tone was delivered to the RF port at 0 dBm. The resulting IF spectrum is plotted in Fig. 3 where the primary responses are at 910 MHz and 1 GHz IF frequency. These primary conversion levels change by only about 3 dB over the +3 to +15 dBm (per sinusoid) LO power range but the various comb-like products change by 30 dB or more in places.

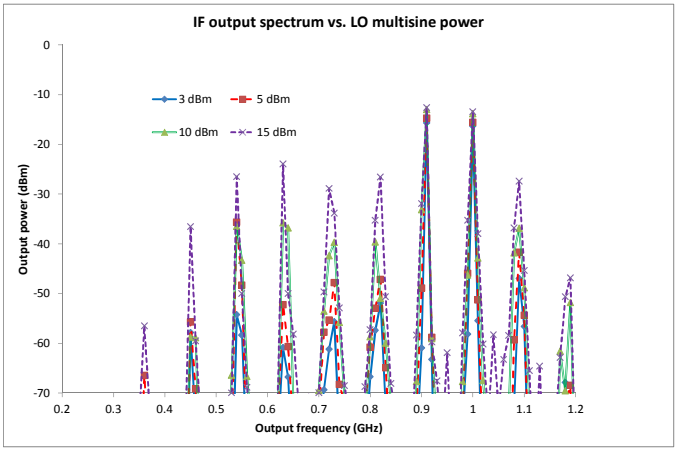

Fig. 3. The spur generation capability as a function of LO drive in a two-sine LO scenario is shown here for a passive doubly-balanced mixer. The RF applied was a single sinusoid.

As in traditional multisine measurements, the phase alignment plays a strong role in linearity. A two-tone IMD measurement (two tones applied to the RF port with 3 MHz spacing) was performed on a W-band converter with both a single-tone LO and with a three-tone LO and the phase alignment of the latter group was varied. An IMD product was computed by averaging all of the 3rd order (from the RF perspective) components due to the various LOs and the results are plotted in Fig. 4 (aside: this is an *ad hoc* definition). For the multisine LO (spacing of 1.7 MHz to give some level of relative prime-ness), the various individual 3rd order intermodulation products (IM3) varied by about 3 dB (amongst themselves) but the general product levels were higher and the slope more elevated with aligned phase. The slope change was not expected and is under further study.

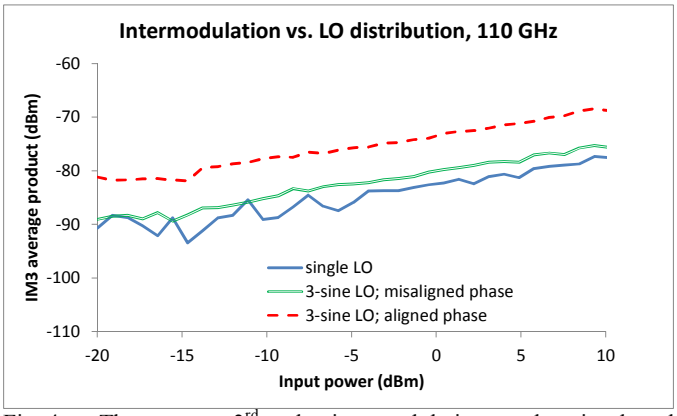

Fig. 4. The average 3rd order intermodulation product is plotted here for a converter with different LO configurations. With the multisine LO, phase alignment played a role.

In this last measurement and the next one, the description of the signal configuration has a high potential for lack of clarity. The distribution is shown in Fig. 5.

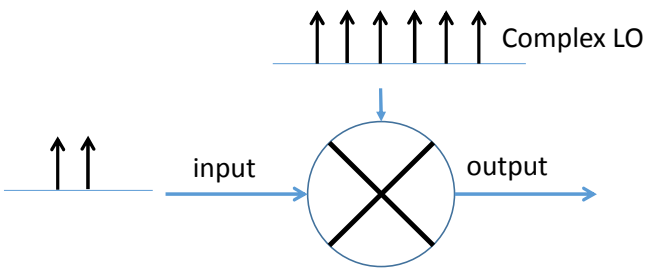

Fig. 5. The signal distribution for the measurements of Figs. 4 and 6 is shown here. There are many locations of IM products at the output and an average of those values was used for the multisine case and the dominant value was used for the pseudo-random case.

To explore this further, consider an IM3 measurement where the LO is one of two pseudo-random waveforms (each similar to that illustrated in Fig. 2). To coincide with a shifted, but reasonably wideband system, the baseband waveform was upconverted to 60 GHz and band-limited to 1 GHz. While this may not satisfy a wide variety of applications, it will perhaps help illustrate behaviors. The two baseband waveforms had the same average power and the same peak time domain amplitude but differed in bit period so the power spectral distributions were quite different. Two tones were input to the RF with 100 MHz spacing and the upper 3rd order product is plotted in Fig. 6.

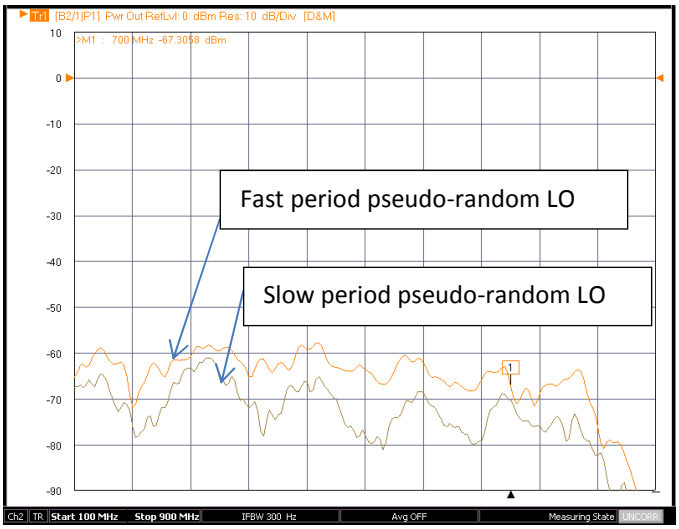

Fig. 6. The upper IM3 product (in dBm terms) is plotted here for a converter excited on the input port by two tones (100 MHz spacing) and on the LO by one of two upconverted pseudo-random waveforms. As expected, the IM response is heavily dependent on the LO waveform details.

III. Conversion Efficiency

While not as waveform-specific as a linearity measurement, it would not be surprising if conversion efficiency/gain had some dependence on the LO details. Even ignoring localized starvation questions, the fraction of time that the mixer diodes/transistors/switches are in the conducting state will be dependent on multisine phase composition or pseudo-random sequence configuration. When LO amplitude variations are added in, desense responses will be likely except in the weakest of drive scenarios.

Consider first a simple measurement of converter output power in a power sweep (of the input sinusoid, not the LO) where the input frequency was at 40 GHz. A single tone LO was used first and generated the solid blue curve in Fig. 7. Two different three-tone LOs were then used with the same average power as the single tone and with different internal phase relationships (set 2 being close to aligned but not perfectly due to some hardware limitations). A substantial conversion efficiency variance was apparent.

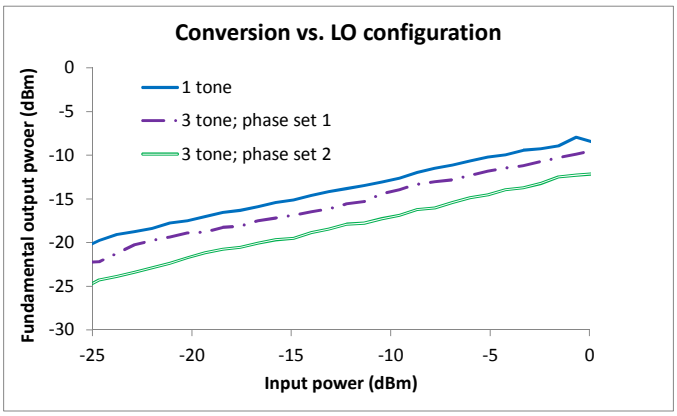

Fig. 7. The converted output power as a function of RF drive and LO configuration is plotted here.

Next, the average LO power was corrected for the difference in fractional on-time of the mixer diodes when using the two different 3-tone LO waveforms. While this is an extremely coarse procedure and ignores many waveform nuances, the conversion levels are now closer as shown in Fig. 8. Also, the degree of convergence is likely to be dependent on the mixer/converter technology being employed (this was performed using simple GaAs Schottky-based mixers).

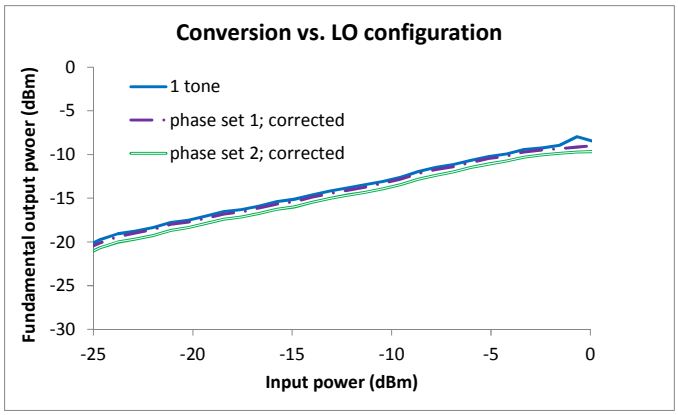

Fig. 8. The same measurement as in Fig. 7 is illustrated here except the three-tone LO power levels were corrected for the on-state timing differences for those waveforms.

With a pseudo-random LO and a sinusoidal input, conversion was measured using an integration bandwidth of 100 kHz and plotted versus input power for three different LO waveforms (see Fig. 9). The peak time domain amplitudes were the same as were peak spectral power levels but the register lengths and the bit periods were not (the latter ranging from about 2 ns down to about 500 ps). The output power levels are similar but the details of the LO power distribution functions had an impact. The fractional on-times were equivalent in these cases so some of the effects in Fig. 7 do not apply. Not surprisingly, the compression points are quite dependent on the waveform. In this case, the longer periods A and B lead to a near-starvation state for this particular mixer and hence reduced conversion and compression point.

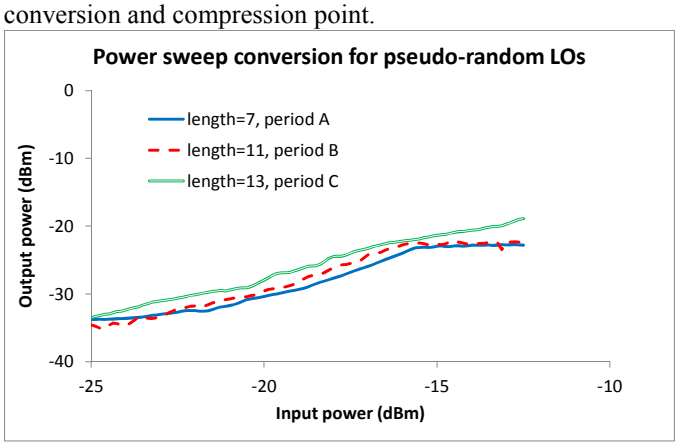

Fig. 9. Conversion behavior for a mixer with a pseudo-random LO is shown here versus RF input power.

IV. Noise Figure and/or Noise Power

As discussed in [7] and in many other places, the traditional noise figure definitions, both in terms of the standards and since they are based on ratios of signal-to-noise ratios, are potentially problematic for frequency converters. An ambiguity arises on which image contributions should be counted as 'signals' since that interpretation can be application-dependent. In the complex LO case, the situation is even worse since it may not even be known, *a priori,* how many image bands are of interest. For the purposes of this work, we will rely on noise power in a defined bandwidth. While this is somewhat arbitrary, it is definable and can be easily converted to a noise temperature.

In terms of practical noise contributions, consider first a two-tone LO and a downconverter application. If the LO spacing is relatively large (relative to the IF and the measurement bandwidth), there are at least 4 bandwidth sections at the input adding noise power as suggested by Fig. 10. These will all be at least partially correlated (depending on the LO signal relationships). As the spacing drops, however, these response areas can start to overlap thus changing the correlation.

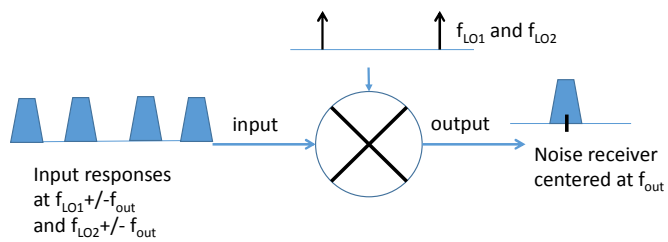

Fig. 10. An example mixer noise band relationship is shown here for the complex LO case.

While this may be a slightly odd physical example, it acts here as a simpler surrogate for the potentially complicated relationship between these noise sidebands for a pseudo-random LO. To explore the effect in this basic two-tone LO setting, the output noise power in a 10 kHz bandwidth was measured for a variety of LO tone spacings (termed LO spectral density in the plots) and the results are shown in Fig. 11. Very little happens in this case until the spacing gets on the order of and below the measurement bandwidth. As might be suspected from Fig. 3, there are in practice quite a few more contributing noise sidebands than suggested by Fig. 7 but for the mixer and LO levels used in the measurement of Fig. 11, these other responses were down at least 20 dB. In the Fig. 11 measurements, substituting LO generators with 10+ dB phase noise differences (at similar offsets) and different spur profiles did not change the results. Also the measured conversion efficiency did not change, beyond repeatability limits, between the various LO configurations. An uncertainty analysis of this measurement is in process.

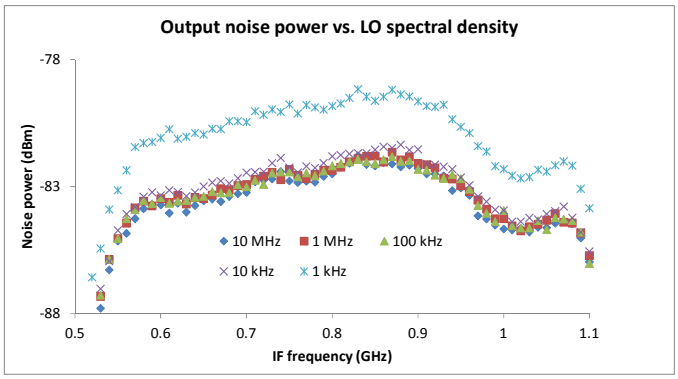

Fig. 11. The output noise power versus LO density (multisine spacing) is shown here plotted against output (IF) frequency for one example system.

Moving to a more elaborate pseudo-random LO configuration, three configurations with different bit period waveforms were studied. The output spectra are quite varied although, again, the LO peak spectral powers and time domain peak amplitudes were the same. The measured noise powers are shown in Fig. 12. Although the sequence lengths are different, the more important change was that the bit periods shrank consecutively through the series from about 2 ns down to about 500 ps. The baseband signals were upconverted to 60 GHz with a 2 GHz filtered LO bandwidth. Because the spectral densities were so different, the number of contributing sidebands was also different. Since the output frequency was on the same order as the comb spacing of the LO, there was also varying overlap and hence correlation differences. Not surprisingly, there are large differences in measured noise power.

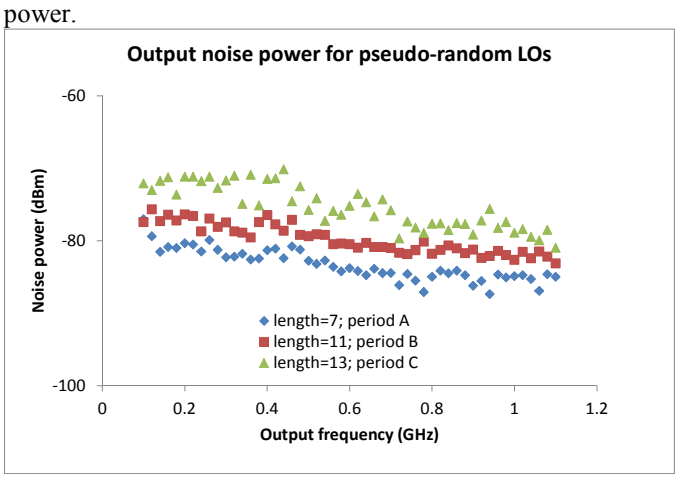

Fig. 11. The measured noise powers for a converter using three different pseudo-random LO waveforms are plotted here. While peak levels were the same, spectral distributions and implied sideband correlation levels differed.

V. Conclusion

Complex-LO-based systems offer advantages for a number of applications but they do place stress on the ability to characterize frequency converting subsystems. While it is perhaps obvious that linearity measurements will likely be LO-waveform-specific, conversion efficiency and noise measurements also show large dependencies even taking into account certain LO power characteristics. Some of the mechanisms discussed here may help with characterization processes and in better understanding where measurement generalizations are possible.

References

[1] M. Mishali and Y. C. Eldar,"From theory to practice: sub-Nyquist sampling of sparse wideband analog signals," *IEEE J. Sel. Topics in Sig. Proc.*, vol. 4, pp. 375-391, Apr. 2010.

[2] M. Mishali, Y. C. Eldar, O. Dounaevsky, and E. Shoshan, "Sub-Nyquist acquisition hardware for wideband communication," *SiPS 2010,* Oct. 2010, pp. 156-161.

[3] M. Mishali and Y. C. Elder, "Sub-Nyquist sampling," *IEEE Sig. Proc. Mag.*, pp. 98-124, Nov. 2011.

[4] G. Prisco, M. D'Urso, and G. Buzzo, "Compressive sampling based radar receiver," *Proc. 2013 IEEE Int. Symp. On Phased Array Systems and Tech.,* pp. 185-190, 2013.

[5] L. Dai, Z. Gao, Z. Wang, and Z. Yang, "Spectrum-efficient superimposed pilot design based on structured compressive sensing for downlink large-scale MIMO systems," *Proc. 2014 URSI Gen. Assy. and Sci. Symp.*, 2014, pp. 1-4.

[6] T. Reveyrand, "New sampling paradigm dedicated to RF ultra-wideband receivers," *presented at 79th ARFTG Conf.,* Montreal, June 2012.

[7] S. A. Maas, *Microwave Mixers*, Boston, Artech House, 1993.

[8] P. Cruz, N. B. Carvalho, and K. A. Remley, "Evaluation of nonlinear distortion in ADCs using multisines," *2008 IEEE MTT Int. Micr. Symp. Dig.*, pp. 1433-1436, June 2008.

[9] K. A. Remley, "Multisine excitation for ACPR measurements," *2003 IEEE MTT-S Int. Micr. Symp. Dig.*, pp. 2141-2144, June 2003.

A comparison of MIMO antenna efficiency measurements performed in Anechoic Chamber and Reverberation Chamber

Tian-Hong Loh [1], and Wanquan Qi [2]

[1] National Physical Laboratory, Hampton Road, Teddington, Middlesex, TW11 0LW, UK

[2] Beijing Institute of Radio Metrology and Measurement, Yongdin Road, Haidian District, Beijing, China

Abstract — Multiple-input-multiple-output (MIMO) antenna will play a key role in the development of fifth generation (5G) wireless mobile communication systems due to their performance-enhancement capability in multipath environment. Antenna radiation efficiency is an important parameter for MIMO antenna system. In this paper, we present a comparison of MIMO antenna efficiency measurements performed in Anechoic Chamber (AC) and Reverberation Chamber (RC) at the UK National Physical Laboratory. Two commercial available directional dual polarized full LTE band MIMO antennas were measured both in AC and RC between 1 GHz and 3 GHz.

Index Terms — Multiple-Input-Multiple-Output, Radiation Pattern, Antenna Gain, Antenna Radiation Efficiency, Anechoic Chamber, Reverberation Chamber.

I. Introduction

Over the past two decades the market for modern wireless communication systems has grown rapidly in response to consumer demand. The use of multiple-input-multiple-output (MIMO) antennas, coupled with modulation formats, such as Orthogonal Frequency Division Multiple Access (OFDMA) can provide both increased channel capacity and protection against multi-path fading. This has been exploited and has encouraged, in recent years, extensive research activities in the application of MIMO technologies for these wireless systems, due to their rich scattering nature that provides improved spectral efficiencies and increased network capacity.

To date, MIMO technologies have been embedded in the fourth generation (4G) wireless communication systems such as 3GPP Long-Term-Evolution (LTE), WiMAX and Wi-Fi [1]. Furthermore, massive MIMO communication is an exciting area of fifth generation (5G) wireless research and it is envisaged that it becomes one of the major drivers for new radio access technologies in 5G [2].

In early literature on MIMO, the antenna elements were assumed isotropic and lossless [3]-[4]. However, in practice, they are often required to be compact for mobile communications where antenna characteristic such as antenna radiation pattern, antenna efficiency, correlation and mutual coupling cannot be omitted [5]-[6]. These are particularly important factors for the development of the 5G wireless communication systems as they promise to have seamless connectivity, which need to be further evolved beyond the current state of the art in order to accommodate a wide variety of issues and challenges. Therefore, system developers, manufacturers, and researchers need a good understanding of the real radiation characteristics from such devices in order to inform design and deployment choices.

Antenna radiation efficiency is one of the most important antenna parameter [7] as it would have significant effect on communications performance, reliability and efficiency of the system. It takes into account losses at the input terminals and within the structure of the antenna [8]. There are particular challenges in assessing the radiation efficiency of MIMO antennas as it has been demonstrated that both diversity gain and MIMO capacity depend upon the number of antennas, signal-to-noise ratio (SNR) and radiation efficiency on a complex way [9]. It should be noted that MIMO antenna radiation efficiency decreases by small array spacing where the reduction of efficiency reduces the channel capacity [10]. This will further pose additional difficulty and challenge for characterizing the antenna radiation efficiency of massive MIMO antenna.

The fundamental operating principles of anechoic chamber (AC) and reverberation chamber (RC) are different for antenna radiation efficiency measurements. AC is an ideal radio frequency free space environment, whereas RC is an over-moded reflecting environment providing statistically homogeneous and isotropic fields within its working volume. Antenna radiation efficiency measurements in AC are often affected by critical problems regarding measurement repeatability which is strongly dependent on the measurement configuration and the identification of the most sensitive parts of the antenna under test (AUT). Also an accurate reference gain antenna is required if antenna substitution method is employed for the AUT gain measurement. On the other hand, RC tests do not require accurate AUT positioning but require an accurate reference efficiency antenna.

There is limited number of literatures [11]-[12] presenting work relating to charactering MIMO antennas and comparing between AC and RC. Nevertheless, the main focus in [11]-[12] is on the characterization of the maximum-ratio-combining diversity gain and the ergodic MIMO capacity of MIMO antennas. The relevant AC diversity evaluations require measurement of embedded far-field functions and embedded radiation efficiencies at every antenna port. But considering the time consuming radiation pattern

978-1-4799-8887-7/15/$31.00 ©2015 European Union

measurements in AC, the authors have assumed symmetric property of the MIMO antenna and only perform embedded far-field functions and embedded radiation efficiencies at one port. In this paper, we present a study into comparing the measured results obtained in AC and RC for two different directional dual polarized full LTE band MIMO antennas. The work aims to evaluate the antenna radiation efficiency at every antenna ports as well as the antenna radiation efficiency when the ports are combined using a combiner.

The paper is organized as follows: Section II presents the formula used for the radiation efficiency evaluation in AC and RC. Section III presents the details of measurement facilities and experimental setups for the radiation efficiency measurements of the MIMO antennas. Section IV shows a comparison between the radiation efficiency measurement results obtained from AC and RC. Finally, conclusions are drawn in Section V.

II. Theory

The following presents the formula used for the radiation efficiency evaluation in AC and RC, respectively.

A. Radiation Efficiency using anechoic chamber

For AC, antenna radiation efficiency can be calculated using the antenna's gain and directivity. The directivity is a measure of the concentration of the radiation in a desired direction $(\theta_0, \emptyset_0)$ and the gain is the directivity including the losses up to the antenna output. These are defined as [13]:

$$\eta = G(\theta_0, \emptyset_0)/D(\theta_0, \emptyset_0). \quad (1)$$

$$D(\theta_0, \emptyset_0) = F_{Nor}(\theta_0, \emptyset_0)/F_{Nor_{Av}}. \quad (2)$$

$$F_{Nor_{Av}} = \frac{1}{4\pi}\iint_{4\pi} F_{Nor}(\theta, \emptyset)\, d\Omega. \quad (3)$$

where $F_{Nor}(\theta_0, \emptyset_0)$ is the normalized radiation intensity for direction $(\theta_0, \emptyset_0)$, and $F_{Nor_{Av}}$ is the average value of normalized radiation intensity over 4π space.

B. Radiation Efficiency using reverberation chamber

For RC, antenna radiation efficiency can be calculated using the following formula [14]:

$$\eta_{AUT} = F_{AUT}.F_{REF}.\eta_{REF} \quad (4)$$

$$F_{AUT} = \frac{\langle |S_{21_{AUT}}|^2 \rangle}{\left(1-|\langle S_{22_{AUT}}\rangle|^2\right)\left(1-|\langle S_{22_{AUT}}\rangle|^2\right)} \quad (5)$$

$$F_{REF} = \frac{\left(1-|\langle S_{22_{REF}}\rangle|^2\right)\left(1-|\langle S_{11_{REF}}\rangle|^2\right)}{\langle |S_{21_{REF}}|^2 \rangle} \quad (6)$$

where η represents the efficiency value. AUT and REF are for the antenna under test and the reference antenna, respectively.

III. Experimental setup

All the radiation efficiency measurements were performed in the NPL AC and RC facilities. Two different commercially available directional dual polarized full LTE band two-port MIMO antennas were measured, namely, Laird PAS69278 and Poynting XPOL-A0002. An ETS-Lindgren 3117 double-ridged waveguide horn antenna was used as the Tx antenna in both AC and RC. The following presents the experimental setup for the radiation efficiency measurement in AC and RC, respectively. To assess the MIMO AUT as a single-port AUT a power combiner Mini-Circuits ZN2PD2-50-S+ was used. A four-port Rohde & Schwarz ZVB8 VNA was used with output power of 0 dBm.

A. Anechoic Chamber

The anechoic chamber has a dimension of 7 m × 6.2 m × 6.2 m and has two low permittivity mounts, for the transmitting (Tx) and receiving (Rx) antennas (see Figs. 1(a) and 1(b), respectively). The roll-over-azimuth positioner system receiving end enables the three-dimensional (3D) radiation pattern of the Rx AUT located at the centre of rotation to be acquired over a spherical surface with a Tx probe antenna located at a fixed distance oriented transversely to the spherical surface with a particular polarization angle where vertical polarization (VP) and horizontal polarization (HP) are often been chosen.

Fig. 1. NPL AC setup: (a) Transmitting tower with Tx ETS 3117 double-ridge horn antenna; (b) Receiving roll-over-azimuth positioner tower with the Laird PAS69278 MIMO AUT.

The distance between the Tx antenna and the Rx AUT was 2.8 m and the height of the antennas above the chamber ground was 3.058 m. Both the VP and HP radiation pattern measurements were performed with an angular resolution of 5° in the roll and azimuth spherical axes. An ETS-Lindgren 3117 double-ridged waveguide horn antenna was used as the reference gain antenna.

B. Reverberation Chamber

The NPL RC has dimensions 6.5 m × 5.85 m ×3.5 m with spangle-galvanized mild stainless-steel walls and aluminium inner door skins (see Fig. 2). Three circular metallic plates are horizontally fixed to the vertical rotation paddle axis, which supports various rectangular aluminium tuner blades. An ETS-Lindgren 3117 double-ridged waveguide horn antenna was used as the reference efficiency antenna. Note that the stationary *S*-parameters was acquired for each of 1000 paddle steps (i.e. the paddle rotates a one-thousandth of a complete revolution).

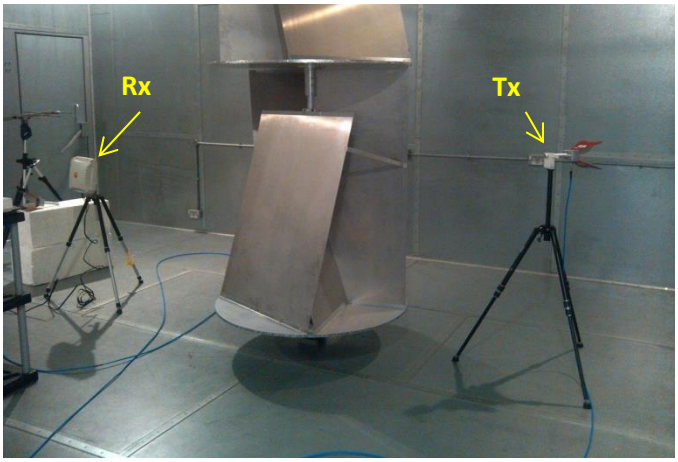

Fig. 2. . NPL RC setup for antenna radiation efficiency measurement.

IV. Measurement Results

As shown in Figs. 3 and 4, the measurement results obtained in AC and RC are compared for the Laird PAS69278 and Poynting XPOL-A0002, respectively.

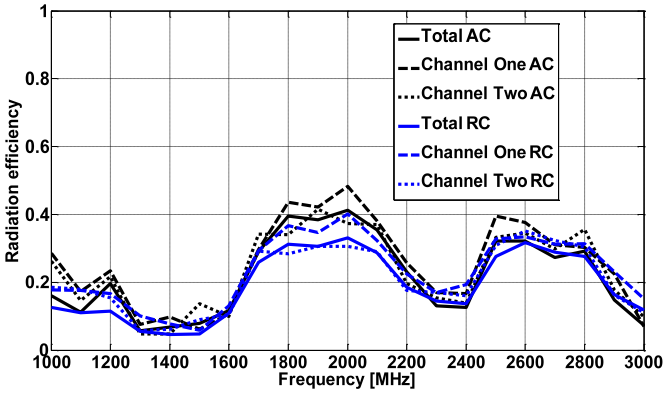

Fig. 3. Antenna radiation efficiency comparison between AC and RC for Poynting XPOL-A0002 AUT.

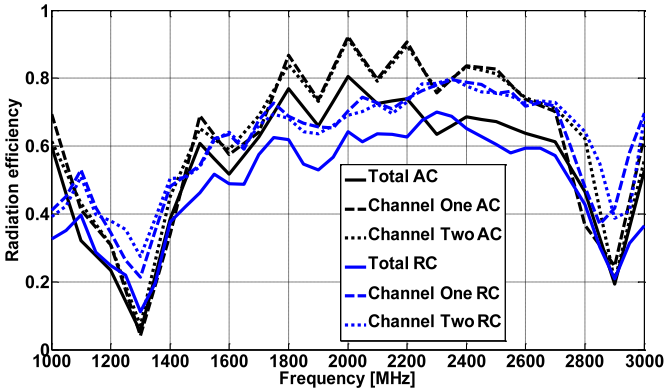

Fig. 4. Antenna radiation efficiency comparison between AC and RC for Laird PAS69278 AUT.

One notes that the legend text 'Total' means that the two-port are combined into one-port to connect to VNA (i.e. Port 1 at the VNA was connected to Tx and Port 2 at the VNA was connected to the combined port (using combiner) at Rx) whereas 'Channel One' and 'Channel Two' means that the two ports of the MIMO AUT are each connected to a port at VNA (i.e. Port 1 at the VNA was connected to Tx and Ports 2 and 3 at the VNA was connected to the two ports at Rx).

One observes from the above that the comparisons show reasonable agreements between AC and RC. Nevertheless, one notes that the antenna radiation efficiency is different at every antenna port as well as when the ports are combined.

V. Conclusion

In this paper, we have presented a study into comparing the MIMO antenna efficiency measured results obtained in AC and RC for two different directional dual polarized two-port full LTE band MIMO antennas between 1 GHz and 3 GHz. We have demonstrated that the antenna radiation efficiency is different at every antenna ports as well as when the ports are combined. Considering that massive MIMO communication is envisaged to become one of the major drivers for new radio access technologies in 5G, one needs to further research on novel cost-effective measurement techniques to fully characterize its radiation efficiency.

References

[1] T. Brown, P. Kyritsi, and E. D. Carvalho, *Practical Guide to MIMO Radio Channel: with MATLAB Examples*, Chichester: John Wiley & Sons, 2012.

[2] NetWorld2020 ETP (European Technology Platform for Communications Networks and Services), Expert Working Group on 5G: Challenges, Research Priorities, and Recommendations, Joint White Paper (Draft version published for public consultation), August 2014. Available: http://networld2020.eu/wp-content/uploads/2014/02/NetWorld2020_Joint-Whitepaper-V8_public-consultation.pdf.

[3] C. J. Foschini, "Layered space-time architecture for wireless communication in a fading environment when using multi-

element antennas,” *Bell Labs Tech. Journal*, vol. 1, pp. 41-59, 1996.

[4] A. Paulraj, R. Nabar and D. Gore, *Introduction to space-time wireless communication*, Cambridge university press, 2003.

[5] X. Chen, P.-S. Kildal, and J. Carlsson, “Measurement uncertainties of capacities of multi-antenna system in anechoic chamber and reverberation chamber”, *the 8th Int. Symp. on Wireless Com. Sys.(ISWCS 2011)*, pp. 216 – 220, Nov. 2011.

[6] T. H. Loh, "Non-invasive measurement of electrically small ultra-wideband and smart antennas", *Invited Paper in the 9th Loughborough Antennas and Propagation Conference (LAPC 2013)*, pp. 456 – 460, Nov. 2013.

[7] Y. Huang; Y. Lu; S. Boyes, and T.-H. Loh, “Source-stirred chamber/cap method for antenna radiation efficiency measurements”, *the 5th European Conference on Antennas and Propagation (EUCAP 2011)*, pp.164 – 168, Apr. 2011.

[8] C. A. Balanis, Antenna Theory: Analysis and Design, 3rd Edition, John Wiley & Sons, Inc. 2005.

[9] J.F. Valenzuela-Valdes, M.A. Garcia-Fernandez, A.M. Martinez-Gonzalez, and D.A. Sanchez-Hernandez, “The Influence of Efficiency on Receive Diversity and MIMO Capacity for Rayleigh-Fading Channels”, *IEEE Trans. on AP*, vol.56, no.5, pp.1444 – 1450, May 2008.

[10] Arai, H., "An optimum design of handset antenna for MIMO systems," *the 7th European Conference on Antennas and Propagation (EuCAP 2013)*, pp.224 – 227, Apr. 2013.

[11] X. P. Chen, S. Kildal, J. Carlsson, and J. Yang, "Comparison of ergodic capacities from wideband MIMO antenna measurements in reverberation chamber and anechoic chamber," *IEEE Antennas and Wireless Propagation Letters*, Vol. 10, 466-469, 2011.

[12] X. Chen, *Characterization of MIMO Antennas and Terminals: Measurements in Reverberation Chambers*, PhD Thesis, Chalmers University of Technology, 2012.

[13] J. S. Holllis, *et al.*, *Microwave Antenna Measurements*, Scientific-Atlanta Inc. 1985.

[14] B. E. 61000-4-21:2011, "Electromagnetic Compatibility, Part 4-21: Testing and measurement techniques - Reverberation chamber test methods," ed: BSI Standards Publication, 2011.

Automated Wideband Test System, Measurement Uncertainty, and Design of On-chip Six-Port Reflectometers for 5G Applications

Byul Hur and William R. Eisenstadt
Dept. of ECE, Univ. of Florida, Gainesville, FL

Abstract—This paper introduces an automated wideband test system, measurement uncertainty, and designs of on-chip six-port reflectometers (SPRs) that can be used for 5G applications. The trial frequency bands of 5G technology research and development (R&D) include 15 GHz, 28 GHz, and 38 GHz. Reflection measurements at these high frequencies are an essential part of 5G R&D. A six-port reflectometer (SPR) can be used for the embedded reflection measurements. However, the complexity of its calibration makes measurements challenging. Performing multiple measurements at wideband frequencies is even more challenging. An automated test system of on-chip SPRs in this paper can alleviate this problem. The details of the automated test system are introduced. Automated measurements were performed from 12 GHz to 18 GHz, including 15 GHz. The discussion of the measurement uncertainty is included. The design, layout, and simulation results of a 28-GHz SPR are also presented.

Index Terms — Reflectometry, Built-in self-test, Automatic testing, Six-port reflectometer, embedded IC testing

I. Introduction

The 5th generation of mobile wireless networks can provide benefits such as increasing data rates and capacity. The 5G technology may offer better solutions to overcome the obstacles of the previous generations [1]. Multiple frequency bandwidths for 5G technology are under investigation, which include high frequency bands such as 15 GHz, 28 GHz, and 38 GHz [2],[3].

Refection coefficient measurements at these high frequencies are an essential part of 5G research and development (R&D). On-wafer radio frequency (RF) tests at these high frequencies can be performed not only for the R&D effort but also for the production of the RF integrated circuits (ICs). In order to reduce test costs of ICs, reflection coefficient measurement circuits can be embedded into a chip. Embedding the circuits can provide on-chip reflection coefficient measurement information. However, traditional vector network analyzer (VNA) method involves many RF hardware components, and the circuit size tends to become too large for an embedded purpose. An alternative method of reflection coefficient measurements, a six-port reflectometer (SPR), can be used for embedded applications because a SPR involves less circuit components [4]-[6]. However, the calibration method of a SPR is more complex than a traditional 2-term error correction. Also, test procedures of a SPR tend to be more complicated.

SPR measurements may involve multiple steps of adjusting calibration loads, and the corresponding measured results are processed to determine the reflection coefficients of a device-under-test (DUT). If calibration load adjustments and test equipment controls are carried out manually, complex test procedures may result in significant measurement inaccuracy for on-wafer tests and measurements. Moreover, it becomes even more challenging in repeating test procedures at wideband multiple frequencies. Therefore, an automation of SPR tests such as an automated wideband test system introduced in this paper is essential to alleviate the problem. This automated test system can reduce measurement errors caused by manual adjustments and controls, and it is suitable, particularly, for testing on-chip SPRs at wideband multiple frequencies. The details of the automated test system using an on-chip SPR are presented. The wideband measurements were performed from 12 GHz to 18 GHz, which include 15 GHz that is one of the 5G trial frequency bands. The discussion and statistical analysis of the measurement uncertainties at these wideband multiple frequencies were presented. Moreover, the design, layout, and simulation results of a SPR at 28 GHz which is also one of the 5G trial frequency bands are followed.

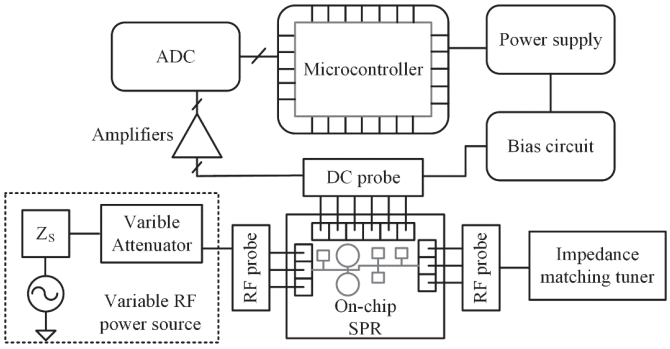

Fig. 1. A simplified block diagram of an automated wideband test system of an on-chip six-port reflectometer.

II. Automated Wideband Test System of On-chip SPRs for Embedded Testing

A simplified block diagram of the automated test system of an on-chip SPR is shown in Fig 1. The test system consists of a SPR IC, a microcontroller unit (MCU), an analog-to-digital converter (ADC) unit, amplifiers, variable RF power source components, and an impedance matching tuner.

Modern MCUs include an internal ADC and amplifier units. However, these units are drawn separately in Fig. 1 to emphasize the necessity of the circuit elements and the

978-1-4799-8887-7/15/$31.00 ©2015 IEEE

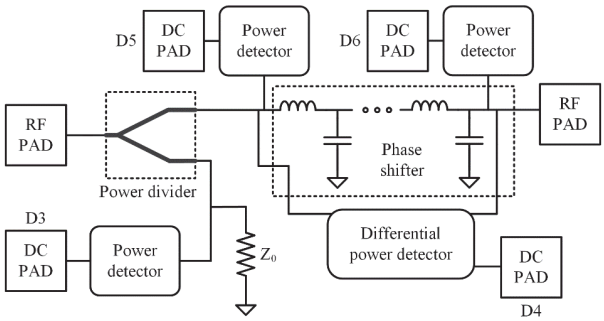

Fig. 2. A simplified block diagram of an on-chip SPR.

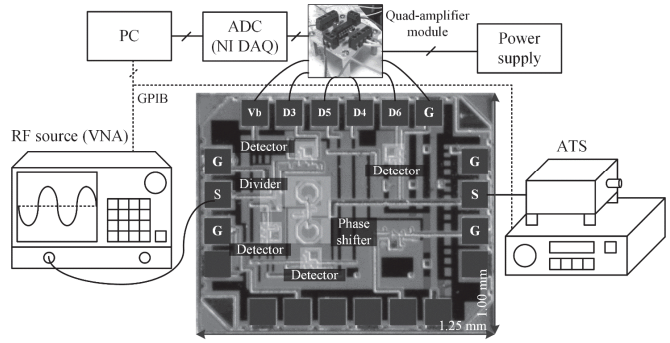

Fig. 3. A simplified block diagram of the automated wideband test system of an on-chip SPR.

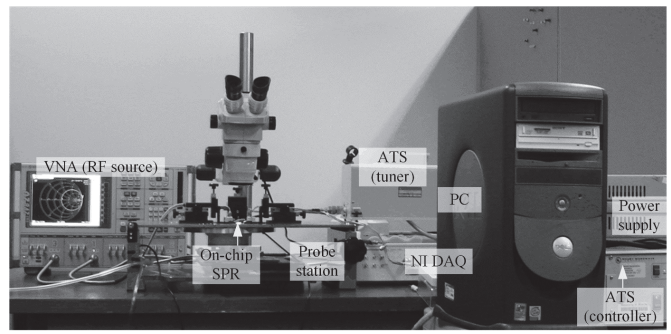

Fig. 4. A photograph of the automated wideband test system of an on-chip SPR.

operation of the test system. The amplifiers connected to the input nodes of the ADC unit can increase sensitivity of the RF power measurements. The converted digital data of the ADC unit is transmitted to the MCU. The MCU controls variable RF power source components and an impedance matching tuner. The variable RF power source components include a local programmable oscillator and a variable attenuator [7]. The MCU also controls an impedance matching tuner to provide proper load impedances for calibrations and measurements. The MCU can generate digital or analog control signals for an impedance matching tuner.

The bias circuit block in Fig. 1 includes bias circuits or power management ICs that can provide multiple levels of supply voltages because the required supply voltage levels for a MCU and the other SPR components can be different. The bias circuit block also includes design techniques which isolate the digital supply voltage of a MCU in order to reduce unwanted supply noise.

III. Design and Calibration of On-chip SPRs

An SPR design that is suitable for on-chip applications includes a power divider, a phase shifter, and power detectors. The on-chip SPR was demonstrated in a F20 GaAs process by Widemann [8]. Power detector components were designed using diodes. Another on-chip SPR with a similar structure was designed and fabricated by Lee [9]. This on-chip SPR was used as a DUT for tests and measurements in this paper. A simplified block diagram of the on-chip SPR is shown in Fig. 2. The power detectors were designed using diode connected bipolar junction transistors (BJTs). The on-chip SPR, depicted in Fig. 3, was fabricated in a 130nm BiCMOS process. A resistive divider is used for a power divider component. Two inductors and one capacitor are used for a phase shifter component. Differential amplitude detectors are used, which can also work as single-ended detectors with proper configurations [10]. The tested operating frequency was 20 GHz. The size of the chip is 1.25 mm × 1.00 mm including RF and DC PADs, and test circuits.

The SPR calibration procedures start with detector characterizations. Next, an initial value estimation of *w1*, *w2*, *Z*, and *R* can be processed. There are various methods of finding these initial values in the literature [11],[12]. The calibration method utilizes minimum five unknown loads with a constant magnitude of reflection coefficients and well-distributed phases [13]. Next, a six- to four-port reduction is processed to decrease the number of required coefficients of the SPR. Then, an error-box transformation is performed for mapping of the reflection coefficient from *W* plane to Γ plane. Important variables of the SPR calibration, a, b and c, can be found using three known loads and by solving three linear equations.

IV. Automated Wideband Measurement Procedures of an On-chip SPR

A simplified block diagram of the automated measurement system for an on-chip SPR is shown in Fig 3. A vector network analyzer (VNA) is employed as variable RF power source equipment. An automated tuner system (ATS) is utilized as an impedance matching tuner. National Instrument data acquisition (NI DAQ) and custom built quad-amplifier units are used as ADC and amplifier units, respectively. A custom PC application software controls the devices and equipment through USB and GPIB interfaces. The control software is developed using C and MATLAB languages [14]. The control software communicates with the VNA and ATS using NI-488.2 standard and SCPI commands. The control software enables successful multiple loops of the automated measurements in multiple frequencies if the devices and equipment are properly configured. Fig. 4 shows the

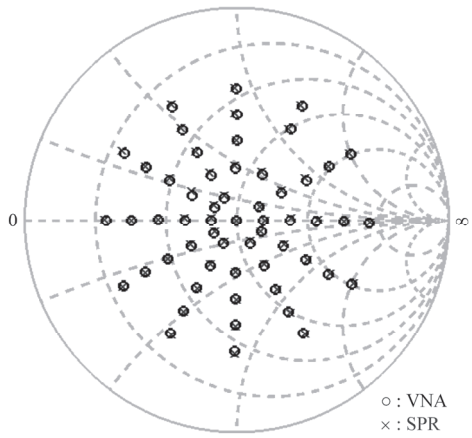

Fig. 5. Overlapped measurements at 12 GHz with selected test points

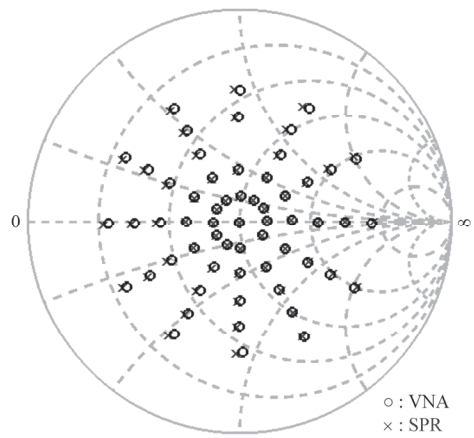

Fig. 6. Overlapped measurements at 15 GHz with selected test points.

configuration of the test system. The on-chip SPR as a DUT is placed on the chuck of the probe station.

The automated measurement procedures start with characterizing the impedance tuner at multiple desired frequencies using the VNA [15]. It is recommended to find minimum loads with a constant magnitude, well distributed phases, and open and short loads. Various test load impedances can be created by changing the motor positions of the ATS. The motor positions for the load impedances for the calibration and measurements are found and recorded to the memory storage of a PC. Then, the in-situ power detectors are carried out in case pre-characterized data is not given. The in-situ detector characterizations are processed by recording detector output voltages at swept RF source power levels from low to high at multiple frequencies. Finally, the recorded output levels are processed for post calibrations and optimizations to determine reflection coefficients and display them on Smith chart.

V. Wideband Measurements including 15 GHz and Measurement Uncertainties

The accuracy of the on-wafer RF measurements depends on many factors including maintaining signal integrity between the die and RF probes. If significant mechanical vibrations are present, then additional electrical noise and inaccuracies of on-chip measurements can be introduced. Therefore, it is preferred to use an electrically tunable impedance unit instead of a motorized impedance tuner unit for an on-chip SPR test. However, a motorized impedance tuner was used in this paper, and good verification results of the test system were obtained even in a challenging case. The automation of the test system made the on-chip SPR measurements at wideband multiple frequencies possible. The automated SPR measurements were carried out from 12 GHz to 18 GHz with 1-GHz steps. Fig. 5 shows the 12-GHz SPR measurement results which are the overlapped measurement results of a matched load and five sets of loads with the same magnitude and 30-degree phase steps by the VNA and SPR in Smith chart. Likewise, the 15-GHz and 18-GHz SPR measurement results are shown in Fig. 6 and Fig. 7. Good agreements are shown in the reflection coefficient measurements between the VNA and the SPR for 12-GHz, 15-GHz, and 18-GHz cases. The limitation of the measurement results at high frequencies can be introduced by the test equipment. For instance, in this test setup, the highest operating frequency of the impedance matching tuner by specifications is 18 GHz. It can be seen that the measured area of the 18-GHz case in Smith chart has become smaller than the area of the 12-GHz case. It is because the impedance matching tuner introduces more loss as the test frequencies become higher. Some of the sample impedances with significant errors that were introduced during the tuner characterization or measurements were not included. Measurement errors can be introduced by many factors including characterization errors of the impedance tuner and detectors, and mechanical vibrations and shocks. As it is shown in Fig. 6, the 15-GHz reflection measurement results are successfully demonstrated, where the frequency band is one of the 5G frequency bands. Although they were not shown, authors would like to take a note that the measurement results for other frequencies such as 13 GHz, 14GHz, 15 GHz, and so forth, show good agreements similar to 12-GHz an 18-GHz results.

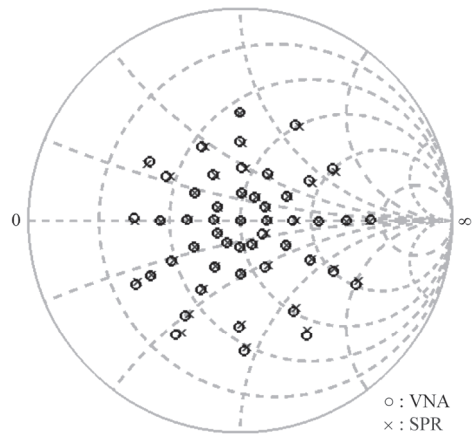

Fig. 7. Overlapped measurements at 18 GHz with selected test points.

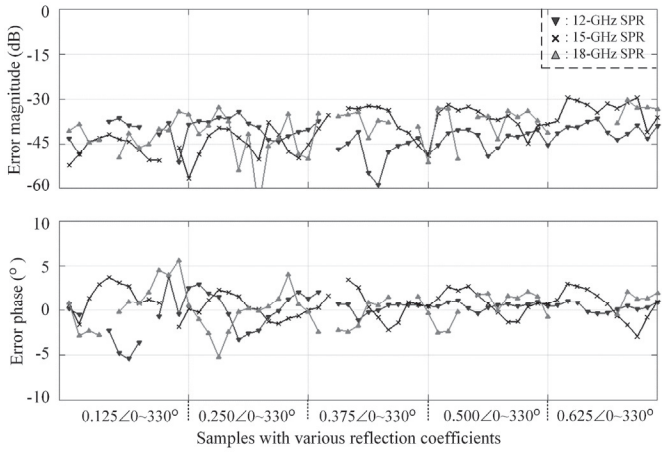

Fig. 8. Error magnitudes and error phases of the 12-GHz, 15-GHz, and 18-GHz SPR measurements.

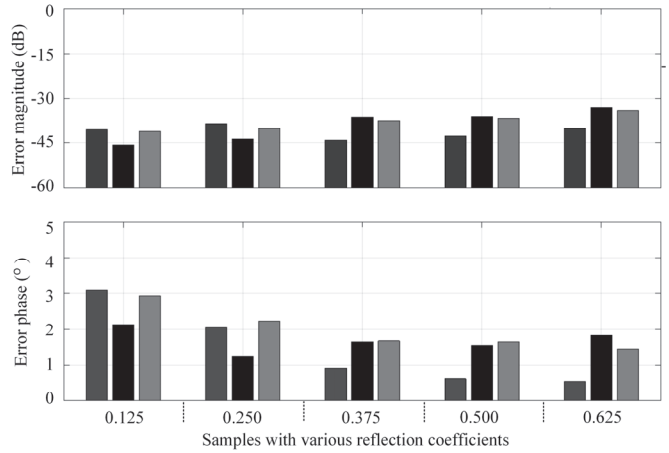

Fig. 9. Statistical analysis of the error magnitudes and error phases of the 12-GHz, 15-GHz, and 18-GHz SPR measurements.

Measurement uncertainties between VNA and SPR measurements were presented by the calculation of the relative distance and angle between samples as shown in Fig. 8. Let us say that $\mathbf{z_V}$ and $\mathbf{z_S}$ are the reflection coefficients from VNA and SPR measurements, respectively. The relative distance can be obtained by taking absolute value of subtracting the refection coefficients.

$$\text{Error magnitude} = |\mathbf{z_S} - \mathbf{z_V}|$$

The relative phase referenced by the reflection coefficient of a VNA can be obtained by the subtraction of taking angles of the reflection coefficients.

$$\text{Error phase} = \angle \mathbf{z_S} - \angle \mathbf{z_V}$$

The graph at the top of Fig. 8 describes the magnitude errors in a log scale between the VNA and SPR measurements for 12 GHz, 15 GHz, and 18 GHz. The 12 samples with the same magnitude are grouped, which varies from 0 to 330º with 30º steps. Five groups with different magnitudes at three test frequencies were presented.

The relative magnitudes of the 15-GHz SPR results are drawn as dark color lines and cross markers. The relative magnitudes of the 12-GHz and 18-GHz SPRs are drawn as gray and lighter gray color lines, and downward- and upward-pointing triangles, respectively. The error magnitudes are small and less than –30 dB except the samples with the magnitude of 0.625. The error magnitudes describe the tendency that they get slightly worse as the magnitude of the samples becomes bigger.

The relative phases of the 15-GHz SPR results are shown at the bottom of the Fig 8. The error phases are about less than ±6º for 12-GHz, 15-GHz, and 18-GHz SPRs. The error phases tend to get smaller as the magnitude of the reflection coefficients becomes bigger. These results in error magnitudes and phases do not imply a general tendency for SPR measurements since measurement accuracy of SPRs can vary by many factors.

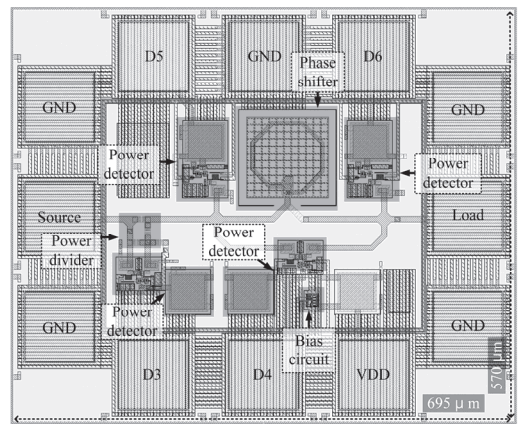

Fig. 10. A screenshot of the 28-GHz SPR design in a 130nm BiCMOS process.

The statistical analysis of the error magnitudes and phases is presented in Fig. 9. The average values of the error magnitudes are shown at the top of Fig. 9. They increase gradually as the frequencies becomes higher. The root mean square (RMS) values of error phases are shown at the bottom of the Fig. 9 They show the gradual decrease of the error phases.

VI. Design of the 28-GHz SPR for 5G Applications

The 28-GHz frequency band [16] is also one of the 5G trial bands that is used by companies including SAMSUNG electronics. The 28-GHz SPR is designed in a 130-nm BiCMOS process. The screenshot of the layout of the 28-GHz SPR is shown in Fig. 10. The 28-GHz SPR is implemented using a RF power divider, phase shifters, and RF power detectors. The restive divider is used as a power divider. Single on-chip inductor is used as a phase shift component. The single ended and differential power detectors are designed using BJT transistors. P-N junctions of the BJT transistors are used as RF diodes. The two internal bias voltages of the RF

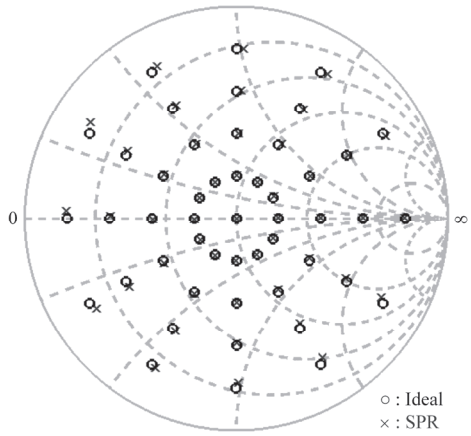

Fig. 11. Overlapped simulations at 28 GHz with selected test points.

power detectors are supplied by an on-chip bias circuit. The chip area including PADs is 695 µm × 570 µm.

The simulation results at 28 GHz are shown in Fig. 11. The swept magnitudes of the sample loads are from 0.2 to 0.8 with 0.2 steps. The swept phases are from 0 to 330º with 30º steps. The successful simulations are carried out, and the results shows good agreements. However, there are a few slight mismatches by SPR simulations. The minor errors result from many factors including methods of detector characterizations, SPR calibration parameters, and circuit simulation parameters [17]-[19].

VII. Conclusion

The automated wideband test system of an on-chip SPR for 5G applications was presented with successful measurement results (12 GHz ~ 18 GHz) including 15 GHz. The 28-GHz SPR circuit was introduced with the layout and simulations. The automated test system can be applied to various on-chip SPRs such as 38-GHz SPRs with proper considerations of specifications. The further SPR R&D is planned for the miniaturization and automation of the SPR system.

Acknowledgements

The authors would like to thank Ming-Che Lee for his prior work, Modelithics, Inc., Dr. Lawrence Dunleavy, Dr. Thomas Weller, Hugo Morales for the contribution and support for this work, Rohde & Schwarz and Sara Smith for the VNA equipment support, the Rev. Dr. Danny Austin for revising the manuscript for publication, Dr. Jinseop Lee for the mathematical analysis, and Soohee Park for assistance in writing the manuscript.

This work was supported in part by the National Science Foundation (NSF) under the SBIR Phase I grant (NSF Project # IIP-1013695, Aug. 2010 to Dec. 2010).

References

[1] C.-X. Wang, et al., "Cellular architecture and key technologies for 5G wireless communication networks," *IEEE Commun. Mag.*, vol. 52, no. 2, pp. 122-130, Feb. 2014.

[2] J. Gozalvez, "Prestandard 5G Developments [Mobile Radio]," *IEEE Veh. Technol. Mag.*, vol. 9, no. 4, pp. 14-28, Dec. 2014.

[3] T.S. Rappaport, et al., "Millimeter Wave Mobile Communications for 5G Cellular: It Will Work!," *IEEE Access*, vol.1, pp. 335-349, May 2013.

[4] G.F. Engen, "The six-port reflectometer: An alternative network analyzer," *IEEE Trans. Microw. Theory Techn.*, vol. 25, no. 12, pp. 1075-1080, Dec. 1977.

[5] G.F. Engen, "A (historical) review of the six-port measurement technique," *IEEE Trans. Microw. Theory Techn.*, vol. 45, no. 12, pp. 2414-2417, Dec. 1997.

[6] S.O. Tatu, E. Moldovan, K. Wu; B.R. Bosisio, "A new direct millimeter wave six-port receiver," *IEEE Trans. Microw. Theory Techn.,* vol. 49, no. 12, pp. 2517-2522, Dec. 2001.

[7] B. Hur and W.R. Eisenstadt, "CMOS programmable gain distributed amplifier with 0.5-dB gain steps," *IEEE Trans. Microw. Theory Tech.*, vol. 59, no. 6, pp. 1552-1559, Jun. 2011.

[8] F. Wiedmann, B. Huyart, E. Bergeault, L. Jallet, "New structure for a six-port reflectometer in monolithic microwave integrated-circuit technology," *IEEE Trans. Instrum. Meas.*, vol. 46, pp. 527-530, Apr. 1997.

[9] M.-C. Lee, "Embedded S-parameter Measurement," Ph.D. dissertation, Dept. Elect. Comput. Eng., Univ. of Florida, Gainesville, FL, 2010.

[10] M.-C. Lee; W.R. Eisenstadt, "A wide-band differential and single-ended microwave amplitude detector," in *IEEE Wireless and Microwave Technology Conference*, Melbourne, FL, Apr. 2010, pp. 1-5.

[11] U. Stumper, "Finding initial estimates needed for the Engen method of calibrating single six-port reflectometers," *IEEE Trans. Microw. Theory Techn.*, vol. 38, pp. 946-949, Jul. 1990.

[12] G.F. Engen, "Calibrating the Six-Port Reflectometer by Means of Sliding Terminations," *IEEE Trans. Microw. Theory Techn.*, vol. 26, no. 12, pp.951-957, Dec. 1978.

[13] F. Wiedmann, B. Huyart, E. Bergeault, L. Jallet, "A new robust method for six-port reflectometer calibration," *IEEE Trans. Instrum. Meas.*, vol. 48, pp. 927-931, Oct. 1999.

[14] B. Hur, W.R. Eisenstadt, "Tunable Broadband MMIC Active Directional Coupler," *IEEE Trans. Microw. Theory Tech.*, vol. 61, no. 1, pp. 168-176, Jan. 2013.

[15] B. Hur, "Radio Frequency Integrated Circuits and Systems for Test and Characterization," Ph.D. dissertation, Dept. Elect. Comput. Eng., Univ. of Florida, Gainesville, FL, 2011, unpublished.

[16] Y. Azar; et al., "28 GHz propagation measurements for outdoor cellular communications using steerable beam antennas in New York city," in *IEEE International Conference on Communications*, Budapest, Jun. 2013. pp. 5143-5147.

[17] W. R. Eisenstadt, B. Hur, "Embedded RF Test Circuits: RF Power Detectors, RF Power Control Circuits, Directional Couplers, and 77- GHz Six-Port Reflectometer," *J. of Inform. and Commun. Convergence Eng*., vol. 11, pp. 56-61, Mar. 2013.

[18] K. Mayaram, ; et al, "Computer-aided circuit analysis tools for RFIC simulation: algorithms, features, and limitations," *IEEE Trans. Circuits Syst. II, Analog Digit. Signal Process.*, vol. 47, no. 4, pp. 274,-286, Apr. 2000

[19] F.M. Ghannouchi, R.G. Bosisio, "A comparative worst-case error analysis of some proposed six-port designs," *IEEE Trans. Instrum. Meas.*, vol. 37, no. 4, pp.552-556, Dec. 1988

Rectangular-Waveguide Impedance

Dylan F. Williams, Jeff Jargon, Uwe Arz and Paul Hale

***Abstract*—We discuss the role of the wave impedance in power and temporal measurements and present an approach for accurately estimating the complex wave impedance of the TE_{10} mode in lossy rectangular waveguide from propagation-constant measurements.**

***Index Terms*—Calibration, rectangular waveguide, uncertainty analysis, vector network analyzer, wave impedance.**

I. Introduction

THE wave impedance of a TE or TM mode in a lossless hollow rectangular waveguide is defined as the ratio of the electric to magnetic field carried by the forward propagating mode in the guide. When the dominant TE_{10} mode is the only propagating mode in rectangular waveguide, its wave impedance plays a role similar to that of the characteristic impedance in quasi-TEM guides. In this paper, we will estimate the wave impedance of the TE_{10} mode in a lossy rectangular waveguide from measurements of the propagation constant and discuss the role that impedance plays in power and temporal measurements.

Rectangular-waveguide vector-network-analyzer (VNA) calibrations are designed to measure ratios of the complex amplitudes of forward and backward TE_{10} modes ("traveling waves" in the nomenclature of [1]) supported by the guides. Most often, these calibrations do not impedance transform the measured scattering parameters to a common constant real reference impedance, as is most often done in on-wafer and coaxial calibrations, but rather implicitly set the reference impedance of these calibrations to the wave impedance (*i.e.*, characteristic impedance) of the TE_{10} mode. This can be easily verified by noting that most rectangular-waveguide calibrations are based on setting the reflection coefficients of a waveguide section or sliding load to zero.

While the wave impedance reflects the relationship between the electric and magnetic fields of the propagating modes supported in hollow rectangular waveguides, most VNA calibrations do not determine that wave impedance at all. Until recently, these calibrations have been focused on controlling reflections and maximizing power flow, tasks for which the wave impedance is not required.

However, accurately measuring power in rectangular waveguides requires a knowledge of the phase of the wave impedance [1]. This is because the integral of the Poynting vector over the guide cross section cannot be evaluated without knowing the phase relationships between the electric and magnetic fields there.

Characterizing communications signals in rectangular metal waveguides requires determining not just power flow and reflection coefficients, but also the temporal characteristics of the signal in the guides. For example, we can now manufacture small electro-optic probes with sufficient sensitivity to directly measure the temporal voltage of a modulated signal in a rectangular wave [2] and on-going work promises to develop direct electric-field measurements in rectangular waveguide based on quantum rubidium or cesium standards [3;4].

However, in rectangular waveguide, we cannot identify a single "signal" in the guide, as the magnitude of the wave impedance of the guide varies with frequency, leading to differences in the temporal electric-field and magnetic-field waveforms. For the TE_{10} mode, for example, the electric field is very large and the magnetic field very small just above cutoff, but as the frequency increases, the electric field falls and magnetic field rises.

In this paper we will develop a practical expression for determining the wave impedance of the TE_{10} mode in lossy rectangular waveguides from measurements of the propagation constant of the mode, which is easily measured by the thru-reflect-line (TRL) calibration. We will then present recommendations for how to apply the wave impedance in rectangular-waveguide metrology.

II. Lossless Rectangular Waveguide

The modal fields of the dominant TE_{10} in lossless rectangular waveguide are given by equation 3.107 in [5] as

$$\begin{aligned} h_z &= \cos\left(\frac{\pi x}{a}\right) \\ h_x &= j\frac{\beta}{k_c^2}\frac{\pi}{a}\sin\left(\frac{\pi x}{a}\right) = j\frac{\beta}{k_c}\sin\left(\frac{\pi x}{a}\right) \\ e_y &= -Z_h\frac{j\beta}{k_c^2}\frac{\pi}{a}\sin\left(\frac{\pi x}{a}\right) = -Z_h\frac{j\beta}{k_c}\sin\left(\frac{\pi x}{a}\right), \end{aligned} \tag{1}$$

where a is the width of the waveguide, b is the height of the waveguide, $k_c = \pi/a$, $\beta = \sqrt{k_0^2 - k_c^2}$ is the propagation factor of the lossless mode, $Z_h = (k_0/\beta)\, Z_{\text{free-space}}$ is the wave impedance of the TE_{10} mode, and $k_0 = \omega/c$ and $Z_{\text{free-space}} = \sqrt{\mu_0/\varepsilon_0}$ are the wave number and impedance of free space, respectively. The factor $e^{-j\beta z}$ describes the evolution of these lossless modes in the direction of propagation z.

Manuscript received March 15, 2015. D. F. Williams, J. Jargon and P. D. Hale are with the National Institute of Standards and Technology, Boulder, CO 80305 USA (phone: 303-497-3138; e-mail: dylan.williams@nist.gov). U. Arz is with the Physikalisch-Technische Bundesanstalt, Bundesallee 100 D-38116 Braunschweig Germany.

III. Lossy Rectangular Waveguide

Estimating metal loss at microwave frequencies is usually quite difficult. One of the most effective strategies for estimating the characteristic impedance of lossy printed transmission lines is to use direct measurements of the propagation constant derived from the TRL calibration to estimate the loss of the lines, and then to use these measurements to estimate the characteristic impedance of the lossy lines. In this section we will outline a similar procedure for lossy rectangular waveguide. This will require applying the general waveguide circuit theory of [1], and some of the results of [6], which treats the temporal behavior of the theory's equivalent voltages and currents.

A. *Voltage and current description*

To apply the general waveguide circuit theory of [1;6], we start by defining a voltage v and current i that mimic the power and temporal behavior of the electric and magnetic fields in the guide. This simplifies the application of the circuit theory of [1] to the problem. As we will see shortly, there is no loss of generality in doing this.

While a number of definitions for the voltage v and current i are possible, we must keep in mind that different definitions only scale the impedance by a constant frequency-independent factor. We will use a causal power-voltage definition and define the voltage v as the integral of the electric field in the middle of the guide (i.e. integrating over the path at $x = a/2$ from $y = 0$ to $y = b$). The power-voltage characteristic impedance Z_0 of the lossless mode is then given by

$$Z_0 = \frac{|v_0|^2}{p_0^*} = \frac{b^2 Z_\mathrm{h}^2 (\beta/k_\mathrm{c})^2}{\frac{1}{4} ab (\beta/k_\mathrm{c})^2 Z_\mathrm{h}} = 4\frac{b}{a} Z_\mathrm{h} \,, \tag{2}$$

where $v_0 = jbZ_\mathrm{h}\frac{\beta}{k_\mathrm{c}}$ is the voltage obtained by integrating the modal electric field in the middle of the guide at $x = a/2$ from $y = 0$ to $y = b$, and $p_0 = \frac{1}{4}ab\left(\frac{\beta}{k_\mathrm{c}}\right)^2 Z_\mathrm{h}$ is the integral of the Poynting vector over the guide. Note that Z_0 is a scaled version of the wave impedance Z_h. We will call Z_0 the characteristic impedance of the lossless guide both to maintain consistency with the nomenclature of [1;6], but also to distinguish it from the wave impedance.

Alternatively, we could set v_0 equal to e_y at some point in the guide (*e.g.*, its center), in which case the voltage would be equal to the total electric field at the center of the guide. These expressions only differ by a fixed frequency-independent constant from the power-current, voltage-current and wave impedances, and do not imply any loss of generality.

B. *Separating longitudinal and transverse currents*

Our goal here is to develop formulas for estimating the characteristic impedance Z of the lossy guide from measurements of the propagation constant γ. We can now apply equations (33)-(36) in [1] for the capacitance C, inductance L, conductance G, and resistance R per unit length of the rectangular waveguide. This will allow us to separate the impacts of the longitudinal and transverse currents in the guide on the loss and characteristic impedance. They are

$$\begin{aligned}
C &= \frac{1}{|v_0|^2}\left[\int_S \varepsilon'|e_\mathrm{t}|^2\,\mathrm{d}S - \int_S \mu'|h_z|^2\,\mathrm{d}S\right] \\
L &= \frac{1}{|i_0|^2}\left[\int_S \mu'|h_\mathrm{t}|^2\,\mathrm{d}S - \int_S \varepsilon'|e_z|^2\,\mathrm{d}S\right] \\
G &= \frac{\omega}{|v_0|^2}\left[\int_S \varepsilon''|e_\mathrm{t}|^2\,\mathrm{d}S + \int_S \mu''|h_z|^2\,\mathrm{d}S\right] \\
R &= \frac{\omega}{|i_0|^2}\left[\int_S \mu''|h_\mathrm{t}|^2\,\mathrm{d}S + \int_S \varepsilon''|e_z|^2\,\mathrm{d}S\right],
\end{aligned} \tag{3}$$

where the integrals are performed over the cross section of the guide, i_0 is defined by $v_0 i_0^* = p_0$, $\varepsilon = \varepsilon' - j\varepsilon''$ and $\mu = \mu' - j\mu''$. These expressions ensure that the common relationships in (37) and (38) of [1] between the propagation constant γ, the characteristic impedance Z, and the per-unit-length parameters R, L, C, and G hold. That is, that $\gamma = \sqrt{(R + j\omega L)(G + j\omega C)}$ and $Z = \sqrt{(R + j\omega L)/(G + j\omega C)}$.

The expressions in (3) simplify in quasi-TEM lines since e_z and h_z can be ignored there. In this case, only h_t contributes to the currents in the metal, and adds to R and L. When there is no dielectric loss, C becomes constant and G is zero, allowing Z to be accurately estimated from measurements of the propagation constant with $Z = \gamma/j\omega C$ [7;8].

However, in rectangular waveguides, h_z cannot be neglected. The magnetic field h_z not only contributes to C, but currents in the metal due to h_z add to G, complicating the problem of determining the characteristic impedance of the guide from measurements of γ. Nevertheless, we can integrate the expressions in (3) and develop an approximation for Z in terms of the measured propagation constant γ.

The integral of $\varepsilon'|e_t|^2$ and of $\mu'|h_z|^2$ in the expression for C and integral of $\mu'|h_t|^2$ in the expression for L in (3) can be easily evaluated from the fields in (1). The principal contributions to R and G in (3) are from the electric fields in the metal that arise from the currents at the surfaces of metal walls of the rectangular waveguide. When the skin-depth approximation is valid, we can write the current in the metal walls as $J = (J_s/\delta)e^{-d/\delta}$, where δ is the skin depth and the surface current density J_s is equal to $\hat{n} \times h$ at the surface of the metal, where $\hat{n}$ is the unit vector normal to the metal surface [5]. We can also approximate the imaginary part of the dielectric constant of the metal as $\varepsilon'' \cong \sigma/\omega$, where σ is the conductivity of the metal. These relations allow the integrals of $\varepsilon''|e|^2$ in the expressions for R and G to be evaluated from the magnetic field of the lossless guide given in (1).

From these approximations, we obtain

$$\begin{aligned}
G + j\omega C &\cong \frac{1}{2|v_0|^2}\left(\frac{1+j}{\sigma\delta}(a+2b) + j\omega\mu ab\frac{\beta^2}{k_c^2}\right) \\
R + j\omega L &\cong \frac{1}{2|i_0|^2}\frac{\beta^2}{k_c^2}\left(\frac{1+j}{\sigma\delta}a + j\omega\mu ba\right),
\end{aligned} \tag{4}$$

where the imaginary part of the term $1+j$ in (4) accounts for the stored magnetic energy in the metal. From (4) we now have

$$\frac{R}{\omega L_0} \pm \frac{G}{\omega C_0} = \frac{R}{\omega L_0}\left(1 \pm \frac{a+2b}{a}\frac{k_c^2}{\beta^2}\right), \tag{5}$$

where the capacitance C_0 and the inductance L_0 of the lossless guide are given by

$$\begin{aligned} C_0 &= \frac{1}{2|v_0|^2}\mu ab\frac{\beta^2}{k_c^2} \\ L_0 &= \frac{1}{2|i_0|^2}\mu ab\frac{\beta^2}{k_c^2}. \end{aligned} \tag{6}$$

We can now write the propagation constant γ and characteristic impedance Z of the dominant mode of the rectangular waveguide as

$$\begin{aligned} \gamma &= \sqrt{(R+j\omega L)(G+j\omega C)} \\ &\approx \sqrt{((1+j)R+j\omega L_0)((1+j)G+j\omega C_0)} \end{aligned} \tag{7}$$

and

$$\begin{aligned} Z &= \sqrt{\frac{R+j\omega L}{G+j\omega C}} \\ &\approx \sqrt{\frac{(1+j)R+j\omega L_0}{(1+j)G+j\omega C_0}}. \end{aligned} \tag{8}$$

C. Approximation for characteristic impedance

Now we can use measurements of the propagation constant γ to approximate $R/\omega L_0$ and $G/\omega C_0$, and then estimate Z. From (8) we see that both the resistive and conductive losses add to the total loss, which gives the approximation

$$\begin{aligned} \gamma &\approx j\beta\sqrt{\left(1-j\frac{R}{\omega L_0}\right)\left(1-j\frac{G}{\omega C_0}\right)} \\ &\approx j\beta\left(1-\tfrac{1}{2}j\left(\frac{R}{\omega L_0}+\frac{G}{\omega C_0}\right)\right), \end{aligned} \tag{9}$$

or

$$\frac{R}{\omega L_0}+\frac{G}{\omega C_0} \approx 2\frac{\alpha}{\beta}. \tag{10}$$

We can now estimate the characteristic impedance Z of the lossy guide in terms of the dimensions of the guide, the easily calculated characteristic impedance Z_0 of the lossless mode, and the easily measured propagation constant $\gamma = \alpha + j\beta$ of the lossy mode with

$$\begin{aligned} Z &= Z_0\left(1+\frac{1-j}{2}\left(\frac{R}{\omega L_0}-\frac{G}{\omega C_0}\right)\right) \\ &\approx Z_0\left(1+(1-j)\frac{\alpha}{\beta}\left(\frac{1-\frac{a+2b}{a}\frac{k_c^2}{\beta^2}}{1+\frac{a+2b}{a}\frac{k_c^2}{\beta^2}}\right)\right). \end{aligned} \tag{11}$$

The formula $\gamma = jk_0\sqrt{\varepsilon_{\text{eff}}}$ can be useful in this context. It relates the propagation constant to the effective relative dielectric constant ε_{eff} defined in [1] and is often used by VNA calibration software to represent the propagation constant γ.

D. Approximation for the wave impedance

Recognizing that the characteristic impedance Z is just a scaled version of the wave impedance Z_h, we also have

$$Z_h \approx Z_{h\,\text{lossless}}\left(1+(1-j)\frac{\alpha}{\beta}\left(\frac{1-\frac{a+2b}{a}\frac{k_c^2}{\beta^2}}{1+\frac{a+2b}{a}\frac{k_c^2}{\beta^2}}\right)\right), \tag{12}$$

where $Z_{h\,\text{lossless}}$ is the wave impedance of a lossless section of guide with the same dimensions.

IV. Discussion

As a general rule, most frequency-point-by-frequency-point rectangular-waveguide circuit designs can be accomplished with the traditional TE_{10} scattering parameters determined by VNA calibration algorithms that leave the reference-impedance of rectangular-waveguide calibrations set to the wave impedance of the guide. It would be very disruptive to try to change this industry-wide practice.

Nevertheless, the wave impedance is required for accurate power and temporal waveform measurements in rectangular waveguide [6]. For example, the cross-term in equation (49) of [1] relating the power to wave amplitudes cannot be evaluated without knowing the phase of the characteristic impedance of the guide. Equations (11) and (12) above allow the importance of this term to be evaluated directly.

Figure 1 plots the wave impedance Z_h of the TE_{10} mode in a lossless rectangular waveguide as a function of the frequency f normalized by the cutoff frequency f_c. Clearly the wave impedance varies rapidly near the cutoff frequency and the temporal electric-field and magnetic-field of waveforms with energy concentrated at these frequencies will differ considerably. Figure 2 compares the extreme case of the normalized electric and magnetic fields of five zero-phase tones with energy equally distributed between 1.05 f_c and 1.35 f_c. Here, the electric and magnetic field waveforms are quite different, as we would expect, given the rise of the wave impedance Z_h near f_c.

However, most rectangular waveguide is only used between 1.25 f_c and 1.9 f_c. As a result, the variation of the wave impedance over the band is smaller, making differences in the temporal electric and magnetic-field waveforms difficult to detect. The figure of merit $q = (Z_h(f_1)-Z_h(f_2))/\ Z_h(0.5*(f_1+f_2))$, where f_1 and f_2 are the lower and upper edges of the signal, is a convenient metric for estimating the relative differences in the

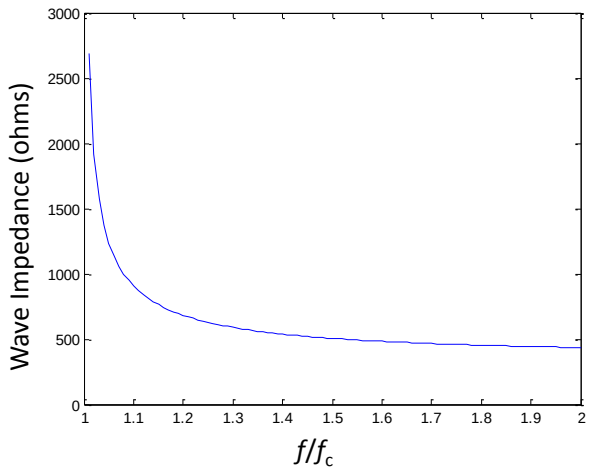

Fig. 1. The characteristic impedance of a uniform section of lossless rectangular waveguide.

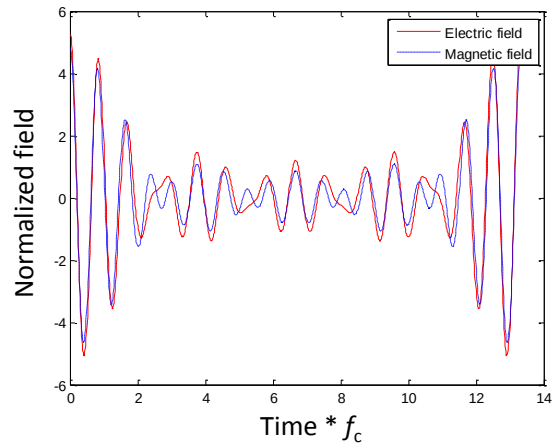

Fig. 2. Normalized electric and magnetic fields of a set of five zero-phase tones with equal power in a uniform section of lossless rectangular waveguide.

electric-field and magnetic-field of waveforms with a relatively small fractional bandwidth. In our extreme example, this ratio was approximately 1, whereas q is only about 0.05 for a modulated signal with a 10 % bandwidth located near the center of the waveguide band. Thus we would expect that in many practical instances, the differences between the electric-field and magnetic-field waveforms will be small as well.

Nevertheless, even these small differences may be important in precision metrology. In some cases, it may even be important to estimate and correct for the shift of the impedance of the TE_{10} mode due to waveguide losses.

Here again, the wave impedance or characteristic impedance can be estimated from (11) and (12). Then the normalizing voltage v_0 or current i_0 in the theories of [1;6] can be set so that v and i correspond to the desired electric and magnetic field quantities of interest. Now v and i can be calculated from equations (55-56) of [1] with Z_{ref} set to the characteristic impedance of the guide, which is directly proportional to the wave impedance Z_h. If loss is included, (64) of [1] should be applied to transitions to other media. This will correctly relate the powers and temporal behavior v and i to the electric-field and magnetic-field waveforms of the TE_{10} modes supported by the guides.

The theories of [1;6] can also be used to set the reference impedance of measured scattering parameters in the rectangular-waveguide sections to a constant real value. This can be useful when using software packages based on fixed, real and frequency-independent reference impedances. However, care should be taken in these situations to clearly communicate that a reference-impedance transformation was applied to the measurements, and to clearly specify the value of the resulting reference impedance in the rectangular-waveguide sections.

References

[1] R. B. Marks and D. F. Williams, "A general waveguide circuit theory," *J. Res. Nat. Instit. Standards and Technol.*, vol. 97, no. 5, pp. 533-562, Sept.1992.

[2] D. J. Lee, J. Y. Kwon, Y. P. Hong, and J. A. Jargon, "Photonic-Assisted Endoscopic Analysis of W-Band Waveguide," *IEEE Photonics Conference*, pp. 216-217, 2014.

[3] C. L. Holloway, J. A. Gordon, A. Schwarzkopf, D. A. Anderson, S. A. Miller, N. Thaicharoen, and G. Raithel, "Sub-wavelength imaging and field mapping via electromagnetically induced transparency and Autler-Townes splitting in Rydberg atoms," *Applied Physics Letters*, vol. 104, no. 244102, pp. 1-5, 2014.

[4] C. L. Holloway, J. A. Gordon, S. Jefferts, A. Schwarzkopf, D. A. Anderson, S. A. Miller, N. Thaicharoen, and G. Raithel, "Broadband Rydberg Atom-Based Electric-Field Probe for SI-Traceable, Self-Calibrated Measurements," *Antennas and Propagation, IEEE Transactions on*, vol. 62, no. 12, pp. 6169-6182, Dec.2014.

[5] R. E. Collin, *Foundations for Microwave Engineering* McGraw-Hill, Inc., 1966.

[6] D. F. Williams and B. Alpert, "Causality and waveguide circuit theory," *IEEE Trans. Microwave Theory Tech.*, vol. 49, no. 4, pp. 615-623, Apr.2001.

[7] R. B. Marks and D. F. Williams, "Characteristic Impedance Determination using Propagation Constant Measurement," *IEEE Microwave and*

Guided Wave Letters, vol. 1, no. 6, pp. 141-143, June1991.

[8] D. F. Williams and R. B. Marks, "Transmission Line Capacitance Measurement," *IEEE Microwave and Guided Wave Letters*, vol. 1, no. 9, pp. 243-245, Sept.1991.

Power Control for S-parameters and Large Signal Characterization at (sub)-mmWave frequencies

L. Galatro, S. Galbano, A. Santaniello, M. Spirito

Electronics Research Laboratory, Delft University of Technology

Mekelweg 4, 2628CD Delft, Netherlands

Abstract — In this contribution we present a frequency scalable approach to achieve an accurate power control for levelled s-parameters and large signal characterization of devices working at millimeter and sub-millimeter waves. The method is based on a software-aided control loop that mimics the behavior of an automatic level control system, allowing to dynamically adjust the power delivered to the DUT at every frequency. The proposed hardware configuration employs only the VNA mm-wave extender modules, bypassing the need of expensive add-on test-sets.

Measurement results are provided in WR-10, WR-05 and WR-03 waveguide bands to show the applicability of the method at different frequencies and different hardware setups (i.e., VNA extender modules from different vendors). The power control at the system ports and the capabilities of the proposed setup for power controlled S-parameters and large signal measurements are reported.

Index Terms — mm-wave characterization, vector network analyzer (VNA), S-parameters, large signal characterization.

I. Introduction

SiGe bipolar technology is continuously increasing the device maximum operating frequencies, in terms of f_T and f_{MAX}, currently approaching 0.5 THz [1]. In this framework, large emphasis is placed on demonstrating the capabilities of SiGe in real life application, aiming at large volume markets. In order to foster the technology improvements, there is an increased need for accurate small and large signal characterization test-benches which could support device model validation together with technology optimization.

When considering measurements at mm-wave and submm-wave, one of the limitations is the measurement dynamic range reduction. As frequency increases the power available decreases while the noise floor, which is set by the measurement instruments, remains ideally constant, bringing to a reduction of the dynamic range. In standard VNA configurations, the maximization of the dynamic range (for a given power level) is achieved by means of the automatic level control (ALC). The ALC dynamically adjusts the power available from the source by sampling the test channel in a feedback loop, resulting in an output of the source transmitter essentially constant, thus maximizing the measurement dynamic range. When measuring at frequencies higher than 75 GHz, mm-wave extenders are employed, excluding the ALC from the measurement loop and disallowing power level control. As shown in Fig 1, available power at the extender ports can present large fluctuations in standard setups, which would cause a (potential) loss of dynamic range as high as 10 dB, when the power is backed off from maximum drive. Furthermore, when the source power is not controllable, ensuring a small signal stimulus to a DUT (active device) during s-parameters measurement becomes problematic.

In this paper we present a hardware and calibration procedure to achieve a frequency scalable method for absolute power control and measurement in small signal and large signal measurements. The presented method, based on a software based loop, allows refined control of the power presented at the DUT in the entire frequency band covered by the VNA extender.

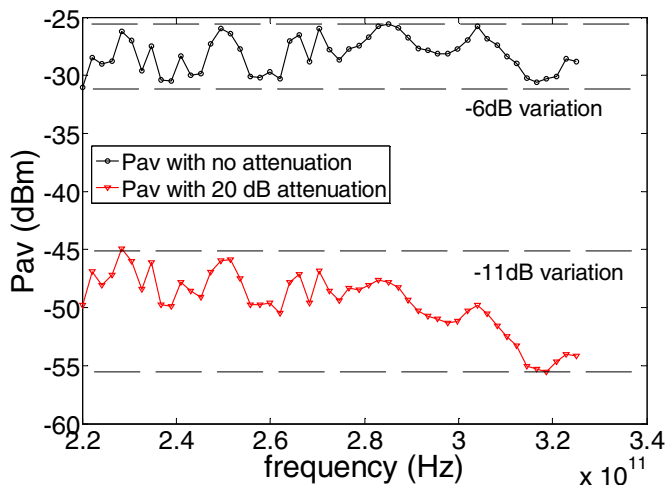

Fig. 1. Output power versus frequency of a mm-wave extender module in the WR-03 range, at different value of external attenuation.

The control of the available power enables the possibility for power controlled s-parameter measurements as well as large signal characterization of devices at every frequency covered by the VNA extenders. In this work, measurement data are presented in the WR-10, WR-05 and WR-03 waveguide bands.

II. System Architecture

Fig 2 shows the schematic representation of the proposed test-bench. In this setup, the test-set is equipped with two VNA extender modules, allowing full two-port calibrated s-

978-1-4799-8887-7/15/$31.00 ©2015 IEEE

parameters. Currently, modules for different waveguide bandwidths are commercially available, covering an overall frequency range from 50 GHz to 1.1 THz [2], and the designed setup is suitable for all the possible waveguide bandwidths. The generation of the RF and LO signals providing the feed to the mm-wave extenders is performed using the internal sources of the VNA, when using a two-source analyzer.

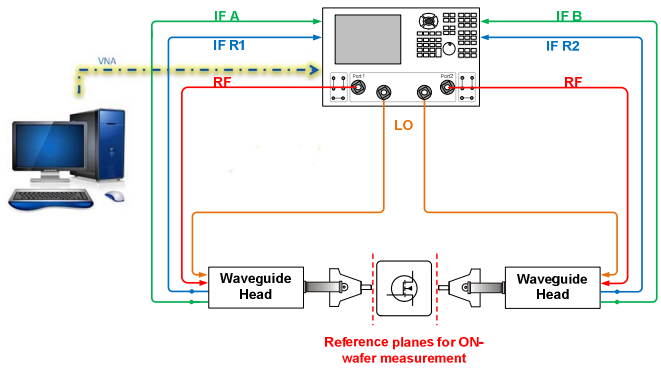

Fig. 2. Simplified schematic for the proposed measurement setup.

The acquisition of the coupled waves is performed using the VNA receivers. The values of the scattered waves are then sampled and sent to an external controlling PC, where all the computation is performed. In addition to the previous components, not shown in the schematic, a power meter is needed to perform the absolute power calibration, as it will be discussed in following sections. In this setup a calorimeter based power meter has been used, allowing power measurement from 75 GHz to 1.1 THz [2]. Finally, for on-wafer DUT measurements, wafer probes need to be used.

III. The Proposed Method

In order to properly control the power, the knowledge of the absolute power at the reference port, together with the chain gain/losses of the mm-wave extender modules are required. Once these parameters are known, the software aided-solution could mimic the behavior of a closed-loop control system.

The proposed calibration procedure that allows the refined power control at the input of the DUT requires four steps. First, a conventional off-wafer two-port calibration (i.e., TRL [3] or LRM [4]) is performed at the mm-wave modules waveguide sections. Then a power calibration, as described in [5], is performed at the waveguide port in order to have a complete knowledge of the absolute power at the output of the module. The power calibration is performed by connecting the power meter at the port 1 calibration reference plane, as set from the off-wafer calibration. After the power measurement is performed, a link between absolute power and the waves measured at the VNA receiver is created by means of an additional error term [5].

Once the power at the waveguide reference planes can be correctly measured, a last OFF-wafer step must be performed in order to characterize the relation between the RF source power, set in the VNA, and the power available at waveguide Port-1 and Port-2. This step is the so-called "power leveling". During power leveling, a large number of frequency sweeps is performed, varying the VNA RF source power level while measuring the related output power at the waveguide port and the reflection coefficient Γ at both Port-1 and Port-2, which are connected to a 50Ohm termination. Hence, the power available at the same reference planes, at each frequency, can be computed as:

$$P_{av_{Port=1,Port=2}}|_f = \frac{P_{in_{Port=1,Port=2}}}{\left(1-\left|\Gamma_{Port=1,Port=2}\right|^2\right)} \qquad (1)$$

The result, as depicted in Fig. 3, is a look-up table, showing the power available at the specified port as a function of both the source power provided by the VNA, P_{RF}, and the frequency. Once the power leveling is performed, the system is able to compute the source power level that must be set in the PNA in order to have the desired power available at Port-1 and Port-2, for all the frequencies of interest.

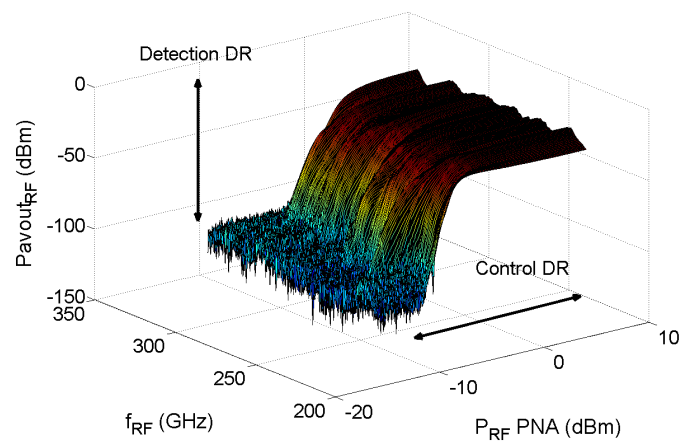

Fig. 3. Power leveling results for Port1 of the proposed setup, in the WR-3 waveguide band. The plot depicts the value of the output power at the port of the extender module as a function of the source power provided by the VNA and the frequency.

In order to move the calibration reference plane to the probe tips, a further calibration step is needed, consisting in the de-embedding of the wafer probes. This de-embedding procedure can be performed on alumina based impedance standard substrate (ISS) or on a calibration kit manufactured on fused-silica substrate as described in [6], using standard two-port de-embedding procedures.

IV. Experimental Results

A. Power Control

After the setup is properly calibrated and the power leveling is performed, it is possible to accurately control the power at the output of the extenders, or at the probe tips if an on-wafer configuration is selected.

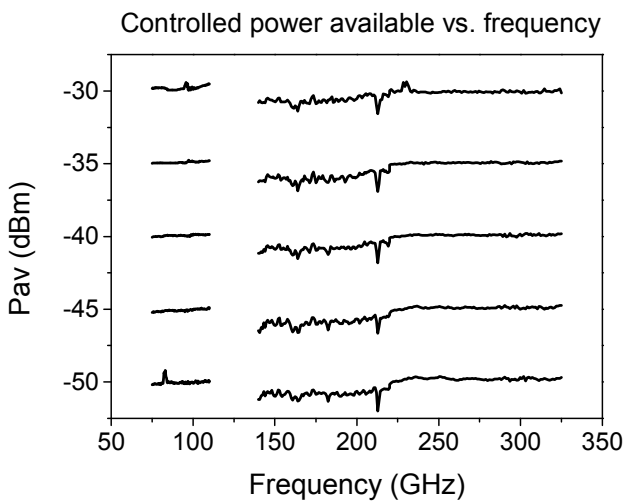

Fig. 4. Power available at Port1 of the proposed setup versus frequency in the WR-10, WR-5 and WR-3 waveguide bands, after power leveling. The plot shows the measured output power for different values of power set from the user, versus frequency.

In Fig. 4 values of power available at the waveguide ports of the mm-wave extenders are shown for the three considered frequency ranges after the power leveling is applied. The accuracy in power control depends on the frequency range and on the hardware implementation of the up-conversion chain, which depends on the manufacturer. For the considered configuration, the largest spread in control level is obtained in the WR-5 frequency range, where the power control can only be set with a ±0.75dB error. Note, that the read out in the absolute power provides an accurate value independent of the uncertainty in the set power.

B. Stability

In order to showcase the performance of the proposed setup in terms of measurement stability, repeated measurements have been performed in a limited time period over the different waveguide bands, and the results have been used to extract the stability of the measurements in terms of standard deviation, versus frequency.

First, 100 consecutive measurements have been performed in the entire frequency range. Then, another measurement has been performed after 10 minutes, in which the system has been turned off. In Fig. 5 the variation of the mean value of the available power, normalized to the available power at thermal regime, is shown versus time. For all the considered waveguide bands, the result highlights an RC time constant behavior, which can be associated to a thermal transient. The average available power thus vary from an initial value, measured when the system is in a "cold state", to a regime value when the thermal transient is completed. When the RF and LO signals are switched off for a sufficiently long time period, the system returns to its initial state.

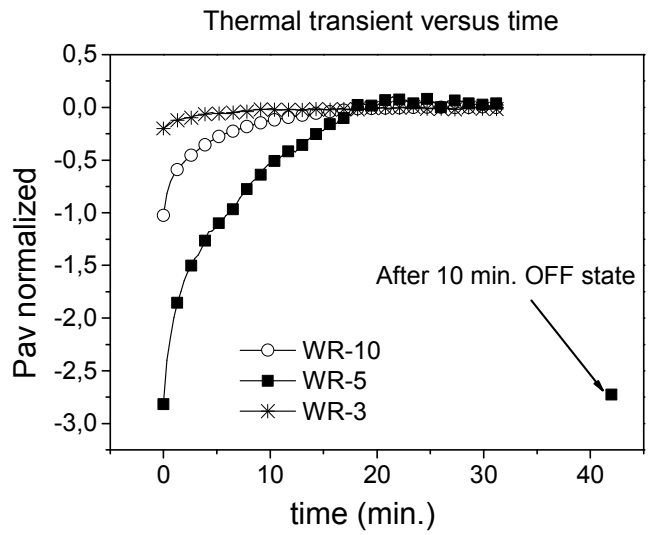

Fig. 5. Average available power, normalized to the regime value, measured at port-1 of the designed setup, for WR-10, WR5 and WR-3 waveguide bands, for the same power set from the user equal to -30 dBm, over 100 consecutive measurements.

As shown in Fig. 5, the characteristics of the thermal transient, in terms of time constant and power variation, are strongly dependent on the considered module, being frequency and manufacturer dependent.

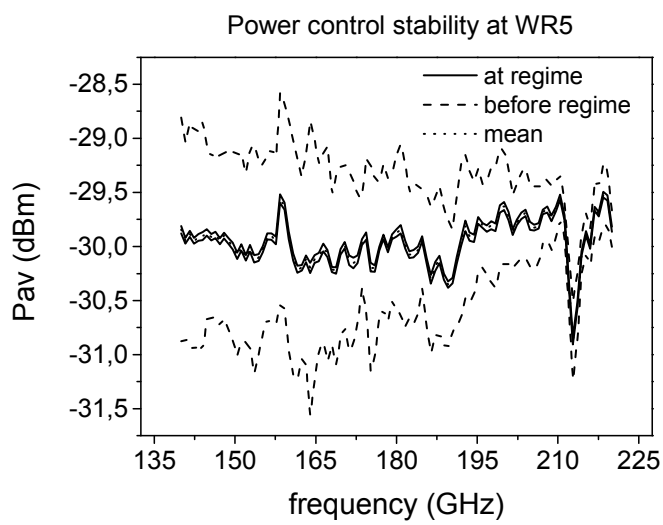

Fig. 6. Stability of the power control in the WR-5 waveguide band. The dashed lines represent the stability boundaries defined using the standard deviation extracted from the 100 measurements considered in Fig.5. The solid lines define the stability boundaries using the standard deviation extracted from measurements when thermal stability is reached.

This thermal transient has to be taken into account when defining the stability of the measurement setup. In fact, the measurement repeatability strongly depends on the region of the transient in which the specific measurement is performed. In order to define the impact of the thermal drift on the stability performances, first the standard deviation versus frequency has been extracted from the 100 repeated measurements shown in Fig. 5. Then the same procedure has been performed only considering measurements obtained at the thermal regime. The results are showcased in Fig. 6, where the stability boundaries defined using the two different standard deviations are sketched for the WR-5 waveguide band. This plot shows a drastic improvement in terms of stability when performing measurements at thermal regime, with the average value of standard deviation varying from 2 dB to 0.03 dB.

C. Large signal capabilities

The procedure described in section III allows the refined control of the available power at both ports of the measurement setup. When the power measurement and control capabilities are enabled, large signal measurements can be also performed.

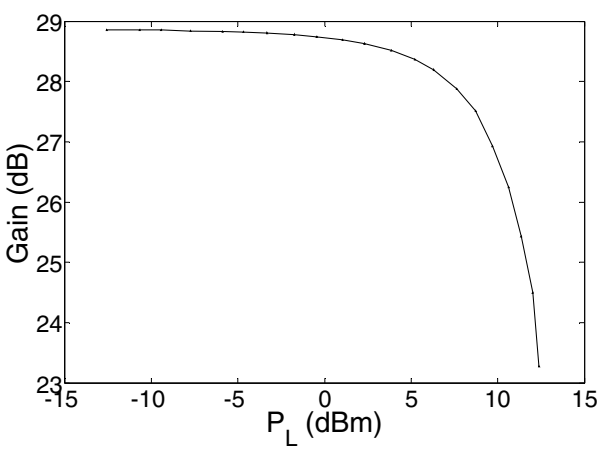

Fig. 5. Gain vs. power delivered to the load measured for a Norden Millimeter N09-2412 amplifier at 90 GHz

In order to showcase the capabilities of the system for large signal measurements, a Norden Millimeter N09-2412 amplifier has been measured in the frequency range from 75 to 110 GHz, for an input power range from -40 to -10 dBm. Fig. 5 shows the results in terms of power gain versus power delivered to the load obtained at 90 GHz.

V. Conclusions

In this work a novel method to achieve power control for s-parameters and large signal characterization for mm-wave and sub-mm-wave devices has been presented. The method aims to maximize the measurement dynamic range in setups in which mm-wave extender modules are used, allowing a refined control of the power available at the DUT. The system architecture has been described, together with all the calibration steps required for achieving the power level control.

Measurement results have been shown highlighting the power level control capabilities at the mm-wave extender ports in the WR-10, WR-5 and WR-3 waveguide bandwidths. A study has also been performed in order to showcase the stability performances of the proposed setup and their dependence on the system thermal state. Finally the capability of the designed setup for large signal measurements in the WR-10 frequency range has been demonstrated.

Acknowledgments

This research work is supported by the CATRENE – CT209 – RF2THZ SiSOC project and the European Union's Seventh Programme for research No 316755.

References

[1] B. Heinemann, R. Barth, D. Bolze, J. Drews, G. G. Fischer, A. Fox, O. Fursenko, T. Grabolla, U. Haak, D. Knoll, R. Kurps, M. Lisker, S. Marschmeyer, H. Rucker, D. Schmidt, J. Schmidt, M. A. Schubert, B. Tillack, C. Wipf, D. Wolansky, Y. Yamamoto, "SiGe HBT technology with fT/fmax of 300GHz/500GHz and 2.0 ps CML gate delay", *Electron Devices Meeting (IEDM)*, 2010 IEEE International , vol. 30, no. 5, pp 1-4, 6-8 Dec. 2010

[2] Virginia Diodes [Online], available: *www.vadiodes.com*

[3] G. F. Engen and C. A. Hoer, "Thru-reflect-line: An improved technique for calibrating the dual 6-port automatic network analyzer", *IEEE Trans. Microw. Theory Tech.,* vol. MTT-27, no. 12, pp. 987-993, Dec. 1979

[4] H. J. Eul, B. Schiek, "Thru-Match-Reflect: One Result of a Rigorous Theory for De-Embedding and Network Analyzer Calibration," *Microwave Conference, 1988. 18th European* , vol., no., pp.909,914, 12-15 Sept. 1988

[5] A. Ferrero, U. Pisani, "An Improved Calibration Technique for On-Wafer Large Signal Transistor Characterization", *IEEE Trans. Instrum. Meas.*, vol. IM-47, pp.260-364, Apr. 1993

[6] M. Spirito, G. Gentile, A. Akhnoukh, "Multimode analysis of transmission lines and substrates for (sub)mm-wave calibration," *82nd ARFTG Conf. Dig.*, vol., no., pp.1,6, 18-21 Nov. 2013

Full-Wave Electromagnetic Modeling of Sub-millimeter Wave HEMT Parasitics

Yasir Karisan*, Cosan Caglayan, Georgios C. Trichopoulos, and Kubilay Sertel
The ElectroScience Laboratory, The Ohio State University
1330 Kinnear Rd, Columbus, OH 43212
Email: {karisan.1, caglayan.1, trichopoulos.1, sertel.1}@osu.edu

***Abstract*—We present a new distributed parasitic equivalent circuit model to accurately reproduce the frequency response of electromagnetic field couplings within the structure of submillimeter-wave high electron mobility transistors in the millimeter-wave and terahertz bands. To construct the proposed circuit model, we develop a multi-step parameter extraction algorithm, and demonstrate its accuracy through comprehensive comparisons between full-wave simulated, measured and modeled frequency responses of the presented test patterns up to 750 GHz.**

***Index Terms*—HEMT, distributed parasitic equivalent circuit model, electromagnetic coupling, parameter extraction.**

I. Introduction

Through aggressive scaling of channel length to deep sub-micron dimensions, high electron mobility transistors (HEMTs) with cutoff frequencies in the terahertz (THz) regime can now be realized [1]. Consequently, new challenges emerge in terms of device characterization and subsequent integration into high frequency electronic circuitry. From the standpoint of a circuit designer, compact transistor models with wideband accuracy is a very critical tool for minimizing the number of design iterations for microwave monolithic integrated circuits (MMICs). In particular, the effect of geometry- and material-dependent parasitic couplings, as a result of electromagnetic (EM) field interactions within the device structure, becomes increasingly more pronounced compared to intrinsic device behavior, as new transistor technologies with smaller feature sizes are introduced. Accordingly, availability of small-signal equivalent circuits that account for intrinsic and extrinsic device characteristics concurrently becomes indispensable for realizing high performance sub-mmW MMICs.

In conventional HEMT equivalent circuits, parasitic coupling is modeled using lumped resistive and reactive elements. However, as the frequency of application is raised into sub-mmW band, the physical device dimensions become comparable to the operation wavelength. As such, it becomes imperative to model the device electrodes as distributed elements in order to maintain the modeling accuracy in the THz band.

Over the past decade, distributed parasitic equivalent circuit extraction of HEMTs has been focused on optimization of equivalent circuit parameters to fit the experimental data [2]. The main drawback of parameter extraction from a single S-parameter measurement is that there exist more unknowns than the number of equations provided by the measured data. Perhaps more importantly, the accuracy of pure optimization-driven methods is dependent heavily on the quality of the starting parameter values (i.e., initial guesses). Here, we present an alternative multi-step approach that relies on several full-wave electromagnetic simulations of the device layout. As such, the ill-conditioned parameter-fitting problem of measurement based equivalent circuit extraction is circumvented.

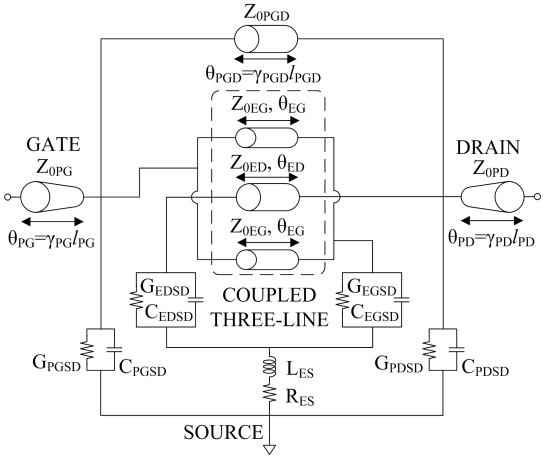

Fig. 1: Distributed parasitic equivalent circuit model of HEMT- for submillimeter-wavelengths.

In order capture for the wave propagation effects along the device electrodes at THz frequencies, a distributed parasitic equivalent circuit model is proposed here. Based on this distributed parasitic circuit model, we develop a systematic parameter extraction algorithm to determine the lumped and distributed circuit components. The accuracy of this new methodology is validated through comparisons between simulated and measured frequency responses, as well as the computed response of the circuit model for 10-750GHz band.

II. Parasitic Equivalent Circuit Modeling by Full-Wave EM Simulations

A. Distributed Parasitic Equivalent Circuit for THz HEMTs

To extend the validity of lumped-element device models to THz regime, we propose the distributed parasitic equivalent circuit model of HEMT shown in Fig. 1. Lumped-element equivalent circuit ignores distributed behavior of gate and drain electrodes, and the capacitive/inductive coupling between them in THz range. Hence, gate, drain, and source electrodes need to be modeled as a coupled three-line structure [3].

978-1-4799-8887-7/15/$31.00 ©2015 IEEE

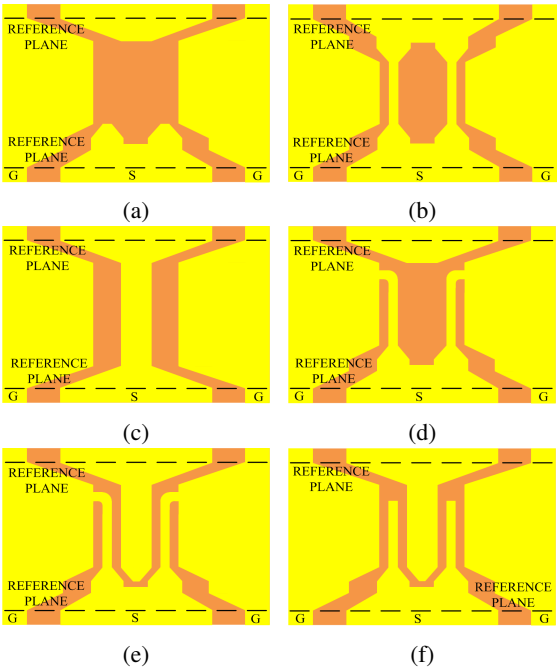

Fig. 2: Layouts of the on-wafer test structures designed for HEMT distributed-element extrinsic equivalent circuit extraction. (a) PADS. (b) THRU1. (c) THRU2. (d) SHORT1. (e) SHORT2. (f) OPEN.

The parameter extraction algorithm proposed here relies on partitioning the parasitic equivalent circuit of Fig. 1 into six strategically-chosen sub-circuits. Corresponding to each sub-circuit is a modified device layout, as depicted in Fig. 2. In the first step, only the contact pads of the HEMT are kept to quantify the electric field coupling, and the dielectric leakage through the substrate. In the second step, a symmetric double gate configuration is used to inspect the behavior of gate electrode characteristic impedance $Z_{0\mathrm{EG}}$, attenuation constant α_{EG}, and effective dielectric constant $\epsilon_{\mathrm{EFF\text{-}EG}}$. Likewise, Step III is designed to evaluate the distributed parameters of the drain electrode. In the fourth step, a short-circuited device configuration without drain drain electrode is employed to extract the source electrode resistance R_{ES} and inductance L_{ES}. In the fifth step, the drain electrode is introduced to observe the effect of gate-to-drain mutual inductance L_{MGD} and the consequent inductive feedback. In the sixth and final step, overall topography of HEMT is simulated without any modification to identify the fringing inter-electrode capacitance-conductance pairs of (C_{EGD}, G_{EGD}), (C_{EGSD}, G_{EGSD}), and (C_{EDSD}, G_{EDSD}).

III. Verification of Distributed Circuit Model

To demonstrate the accuracy of the proposed algorithm, representative device structures and the respective test patterns are first are simulated using a commercial full-wave FEM solver (HFSS v15 [4]). In addition, the suggested test structures are fabricated by depositing single-layer metal on a semi-insulating GaAs substrate. The S-parameter measurements are taken using a non-contact probe setup [5] over the mmW and sub-mmW frequency range of 90-500 GHz.

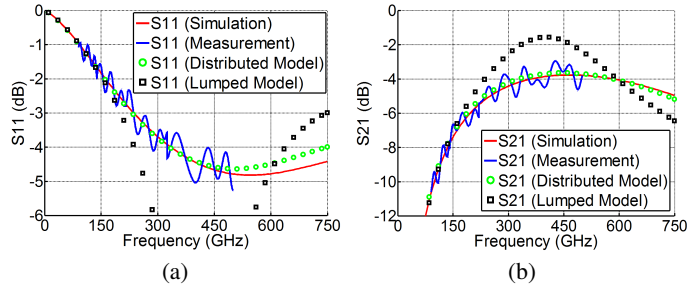

Fig. 3: Comparison of predicted, measured, and modeled S-parameters for open test pattern. (a) Reflection coefficient S_{11}^{OPEN}. (b) Transmission coefficient S_{21}^{OPEN}.

Plotted in Figs. 3(a) and 3(b) are the comparison of simulated, measured, and modeled S-parameters for open test pattern in Step VI of parasitic extraction. The S-parameters acquired from full-wave EM simulation show close agreement with the measured data over a very wide frequency bandwidth. More importantly, the computed S-parameters based on the proposed distributed equivalent circuit in Fig. 1 can accurately reconstruct the frequency response of EM field couplings over the mmW and sub-mmW bands. However, the traditional lumped-element model [6] fails to capture attenuation and propagation delay across device terminals in sub-mmW region.

IV. Conclusion

We developed a new distributed-element parasitic equivalent circuit model for sub-micron gate-length HEMTs that can accurately reproduce the frequency response of EM field couplings in the THz band. To do so, we employed a novel multi-step distributed parasitic model extraction algorithm. The accuracy of the suggested extraction methodology was demonstrated through comparisons between simulated, measured, and modeled frequency responses of the proposed test fixtures up to 750 GHz. The proposed distributed model and the previously studied lumped model have been extracted concurrently to clearly demonstrate the shortcomings of lumped-element HEMT equivalnet circuits at sub-mmW frequencies.

References

[1] K. Shinohara, Y. Yamashita, A. Endoh, I. Watanabe, K. Hikosaka, T. Matsui, T. Mimura, and S. Hiyamizu, "547-GHz fT In0.7Ga0.3As-In0.52Al0.48As HEMTs with Reduced Source and Drain Resistance," *Electron Device Letters, IEEE*, vol. 25, no. 5, pp. 241–243, May 2004.

[2] S. Lee, P. Roblin, and O. Lopez, "Modeling of Distributed Parasitics in Power FETs," *Electron Devices, IEEE Transactions on*, vol. 49, no. 10, pp. 1799–1806, Oct 2002.

[3] V. Tripathi, "On the Analysis of Symmetrical Three-Line Microstrip Circuits," *Microwave Theory and Techniques, IEEE Transactions on*, vol. 25, no. 9, pp. 726–729, Sep 1977.

[4] High Frequency Structure Simulation (HFSS), Ansoft Corporation, Pittsburgh, PA,, 2007.

[5] C. Caglayan, G. Trichopoulos, and K. Sertel, "Non-Contact Probes for On-Wafer Characterization of Sub-Millimeter-Wave Devices and Integrated Circuits," *Microwave Theory and Techniques, IEEE Transactions on*, vol. 62, no. 11, pp. 2791–2801, Nov 2014.

[6] A. Alt, D. Marti, and C. Bolognesi, "Transistor modeling: Robust small-signal equivalent circuit extraction in various hemt technologies," *Microwave Magazine, IEEE*, vol. 14, no. 4, pp. 83–101, 2013.

AN AUTOMATIZED TIME-DOMAIN SET-UP FOR ON-WAFER CHARATERIZATION, DOHERTY ORIENTED, OF HIGH POWER GaN HEMTS

L. Ayari[1], M. Ayad[2], E. Byk[2], M. Camiade[2], G. Neveux[1] and D. Barataud[1]

[1]XLIM CNRS UMR 7252, University of Limoges, 123, Avenue Albert Thomas, 87060 Limoges, France

[2]United Monolithic Semiconductors SAS, 10, Avenue du Québec, 91140 Villebon-sur-Yvette, France

Lotfi.ayari@xlim.fr

Abstract — This paper presents an automatized on-wafer time-domain active load-pull set-up specifically developed for the characterization of High Power GaN High-Electron Mobility Transistors (HEMTs). This set-up is associated to a specific methodology for the design of Doherty Power Amplifier (DPA). This methodology has been applied to a GaN technology transistor: from the on-wafer measured Time-Domain Waveforms (TDW) acquisition, all data required for the design of a Doherty power amplifier are directly extracted. Designers have the direct knowledge of the optimal characteristics of high power transistors along the output back-off (OBO) at fundamental frequency and also the maximum obtainable operating bandwidth of the final desired Doherty PA.

Index Terms — Time-Domain microwave measurements, GaN HEMTs, Doherty, High Efficiency, MMIC power amplifiers.

I. INTRODUCTION

GaN HEMTs are now mature for the design of High Power Added Efficiency (PAE) microwave DPA over large back-off ranges. In order to design MMIC amplifiers, specific on-wafer microwave time-domain characterization is required. From input and output time-domain voltages and currents, the main parameters required for the design of DPA are automatically extracted for optimum PAE versus OBO. To reach the optimal characteristics of these high power transistors along the OBO, active load-pull capabilities are required to synthesize the optimal impedance loads path at fundamental frequency (f_0).

The next section presents a brief reminder of the basic principles of operation of a Doherty amplifier. The third section describes the automatized on-wafer time-domain active load-pull set-up specifically developed for the characterization of High Power GaN HEMTs. The last section summarizes the methodology to determine, from on-wafer time-domain measurements, all the required characteristics to directly design a DPA.

II. PRINCIPLE OF OPERATION OF DOHERTY POWER AMPLIFIERS

The theory about the Doherty power amplifier is well documented today [1], [2], [3], [4]. Fig. 1 shows a simplified block diagram of a two-stage Doherty and its associated usual PAE characteristic versus output power leading to the definition of the OBO region.

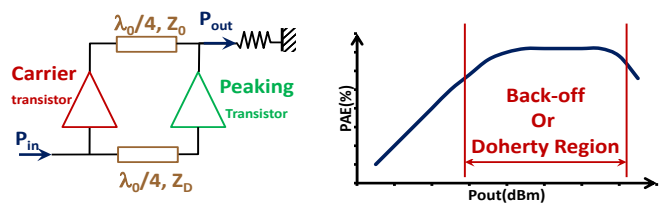

Fig. 1. Block diagram of a DPA and associated typical PAE characteristic versus Output Power defining OBO region.

(1) is the expression of the PAE performance of the DPA (PAE_{DPA}). It can be written as a function of PAE and dissipated power (P_{diss}) of each transistor (Carrier (PAE_c, P_{diss_c}) and peaking (PAE_p, P_{diss_p})).

$$PAE_{DPA} = \frac{P_{diss\_c} \times PAE_c + P_{diss\_p} \times PAE_p}{P_{diss\_c} + P_{diss\_p}} \quad (1)$$

(1) clearly shows that in a DPA, at low level, when the peaking transistor is OFF, $P_{diss\_p} = 0$ and $PAE_{DPA} = PAE_c$. In the other hand, at high level, the two transistors are involved in the PAE performance of the DPA and may provide a high PAE. It is then of prime importance to individually characterize the PAE performance versus output power for different load resistances (R_{load}) as shown in Fig. 2.

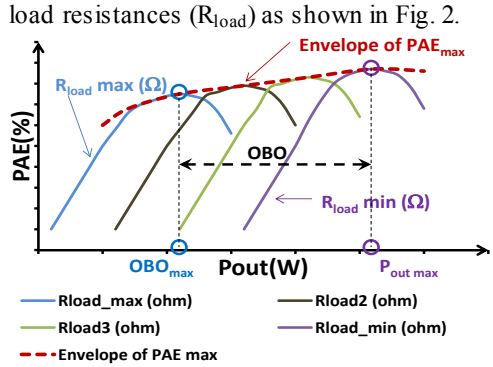

Fig. 2. PAE characteristic versus Output Power, with R_{load} as parameter.

978-1-4799-8887-7/15/$31.00 ©2015 IEEE

Conventional non-linear equivalent electrical drain port model (Fig. 3a) of the HEMT transistor, at f_0 becomes the one represented in Fig. 3b along the envelope of OBO at PAE_{max} defining the Doherty region (OBO) described in Fig. 1.

In Fig. 3b, $V_{out\ max}$ is the amplitude of the output voltage of the peak transistor at f_0 along the envelope of PAE_{max}. This amplitude remains constant for the entire operating Doherty region and is then independent of the OBO point. C_{out} is the equivalent output capacitance of the transistor.

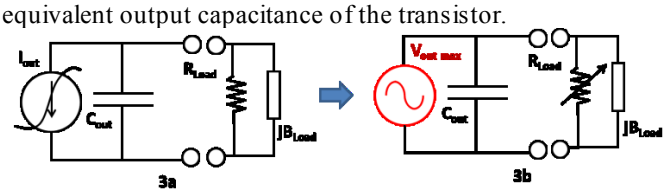

Fig. 3. Conventional equivalent electrical models of HEMT drain port (Fig. 3a) and along the envelope of PAE max (Fig. 3b).

The value of C_{out} is constant along the Doherty region ([0-10] dB OBO range), over a large frequency bandwidth [3–12 GHz]. Therefore, the value of C_{out} is independent of the operating class of the transistor. R_{load} is the optimal load impedance to reach an optimal operation mode of the transistor in the Doherty architecture. Its value varies from R_{load_min} (@$P_{out\ max}$) to R_{load_max} (@OBO max). R_{load_min} and R_{load_max} are fully dependent on the operating class and the OBO. The output time constant $\tau_{out} = C_{out} \times R_{load}$ along the envelope of OBO at PAE_{max} characterizes a given technology and a given operating class of the transistor regardless its gate development. So, the limitation of frequency bandwidth is given by τ_{out_max} at OBO_{max}. Note also that the design should take into account the ratio between R_{load} and 50Ω.

The on-wafer time-domain load-pull measurement set-up specifically developed allows the automatic extraction of all the aforementioned defined characteristics for transistor in the 1GHz to 7GHz fundamental frequency range.

III. MEASUREMENT SYSTEM DESCRIPTION

A. On-wafer time-domain measurement system

A fully calibrated 4-channel time-domain measurement set-up has been developed for the measurement of TDW at both ports of **on-wafer** Device Under Test (DUT) driven by large Continuous Wave (CW) radiofrequency (RF) signal. Fig. 4 presents a block diagram of this measurement set-up built with a Track and Hold Amplifier (THA) based receiver [5] associated with 4 high dynamic range ADCs (12 bits).

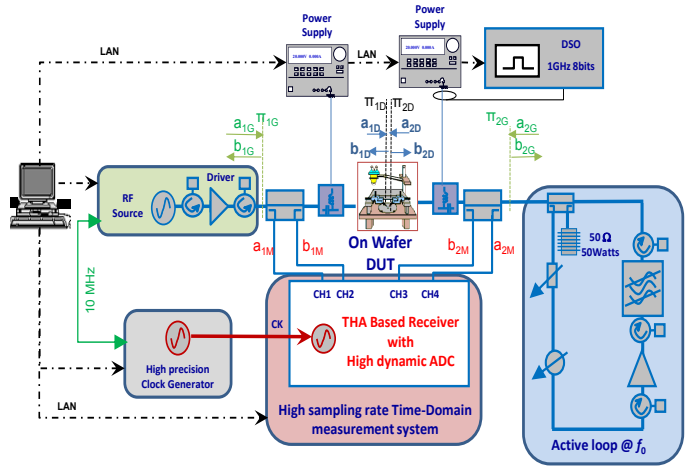

Fig. 4. Block diagram of the on-wafer time-domain measurement set-up.

It achieves an equivalent high sampling rate (1.17 TS/s in this work) thanks to Coherent Time Interleaved Sampling (CTIS) technique [6] in order to accurately characterize DUT driven by repetitive modulated or CW RF large signal. This excitation signal is linearly amplified. 20 dB wideband couplers enable to simultaneously capture the raw voltage waves. The raw acquired data are then processed thanks to the calibration coefficients to obtain corrected incident and reflected voltage waves at both ports of the on-wafer DUT.

It should be noted that R_{load} can reach high values. Thus, the measurement set-up contains an active loop [7] working at f_0 to synthesize high load reflection coefficient close to 1.

B. On-Wafer Time-Domain Calibration procedure

The first step of the on-wafer calibration procedure consists in a Short Open Load Thru relative error correction in order to compute the error coefficients ($\beta_1^i, \delta_1^i, \gamma_1^i, \alpha_2^i, \beta_2^i, \delta_2^i, \gamma_2^i$) of (2) for all the spectral frequencies (index i=1, … N) of interest.

$$\begin{bmatrix} a_{1D}^i \\ b_{1D}^i \\ a_{2D}^i \\ b_{2D}^i \end{bmatrix} = K^i \begin{bmatrix} 1 & \beta_1^i & 0 & 0 \\ \gamma_1^i & \delta_1^i & 0 & 0 \\ 0 & 0 & \alpha_2^i & \beta_2^i \\ 0 & 0 & \gamma_2^i & \delta_2^i \end{bmatrix} \begin{bmatrix} a_{1M}^i \\ b_{1M}^i \\ a_{2M}^i \\ b_{2M}^i \end{bmatrix} \quad (2)$$

For the absolute calibration allowing the determination of the K^i complex coefficient, a through connection is made between the two ports as shown in Fig. 5. Because no on-wafer magnitude and phase reference standards are available, the principle of reciprocity [8], defined by (3) is applied.

$$\begin{bmatrix} a_{1G}^i \\ b_{1G}^i \end{bmatrix} = L^i \begin{bmatrix} 1 & \lambda_1^i \\ \mu_1^N & \nu_1^i \end{bmatrix} \left(K^i \begin{bmatrix} 1 & \beta_1^i \\ \gamma_1^i & \delta_1^i \end{bmatrix} \right)^{-1} \begin{bmatrix} a_{1D}^i \\ b_{1D}^i \end{bmatrix} \quad (3)$$

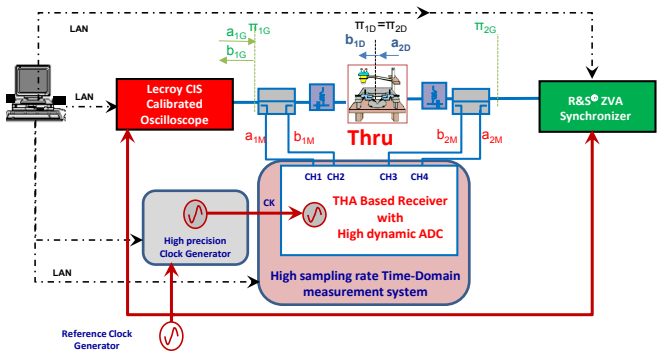

Fig. 5. Measurement setup configuration for Absolute Calibration.

A classical Short Open Load calibration is performed at the π_{1G} plane with the probes connected to a Thru line and the generator of Fig. 4 connected to π_{2G} plane. It results in the determination of the coefficients (λ_1^i, μ_1^i, ν_1^i). Then, using the configuration of Fig. 5, the synchronizer of a ZVA Vector Network Analyzer is utilized as a harmonic phase generator. This signal is measured with a calibrated oscilloscope based on the CTIS principle [6]. The measured signal becomes the phase and amplitude references for absolute calibration and allows the determination of L^i and then K^i phasors.

IV. Extraction of Transistor Characteristics for DPA from Measurements Results

The proposed Doherty oriented characterization methodology is applied to an 8x125µm unit-cell transistor of a 0.25µm AlGaN/GaN technology. f_0 is equal to 3.9 GHz. The load impedances are tuned to optimize the output voltage/current waveforms of the transistor to reach the optimal PAE performances for different output powers corresponding to a 0dB to 6dB OBO range.

Fig. 6 presents the measured PAE characteristic versus output power, for optimal load impedances when the transistor is working in deep class AB operating mode (V_{gsq}=-3.48V - V_{dsq}=30V - I_{dq}=12mA):

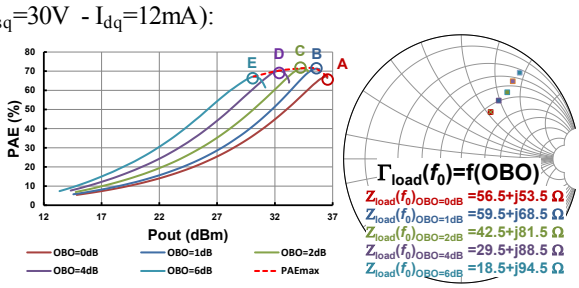

Fig. 6. Measured PAE characteristics versus output power for optimal load impedances with OBO as parameter.

Fig. 7 presents the measured associated TDW at both port of the GaN HEMT for each previous power characteristics of Fig. 6 at all maximum PAE values (A, B, C, D, E points):

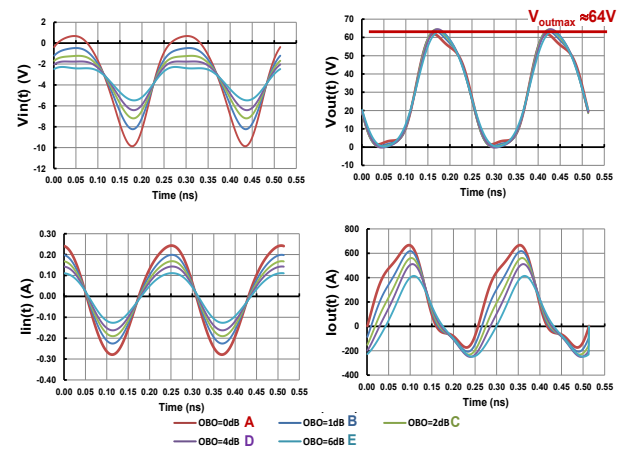

Fig. 7. Measured time-domain waveforms at both port of the GaN HEMT at A, B, C, D, E points of Fig. 6.

It can be clearly observed that, in accordance with the theory, $V_{out\ max}$ remains constant for the entire operating Doherty region. Table 1 summarizes, for the GH25 GaN HEMT transistor working in deep class AB and C, the values of the measured optimal R_{load} and C_{out} represented in the equivalent model of Fig. 3.

TABLE I

Extracted R_{load} and C_{out} of Fig.3 for 2 classes

OBO (dB)	Deep Class AB		Class C	
	R_{load} (Ω)	C_{out} (pF)	R_{load} (Ω)	C_{out} (pF)
0	107	0.39	99	0.43
1	144	0.39	147	0.42
2	199	0.39	202	0.42
4	295	0.42	289	0.42
6	501	0.42	510	0.42

From these TDW, all the required data for the design of a DPA, including the possible maximum operating bandwidth, can be deduced as show in Table 2. Applying Bode and Fano theory [9], the maximum reachable bandwidth is limited by the highest time constant τ_{out_max} that characterizes the technology for a given OBO. For instance, if the designer wants to work with an optimized equal ripple Chebyshev matching circuit leading to a maximum $\Delta\Gamma_{Load} = 0.2$ around Γ_{Load_opt} in order to reach a PAE higher than 90% of PAE_{max} for the maximum OBO, the maximum theoretically attainable actual bandwidth, depending on a finite number (n) of lossless matching elements, will vary from 0.9GHz (n=2) to 1.5GHz (n=∞) for the GaN HEMT technology measured in this work.

TABLE II

EXAMPLE OF CALCULATED DPA CHARACTERISTICS

f_0=3.9GHz	**Class B**	**Class C**
Amplitude $V_{out\ max}$@PAEmax	64 V	63 V
$R_{load\ min}$ @ OBO = 0dB	107 Ω	99 Ω
$R_{load\ max}$ @ OBO = 6dB	501 Ω	510 Ω
C_{out}	0.4 pF	0.4 pF
$\tau_{out\ max}$ @ OBO = 6dB	208.5 ps	204 ps
Operating bandwidth (Chebyshev matching circuit with n=2)	≈0.9 GHz	≈0.9 GHz
PAE_{min} @ OBO 6dB (90% PAE_{max})	60%	71%

V. CONCLUSION

This paper described the fully calibrated, automatized, Doherty oriented, on-wafer time-domain active load-pull set-up specifically developed for the characterization of High Power Gan HEMTs. From the on-wafer measured TDW acquisition along the OBO at f_0, it has been shown that all data required for the design of a DPA using 25µm GaN technology are directly extracted. This set-up is then a helpful tool for designers to easily determine the maximum obtainable operating bandwidth of the final desired Doherty PA.

ACKNOWLEDGEMENT

Professor Juan Obregon from Xlim Laboratory is gratefully acknowledged for helpful discussions.

REFERENCES

[1] W. H. Doherty, "A new high efficiency power amplifier for modulated waves," *Proceedings of the Institute of Radio Engineers.,* vol. 24, no. 9, pp. 1163-1182, 1936.

[2] F. H. raab, "Efficiency of Doherty RF Power Amplifier systems," *IEEE Transactions on broadcasting*, vol. BC-333, no. 3, pp. 77-83, September 1987.

[3] P. Colantonio, F. Giannini, and E. Limiti, "High Efficiency RF and Microwave Solid State Power Amplifiers," *ser. Microwave and Optical Engineering*, New York: Wiley, 2009.

[4] D. Gustafsson, J. C. Cahuana, D. Kuylenstierna, I. Angelov, N.Rorsman, and C. Fager, "A wideband and compact GaN MMIC Doherty amplifier for microwave link applications," *IEEE Trans.Microw. Theory Techn.*, vol. 61, no. 2, pp. 922–930, Feb. 2013.

[5] S. Ahmed and al. "Time-domain interleaved high sampling rate system for large signal characterization of non-linear devices," *79th ARFTG Microwave Measurement Conference,* 2012, pp. 1-4.

[6] Lecroy corp. "Coherent Interleaving Sampling," patent: WO/2006/086257, August 2006.

[7] V. Teppati, A. ferrero, U. Pisani, "Recent Advances in Real-Time Load-Pull Systems," *IEEE Transactions on Instrumentation and Measurement*, vol. 57, no 11, pp. 2640–2646, 2008.

[8] A. Ferrero and U. Pisani, "An improved calibration technique for on-wafer large signal transistor characterization," *IEEE Transactions on Instrumentation and Measurement*, vol. 42, pp. 360–364, Apr. 1994.

[9] Fano R. M. (Jan. and Feb. 1950) "Theoretical Limitations on the Broadband Matching of Arbitrary Impedances", *J. Franklin Inst.*, vol. 249, pp. 57-83 and 139 -155.

Physical Models for 2.4 mm and 3.5 mm Coaxial VNA Calibration Kits Developed within the NIST Microwave Uncertainty Framework

Jeffrey A. Jargon[1], Chihyun Cho[2], Dylan F. Williams[1], and Paul D. Hale[1]

[1]National Institute of Standards and Technology, 325 Broadway, M/S 815.01, Boulder, CO 80305 USA
[2]Center for Electromagnetic Wave, Korean Research Institute of Standards and Science, Daejeon, Korea
Email: jeffrey.jargon@nist.gov, Tel: +1.303.497.4961

***Abstract* — We developed physical models of commercially-available 2.4 mm and 3.5 mm coaxial calibration kits for vector network analyzers. These models support multiline thru-reflect-line (TRL) and open-short-load-thru (OSLT) calibrations, and include error mechanisms in each of the standards' constituent parameters that can be utilized in the NIST Microwave Uncertainty Framework to propagate uncertainties. For both connector sizes, we calibrated a network analyzer using the two calibration methods, and compared measurements and uncertainties made on a number of verification devices. In both cases, we showed that the two calibrations agree to within their respective uncertainties.**

***Index Terms* — calibration, coaxial, physical models, uncertainty, vector network analyzer, verification.**

I. Introduction

The multiline, thru-reflect-line (TRL) calibration [1] is perhaps the most fundamental and accurate vector network analyzer (VNA) calibration for coaxial circuits. Multiline TRL calibrations measure the propagation constant of the line standards so that the characteristic impedance can be transformed to a selected reference impedance, and offer high bandwidth and accuracy through the use of multiple transmission line standards. However, a set of coaxial lines, some relatively long, is required to obtain a wide-band measurement. Coaxial airlines also require considerable care to ensure good connections without damaging the standards. Furthermore, a set of lines can be costly, and measurements are time-consuming.

Other types of VNA calibrations make use of compact, lumped-element standards; the most common being open-short-load-thru (OSLT) and line-reflect-match (LRM) methods [2]. They provide calibration procedures that are easier to perform, oftentimes at the cost of lower accuracy.

In this paper, we utilize the NIST Microwave Uncertainty Framework [3-6] to develop physical models of commercially available 2.4 mm and 3.5 mm multiline TRL and OSLT coaxial calibrations kits. The NIST Microwave Uncertainty Framework utilizes parallel sensitivity and Monte-Carlo analyses, and enables us to capture and propagate the significant S-parameter measurement uncertainties and statistical correlations between them [7]. By identifying and modeling the physical error mechanisms in the calibration standards, we can determine the statistical correlations between both the scattering parameters at a single frequency and uncertainties at different frequencies. These uncertainties can then be propagated to the measurements of the devices under test. In the following sections, we describe our methodology in further detail, and compare measurements and uncertainties made on a number of verification devices.

I. 3.5 mm Coaxial Calibrations

For the 3.5 mm coaxial devices, we began by modeling the multiline TRL calibration standards (a thru connection, an offset short, and six airlines of varying lengths) for purposes of determining uncertainties. Table I lists the line lengths and associated uncertainties for the multiline TRL standards, and Table II lists the other sources of uncertainty for the standards. Our values and distributions of the uncertainties come from a variety of sources, including manufacturers' specifications and an IEEE standard [8].

The NIST Microwave Uncertainty Framework was employed to construct models for the calibration standards. The airline and offset-short standards were modeled with closed-form expressions for coaxial lines of finite metal conductivity [9]. The framework was also used for automatically propagating the uncertainties to the calibrated verification devices in conjunction with the calibration engine, StatistiCAL™ [10, 11], which utilizes a "mix-and-match" philosophy to VNA calibrations.

Next, the OSLT standards were modeled with the values and uncertainties listed in Tables II and III. We compared our physical models of the open and short to the polynomial models specified by the manufacturer [12], as shown in Figures 1-4. Figures 1 and 3 plot the magnitudes of the reflection coefficients as a function of frequency, while Figures 2 and 4 plot the differences in phase with respect to those of the physical models. Additionally, we compared our physical models to measurements of the standards using the multiline TRL calibration, the results of which are also displayed in Figures 1-4. We see that our physical models closely match the polynomial models, and the uncertainty bounds of our physical models, depicted by the dotted curves, span the majority of the measured values. We modeled the load standard as a simple 50 Ohm resistor after observing that the magnitudes of the measured reflection coefficients for both the male and female connectors were less than -40 dB at most frequencies, as displayed in Figure 5.

Table I. Lengths and uncertainties of the 3.5 mm TRL standards.

Line Designation	Length (mm) ± Uncertainty (Distribution)
Thru	0.000 ± 0.009 (Rectangular)
AL3527	16.154 ± 0.009 (Rectangular)
AL3530	37.504 ± 0.009 (Rectangular)
MMC225	22.500 ± 0.009 (Rectangular)
MMC244	24.400 ± 0.009 (Rectangular)
MMC250	25.000 ± 0.009 (Rectangular)
MMC300	30.000 ± 0.009 (Rectangular)
Offset Shorts	9.520 ± 0.009 (Rectangular)

Table II. Physical error mechanisms of the 3.5 mm standards.

Mechanism (units)	Value ± Uncertainty (Distribution)
Inner Cond. Diameter (mm)	1.5199 ± 0.002 (Rectangular)
Outer Cond. Diameter (mm)	3.5 ± 0.002 (Rectangular)
Pin Diameter (mm)	0.927 ± 0.008 (Rectangular)
Pin Depth (mm)	0.0153 ± 0.0153 (Rectangular)
Metal Conductivity (S/m)	$7.9\times10^6 \pm 4\times10^6$ (Rectangular)
Relative Dielectric Constant	1 ± 0
Dielectric Loss Tangent	0 ± 0

Table III. Physical error mechanisms of the 3.5 mm OSLT standards.

Mechanism (units)	Value ± Uncertainty (Distribution)
Open Offset Length (mm)	9.51 ± 0.05 (Rectangular)
Open Metal Conductivity (S/m)	$5\times10^6 \pm 4\times10^6$ (Rectangular)
Open Conductance (1/Ω)	0 ± 0
Open Capacitance (pF)	0 ± 0
Short Offset Length (mm)	9.52 ± 0.05 (Rectangular)
Short Metal Conductivity (S/m)	$6\times10^6 \pm 5\times10^6$ (Rectangular)
Short Resistance (Ω)	0 ± 0
Short Inductance (nH)	0 ± 0
Load Resistance (Ω)	50.0 ± 0.1
Load Inductance (nH)	0 ± 0

Once the multiline TRL and OSLT calibration standards were defined, we used both sets of standards to calibrate the measurements of verification devices for comparison purposes. Figures 6-9 show calibrated S-parameters and corresponding 95 % confidence bounds calculated from the sensitivity analysis performed in the NIST Uncertainty Framework for a 20 dB attenuator, a 40 dB attenuator, and a Beatty line. Additionally, the figures show results obtained with MultiCal™ [13], the original implementation of multiline TRL that does not provide uncertainty bounds. Dotted curves in the figures correspond to confidence bounds determined in the Uncertainty Framework.

In each of the figures, the measurements calibrated with both implementations of multiline TRL agree very well, while the OSLT-calibrated measurements and associated uncertainties are visibly noisier. For the 20 dB and 40 dB attenuators, the mean confidence intervals for $|S_{21}|$ are approximately ± 0.025 dB for multiline TRL and ± 0.022 dB for OSLT. For the Beatty line, the mean confidence intervals for $|S_{21}|$ are approximately ± 0.027 dB for multiline TRL and ± 0.097 dB for OSLT, while the mean upper confidence intervals for $|S_{11}|$ are +0.117 dB for multiline TRL and +0.547 dB for OSLT.

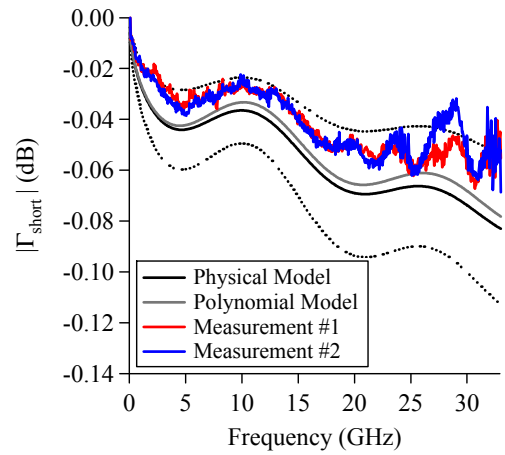

Fig. 1. Comparing the physical and polynomial models to the two TRL-calibrated measurements of the magnitudes of the 3.5 mm short standard's reflection coefficients.

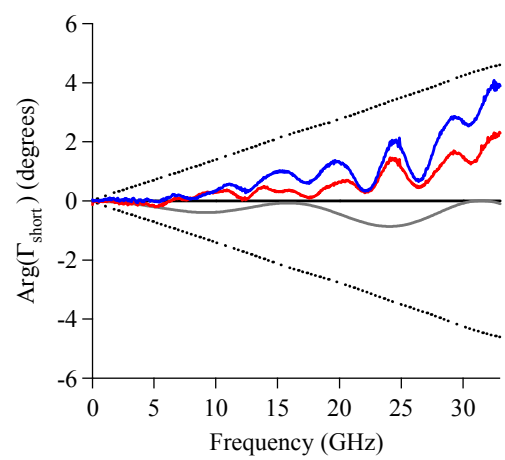

Fig. 2. Comparing the physical and polynomial models to the two TRL-calibrated measurements of the phases of the 3.5 mm short standard's reflection coefficients.

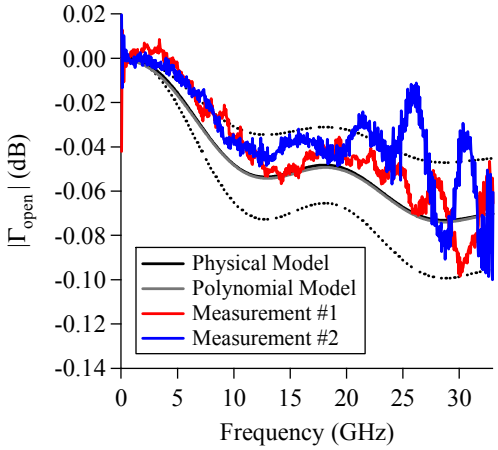

Fig. 3. Comparing the physical and polynomial models to the two TRL-calibrated measurements of the magnitudes of the 3.5 mm open standard's reflection coefficients.

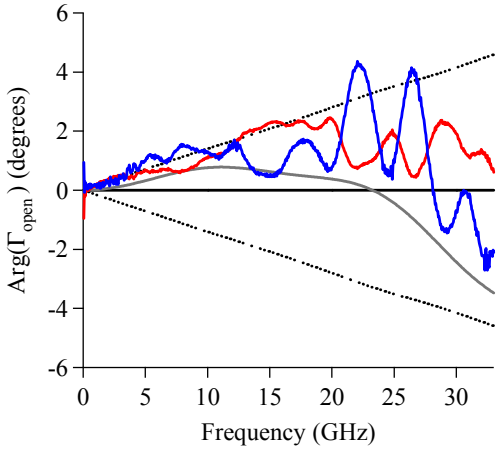

Fig. 4. Comparing the physical and polynomial models to the two TRL-calibrated measurements of the phases of the 3.5 mm open standard's reflection coefficients.

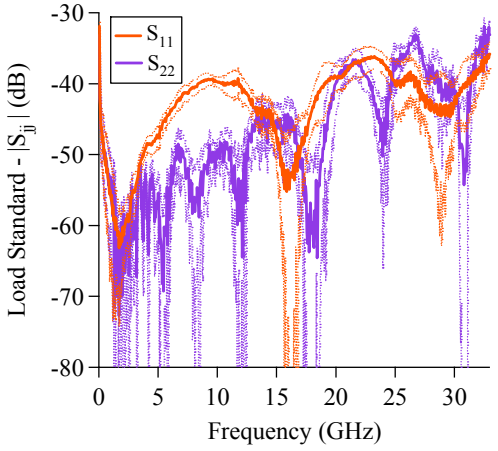

Fig. 5. Calibrated measurements of the magnitudes of the 3.5 mm load standard's reflection coefficients.

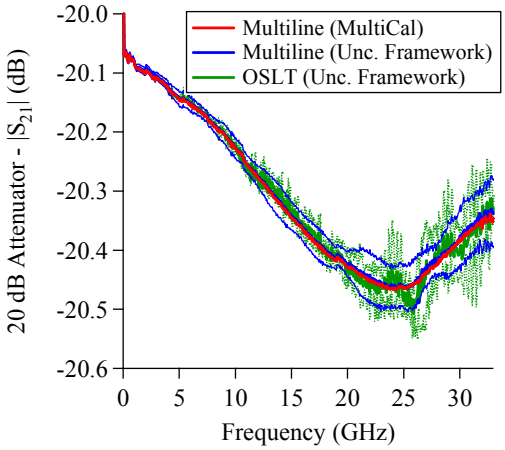

Fig. 6. Comparing measurements and 95% confidence intervals of the 20-dB attenuator's transmission coefficients with 3.5 mm multiline TRL and OSLT calibrations.

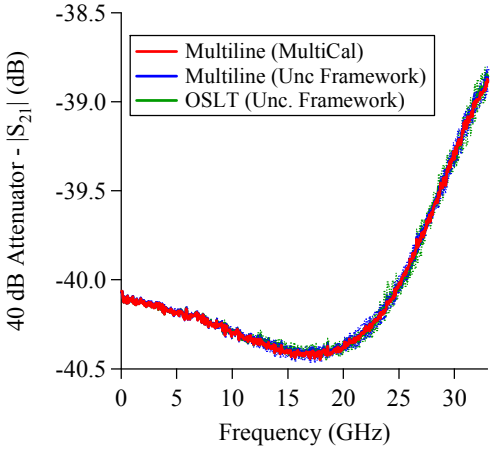

Fig. 7. Comparing measurements and 95% confidence intervals of the 40-dB attenuator's transmission coefficients with 3.5 mm multiline TRL and OSLT calibrations.

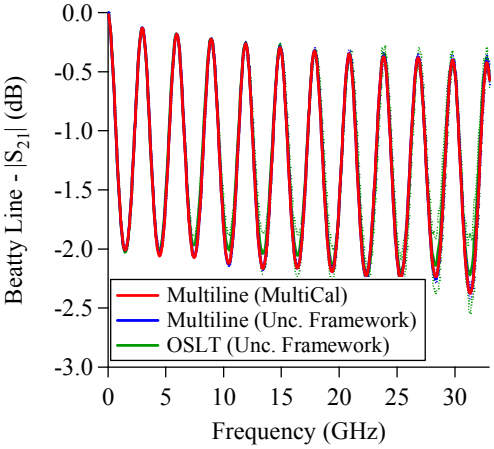

Fig. 8. Comparing measurements and 95% confidence intervals of the Beatty line's transmission coefficients with 3.5 mm multiline TRL and OSLT calibrations.

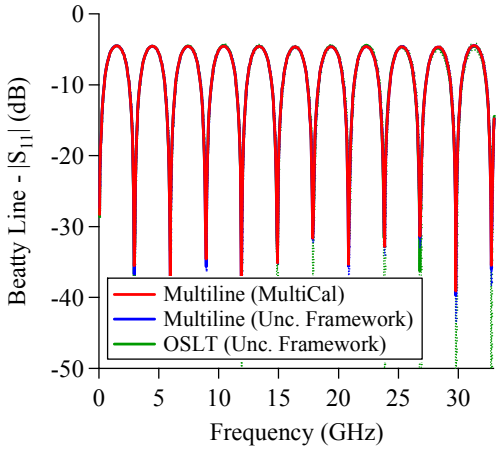

Fig. 9. Comparing measurements and 95% confidence intervals of the Beatty line's reflection coefficients with 3.5 mm multiline TRL and OSLT calibrations.

III. 2.4 MM COAXIAL CALIBRATIONS

For the 2.4 mm coaxial devices, we employed a similar strategy. Once again, we began by modeling the multiline TRL calibration standards, which consisted of a thru connection, an offset short, and three airlines of varying lengths. Table IV lists the line lengths and associated uncertainties for the multiline TRL standards, and Table V lists the other sources of uncertainty for the standards.

The NIST Microwave Uncertainty Framework was again employed to construct models for the calibration standards and propagate the uncertainties to the calibrated verification devices.

Next, the OSLT standards were modeled with the values and uncertainties listed in Tables V and VI. We compared our physical models of the offset open and short to the polynomial models specified by the manufacturer [12], as shown in Figures 10-13. Figures 10 and 12 plot the magnitudes of the reflection coefficients as a function of frequency, while Figures 11 and 13 plot the differences in phase with respect to those of the physical models. Additionally, we compared our physical models to measurements of the standards using the multiline TRL calibration, the results of which are also displayed in Figures 10-13. And similar to the 3.5 mm coaxial case, our physical models closely match the polynomial models, and the uncertainty bounds of our models, depicted by the dotted curves, span the majority of the measured values. This time, however, rather than modeling the load standard as a simple 50 Ohm resistor, we defined our load using the measured reflection coefficients from the multiline TRL calibration since the load was only specified to be 50 Ohms at frequencies less than 4 GHz. Figure 14 plots the magnitudes of the reflection coefficients. The values are clearly greater than -40 dB at most frequencies. Furthermore, we found it difficult to develop a simple physical model that accurately matched the measured results.

Table IV. Lengths and uncertainties of the 2.4 mm TRL standards.

Line Designation	**Length (mm) ± Uncertainty (Distribution)**
Thru	0.000 ± 0.005 (Rectangular)
AL15	14.996 ± 0.005 (Rectangular)
AL17	17.496 ± 0.005 (Rectangular)
AL30	29.992 ± 0.005 (Rectangular)
Offset Shorts	0.000 ± 0.005 (Rectangular)

Table V. Physical error mechanisms of the 2.4 mm standards.

Mechanism (units)	**Value ± Uncertainty (Distribution)**
Inner Cond. Diameter (mm)	1.0423 ± 0.004 (Rectangular)
Outer Cond. Diameter (mm)	2.4 ± 0.005 (Rectangular)
Pin Diameter (mm)	0.511 ± 0.005 (Rectangular)
Pin Depth (mm)	0.0065 ± 0.0065 (Rectangular)
Metal Conductivity (S/m)	$6\times10^6 \pm 5\times10^6$ (Rectangular)
Relative Dielectric Constant	1 ± 0
Dielectric Loss Tangent	0 ± 0

Table VI. Physical error mechanisms of the 2.4 mm OSLT standards.

Mechanism (units)	**Value ± Uncertainty (Distribution)**
Open Offset Length (mm)	6.75 ± 0.02 (Rectangular)
Open Metal Conductivity (S/m)	$5\times10^6 \pm 4\times10^6$ (Rectangular)
Open Conductance (1/Ω)	0 ± 0
Open Capacitance (pF)	0 ± 0
Short Offset Length (mm)	6.75 ± 0.02 (Rectangular)
Short Metal Conductivity (S/m)	$6\times10^6 \pm 5\times10^6$ (Rectangular)
Short Resistance (Ω)	0 ± 0
Short Inductance (nH)	0 ± 0

Once the multiline TRL and OSLT calibration standards were defined, we used both calibrations to measure a set of verification devices for comparison purposes. Figures 15-19 show calibrated S-parameters and corresponding 95 % confidence bounds calculated in the NIST Uncertainty Framework for an offset short, a load, and an airline. Additionally, the figures show results using MultiCal™.

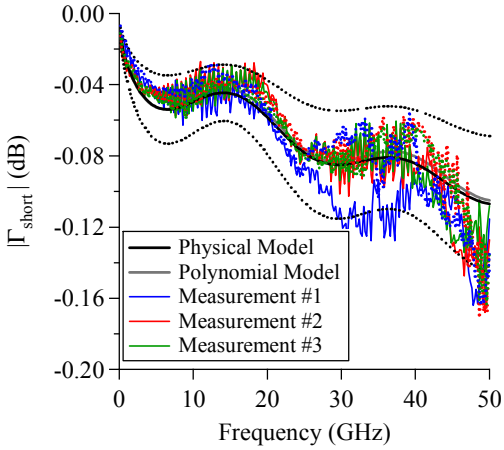

Fig. 10. Comparing the physical and polynomial models to the three TRL-calibrated measurements of the magnitudes of the 2.4 mm short standard's reflection coefficients.

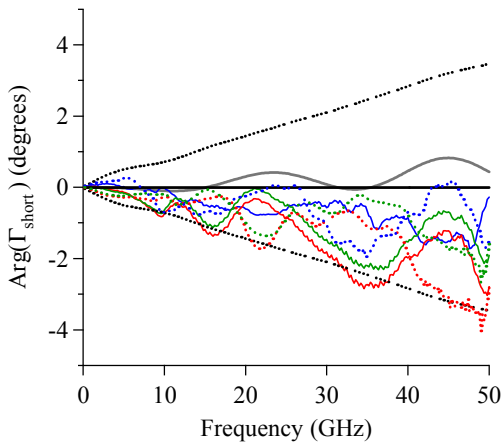

Fig. 11. Comparing the physical and polynomial models to the three TRL-calibrated measurements of the phases of the 2.4 mm short standard's reflection coefficients.

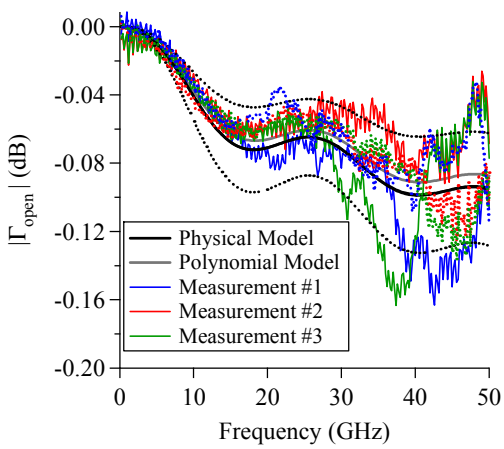

Fig. 12. Comparing the physical and polynomial models to the three TRL-calibrated measurements of the magnitudes of the 2.4 mm open standard's reflection coefficients.

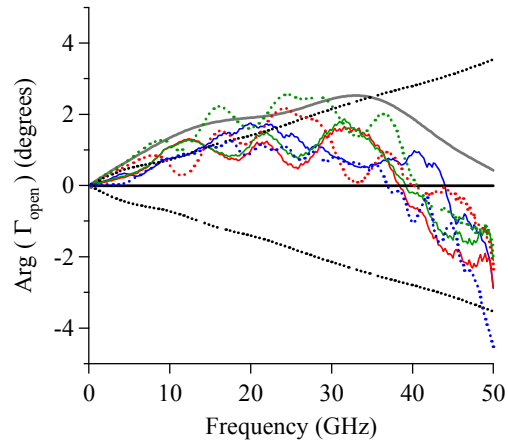

Fig. 13. Comparing the physical and polynomial models to the three TRL-calibrated measurements of the phases of the 2.4 mm open standard's reflection coefficients.

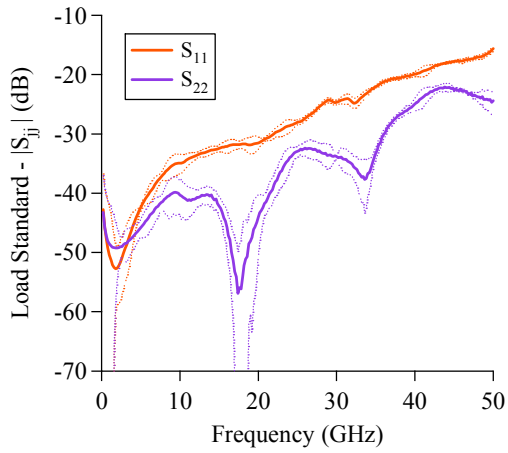

Fig. 14. Calibrated measurements of the magnitudes of the 2.4 mm load standard's reflection coefficients.

In each of the figures, we compared the calibrated measurements using both implementations of multiline TRL and found that they agree very well. For the airline, the mean confidence intervals for $|S_{21}|$ are approximately ± 0.030 dB for multiline TRL and ± 0.015 dB for OSLT, and the mean confidence intervals for $\mathrm{Arg}\{S_{21}\}$ are approximately ± 0.381º for multiline TRL and ± 0.402º for OSLT. For the load, the mean upper confidence intervals for $|S_{11}|$ are +3.51 dB for multiline TRL and +3.82 dB for OSLT. For the offset short, the mean confidence intervals for $|S_{11}|$ are approximately ± 0.050 dB for multiline TRL and ± 0.025 dB for OSLT, and the mean confidence intervals for $\mathrm{Arg}\{S_{11}\}$ are approximately ± 0.521º for multiline TRL and ± 1.790º for OSLT.

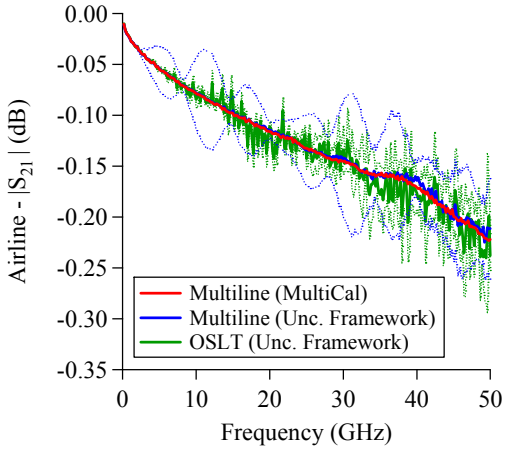

Fig. 15. Comparing measurements and 95% confidence intervals of the magnitudes of the airline's transmission coefficients with 2.4 mm TRL and OSLT calibrations.

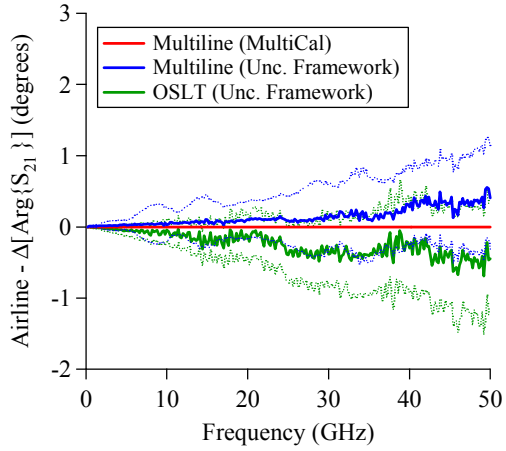

Fig. 16. Comparing measurements and 95% confidence intervals of the phases of the airline's transmission coefficients with 2.4 mm TRL and OSLT calibrations.

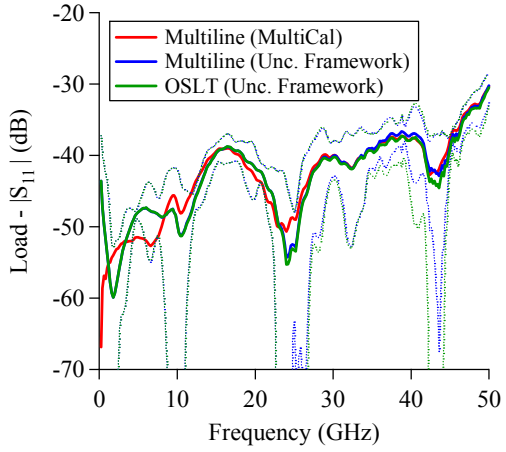

Fig. 17. Comparing measurements and 95% confidence intervals of the load's reflection coefficients with 2.4 mm multiline TRL and OSLT calibrations.

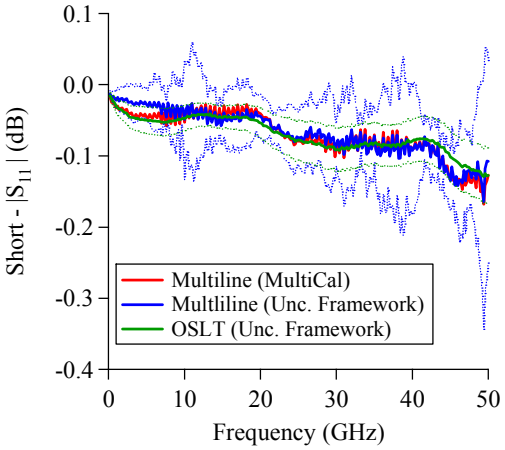

Fig. 18. Comparing measurements and 95% confidence intervals of the magnitudes of the short's reflection coefficients with 2.4 mm TRL and OSLT calibrations.

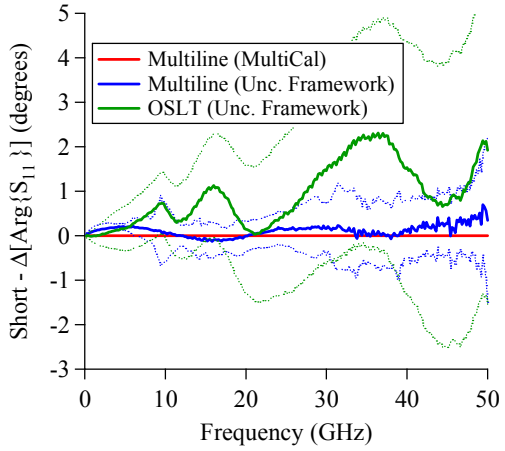

Fig. 19. Comparing measurements and 95% confidence intervals of the phases of the short's reflection coefficients with 2.4 mm TRL and OSLT calibrations.

IV. Conclusions

We have developed physical models of 2.4 mm and 3.5 mm coaxial calibration kits for vector network analyzers that support multiline TRL and OSLT calibrations within the NIST Microwave Uncertainty Framework. In both cases, the verification devices measured with the two calibration approaches agree to within their respective uncertainties. Although other sources of uncertainty may be included in a final uncertainty analysis, we believe these minor additions will not significantly affect the overall uncertainties.

Acknowledgement

This work was supported by the U.S. Department of Commerce, and is not subject to U.S. copyright.

REFERENCES

[1] R. B. Marks, "A multiline method of network analyzer calibration," *IEEE Trans. Microwave Theory Tech*., vol. 39, no. 7, pp. 1205–1215, July 1991.

[2] D. K. Rytting, "Network analyzer error models and calibration methods," *52nd ARFTG Conference*, Short Course on Computer-Aided RF and Microwave Testing and Design, Dec. 1998.

[3] D. F. Williams, NIST Microwave Uncertainty Framework, Beta Version, http://www.nist.gov/ctl/rf-technology/related-software.cfm, 2015.

[4] J. A. Jargon, D. F. Williams, T. M. Wallis, D. X. LeGolvan, and P. D. Hale, "Establishing Traceability of an Electronic Calibration Unit Using the NIST Microwave Uncertainty Framework," *79th ARFTG Microwave Measurement Conference*, Montreal, CANADA, Jun. 2012.

[5] J. A. Jargon, U. Arz, and D. F. Williams, "Characterizing WR-8 Waveguide-to-CPW Probes Using Two Methods Implemented within the NIST Uncertainty Framework," *80th ARFTG Microwave Measurement Conference*, San Diego, CA, Nov. 2012.

[6] J. A. Jargon, D. F. Williams, P. D. Hale, and M. D. Janezic, "Characterizing a Noninsertable Directional Device Using the NIST Uncertainty Framework," *83rd ARFTG Microwave Measurement Conference*, Tampa Bay, FL, Jun. 2014.

[7] A. Lewandowski, D. F. Williams, P. D. Hale, C. M. Wang, and A. Dienstfrey, "Covariance-matrix-based vector-network-analyzer uncertainty analysis for time-and frequency-domain measurements," *IEEE Trans. Microwave Theory Tech*., vol. 58, no. 7, pp. 1877-1886, July 2010.

[8] IEEE Standard 287-2007 - Standard for Precision Coaxial Connectors (DC to 110 GHz).

[9] A. Lewandowski, "Multi-frequency approach to vector-network analyzer scattering-parameter measurements," Ph.D. Thesis, Warsaw University of Technology, 2010.

[10] D. F. Williams, StatistiCAL VNA Calibration Software Package, http://www.nist.gov/ctl/rf-technology/related-software.cfm, 2015.

[11] D.F. Williams, C.M. Wang, and U. Arz, "An optimal vector-network-analyzer calibration algorithm," *IEEE Trans. Microwave Theory and Tech*., vol. 51, no. 12, pp. 2391-2401, Dec. 2003.

[12] Agilent, "Network Analysis: Specifying calibration standards for the HP 8510 network analyzer," Product Note 8510-5B, 2006.

[13] R. B. Marks and D. F. Williams, MultiCal™ , Version 1.04e, http://www.nist.gov/ctl/rf-technology/related-software.cfm.

Transient Temperature Measurement of Microwave Devices

Dustin Kendig[1], Kazuaki Yazawa[1,2], Ali Shakouri[2]
1Microsanj, LLC, Santa Clara, CA USA
2 Purdue University, West Lafayette, IN USA
Email: info@microsanj.com, Phone: 1-408-256-1255

SUMMARY

Introduction

Decreased feature sizes with today's advanced microwave devices has led to increased functionality and decreasing chip sizes. Not only higher power density but also localized hotspots have become a significant concern for transistor performance and long term reliability. Arrhenius's law in chemical reaction dominates the reliability of highly doped semiconductors designed for higher switching speeds. With higher integration, the device features are significantly small such as a 100 nm line width line for a transistor gate electrode. As the dimensions decrease, the thermal time constant decreases simultaneously. Hence, it is major challenge to detect and measure hotspot temperatures.

Transient thermoreflectance thermal imaging

We have developed thermoreflectance thermal imaging equipment and commercialized imaging systems using an industrial grade CCD imager, an optical microscope, and a LED illumination module. Fig. 1 shows the pictures of the equipment and Fig. 2 shows the schematic diagram of component connections for the equipment. Thermoreflectance uses a light reflection change with changing temperature at the material's surface. This occurs because the surface property is slightly modified by thermal expansion of the crystal as the temperature changes, hence the refraction index is changed resulting in a change in the reflection intensity. The thermoreflectance technique is a non-contact and non-destructive method and typically uses visible wavelength illumination. Therefore, the spatial resolution is in the submicron range. Our equipment has the electronic circuity to precisely lock-in the signals for LED illumination, provide the timing to capture an image, and applies a pulse modulated bias to the device under test. A proportional constant of reflectivity change by changing temperature is usually very small, being in the order of 10^{-4}, so image averaging is important to reduce measurement error. To obtain a transient series of images, we use a time-shift technique for a repeating device bias. The timing delay of for obtaining an image relative to the device excitation is precisely controlled, as shown in Fig. 3. A time series of thermal images can be captured by continuously shifting this delay. To calibrate temperature automatically, the reflection intensity is measured at both the on and off portions of the device bias

978-1-4799-8887-7/15/$31.00 ©2015 IEEE

cycle, and the difference noted. This eliminates the impact of background temperature change. As a result, this method enables 100 nsec time resolution with a 200-300 nm spatial resolution.

Measurement setup

Before obtaining an image, the optical surface property for the thermoreflectance coefficient C_{th} must be taken. The device under test (DUT) is placed on the thermal chuck, which is a small thermally controlled stage. By knowing the temperature of the device, thermoreflectance images by changing the stage temperature can be used to calculate the thermoreflectance coefficient. Since the reflectance is a function of the illumination wavelength, the coefficient is wavelength specific. For gold, a common semiconductor material, green light (530 nm) illumination results in $3x10^{-4}$ [1/K] for C_{th}. A very thin passivation coating is usually not a problem since it is nearly transparent, so that the illumination light is reflected by the underlying gold surface.

Sample measurement

A transient thermal imaging example for a Heterojunction Bipolar Transistor (HBT) and a High Electron Mobility Transistor (HEMT) are shown below.

Fig. 4 (a) shows the optical image of the HBT device with no bias. The horizontal short and thin line is the base electrode and is the area of interest. Fig. 4 (b)-(f) show the time series of thermal images after a 3V, 20 mA step bias is applied. We used 530 nm (green) light illumination for this device. In a very short time, less than 10 μsec, the hotspot is isolated from the surrounding features. The heat then diffuses to surrounding areas along the high thermal conductivity material, in this case the gold trace. As seen in Fig. 5 (b), the time response to the 100 μsec step input shows the higher temperature at the base electrode and the slightly lower temperature at the lower side pad. The temperature profile for the base area smoothly increases up to about 40 μsec and is slightly modified afterward. This is the time range for which thermal diffusion has a larger effect resulting in a slowing down of the temperature rise at the hotspot. To investigate a smaller time scale, a 1 μsec step pulse is applied to the same device, see Fig. 6. Since the blue dots represent the area influenced by the heat diffusion from the hotspot, even after powering off, the temperature still increases slightly because the heat received from the hotspot is exceeds the rate of cooling down at that location.

Fig. 7 shows an example of a HEMT device. Fig. 7 (a) shows the optical image with a 20x objective magnification and (b) shows the thermal image at 1 msec after an applied step bias 8 V, 70 mA with 530 nm LED illumination. The thermal time constant of the chip alone is in the range of 1 msec, therefore this temperature is nearly at equilibrium. The peak temperature is observed at the drain (center finger). The two very thin gate fingers have 250 nm line widths, slightly thinner than the diffraction limit determined by the illumination wavelength. Nevertheless we can observe the heating at the gate as shown in Fig. 8. In future work we will demonstrate a sophisticated method to determine the temperature signature for 100 nm linewidths.

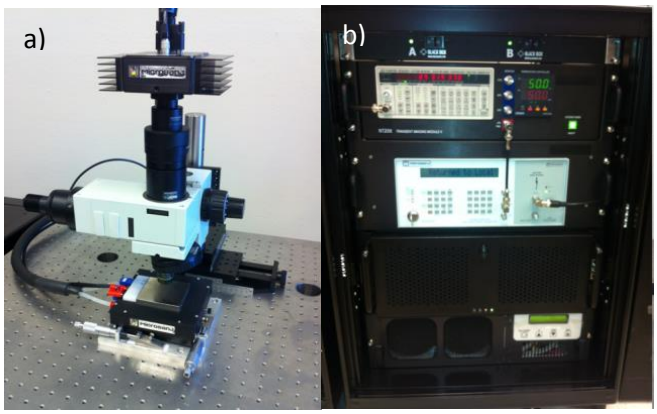

Figure 1: Picture of the system a) microscope setup and b) signal inter-lock and processing unit.

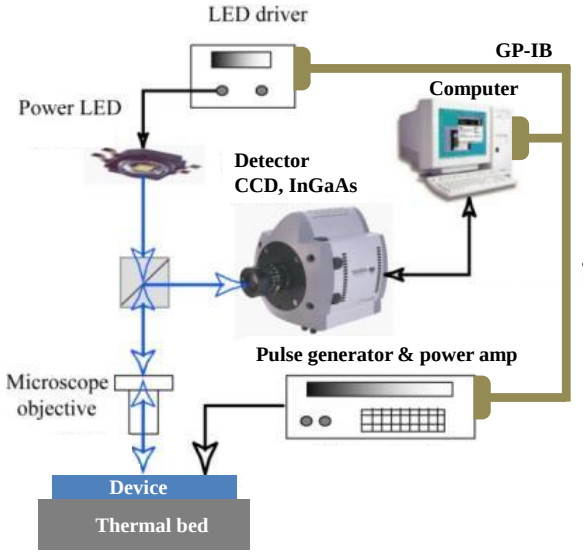

Figure 2: Schematic of the setup

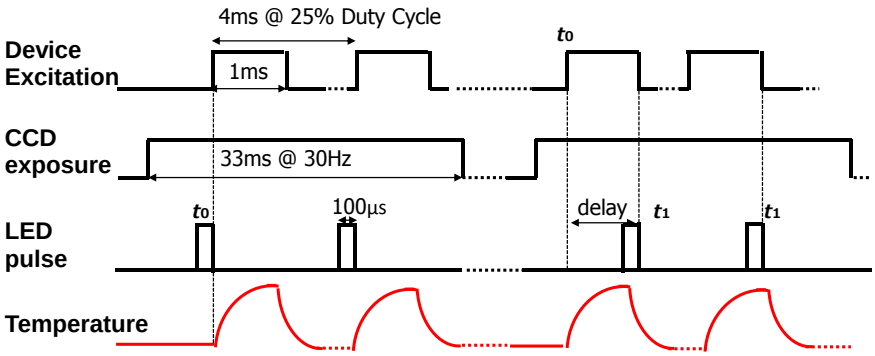

Figure 3: Timing diagram for an example of transient thermoreflectance measurement.

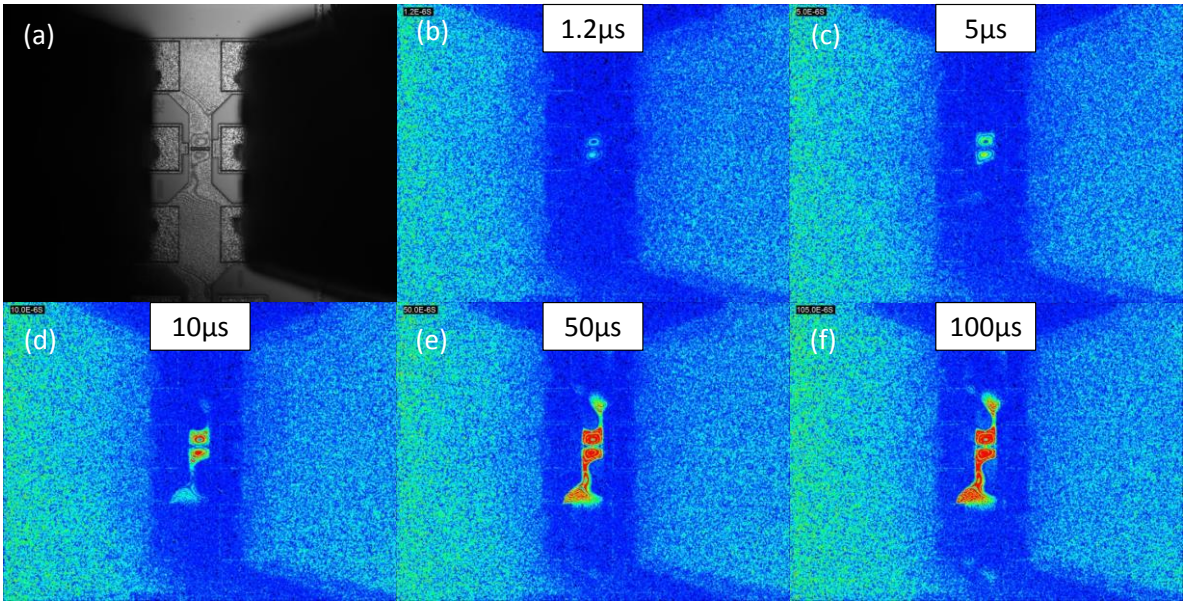

Figure 4: (a) Optical image of a HBT, (b)-(f) Thermal images in time series of the device.

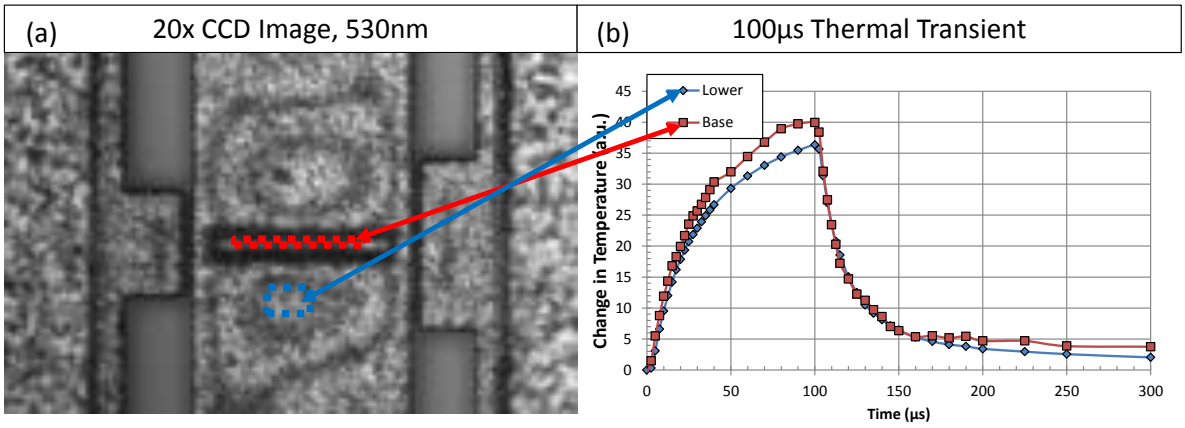

Figure 5: (a) Zoom up the junction area and (b) Temperature response profile

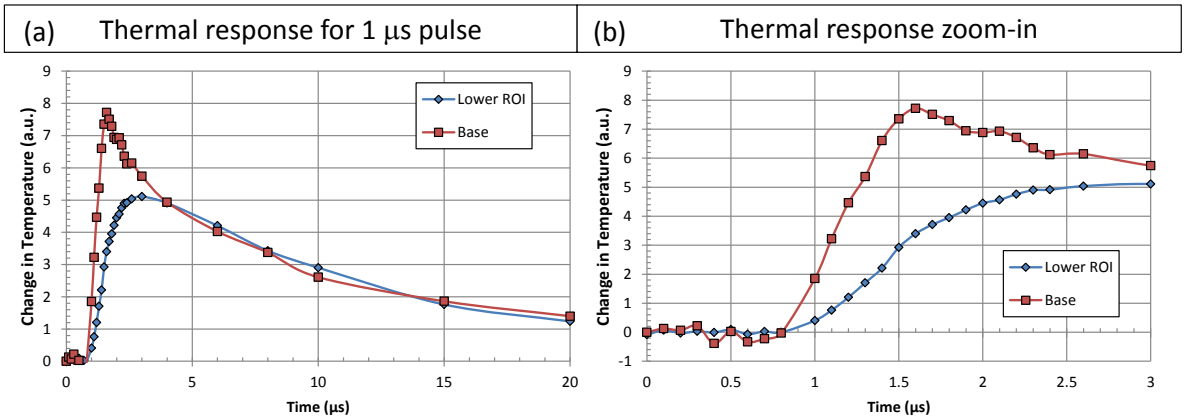

Figure 6: HBT time responses to 1 µsec step pulse input (a) is full scale, (b) is zoom-in.

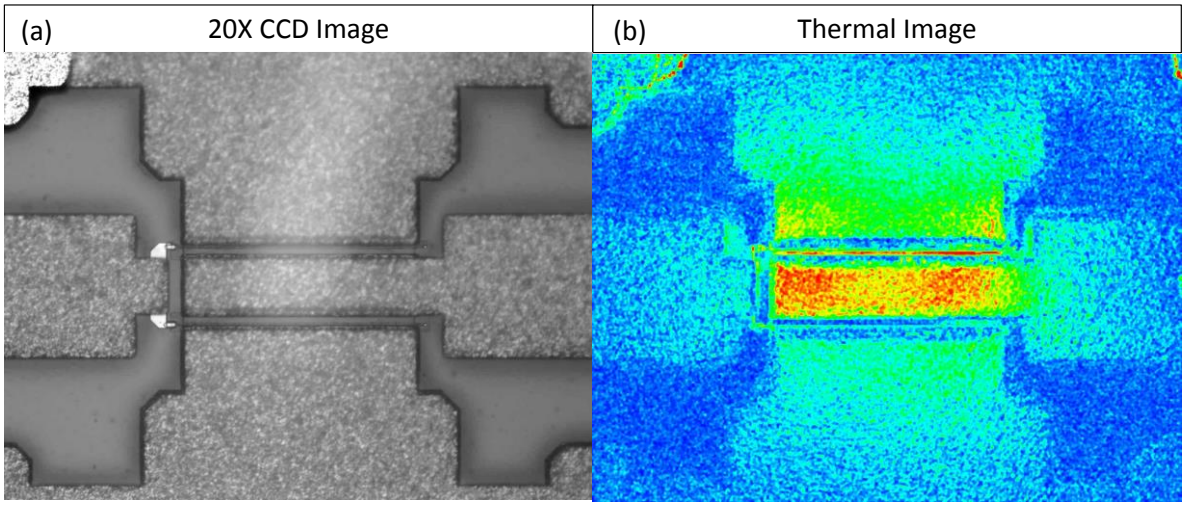

Figure 7: HEMT device. (a) shows the optical image and (b) shows the thermal image

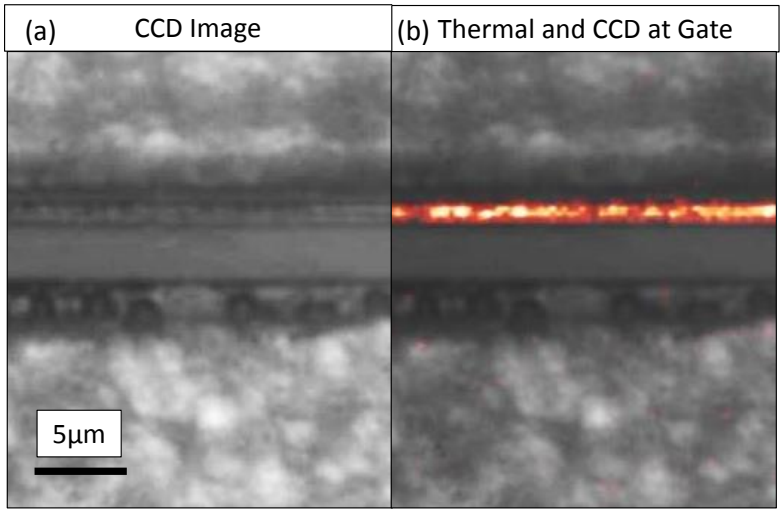

Figure 8: Zoom up image at the Gate (250 nm width). (a) shows optical image and (b) shows overlay of optical image and thermal image.

Novel Components for a Fully Automated PIM and S-Parameter Test System

Martin Graßl and Wolfgang Zißler

Spinner GmbH, Aiblinger Str. 30, 83620 Feldkirchen-Westerham

m.grassl@spinner-group.com, w.zissler@spinner-group.com

Abstract – As the spectrum utilization in modern mobile communication systems increases steadily, noise created by passive intermodulation becomes more likely. Thus passive intermodulation measurements are an obligatory part in the production of components for mobile communication infrastructure. However, these measurements are time-consuming and also costly. This paper describes a measurement system that reduces testing time by combination of S-Parameter and PIM measurements as well as automatic connecting of the device under test (DUT) to the test port.

Index Terms — Passive intermodulation, PIM, PIM distortion measurement, quick-lock connector, rotary joint, switch.

I. Introduction

Passive intermodulation is an obstacle in mobile communication systems for a long time already. To understand the effect of PIM on a mobile communication system it is good to have a look at the most simplified case where two sinusoidal carriers with the frequencies f_1 and f_2 are transmitted over a single path. In case the transmission path is not linear, intermodulation products with the following frequencies will be generated:

$$f_{IM} = |k_1 f_1 \pm k_2 f_2|$$

k_1 and k_2 are natural numbers and $k_1 + k_2$ is the order of the intermodulation product. If we assume the two carriers are both in the downlink band of LTE2.6 mobile communication standard and have the frequencies 2.62 GHz and 2.69 GHz the spectrum on the transmission path will look like this:

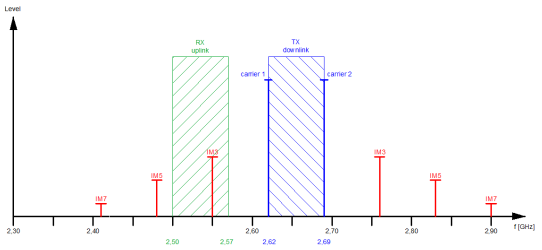

Fig. 1. Schematic representation of intermodulation products

In this case an intermodulation product will appear in the uplink band of LTE 2.6. Here it is of the 3rd order. It creates an additional interference which will degrade the signal to noise ratio and thus cause a drop in the channel capacity. As this noise can't be filtered it must be ensured that as little PIM as possible is created. This can only be achieved by designing highly linear components for the transmission path.

The well-known causes for nonlinearities in passive components are inappropriate materials and poor RF contacts. The first point can be avoided easily. To ensure proper contact usually causes more problems. A more detailed description of passive intermodulation and the causes for it can be found in [1].

II. System for Automatic Measurement of S-Parameters and PIM

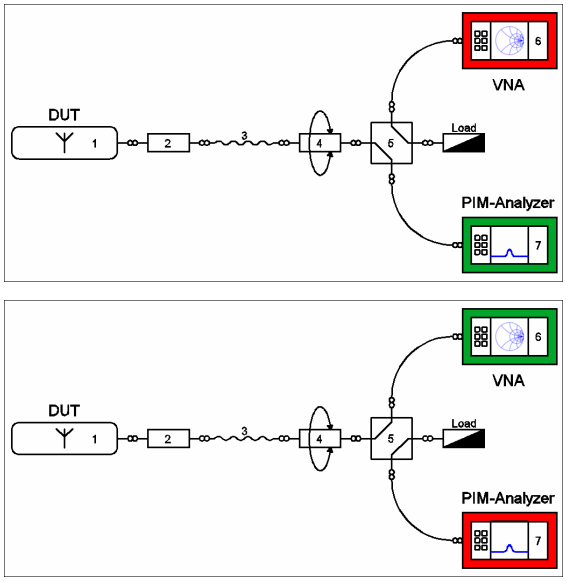

Fig. 2. Schematic representation of the measurement system in both switching states

Fig. 2 shows the principle structure of the measurement system. The DUT (1), in this case an antenna, is fixed in a jig and the RF ports are contacted automatically by quick-lock connectors

978-1-4799-8887-7/15/$31.00 ©2015 IEEE

(2). A test cable (3) follows which is connected to a rotary joint (4) for torque relief. The rotary joint is connected to a low PIM switch (5) which can automatically switch between a network analyzer and a PIM analyzer.

In the following sections the components will be described in detail.

III. Quick-lock connectors for automatic connection of the DUT using the new 4.3-10 connector interface

The standard connector interface currently used in mobile communication applications is still the 7-16 type. For this connector the proper RF contact is ensured by a high axial contact force created by a massive coupling nut. This is a disadvantage if quick-lock connectors with good PIM performance are required. If the quick-lock connector would be just pressed on the counterpart, the necessary force to achieve an RF contact with low intermodulation level, typically several thousand netwons, would in many cases damage the DUT. Alternatively, the automatic tightening of a coupling nut could be applied but it would need a quite complicated design. Preferably, the quick-lock connector would have excellent PIM performance even if pressed on with a rather low force (e.g. 80 N). The solution for that is the newly developed 4.3-10 interface which will most likely replace the 7-16 interface in many applications.

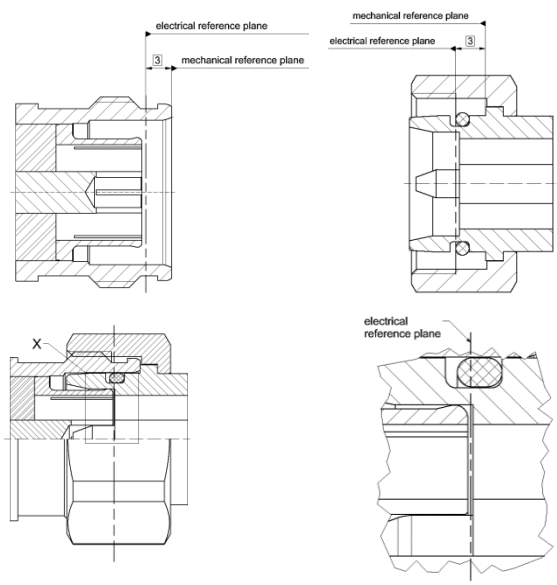

Fig 3. 4.3-10 connector interface in unmated and mated condition

Fig. 3 shows the connector interface drawing of 4.3-10. In contrary to other RF connectors the 4.3-10 connector has no axial RF contact on the outer conductor but a radial contact bushing instead. A mechanical stop (mechanical reference plane) is provided outside the RF region. The outer conductor contact bushing will provide a constant contact force completely independent of the axial force applied to the mechanical stop. This results in an excellent PIM performance in case of a press-on quick-lock connector. Also, when used with a coupling nut the 4.3-10-connector ensures good PIM even if it is tightened with a torque below the nominal coupling torque. This reduces costs for trouble shooting at mobile communication base station sites. Besides size and weight reduction compared to the 7-16 type these were the main reasons to develop the 4.3-10-connector interface.

A complete quick-lock connector is displayed in Fig. 4. It has 4.3-10 connectors on both ends. The left side will be connected to the DUT, the right side will be connected to the test port using a cable. The middle part can be fixed in a wall plate that will be moved towards the DUT. It contains spring elements that allow for an axial, transversal and angular alignment of the connector and thus will compensate position tolerances of the DUT and the test fixture.

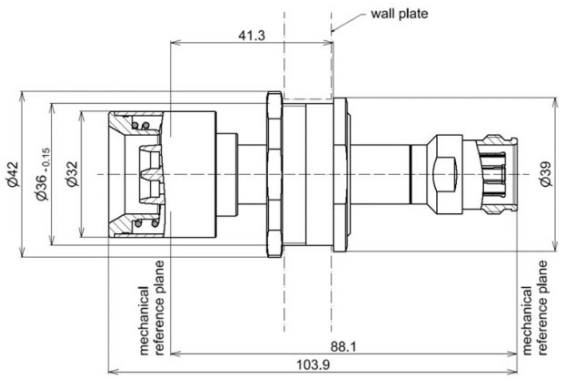

Fig 4. Quick-lock connector with automatic compensation of position tolerances

With this type of connector repeatable VSWR measurements as well as PIM measurements with residual intermodulation of typical -170 dBc at 2 x 20 W are achieved.

IV. Torsion-relief of measurement cables using low intermodulation rotary joints

The flexing cycles of test port cables are always an issue when PIM measurements are done. In case of testing high volumes of mobile communication products such as antennas or diplexers several hundreds of flexing cycles per day are common and the costs for replacement of worn-out cables are significant.

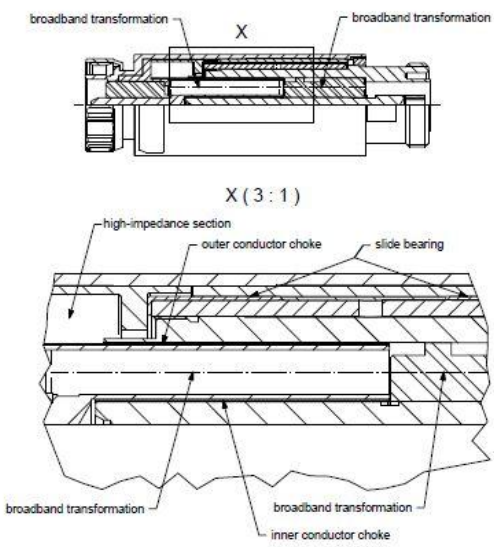

Fig. 5. Design of the non-contacting rotary joint

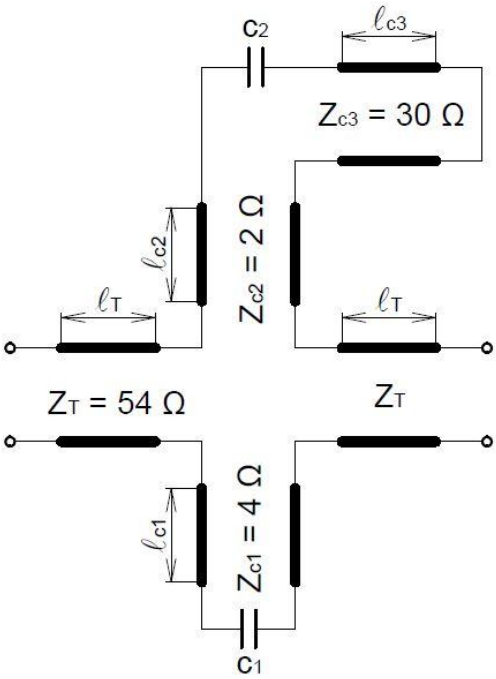

Fig. 6. Equivalent circuit of the rotary joint

In order to increase the service life of the testing cables a strain- and torsion-relieve is provided in our measurement system using low intermodulation rotary joints. Fig. 5 shows the design based on 7-16 connectors and Fig. 6 an equivalent circuit of the structure. It contains a slide bearing to make the rotor moveable against the stator without galvanic contact. The inner conductors of the fixed and the rotating part are coupled by an open ended coaxial line (choke) with the impedance $Z_{c1}$of approx. 4 Ω and a length l_{c1} of one quarter wavelength of the band center frequency. The fringing capacitance of the open end is represented by C_1 in the equivalent circuit. The outer conductors are also coupled by a choke. It has a characteristic impedance $Z_{c2}$of approx. 2 Ω and a length l_{c2}that also equals one quarter wavelength at the band center frequency. It is followed by a high-impedance section with an impedance Z_{c3} of 30 Ω and a length l_{c3}. The change in the characteristic impedance from 2 Ω to 30 Ω behaves similar to an open end of a coaxial line which cannot be realized at this position. In Fig. 5 the 30 Ω line is represented by the small cavity following the outer conductor choke. The equivalent circuit in Fig. 6 shows another capacitance C_2 between the outer conductor choke and the 30 Ω line. It represents the slide bearing of the rotary joint.

A design with only inner and outer conductor chokes would have one reflection minimum and could not cover a sufficiently wide frequency range for the intended application. For that reason a broadband transformation has been added. It is represented by the two line sections beside the chokes with a characteristic impedance of approx. 54 Ω and again a length l_T of a quarter wavelength at the band center frequency. This broadband transformation creates two more reflection minima and increases the bandwidth significantly.

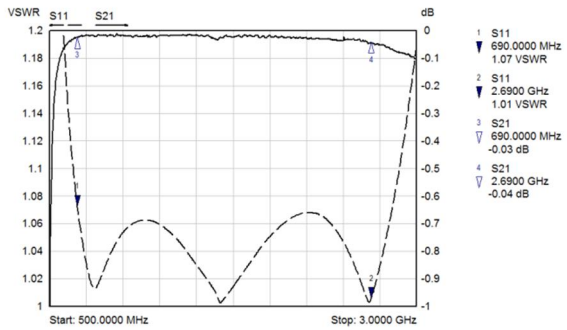

Fig. 7. Measurement results of the non-contacting rotary joint

Fig. 7 shows the measured return loss and insertion loss of the structure. The VSWR exhibits the three reflection minima mentioned above. With a frequency range from 0.69 GHz to 2.69 GHz the rotary joint covers all today's mobile communication standards with a VSWR better than 1.10. As the whole design is realized without sliding contacts the intermodulation values of this structure are in the range of the system value of the PIM test bench, even during rotation. Furthermore, as no grinding occurs between metallic surfaces, no metal particles are created that could degrade the intermodulation performance over the lifetime. Thus, in contrary to a solution with sliding contacts the PIM values will remain stable with increasing number of rotations.

V. RF SWITCH WITH LOW INTERMODULATION

For a measurement system combining a vector network analyzer and an intermodulation test bench, a two way switch (DPDT) is necessary. This switch has to provide excellent repeatability of return and insertion loss in order to maintain the calibration for the S-Parameter measurements. Also, excellent PIM performance is required for the intermodulation measurements. Commercially available switches all have galvanic contacts for the switching elements und thus they have the risk that the PIM values suffer from metal particles with increasing number of switching cycles. For that reason we use a switch with capacitive couplings for this measurement system.

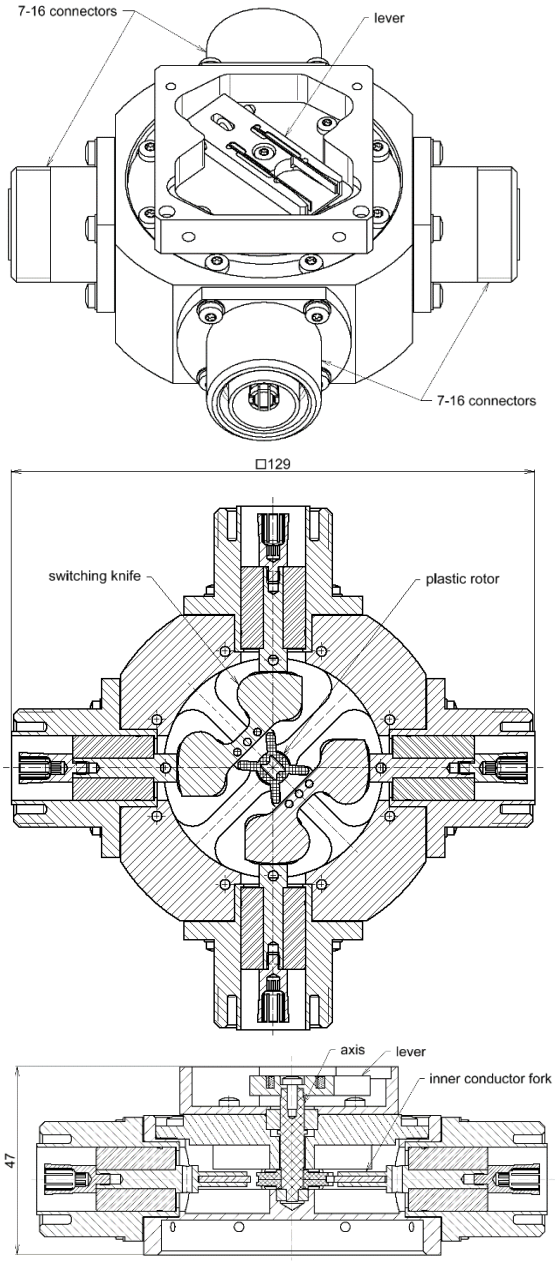

Fig. 8. 3D-view and sectional drawings of the low PIM switch

Fig. 8 illustrates the design of the RF part of the low PIM switch. On top it has a lever that will be moved by an electric drive which is not displayed here. The lever sits on an axis that drives a plastic rotor. The rotor carries the switching knifes. The knives can float in the rotor along the direction of the axle. Both ends of the switching knife are positioned in the inner conductor fork of a coaxial line leading to one of the 7-16 connectors. The fit is very narrow so knife and fork touch each other. To avoid a galvanic contact both parts are coated with a special insulating paint. The close fit together with the dielectric coating results in a quite high capacitance allowing for a lower frequency limit of less than 690 MHz. The narrow fit is also needed for a good repeatability of the S-parameters. As fork and knife touch each other friction occurs between them. But since the particles created are only of dielectric material, no PIM is caused.

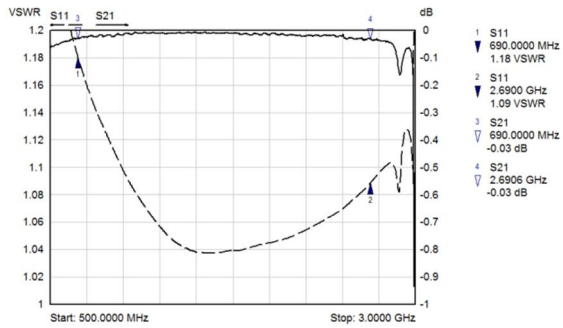

Fig. 9. VSWR and insertion loss in connected position

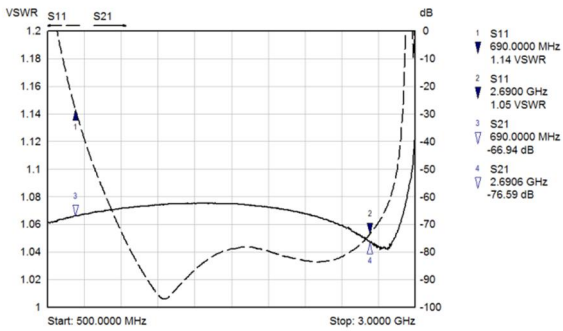

Fig. 10. VSWR and isolation in isolated position

Fig. 9 and 10 show the S-parameter measurement results of the switch. The VSWR is below 1.2 and the insertion loss better than 0.1 dB in the frequency range from 0.69 GHz to 2.69 GHz. Thus it can be used for all today's common mobile communication standards. The isolation is better 60 dB which is necessary to protect the frontend of the VNA when the PIM analyzer is active. The repeatability of S11 after several switching cycles is well below 50 dB so a calibration applied to the measurement system will be maintained.

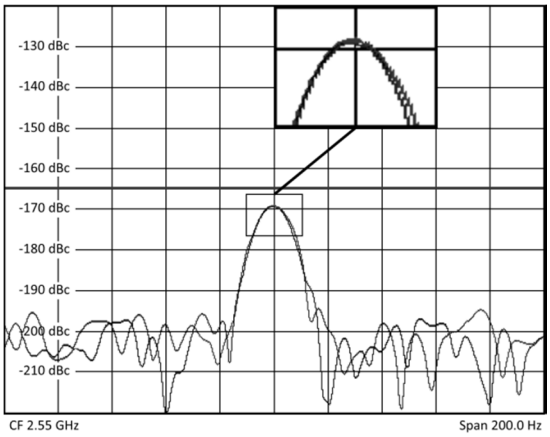

Fig. 11. PIM test results of the switch at LTE2.6 before and after half a million switching cycles

In Fig. 11 the PIM test results before and after the long term durability test are shown. The same carrier frequencies as displayed in Fig. 1 have been used. The test has been done with an RF power of 20 W per carrier. The results before and after the test are almost equal at approx. -170 dBc and thus in the region of the residual system level of the PIM test bench.

VI. Conclusion

A measurement system has been presented that can measure S-parameters and passive intermodulation without disconnecting the DUT. Capacitive coupling has been used for the rotary joint and the switch to avoid intermodulation caused by sliding contacts. It could be demonstrated that the intermodulation performance is stable over at least half a million measuring cycles. Furthermore, the DUT is connected by quick-lock connectors which can be driven automatically. With the proposed measurement system a significant time- and cost-saving is possible compared to setups with separated intermodulation and S-parameter measurement.

References

[1] Lui, P.L., "Passive intermodulation interference in communication systems", *Electronics & Communication Engineering Journal, Volume 2, Issue 3, Page 109-118,* 1990

[2] Lijia Chen, Shu Lin, Jinghui Qiu, Xin Wang, Shaowei Fan, "Analysis and measurement of antenna passive intermodulation", *Electronics and Information Engineering (ICEIE), 2010 International Conference On, Vol. 2*

[3] Tiquan Sun, Fenghui Xu, Juan Lu, Yong Xu, Kun Liu, "Novel and simplified passive intermodulation distortion measurement using vector network analyzer", *Industrial Electronics and Applications (ICIEA), 2014 IEEE 9th Conference on*

[4] Lui P.L., Rawlins, A.D., "The design and improvement of PIMP measurement facilities and the measurement of PIMP in antenna structures", *Passive Intermodulation Products in Antennas and Related Structures, IEE Colloquium on, 1989*

On the Implementation of the LZZ Calibration Technique in the S-Parameters Measurement of Devices Mounted in Test Fixtures

M.A Pulido-Gaytán[1], J.A. Reynoso-Hernández[1], M.C. Maya-Sánchez[1],A. Zárate- de Landa[2] and J.R. Loo-Yau[3]

[1]Centro de Investigación Científica y de Educación Superior de Ensenada (CICESE). Ensenada, B.C., México.
[2]Peregrine Semiconductor. San Diego, CA., United States.
[3]Centro de Investigación y de Estudios Avanzados del I.P.N (CINVESTAV). Guadalajara, Jalisco, México.

Abstract — This paper introduces a methodology for the design and verification of the set of microstrip structures necessary to implement the line, offset-open, offset-short (LZZ) calibration technique in the small-signal characterization of devices mounted in coaxial-to-microstrip test fixtures. The usefulness of the LZZ calibration in such application is verified by comparing the S-parameters of a GaN-HEMT packaged transistor corrected using the LZZ with those corrected using the thru-reflect-line (TRL) calibration technique.

***Index Terms* — LZZ calibration technique, ABCD-parameters, microstrip calibration structures, test fixtures.**

I. Introduction

At microwave frequencies, the use of a calibrated vector network analyzer (VNA) is mandatory to characterize the linear behavior of a device under test (DUT). A number of VNA calibration techniques have been proposed in the literature. Among them, the most commonly used calibration techniques are the thru-reflect-line (TRL) [1], thru-reflect-match (TRM) [2] and thru-reflect-reflect-match (TRRM) [3].

TRL is considered as a reference calibration technique. It allows referring the DUT S-parameters to the measuring system impedance (Z_0) as long as the characteristic impedance of the line is known [4]. In the TRL, the main issue is that multiple lines of different length are required [5] to obtain a wide measurement bandwidth. Thus, the measurement ports have to be moved several times in order to accommodate structures of different size, which reduces the measurement repeatability.

TRM [2] replaces the line used in the TRL by a symmetrical load (match) of known impedance in order to achieve a broadband calibration. Meanwhile, the TRRM [3] is a variation of TRM, where only one known load is used. In general, TRM and TRRM involve the use of at least one load which has to be known over a wide frequency bandwidth. Thus, to accurately calibrate the VNA using the TRM and TRRM procedures, the use of either high technology to fabricate loads of known impedance [6] or the use of complex procedures to estimate it [3], [7] are required.

The recently introduced line, offset-open, offset-short (LZZ) calibration technique [8] uses as standards: a transmission line, a pair of offset-open circuits and a pair of offset-short circuits (Fig. 1). Unlike TRM and TRRM, in the LZZ calibration the use of a precisely characterized load is not required. Moreover, since the LZZ calibration does not use multiple transmission lines for calculating the error calibration terms, it may be implemented using fixed spacing structures, which is an advantage over the TRL calibration technique.

The LZZ calibration technique was introduced in [8] as a reliable method for correcting the S-parameters of on-wafer devices using coplanar waveguide calibration structures. In this paper, a methodology for the design and verification of the set of microstrip calibration structures necessary for implementing the LZZ calibration in the S-parameter measurement of devices mounted in coaxial-to-microstrip test fixtures is introduced.

This paper is organized as follows. Section II presents an overview of the LZZ calibration procedure. In section III, the methodology for the design and verification of the LZZ microstrip calibration structures is described. Section IV shows experimental results of the implementation of the LZZ in the measurement of devices mounted in test fixtures. Finally, the conclusions are presented in section V.

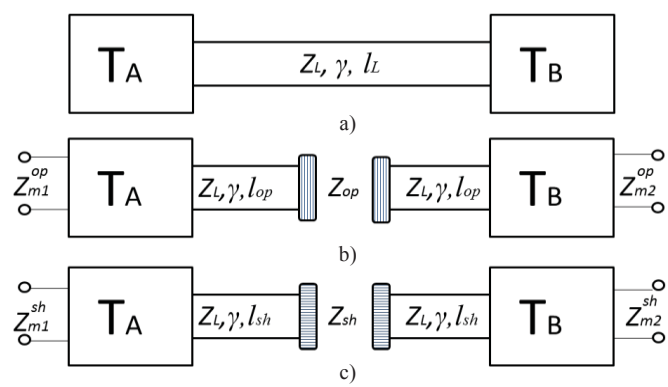

Fig. 1. LZZ calibration elements: a) one transmission line, b) a pair of offset-open circuits and c) a pair of offset-short circuits.

II. Overview of the LZZ Calibration Procedure

The LZZ calibration procedure uses the 8-term error model and the ABCD parameters to represent the VNA and the calibration standards. When using the 8-term error model, a two-port VNA measures the matrix product

$$\mathbf{M_D} = \mathbf{T_A}\mathbf{T_D}\mathbf{T_B}, \tag{1}$$

where $\mathbf{T_A}$ and $\mathbf{T_B}$ are matrices modeling the errors in ports one and two of the VNA. $\mathbf{M_D}$ and $\mathbf{T_D}$ are matrices

978-1-4799-8887-7/15/$31.00 ©2015 IEEE

representing the measured and the actual behavior of a DUT, respectively.

According to [9], the ABCD parameters matrix of a uniform transmission line having length l_L, propagation constant γ and characteristic impedance Z_L may be diagonalized and expressed as[1]

$$\mathbf{T_L} = \mathbf{T_Z}\mathbf{T_\lambda}\mathbf{T_Z^{-1}}, \tag{2}$$

where $\mathbf{T_Z}$ and $\mathbf{T_\lambda}$ are defined as

$$\mathbf{T_Z} = \begin{bmatrix} Z_L & -1 \\ 1 & Z_L^{-1} \end{bmatrix} \tag{3}$$

and

$$\mathbf{T_\lambda} = \begin{bmatrix} \lambda_L & 0 \\ 0 & \lambda_L^{-1} \end{bmatrix}, \tag{4}$$

with $\lambda_L = e^{\gamma l_L}$. Then, by combining (1) and (2), the ABCD parameters representation of the structure shown in Fig.1a may be expressed as

$$\mathbf{M_L} = \mathbf{T_A}\mathbf{T_L}\mathbf{T_B} = \mathbf{T_X}\mathbf{T_\lambda}\mathbf{T_Y}, \tag{5}$$

where

$$\mathbf{T_X} = \mathbf{T_A}\mathbf{T_Z} = \begin{bmatrix} A_X & B_X \\ C_X & D_X \end{bmatrix} = D_X \begin{bmatrix} \overline{A_X} & \overline{B_X} \\ \overline{C_X} & 1 \end{bmatrix} \tag{6}$$

and

$$\mathbf{T_Y} = \mathbf{T_Z^{-1}}\mathbf{T_B} = \begin{bmatrix} A_Y & B_Y \\ C_Y & D_Y \end{bmatrix} = D_Y \begin{bmatrix} \overline{A_Y} & \overline{B_Y} \\ \overline{C_Y} & 1 \end{bmatrix}. \tag{7}$$

Note from (2) that, when a zero-length thru (l_L=0) is used in the LZZ calibration instead of a transmission line, $\mathbf{T_L}$ becomes the identity matrix $\left(\mathbf{T_L} = \mathbf{I} = \mathbf{T_Z}\mathbf{T_Z^{-1}}\right)$. In such a condition, the expressions shown in (5)-(7) cannot be formed since the matrix $\mathbf{T_Z}$ is not uniquely defined (it is difficult to define the impedance of a zero-length thru). This problem arises at frequencies where the electrical length of the transmission line is a multiple of 180° ($\lambda_L = \pm 1$).

Then, by solving (6) and (7) for $\mathbf{T_A}$ and $\mathbf{T_B}$, respectively, and substituting the resulting expressions in (1), the actual ABCD parameters of the DUT may be expressed as

$$\mathbf{T_D} = \mathbf{T_Z}\mathbf{T_X^{-1}}\mathbf{M_D}\mathbf{T_Y^{-1}}\mathbf{T_Z^{-1}}. \tag{8}$$

Thus, in order to determine $\mathbf{T_D}$, the seven terms $\overline{A_X}$, $\overline{B_X}$, $\overline{C_X}$, $\overline{A_Y}$, $\overline{B_Y}$, $\overline{C_Y}$ and $D_X D_Y$, have to be determined using the measurement of the set of calibration elements shown in Fig.1. According to the LZZ procedure described in [8], four of the seven terms, $\overline{A_Y}$, $\overline{B_Y}$, $\overline{C_Y}$ and $D_X D_Y$, may be determined using the measurement of the transmission line, provided that the terms $\overline{A_X}/\overline{C_X}$, $\overline{B_X}$ and $\overline{C_X}$ are known.

In the LZZ calibration [8], the values of $\overline{A_X}/\overline{C_X}$ and $\overline{B_X}$ are determined using the measurement of the two pairs of offset reflecting loads shown in Fig.1b-c along with the measurement of the transmission line. In the LZZ, open-circuited transmission lines of length l_{op} and short-circuited transmission lines of length l_{sh} are used as offset-open and offset-short circuits (Fig.1b-c). The LZZ calibration requires that the offset-open and offset-short circuits be equally shifted, i.e. $\lambda_{sh} = e^{\gamma l_{sh}}$ have to be identical to $\lambda_{op} = e^{\gamma l_{op}}$. The value of $\overline{C_X}$ may be determined using the measurement of any of the symmetrical reflecting loads[2].

In summary, in order to design a set of calibration structures for implementing the LZZ calibration technique there are two important issues that have to be considered: 1) to design two equally shifted pairs of offset reflecting loads and 2) to design a transmission line of electrical length less than 180° at the highest frequency of interest.

III. Design and Verification of LZZ Calibration Structures

A. Design of the LZZ Calibration Structures

A microstrip transmission line and two pairs of offset reflecting loads were fabricated on a substrate RO4003C (ε_r=3.55, H=0.814mm) provided by Rogers Corporation. Before the fabrication, the S-parameters of the structures shown in Fig. 2 were simulated using an electromagnetic simulator (ADS Momentum) in the frequency range of 0.1-6.0 GHz.

An 8 mm length transmission line of characteristic impedance Z_L= 50 Ω and electrical length of 100° at 6 GHz, shown in Fig. 2a, represents the transmission line of the LZZ calibration technique. Symmetrical short-circuited (Fig.2b) and symmetrical open-circuited (Fig.2c) transmission lines of 1 mm length represent the offset reflecting loads of the LZZ calibration. The length of the open-circuited line was iteratively increased from 1 mm until the difference between the simulated phase shifts of the offset-open circuits (λ_{op}) and offset-short circuits (λ_{sh}) was close to zero at 6 GHz. The aim of this adjustment is to compensate in the open-circuited line the phase shift caused by the via-holes used in the short-circuited line. Symmetrical open-circuited 1.15 mm length transmission lines were used as the offset-open.

[1] In the LZZ the characteristic impedance, length and propagation constant of the line have to be known prior to the calibration.

[2] Alternatively, $\overline{C_X}$ may be determined using the measurement of an additional one port load of impedance close to Z_L (LZZM procedure) [10].

As a measure of the correlation between the simulated λ_{op} and λ_{sh}, its phases $\angle\lambda_{op}$ and $\angle\lambda_{sh}$ were used. The values of $\angle\lambda_{op}$ and $\angle\lambda_{sh}$ were calculated as

$$\angle\lambda_{op} = \left(\angle\Gamma_{op}\right)/2 \tag{9}$$

and

$$\angle\lambda_{sh} = \left(\angle\Gamma_{sh} - 180°\right)/2, \tag{10}$$

where Γ_{op} and Γ_{sh} are the reflection coefficients of the offset-open and offset-short circuits obtained from the simulated S-parameters of the structures shown in Fig. 2b-c.

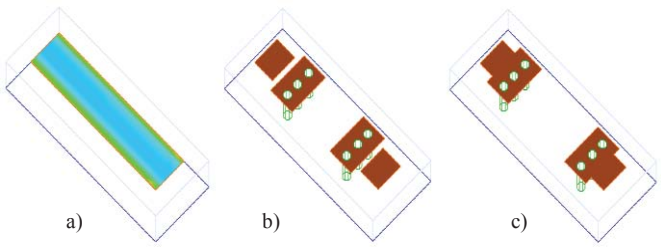

Fig.2. Simulated structures: a) line, b) offset-open circuit and c) offset-short circuit.

B. Verification of the LZZ Calibration Structures

The fabricated microstrip structures were embedded in transmission lines of length $l_{TF} = 28$ mm and characteristic impedance Z_L=50 Ω. Microstrip-to-SMA female connectors were placed at the end of each structure. Fig. 3a shows the fabricated structures.

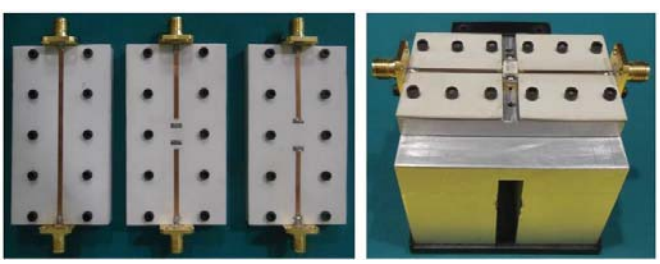

Fig.3. a) LZZ microstrip calibration structures embedded in transmission lines and b) test fixture for characterizing a packaged GaN-HEMT transistor.

In order to verify that the value of the phase shifts of the fabricated offset-open circuits and offset-short circuits are close to each other, measurements of the fabricated reflecting loads were performed using a N5242A PNA-X calibrated at the coaxial reference plane[3].

The measurement of an auxiliary transmission line (referred to as T_{TF}) of length $2 \cdot l_{TF}$ was used to estimate the values of $\angle\lambda_{op}$ and $\angle\lambda_{sh}$ from the S-parameters measurements of the fabricated offset-open circuits and offset-short circuits, as presented next.

Let Γ_R^{cx}, $R = op, sh$, be the reflection coefficient of any of the fabricated offset reflecting loads measured at the coaxial reference plane, and Γ_R the reflection coefficient of the offset reflecting load at the calibration reference plane (Fig. 4). The values of $\angle\lambda_{op}$ and $\angle\lambda_{sh}$ were calculated by comparing the insertion phase of the structure of the line T_{TF} measured at the coaxial plane $\left(\angle S_{21}^{TF}\right)$ with the phase of Γ_R^{cx} as

$$\angle\lambda_{op} = \left(\angle\Gamma_{op}^{cx} - \angle S_{21}^{TF}\right)/2 \tag{11}$$

and

$$\angle\lambda_{sh} = \left(\angle\Gamma_{sh}^{cx} - 180° - \angle S_{21}^{TF}\right)/2 \tag{12}$$

Fig. 5 shows the phase offset of the designed open-circuited and short-circuited transmission lines calculated from EM simulations using (9)-(10) and those calculated from measurements using (11)-(12). In both cases, high correlation is observed between the phases of the offset-open and offset-shorts circuits.

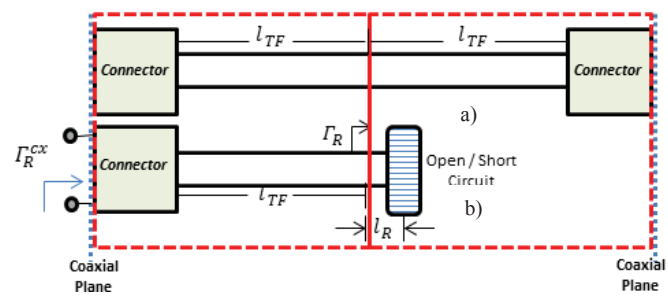

Fig.4. Structures used for the verification of the phase shift of the offset reflecting loads: a) a thru connection b) offset reflecting load.

The value of the propagation constant and characteristic impedance of the transmission line used in the LZZ calibration were determined using two transmission lines of different lengths, using the procedures reported in [11] and [12], respectively[4]. The electrical length of the line used in the LZZ was calculated as 98.7° at 6.0 GHz using the imaginary part of γ and the mechanical length of the line.

IV. Implementation of the LZZ Calibration Using Microstrip Calibration Structures

The LZZ calibration procedure was implemented by using the fabricated set of microstrip calibration structures shown in Fig. 3a. The TRL calibration was implemented by using a pair of offset-short circuits and the transmission line used in the LZZ calibration along with an additional thru structure, i.e. transmission line T_{TF}. Measurements of the TRL and LZZ calibration structures were performed by using an uncalibrated N5242A PNA-X in the frequency range of 1-6 GHz.

[3] A calibrated VNA was used only for verification of the offset loads. The LZZ calibration does not require the use of a calibrated VNA; it may be implemented in either one-tier or two-tier calibrations.

[4] A second transmission line was only used for determining the line propagation constant and characteristic impedance. It is not used in the implementation of the LZZ calibration procedure.

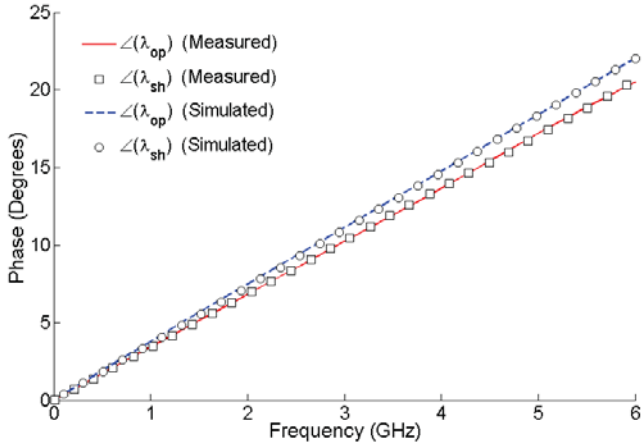

Fig.5. Verification of the phase shift of the designed open-circuited and short-circuited transmission lines.

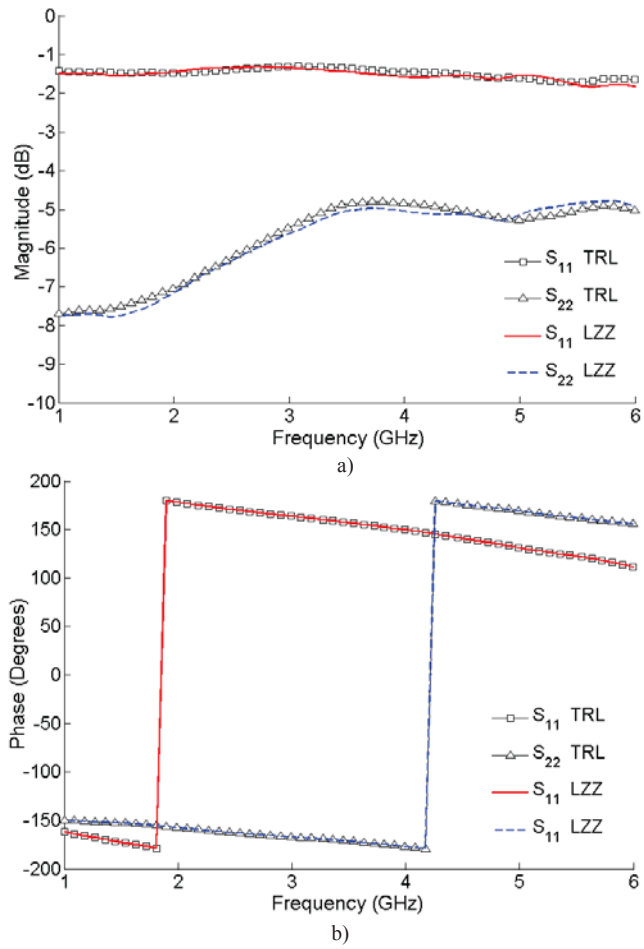

Fig.6. S_{11} and S_{22} parameters of an FET transistor (V_{DS} = 28 V; V_{GS}=-2.8 V) corrected using the LZZ and the TRL methods: a) magnitude and b) phase.

A packaged GaN-HEMT transistor (CGH40010 from Cree) was used as DUT; it was mounted in the coaxial-to-microstrip test fixture shown in Fig. 3b. To demonstrate the usefulness of the LZZ, the DUT S-parameters corrected using the LZZ were compared with those corrected using the TRL. Fig.6 and Fig.7 show the S-parameters of the transistor (V_{DS}=28 V; V_{GS}=-2.8 V) corrected using the TRL and LZZ methods. A high correlation between the S-parameters data corrected using these two calibration techniques is observed.

V. Conclusion

A methodology for the design and verification of the microstrip calibration structures necessary to implement the LZZ calibration technique was introduced in this paper. There are two important points to be considered in the design of the LZZ calibration structures. First, the phase shifts of the offset reflecting loads have to be as close as possible to each other. Second, the electrical length of the transmission line has to be less than 180° over the frequency bandwidth of interest. Results obtained using the designed calibration structures verify the usefulness of the LZZ calibration technique in the measurement of devices mounted in test fixtures.

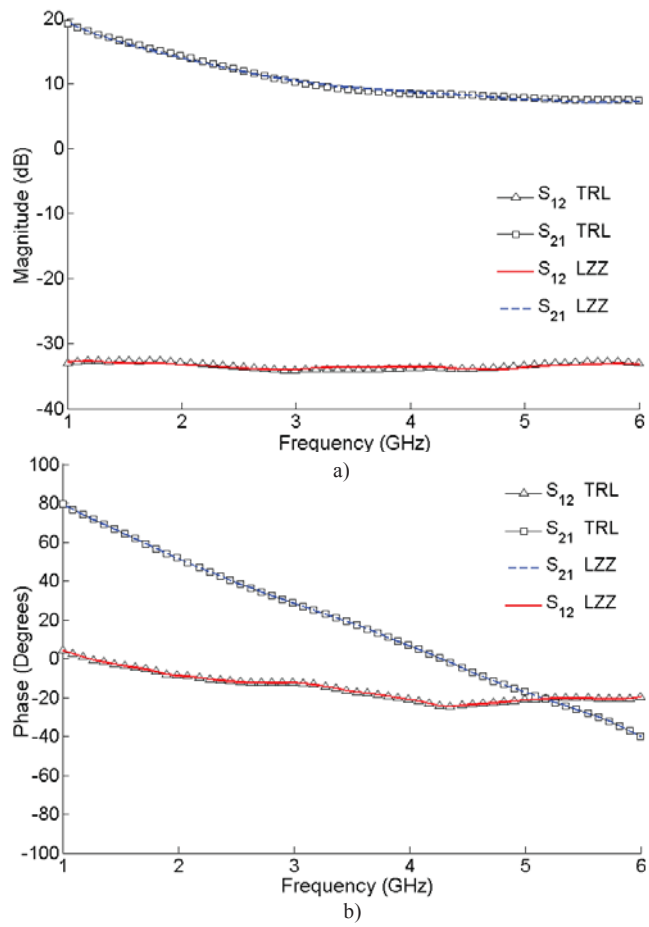

Fig.7. S_{12} and S_{21} parameters of an FET transistor (V_{DS} = 28 V; V_{GS}=-2.8 V) corrected using the LZZ and the TRL methods: a) magnitude and b) phase.

References

[1] G. F. Engen, C. A. Hoer, "Thru-Reflect-Line: An Improved Technique for Calibrating the Dual Six-Port Automatic Network Analyzer," *Microwave Theory and Techniques, IEEE Transactions on*, vol.27, no.12, pp. 987- 993, Dec 1979.

[2] H.-J. Eul, B. Schiek, "Thru-Match-Reflect: One Result of a Rigorous Theory for De-Embedding and Network Analyzer

Calibration," *Microwave Conference, 1988. 18th European*, pp.909-914, 12-15 Sept. 1988.

[3] A. Davidson, K. Jones, E. Strid, "LRM and LRRM Calibrations with Automatic Determination of Load Inductance," *ARFTG Conference Digest-Fall, 36th*, pp.57-63, Nov. 1990.

[4] J.A. Reynoso-Hernandez; M.A. Pulido-Gaytan; A. Zarate-de Landa; J.E. Zuniga-Juarez.; J.R. Monjardin-Lopez; A. Garcia-Osorio; Orozco-D. Navarro; J.R. Loo-Yau; M.C. Maya-Sanchez, "Using lines of arbitrary impedance as standards on the TRL calibration technique," *Microwave Measurement Conference (ARFTG), 81st ARFTG*, pp.1-4, June 2013.

[5] R. B. Marks, "Multiline method of network analyzers calibration," *Microwave Theory and Techniques, IEEE Transactions on,* vol. 39, no.7, pp. 1205-1215, Jul. 1991.

[6] R.F. Scholz, F. Korndorfe, B. Senapati, A. Rumiantsev, "Advanced technique for broadband on-wafer rf device characterization," *ARFTG Conference Digest, 63rd*, pp. 83- 90, Jun. 11, 2004.

[7] L. Hayden, "An Enhanced Line-Reflect-Reflect-Match calibration," *ARFTG Conference Digest, 67th*, Jun. 2006, pp. 146-149.

[8] Pulido-Gaytan, M.A.; Reynoso-Hernandez, J.A.; Zarate-de Landa, A.; Loo-Yau, J.R.; del Carmen Maya-Sanchez, M., "Vector Network Analyzer Calibration Using a Line and Two Offset Reflecting Loads," *Microwave Theory and Techniques, IEEE Transactions on* , vol.61, no.9, pp.3417,3423, Sept. 2013.

[9] J.A. Reynoso-Hernandez, M.A. Pulido-Gaytan, M. C. Maya-Sánchez, J.R. Loo-Yau, "What can the ABCD parameters tell us about the TRL?" *ARFTG Conference Digest, 79th*, Jun. 2012, pp. 1-4.

[10] M.A. Pulido-Gaytan, J.A. Reynoso-Hernandez, A. Zarate-de Landa, M. C. Maya-Sánchez, J.R. Loo-Yau, "LZZM: An extension of the theory of the LZZ calibration technique" *ARFTG Conference Digest, 84th*, Dic. 2014, pp. 1-5.

[11] J.A. Reynoso-Hernandez, "Unified method for determining the complex propagation constant of reflecting and nonreflecting transmission lines," *Microwave and Wireless Components Letters, IEEE*, vol.13, no.8, pp.351-353, Aug. 2003.

[12] J.E. Zuniga-Juarez; J.A. Reynoso-Hernandez,; A. Zarate-de Landa, "A new method for determining the characteristic impedance Zc of transmission lines embedded in symmetrical transitions," *Microwave Symposium Digest, IEEE MTT-S International* , pp.52,55, Jun. 2008.

ACKNOWLEDGEMENT

The authors would like to thank Rogers Corporation for the donation of the RO4003C substrates used in this work. The authors also thank Jesús Ibarra and Benjamín Ramírez for their assistance in the S-parameters measurements.

De-embedding differential noise figure using the correlation of output noise waves

Yogadissen Andee*†, Caroline Arnaud*†, François Graux‡ and François Danneville§
*Univ. Grenoble Alpes, F-38000 Grenoble, France
†CEA, LETI, MINATEC Campus, F-38054 Grenoble, France
Email: yogadissen.andee@cea.fr
‡Rohde&Schwarz, 9-11, rue Jeanne Braconnier, 92366 Meudon-la-Forêt, France
§IEMN, UMR CNRS 8520, Av Poincaré, BP 60069, 59652 Villeneuve d'Ascq cedex, France

***Abstract*—This paper presents a measurement technique for de-embedding the noise figure of all sorts of differential amplifiers having arbitrary common-mode rejection. It is based on the measurement of the correlation of the noise waves at the output ports of the differential amplifier. It makes use of a hybrid coupler and takes into account the phase and amplitude imbalances of the latter. Measurement results of a radio-frequency low-noise amplifier demonstrate the validity of this general technique.**

***Index Terms*—Differential amplifier, noise figure measurement, noise correlation, four-port Network Analyzer**

I. Introduction

Differential circuits are increasingly designed for radio-frequency and other high-frequency applications, taking advantage of their immunity against common-mode noise and interference. While the small-signal behavior of these circuits can be easily characterized using 4-port Network Analyzers [1], it is more difficult to determine their noise performances. The noise figure measurement of differential circuits is a challenging subject, particularly due to the correlation of output noises. In literature, authors of [2] have dealt with the subject by connecting $180°$ hybrid couplers at the input and output ports of a differential amplifier. This technique is interesting as measurements can be done in a single-ended configuration using classical 2-port equipment. However, this de-embedding method assumes a simplified model of the coupler, with symmetrical losses and ideal $180°$ phase difference between the output ports. With this simplified coupler model, only differential-mode signals are propagated so the effect of common-mode signals are not taken into account. In [3], a more accurate procedure to de-embed the noise performance of differential amplifiers is proposed. It takes into account the phase imbalances or asymmetrical amplitude responses of the couplers. This technique is however valid only for specific differential amplifiers: balanced amplifiers and fully-differential amplifiers.

This paper proposes a general technique to de-embed the noise figure of all sorts of differential amplifiers having arbitrary common-mode rejection. It is based on the measurement of the correlation of the noise waves at the output ports of the differential amplifier. It makes use of a $180°$ hybrid coupler and takes into account the phase and amplitude imbalances of the latter.

The relation between differential noise and correlation of output noise waves is briefly presented in section II. The de-embedding technique is developed in section III. The test setup and measurement results are dealt with in section IV and concluding remarks are given in section V.

II. Theory

An analytical expression of the differential noise figure of a 4-port device is given in [4]. This expression is derived from the noise-wave formalism [5], shown in Fig. 1, and the mixed-mode S-parameters described in [1]. The expression of the noise figure is valid for a system where the sources and the loads are reflectionless ($\Gamma_i = 0$).

The differential noise figure given in [4] is:

$$F_{diff} = \frac{\overline{|b_3|^2} + \overline{|b_4|^2} - 2\Re e(\overline{b_3 \cdot b_4^*})}{2kT_0\Delta f\left(|S_{dd21}|^2 + |S_{dc21}|^2\right)} \tag{1}$$

where S_{dd21} and S_{dc21} are the mixed-mode gains which can be calculated from the classical S-parameters [1]. The term $kT_0\Delta f\left(|S_{dd21}|^2 + |S_{dc21}|^2\right)$ is the output noise power of the differential mode due to the two input sources. These two sources have both an available noise power of $kT_0\Delta f$ and are uncorrelated. $\overline{|b_3|^2}$ and $\overline{|b_4|^2}$ are the output noise powers at port 3 and 4 respectively. The term $\overline{b_3 \cdot b_4^*}$ represents the correlation between the output noise waves. It is the only term that cannot be measured using commercially-available equipment.

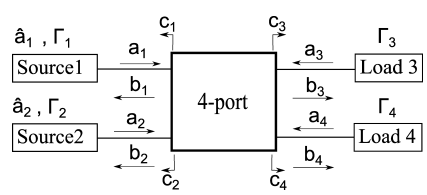

Fig. 1. Noise wave formalism for a 4-port circuit, where a_i is incident noise wave at port i, b_i is the outgoing noise wave and c_i is the internal noise wave. The input ports are connected to 2 sources with generator wave $\hat{a}_i$ and reflection coefficient of Γ_i.

The aim of this work is to develop a technique that measures the exact correlation of the noise waves at the output ports. And based on this measured correlation, the differential noise figure is thereby determined.

978-1-4799-8887-7/15/$31.00 ©2015 IEEE

III. De-embedding technique

The technique consists of connecting a 180° hybrid coupler to the output ports of the differential amplifier. The noise wave at the output of a non-ideal 0/180° hybrid coupler connected to a differential amplifier, as shown in Fig. 2, is given by:

$$b_{out} = S_{31}\, b_3 + S_{32}\, b_4 + c_3 \tag{2}$$

where S_{31} and S_{41} represent the singled-ended scattering parameters of the coupler. b_3 and b_4 are the noise waves at the outputs of the differential amplifier. c_3 is the noise wave generated by the hybrid coupler at its output port. This equation is valid for a system where the components (amplifier and coupler) are considered to be reflectionless. In our study, only components having high input and output return losses are used in order to verify the previous equation. The more general case for components having low return losses will be developed in future work.

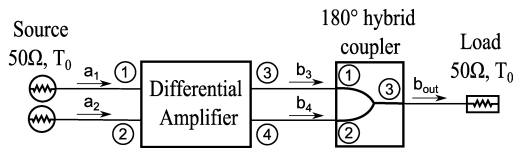

Fig. 2. Configuration 1: The output ports 3 and 4 of the amplifier are connected respectively to the input ports 1 and 2 of the coupler

The output noise power is calculated from (2) by:

$$\begin{aligned}\overline{|b_{out}|^2} &= \overline{b_{out}\cdot b_{out}^*}\\ &= |S_{31}|^2\overline{|b_3|^2} + |S_{32}|^2\overline{|b_4|^2}\\ &+ 2\Re e\left(S_{31}\cdot S_{32}^*\,\overline{b_3\cdot b_4^*}\right) + \overline{|c_3|^2}\end{aligned} \tag{3}$$

where $\overline{|c_3|^2}$ is the noise power generated by the coupler at its output port 3. This noise power can be calculated by Bosma's theorem [6] which states that the noise wave correlation matrix of a passive multiport can be derived directly from the scattering matrix as follows:

$$C_s = kT(I - SS^\dagger) \tag{4}$$

where k is Boltzmann's constant and T is the physical temperature in kelvin. In the case of the hybrid coupler which is a passive 3-port, $\overline{|c_3|^2}$ is given by:

$$\overline{|c_3|^2} = kT_0\Delta f(1 - (|S_{31}|^2 + |S_{32}|^2 + |S_{33}|^2)) \tag{5}$$

As the coupler is considered to have a high output return loss, $|S_{33}|^2$ is negligible compared to the transmission parameters.

The aim of the work is to determine $\Re e(\overline{b_3\cdot b_4^*})$ the real part of correlation term.
Let $\alpha = 2\Re e\left(S_{31}\cdot S_{32}^*\,\overline{b_3\cdot b_4^*}\right)$, α is calculated from (3) and (5).

$$\begin{aligned}\alpha = &\overline{|b_{out}|^2} - |S_{31}|^2\overline{|b_3|^2} - |S_{32}|^2\overline{|b_4|^2}\\ &- \left(1 - (|S_{31}|^2 + |S_{32}|^2)\right) kT_0\Delta f\end{aligned} \tag{6}$$

It depends on the scattering parameters and on the output noise powers $\overline{|b_3|^2}$ and $\overline{|b_4|^2}$ which can all be measured with a network analyzer. α can be expressed in terms of the correlation term as follows:

$$\begin{aligned}2\Re e\left(S_{31}\cdot S_{32}^*\,\overline{b_3\cdot b_4^*}\right) &= 2\Re e(S_{31}\cdot S_{32}^*)\Re e(\overline{b_3\cdot b_4^*})\\ &- 2\Im m(S_{31}\cdot S_{32}^*)\Im m(\overline{b_3\cdot b_4^*})\end{aligned} \tag{7}$$

α depends on both the real part and the imaginary part of the correlation term. As the real and imaginary parts are 2 unknown terms, another equation is necessary.

This equation is found by using another configuration. The output ports 3 and 4 of the amplifier are connected respectively to the input ports 2 and 1 of the coupler, as shown in Fig. 3.

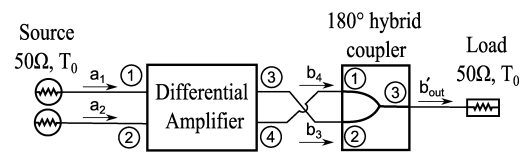

Fig. 3. Configuration 2: The output ports 3 and 4 of the amplifier are connected respectively to the input ports 1 and 2 of the coupler

In this configuration, the output noise wave is given by:

$$b'_{out} = S_{31}\, b_4 + S_{32}\, b_3 + c_3 \tag{8}$$

The output noise power is given by:

$$\begin{aligned}\overline{|b'_{out}|^2} &= |S_{31}|^2\overline{|b_4|^2} + |S_{32}|^2\overline{|b_3|^2}\\ &+ 2\Re e\left(S_{31}\cdot S_{32}^*\,\overline{b_3\cdot b_4^*}\right) + \overline{|c_3|^2}\end{aligned} \tag{9}$$

Let $\alpha' = 2\Re e\left(S_{32}\cdot S_{31}^*\,\overline{b_3\cdot b_4^*}\right)$, α' is calculated from (9) and (5).

$$\begin{aligned}\alpha = &\overline{|b_{out}|^2} - |S_{31}|^2\overline{|b_4|^2} - |S_{32}|^2\overline{|b_4|^2}\\ &- \left(1 - (|S_{31}|^2 + |S_{32}|^2)\right) kT_0\Delta f\end{aligned} \tag{10}$$

As α, α' depends on the the noise powers and scattering parameters which can be easily measured using commercially-available network analyzers. α' can be expressed in terms of the correlation term as:

$$\begin{aligned}2\Re e\left(S_{32}\cdot S_{31}^*\,\overline{b_3\cdot b_4^*}\right) &= 2\Re e(S_{32}\cdot S_{31}^*)\Re e(\overline{b_3\cdot b_4^*})\\ &- 2\Im m(S_{32}\cdot S_{31}^*)\Im m(\overline{b_3\cdot b_4^*})\\ &= 2\Re e(S_{31}\cdot S_{32}^*)\Re e(\overline{b_3\cdot b_4^*})\\ &+ 2\Im m(S_{31}\cdot S_{32}^*)\Im m(\overline{b_3\cdot b_4^*})\end{aligned} \tag{11}$$

The real part of the correlation is determined from (7) and (11):

$$\Re e(\overline{b_3\cdot b_4^*}) = \frac{\alpha + \alpha'}{4\Re e(S_{31}\cdot S_{32}^*)} \tag{12}$$

The differential noise figure is then calculated using (1) and (12).

The equations and procedure have been successfully verified by circuit simulations in Keysight's Advanced Design System.

IV. Measurement setup and experimental results

A. Measurement procedure

This new method is tested on a Rohde&Schwarz radio-frequency differential low noise amplifier (LNA). It has a differential gain of at least 10dB and a common-mode rejection of at most 3dB in the frequency range of 50MHz to 500 MHz, as shown in Fig. 4. A low common-mode rejection is chosen in order to demonstrate that the technique works for arbitrary CMRR. The amplifier has differential 100Ω input and output impedances. The input and output return losses are of at least 15dB. The 4 ports are interfaced with 50Ω SMA connectors which allow measurements with standard 50Ω equipment.

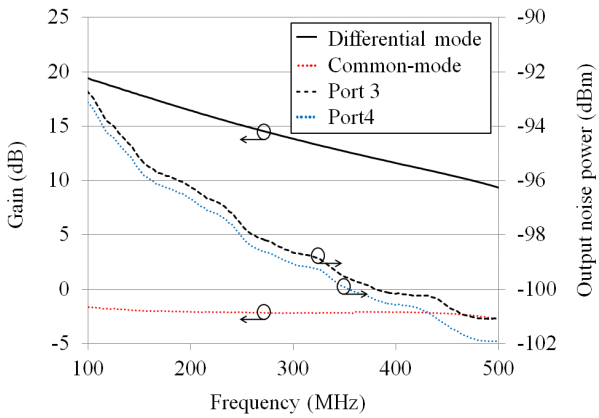

Fig. 4. Mixed-mode gains measured using a Rohde&Schwarz ZVA24 Network Analyzer

1) Noise power measurement at the output ports of the differential amplifier: Two 50Ω sources of a Rohde&Schwarz 4-port Network Analyzer at a noise temperature of $T_0 = 290K$ are connected to the input ports of the amplifier. The output noise powers are measured using 2 receivers of the network analyzer, as shown in Fig. 5. Two low-noise pre-amplifiers of Kuhne Electronic are used to improve the accuracy of the measurements. The measurement uncertainty depends significantly on the noise figure of the receivers [7]. The receivers of the network analyzer have a noise figure of around 40dB. This high noise figure tends to mask the noises generated by the amplifier. The effective noise figure of the receivers are therefore reduced by about 25dB as the pre-amplifiers have a gain of 25dB and a noise figure of 4dB. The uncertainty in the noise power measurements is consequently decreased. After a noise calibration has been performed on the VNA, the output noise powers are measured using the RMS detectors of the receivers. The noise powers measured at the output ports 3 and 4 of the differential LNA are shown in Fig. 4.

2) Noise power measurement for configuration 1: A $180°$ hybrid coupler is then connected to the differential amplifier according to the configuration 1, where the output ports 3&4 of the amplifier are connected respectively to the input ports 1&2 of the coupler. The block diagram of the setup is shown in Fig. 6. A photograph of the measurement setup is also presented in Fig. 7.

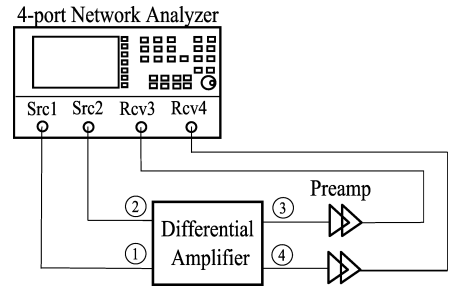

Fig. 5. Measurement setup for the output noise powers

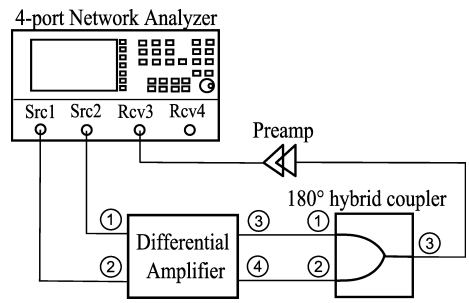

Fig. 6. Measurement setup for configuration1

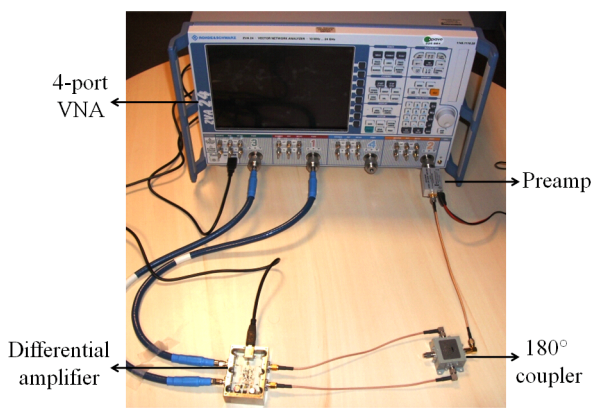

Fig. 7. Photograph of the measurement setup

A UMCC $180°/3dB$ hybrid coupler is used. Its insertion losses, gain and phase imbalances are characterized using the ZVA24 Network analyzer. These characteristics are shown in Fig. 8. The input and output return losses and the isolation are of at least 20dB.The input ports of the 3-port system (amplifier + coupler) are terminated by two 50Ω sources and the noise power at the output of the system is measured with the Network analyzer. As explained previously, a pre-amplifier is used to guarantee the accuracy of the measurements.

3) Noise power measurement for configuration 2: The last step of the measurement procedure consists of connecting the hybrid coupler according to configuration 2. The output ports 3 and 4 of the amplifier are connected respectively to the input ports 2 and 1 of the coupler, as shown in Fig. 9. The noise power at its output port 3 is measured with the analyzer.

The output noise powers and the S-parameters of the coupler

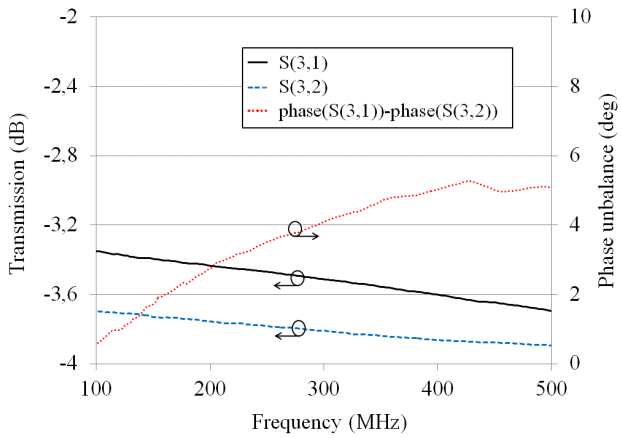

Fig. 8. Measured transmission parameters and phase imbalance of the coupler

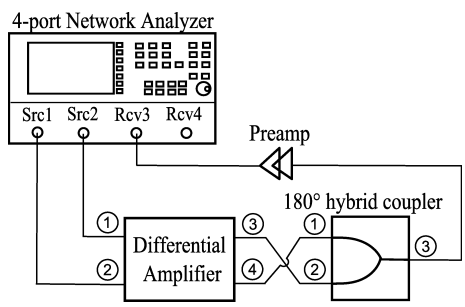

Fig. 9. Measurement setup for configuration2

measured during these steps are used to determine the real part of the correlation of the output noise waves using (12). The real part of the correlation, Fig. 10, is injected in (1) for the calculation of the differential noise figure. The differential noise figure is compared to the noise figure obtained with technique [2].

B. Evaluation of measurement results

A differential noise figure of 3.9 to 4.5dB is measured in the frequency bandwidth of 100 to 500 MHz, as shown in Fig. 10. For completeness, the differential noise of the LNA is also de-embedded using two 180° hybrid couplers and a measurement procedure proposed in [2]. A differential noise figure of 3.3 to 4 dB is obtained. The noise figures given by both techniques are of the same order of magnitude. There are somehow some differences which are partly caused by the measurement uncertainties which depend on multiple factors such as the noise figure of the receivers and the small-signal characteristics of the amplifier and the couplers. However, the main reason for such deviations comes from the simplifications made in [2]. Indeed, in [2], the couplers are assumed to have symmetrical paths as their phase and amplitude imbalances are neglected. It has been demonstrated in [3] that neglecting these imbalances bring some errors. Our de-embedding methodology does not yield these errors as the dissymmetry of the coupler is taken into account.

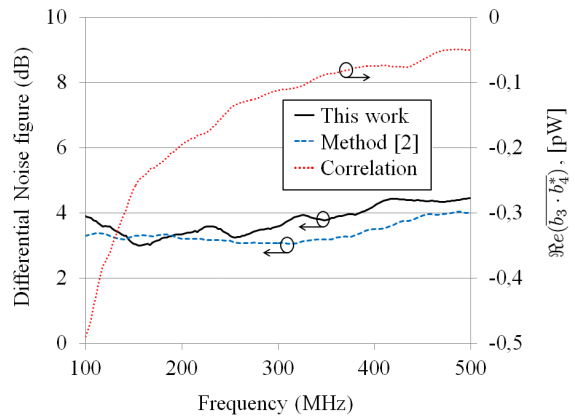

Fig. 10. Comparison between the three different methods

V. Conclusion

A de-embedding technique for the noise figure of differential amplifiers is proposed. It is based on the measurement of the correlation of the noise waves at the output ports of the amplifier. This approach uses a 180° hybrid coupler at the output ports of the differential amplifier. A de-embedding methodology that considers the non-ideal characteristics of the coupler is described. Measurements of a differential low-noise amplifier using a 4-port Network Analyzer have proved the validity of our new method. Future research can be oriented toward improving this theoretical study, by considering differential amplifiers with arbitrary (non-100Ω) input and output impedances.

References

[1] D. E. Bockelman and W. R. Eisenstadt, "Combined differential and common-mode scattering parameter": Theory and simulation," *IEEE Trans. Microw. Theory Tech.*, vol. 43, no. 7, 1995, pp. 1530-1539, Jul. 1995.

[2] A. Abidi and J. Leete,"De-embedding the noise figure of differential amplifiers," *IEEE J. Solid-State Circuits*, vol. 34, no. 6, pp. 882-885, Jun. 1999.

[3] O. Garcia-Perez, L. E. Garcia-Munoz, V. Gonzalez-Posadas and D. Segovia-Vargas, "Noise-Figure Measurement of Differential Amplifiers Using Nonideal Baluns," *IEEE Trans. Microw. Theory Tech.*, vol. 59, no. 6, pp. 1658-1664, Jun. 2011.

[4] Y. Andee, J. Prouvée, F. Graux and F. Danneville, "Determination of noise figure of differential circuits using correlation of output noise waves,"*Electronic Letters*, vol. 50, no. 9, pp. 665-667, Apr. 2014.

[5] J. Randa,"Noise characterization of multiport amplifiers," *IEEE Trans. Microw. Theory Tech.*, vol. 49, no. 10, pp. 17571763, Oct. 2001.

[6] H. Bosma, "On the theory of linear noisy systems," *Ph.D. dissertation*, Dept. Elect. Eng., Eindhoven Univ. Technology, Eindhoven, The Netherlands, 1967

[7] L. Colby and B. Heinz, "Accuracy of Noise Figure Measurement Systems,"*RF & Microwave Symposium and Exhibition, Hewlett Packard*, 1988.

A Simple Adaptive Method of Antenna Frequency Parameters Measurements with Local Reflections

Aleksandr A. Savin[1], Vladimir G. Guba[2], and Olesia N. Bykova[2]

[1]*Tomsk State University of Control Systems and Radioelectronics, 634050, Tomsk, Russia*
[2]*NPK TAIR, a subsidiary of Copper Mountain Technologies, 634041, Tomsk, Russia*

Abstract — This article presents an adaptive method for antenna reflection and transmission parameters measurements using a calibrated vector network analyzer without an anechoic chamber. The method is based on a special distance-frequency system model simulating signals of local reflectors. Antenna parameters are extracted from measurement results by using a special estimation algorithm based on the least mean squares method. Experiment was performed and verified the proposed method. Software implemented this method is developed.

Index Terms — S-parameters, vector network analyzer (VNA), antenna measurements, least mean squares (LMS) algorithm.

I. Introduction

For wireless communication devices the number of which is continuously increasing the key element is an antenna. Its characteristics define the quality of the whole device.

Useful information of the antenna under test (AUT) can be realized either in indoor or outdoor ranges [1]. Indoor range consists in an anechoic chamber with one reference antenna and the AUT. An anechoic chamber with precision metrological parameters is difficult and so expensive to build. But there are some problems in outdoor range also. The outdoor range is sensitive to reflections.

This work introduces an adaptive estimation algorithm that could allow to refuse expensive operation with anechoic chamber, along with eliminating spurious local reflections in outdoor range.

II. System Model and Observed Signals

The main antenna measurement unit is a precision PC-driven vector network analyzer (VNA). PC-driven VNAs increase productivity and lower costs for test, control, and design applications. The VNA consists of transmitting and receiving systems. Let, AUT is connected to first port of the calibrated VNA, and reference antenna is connected to second port of the calibrated VNA (Fig. 1). Forward direction is enough to get information about the reflection and transmission parameters. Cables must be used to connect the antennas to the VNA.

The model of outdoor instrumentation system contains several terms. These terms describe the basic and additional signals. The additional signals arise because there are reflections. Reflected signals arise from local objects such as external metallic elements of the VNA, reference antenna and so on. These signals are separated in the time domain. Note that multiple reflections are possible. The characteristics of signals are individually unknown.

For this model, the measured signal of z can be described as the sum of four components, for example:

$$z = B + A_1 + A_2 + n\,, \qquad (1)$$

where B is the basic signal; A_1 and A_2 are the two additional signals; and n is additive noise. Frequency characteristic of B is equal to the antenna reflection (for S_{11} measurements) or transmission (for S_{21} measurements) parameters. The additional signals distort the measured S-parameters. The measurements are processed to obtain the required estimates of B.

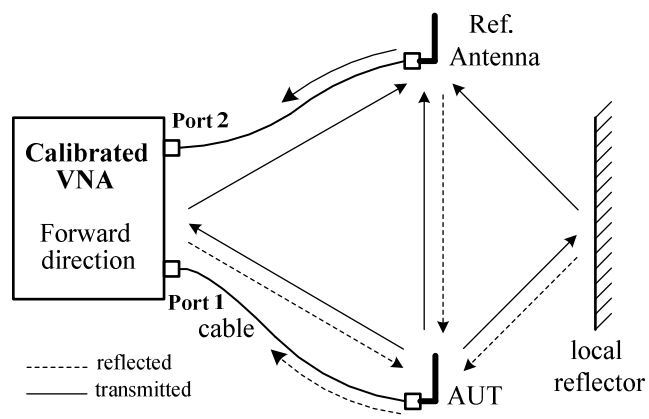

Fig. 1. Representation of the antenna measurement system. Solid lines indicate transmitted signals. Dotted lines indicate reflected signals.

We describe the antenna measurement system in the time domain as a set of three signals (for this example). The system may be expanded to more regular signals. Each signal has known distance (time delay) and unknown frequency characteristics. Fig. 2 shows the set of samples for B (reference values B_1, B_2, B_3, B_4) and all A (reference values A_1, A_2, A_3, A_4) signals in the distance-frequency plane. A similar model is also used for VNA verification [2-6], and navigation signal generator calibration [7]. The components of z can be separated using Fourier analysis.

978-1-4799-8887-7/15/$31.00 ©2015 IEEE

In Fig. 2, f_1 is the start frequency, while f_2, f_3 and f_4 are other reference frequencies, Δf is the frequency step between samples, l_B is the distance of B from the reference plane of VNA, l_1 is the distance of A_1, and l_2 is the distance of A_2 from the reference plane of VNA.

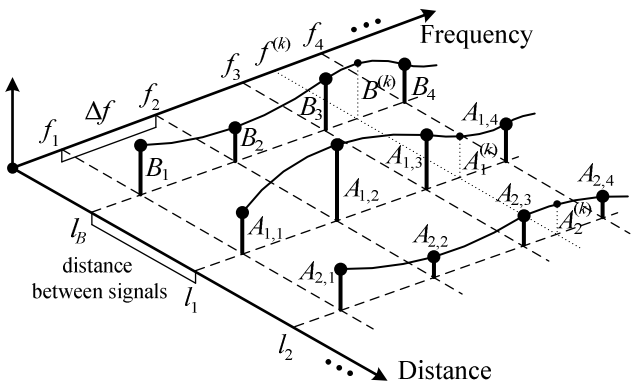

Fig. 2. Distance-frequency model of the measurement system.

The reference calibration plane is located on the end of the cable. The value of l_B is equal to 0 for reflection measurements; and l_B is close to distance between antennas for transmission measurements. The values of l_1 and l_2 are determined by propagation distance between AUT and local reflectors, including the VNA

Sampling function is used to interpolate the frequency characteristics of the signals and to calculate $B^{(k)}$, and all $A^{(k)}$ (measurement frequency point is $f^{(k)}$). Fig. 3 shows the interpolation procedure.

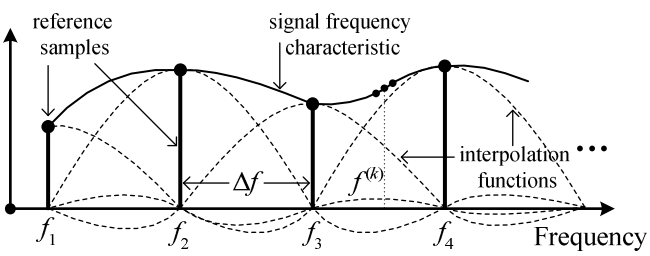

Fig. 3. Set of reference samples and interpolation functions.

The number of reference frequency points N for each signal depends on the frequency range and the frequency step Δf. So, the vector of B consists of N unknown complex constants:

$$\mathbf{B} = \begin{bmatrix} B_1 & B_2 & \dots & B_N \end{bmatrix}^{\mathrm{T}}, \tag{2}$$

the vector of A_1 consists of N unknown complex constants:

$$\mathbf{A}_1 = \begin{bmatrix} A_{1,1} & A_{1,2} & \dots & A_{1,N} \end{bmatrix}^{\mathrm{T}}, \tag{3}$$

Similarly, $\mathbf{A}_2$ can be defined. Note that the model of measurement system may be expanded to more additional signals. The system state vector of $\mathbf{x}$ consists of all unknown parameters of B and A. Coordinates of the state vector are not changed when the VNA measurement samples received. In this model the system state vector is constant:

$$\mathbf{x} = \begin{bmatrix} \mathbf{B}^{\mathrm{T}} & \mathbf{A}_1^{\mathrm{T}} & \mathbf{A}_2^{\mathrm{T}} & \dots \end{bmatrix}^{\mathrm{T}}, \tag{4}$$

The total number of unknown variables is $(K+1)\cdot N$, where K is the number of additional signals. Estimates of the unknown variables can be made from measurements. On the k-th step, dependence of observations $\mathbf{z} = [z^{(1)}\ z^{(2)}\ \dots\ z^{(k)}\ \dots]^{\mathrm{T}}$ on the state vector $\mathbf{x}$ coordinates can be written as:

$$z^{(k)} = B^{(k)} \exp(-j2\pi f^{(k)} l_B / c) + \\ + \sum_{i=1}^{2} A_i^{(k)} \exp(-j2\pi f^{(k)} l_i / c) + n^{(k)}, \tag{5}$$

where $f^{(k)}$ is the current frequency; $c = 3\cdot 10^8$ m/s. An accurate estimates of l_1 and l_2 is not required because complex A. The frequency step between measurements $[f^{(k+1)} - f^{(k)}]$ is less than Δf. To obtain an accurate solution, the value of Δf was selected as:

$$\Delta f = c / \Delta l, \tag{6}$$

where Δl is average of the distances differences.

III. Algorithm

The algorithm for estimating the frequency characteristics of basic and additional signals was developed using the least mean squares method.

The observed signals are interrelated by complex linear expression with the vectors $\mathbf{x}$ from (4). A result can write in a general form:

$$\mathbf{z} = \mathbf{C} \cdot \mathbf{x} + \mathbf{n}, \tag{7}$$

where $\mathbf{n}$ is the vector of measurement noise, and $\mathbf{C}$ is a interpolation matrix. The matrix $\mathbf{C}$ is formed on sampling function and known distances:

$$\mathbf{C} = \begin{bmatrix} \mathbf{W}_B & \mathbf{W}_1 & \mathbf{W}_2 & \dots \end{bmatrix}, \tag{8}$$

where the number of rows of $\mathbf{W}$ matrices is equal to the total number of measurements; the number of columns of $\mathbf{W}$ is equal to N. The element of $\mathbf{W}$ matrices on the k-th row and i-th column is:

$$W^{(k,i)} = \mathrm{sinc}[(f^{(k)} - f_i)/\Delta f] \cdot \exp(-j2\pi f^{(k)} l / c), \tag{9}$$

where $f^{(k)}$ is the measurement frequencies; f_i is the reference frequencies; Δf is the frequency step between reference samples; $l = l_B$ for $\mathbf{W}_B$; $l = l_1$ for $\mathbf{W}_1$ etc.

The solution of the equation (7) for the vector $\mathbf{x}$ with the least mean squares (LMS) method is:

$$\hat{\mathbf{x}} = \left(\mathbf{C}^{\mathrm{H}} \cdot \mathbf{C}\right)^{-1} \cdot \mathbf{C}^{\mathrm{H}} \cdot \mathbf{z}, \tag{10}$$

where H is the operator of Hermitian transpose.

Estimates of the frequency characteristics of each signal must be obtained using the estimates of **x** and the same type of interpolation.

IV. Experimental Results and Discussion

Qualitative experimental studies of the algorithm were performed. The experimental setup included Planar 304/1 VNA [8]. The system was calibrated using the full two-port Short-Open-Load-Adapter method. Studies were conducted in coaxial waveguide with 3.5mm connector coaxial environment, for the frequency range from 10 MHz to 3.2 GHz (in frequency steps of 10 MHz). The intermediate frequency filter band was configured at 100 Hz, with a signal level of -10 dBm.

Fig. 4 demonstrates the measurement setup. The distance between the antennas is 0.7 m. The length of the cable is 0.6 m for first and second ports of the VNA. The VNA size is 0.25 by 0.4 m. Note, for qualitative studies we used two identical 8.5 cm long antennas. The antennas are available with the frequency band 850/900 MHz.

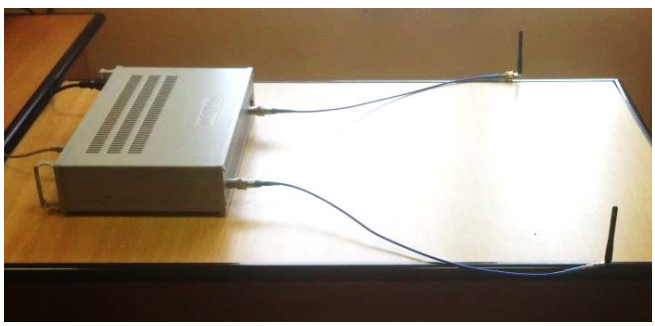

Fig. 4. Photo of the measurement setup.

The measurements were taken for forward directions. Inverse Fourier transformation was performed. The results are shown in Fig. 5 and Fig. 6.

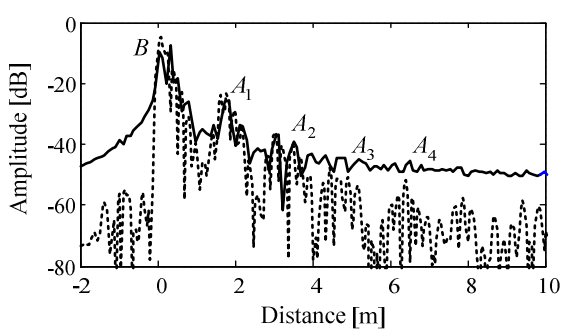

Fig. 5. Reflection time domain diagrams. Solid line is for band pass mode. Dotted line is for low pass mode with Nuttall window.

The residual directivity of the VNA is less than -50 dB (close to distance point of 0 m in Fig. 5). The basic (B) and four additional (A) signals can be identified in the time domain diagrams.

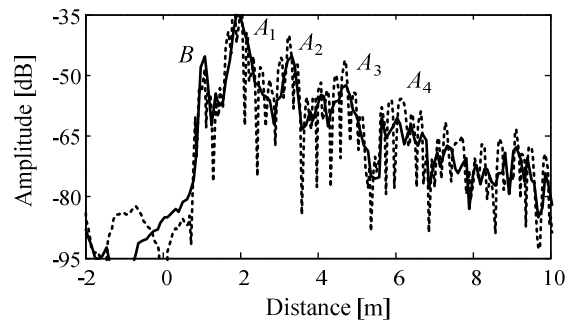

Fig. 6. Transmission time domain diagrams. Solid line is for band pass mode. Dotted line is for low pass mode with Nuttall window.

As show in Fig. 5, the estimates of distances are equal to $l_B = 0$ m; $l_1 = 1.7$ m; $l_2 = 3.4$ m; $l_3 = 4.8$ m; and $l_4 = 6.4$ m. As show in Fig. 6, the estimates of distances are equal to $l_B = 0.9$ m; $l_1 = 1.8$ m; $l_2 = 3.2$ m; $l_3 = 4.5$ m; and $l_4 = 6.2$ m.

The algorithm of (10) was applied to process the measurements in the frequency domain. The frequency step between reference samples was $\Delta f = 200$ MHz. Processing of the reflection and transmission measurements are separately performed by using the corresponding estimates of distances. In the frequency range, the total number of complex unknowns is 85 ($N = 17$) for each type of measurement.

The results of the algorithm were complex estimates of the partial signals. The estimates were obtained from all 320 frequency points. The minimum mean square error at each point was the criterion for obtaining estimates. Results are given in Fig. 7-10.

In Fig. 7 we compare the estimated and the measured reflection coefficients of the AUT. Fig. 8 shows the frequency characteristics of the additional signals.

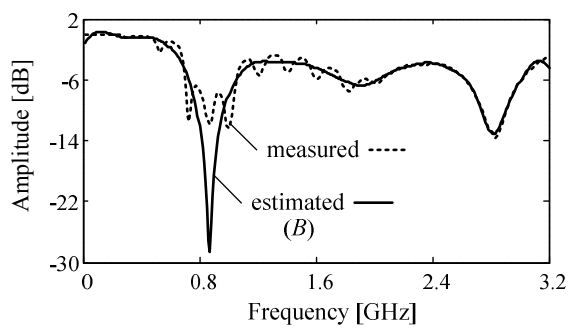

Fig. 7. Comparison of the estimated reflection coefficient (solid line) and the measured reflection coefficient of the AUT (dotted line).

The ripples of the measured reflection are reduced after the adaptive method. An increase of estimates at the edges of the frequency range is due to the type of interpolation. The minimum value of the estimated reflection coefficient is located at a frequency of 870 MHz.

In the following, we compare the estimated and the measured transmission parameters (Fig. 9). Fig. 10 shows the amplitudes of the additional signals.

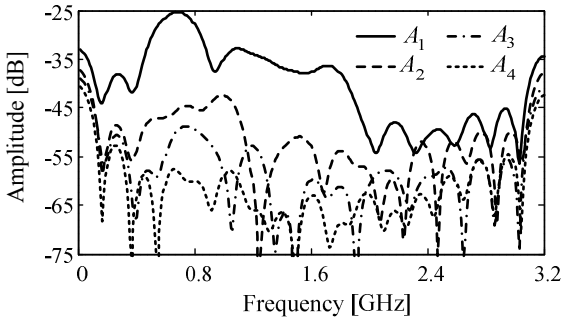

Fig. 8. The estimated signals of local reflectors for reflection measurements.

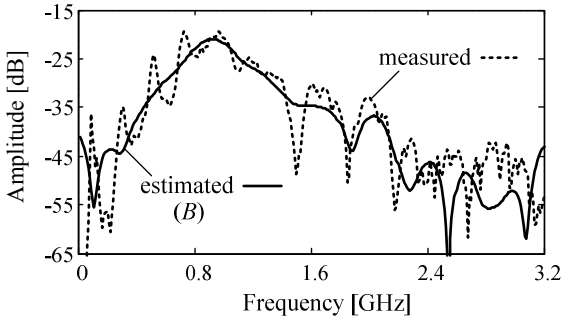

Fig. 9. Comparison of the estimated transmission parameter (solid line) and the measured transmission parameter (dotted line).

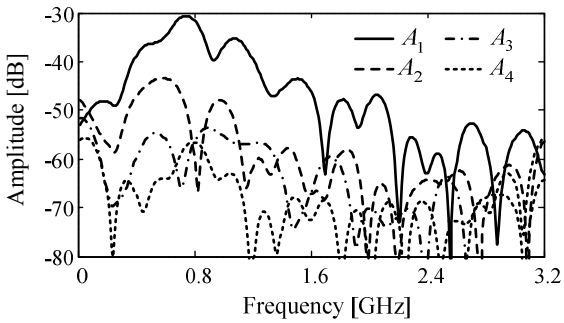

Fig. 10. The estimated signals of local reflectors for transmission measurements.

The ripples of the measured transmission are reduced after the adaptive method. The maximum value of the estimated transmission parameter is -20.98 dB. This value is located at a frequency of 920 MHz. For these conditions, the free-space loss is 28.63 dB.

The algorithm makes a joint estimation of the basic and additional signals (or additional signal is removed from the antenna frequency parameters measurements). The noises are also smoothed. The ripples are reduced after the new method. The reference antenna and the AUT can be raised above the table that can improve the accuracy.

The measurements can be performed in an arbitrary frequency band. In this case, the developed algorithm can also use and the estimates can be obtained for this band [2, 9].

V. Conclusion

Summarizing this work, a new adaptive method was introduced and verified for antenna parameters measurements with local reflections. The method is based on the least mean squares algorithm. The algorithm significantly reduces both the measurement time and the cost of the measurement procedure. Experiment demonstrated suitability of the new method for antenna parameters measurements. Relative to the other algorithm, software using the least mean square algorithm is much simpler to develop. There is no need for an anechoic chamber. Model of measurement system may be expanded to more reflected signals. Consequently, this new method can be of a special interest for cost-effective antenna-range instrumentation.

Acknowledgements

The authors thank Sergey Zaostrovnykh and Alex Goloschokin from Copper Mountain Technologies, Indiana, USA for support of this work and for their helpful discussions.

The work was supported by Russian Foundation for Basic Research RFBR Grant No. 14-07-31312, and Russian President Grant No. MK-3107.2015.8.

References

[1] C. A. Balanis, Antenna Theory, 3rd ed., John Wiley and Sons, Inc., New York, 2005.

[2] A. A. Savin, V. G. Guba, and B. D. Maxson, “Residual Errors Determinations for Vector Network Analyzer at a Low Resolution in the Time Domain,” *82nd ARFTG Microwave Measurement Conference*, 2013, Columbus, Ohio, USA, pp. 15-19.

[3] A. A. Savin, V. G. Guba, A. Rumiantsev, and B. D. Maxson, “Estimation of Complex Residual Errors of Calibrated Two-Port Vector Network Analyzer,” *83rd ARFTG Microwave Measurement Conference*, 2014, Tampa, Florida, USA, pp. 1-4.

[4] A. A. Savin, V. G. Guba, A. Rumiantsev, B. D. Maxon, D. Schubert, and U. Arz, “Adaptive Estimation of Complex Calibration Residual Errors of Wafer-Level S-Parameters Measurement System,” *84th ARFTG Microwave Measurement Symposium*, 2014, Boulder, Colorado, USA, pp. 1-4.

[5] A. A. Savin, “Linear processing of verification data of vector network analyzer for wafer-level application,” *Reports of TUSUR*, 2014, No. 3(33), pp. 53-57. (Russian)

[6] A. A. Savin, “A Novel Factor Verification Technique for One-Port Vector Network Analyzer,” *Proceedings of the 43rd European Microwave Conference*, 2013, Nuremberg, Germany, pp. 60-63.

[7] A. A. Savin, “Analyzer of the GNSS Simulators Parameters,” *IEEE International Workshop on Metrology for Aerospace ed.*, MAS-2014, 2014, Benevento, Italy, pp. 18-22.

[8] Planar 304/1. Vector Network Analyzers. Available: http://www.coppermountaintech.com/products/1/304/

[9] A. A. Savin, and V. G. Guba, “Method for Determining the Components of Systematic Error of Vector Network Analyzer in a Given Frequency Band,” *6th International Conference Acoustooptic and Radar Methods for Information Measurements and Processing*, 2013, Suzdal, Russia. (Russian)

Measurement Setup for X-Parameter Characterization of Bulk Acoustic Wave Resonators

W. Akstaller, A. Tag, C. Musolff, R. Weigel and A. Hagelauer
Institute for Electronics Engineering
University of Erlangen- Nuremberg
Cauerstr. 9, 91058 Erlangen, Germany
Email: wolfgang.akstaller@fau.de

***Abstract*— In this work a modern measurement method has been utilized in order to characterize nonlinear behavior of bulk acoustic wave (BAW) solidly mounted resonators (SMR). Unlike typical nonlinearity characterization methods, the method which was employed here not only records amplitudes, but also the phase of generated harmonics. Furthermore, the relations between the harmonics of different order are given. The modeling approach being used is the poly harmonic distortion (PHD) modeling approach, realized by the measurement of X-Parameters. For that purpose it was necessary to extend a nonlinear vector network analyzer (NVNA) by external components in order to enable high power measurements. Afterwards, several optimization steps were required to perform phase calibration. This difficulty arose due to the high power incident tones and steep resonator impedance curves on the one hand and the limited power provided by the phase calibration standard on the other hand.**

***Index Terms*—Nonlinear Vector Network Analyzer (NVNA), nonlinear characterization, X-parameters, Bulk Acoustic Wave (BAW)**

I. Introduction

Next generation RF frontends will more often make use of multiplexing techniques like carrier aggregation. As an important step towards a 5G standard, such approaches lead to higher data rates by simultaneously using several frequency bands for data transfer. Accordingly, RF frontends become more complex and at the same time the requirements on the linearity increase. Therefore, the demand for accurate modeling procedures enabling precise RF simulations is rising. One of the key components in mobile frontends is the RF filter unit within duplexers and multiplexers which is commonly implemented in acoustic filter technology. The simulation model of the RF filter has to be capable of describing not only the in-band but also the out-of-band behavior. Existing linear models quickly reach their limits and nonlinear models become necessary, because they take effects like intermodulation distortion (IMD) or the generation of harmonic frequencies into account. A behavioral model based on the poly harmonic distortion (PHD) principle can be created as a possible modeling approach.

In this work bulk acoustic wave (BAW) solidly mounted resonators (SMR) are investigated. For the PHD modeling approach, information about the relation of amplitudes and phases of linear spectral components and higher order harmonics dependent on the stimulating signal needs to be acquired. A measurement setup containing a nonlinear vector network analyzer (NVNA), which can measure the needed characteristics of passive one port resonators in BAW technology, is introduced in II. Possible optimization steps are shown in III and obtained measurement results are presented in IV. A conclusion is given in V.

II. Measurement Setup

The PHD modeling procedure is a behavioral model based upon the harmonic superposition principle. This principle states that a device under test (DUT), which is stimulated to nonlinear state by an incident tone (IT), relates additional inserted small signals at harmonic frequencies (called ET: extraction tone, 20 dB below IT, frequency $f = n f_{inc}$) linear to the output spectrum [1]. In practice, this can be used to characterize the response of the DUT to a harmonic input spectrum. This enables the experimenter to determine a set of various equations at different operating points which can describe the linear and nonlinear behavior of the DUT. To obtain this information a measurement setup is needed which has the ability to stimulate a DUT with both the IT and ET and can characterize magnitude and phase of the input and output spectrum.

The implemented measurement setup is based on the NVNA (Keysight PNA-X) and a measurement setup extension [2,3] which was originally designed for active DUTs like power amplifiers. The NVNA has to be modified as is shown in the following simplified figure (Fig. 1) in order to provide the required power levels for the characterization of the BAW resonator's nonlinearities. Therefore, connections of the internal sources on the back panel of the NVNA are attached, combined (C1) and amplified. After amplification, incoming and reflected waves need to be separated using the directional couplers C2 and C3. In order to avoid overdrive effects and not exceeding the maximum input power of the receivers R1 and A [3], it is necessary to reduce the power levels with attenuators in front of the receivers. The stimulating signal can be detected at receiver R1 and the reflected wave coming from the DUT is measured at receiver A.

978-1-4799-8887-7/15/$31.00 ©2015 IEEE

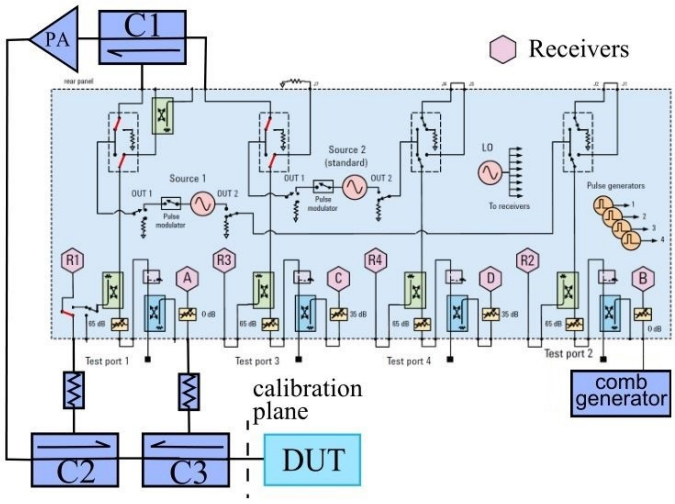

Fig. 1. Measurement setup for the characterization of the one port resonators consisting of the NVNA (Keysight PNA-X) and external circuitry.

Before the measurements can be taken, four different calibration steps have to be performed. These are vector calibration, receiver amplitude calibration, phase calibration and the calibration of the source power. Phase calibration is done by using a comb generator (Keysight U9393F) on receiver B and one on the calibration plane. The comb generator on receiver B is retained in the setup during measurement. With these calibration steps the NVNA is capable of measuring absolute power levels and the phase relations between harmonics of first and higher order. The calibrations are performed at the calibration plane. Further extension of the measurement setup with adapters or wires on the DUT's PCB needs to be considered additionally.

III. Optimization

BAW resonators are typically specified for power levels up to 30 dBm. As a trade-off between sufficient power levels and prevention of overdriving the receivers R1 and A, a value of 30 dB has been chosen for the attenuators in Fig. 1. Additionally, proper phase calibration for a reliable characterization of phase relation between harmonic frequencies requires an optimized measurement setup due to a low output power of the comb generators. Minimal and typical output power P_{out} for a frequency spacing of Δf = 10 MHz between measured points of the used comb generators is shown in Fig. 2 [4]. The minimal specified output power level is P_{out} = -95 dBm and the typical value is P_{out} = -77 dBm for a considered frequency range of 1.5 GHz to 8 GHz. Actual output power dependent on frequency spacing Δf can be calculated with (1) for the mentioned frequency range [3].

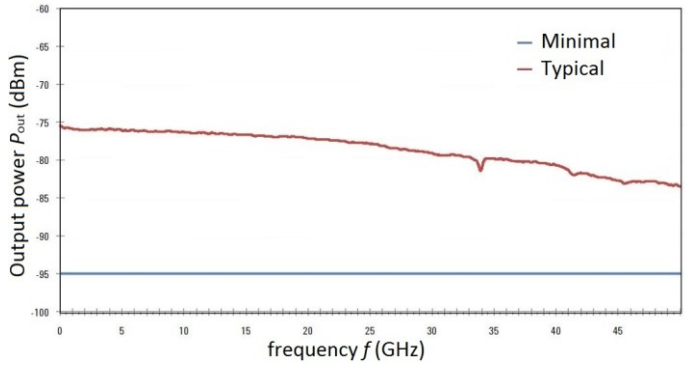

Fig. 2. Output power characteristic of comb generator Keysight U9393F [4].

$$P_{out} = -77\,\text{dBm} + 20\log\left(\frac{\Delta f}{10\text{MHz}}\right) \qquad (1)$$

A frequency spacing of Δf = 4 MHz results in an output power of P_{out} = -85 dBm and seems to be a good trade-off between output power of the comb generator and distance of measurement points to achieve a reasonable graphical resolution. A smaller Δf is even more desirable since BAW resonators have steep admittance curves and BAW filters have steep filter curves. But this would further decrease P_{out}.

The specified noise floor level of the receivers is typically -128 dBm for an IFBW of 10 Hz [3]. To decrease the noise floor level by 3 dB, IFBW has to be reduced to 5 Hz. This doubles the necessary time to calibrate and measure. Generally, for phase measurement and calibration, input power level of the receiver A has to be at least 20 dB and ideally between 30 dB and 40 dB above the noise floor level [3]. Because of the attenuation of the directional coupler C3 of 10 dB and the following 30 dB attenuator in front of the receiver A, the power level of the signal arriving at receiver A is -125 dBm and does not meet the requirement. A solution is to remove the attenuator in front of receiver A during the phase calibration. This increases the power level of the comb generator which reaches receiver A to -95 dBm. In the first step electrical behavior of the attenuator is characterized. Then, phase calibration is performed without the attenuator. Afterwards, the attenuator can be added back to the measurement setup and its influence on the phase calibration is mathematically considered.

In a nutshell, a combination of the optimization steps lead to a comb generator power level at receiver A of 36 dB above noise level during phase calibration. Thus, reproducible characterization of phase relations between first and higher order harmonics is possible.

IV. Measurement Results

In order to obtain only the characteristics of the BAW resonator, the delay of the PCB and the connectors were considered and removed by a RF design environment with the help of X-Parameter simulation [5]. Fig. 3 and Fig. 4 present the magnitude and phase of $S_{13,11}$, an exemplary parameter of the X-parameter data set, measured by using the optimized measurement setup.

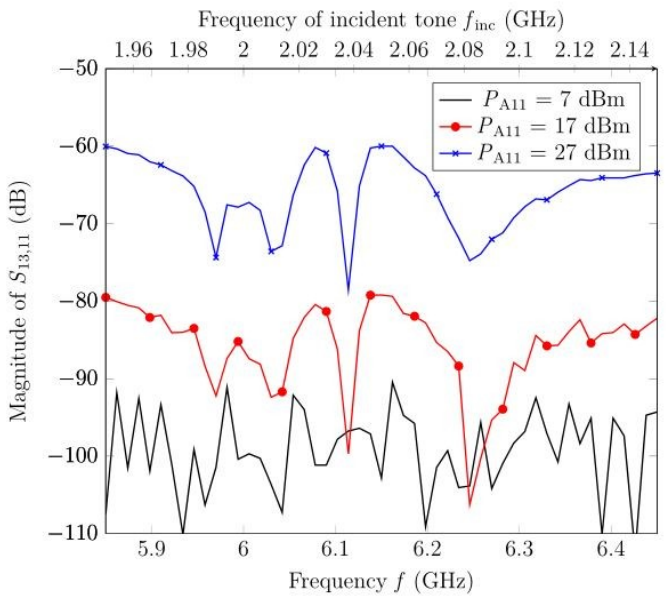

Fig. 3. Magnitude of $S_{13,11}$ for different power levels of IT P_{A11}.

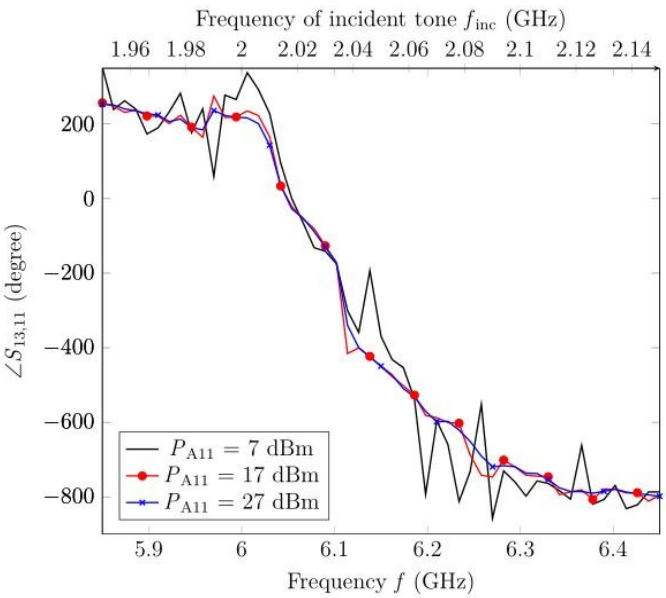

Fig. 4. Phase of $S_{13,11}$ for different power levels of IT P_{A11}.

These diagrams show the magnitude and phase characteristics of parameter $S_{13,11}$ over the frequency range from 5,85 GHz to 6,45 GHz. The indices p, q of parameter $S_{pq,mn}$ stand for port and number of the measured harmonic and m,n for port and number of the stimulating harmonic (ET). Therefore, $S_{13,11}$ is the characteristic of the third harmonic generated by stimulation with an ET at fundamental frequency f_{inc}. The measured magnitudes show similar curve forms. It seems that the distance between the $S_{13,11}$ curves increases proportionally to the increase of the incident power P_{A11}. The measured phases drop between 6 GHz and 6.4 GHz about 1000 degree. Strong influence of noise can be detected in the measurements with a low power level IT of P_{A11} = 7 dBm. Further measurement results are discussed in a publication [6].

V. Conclusion

A central issue was to find a condition of sufficient frequency-resolution because of the steep resonator characteristic and enabling the phase calibration despite limited output power of the phase references. Additionally, requirements of high power measurement had to be considered. For the reproducible characterization of amplitude and phase without undue influence of noise, several optimizations were elaborated. The attenuators were adjusted to find the optimum between sufficient signal level from the phase references during phase calibration and the prevention of overdriving the receivers R1 and A. IFBW was lowered in order to reduce the noise floor levels of the receivers. The distance between the measuring frequency points (frequency-resolution) was enlarged to increase the output power levels of the phase references. Additionally, the attenuator in front of receiver A could be removed during phase calibration. Its influence on the phase calibration was considered by providing the scattering parameters of the attenuator to the NVNA which can use them for a mathematical correction.

The measurement results show that despite all the challenges it is possible to characterize BAW resonators by X-Parameters. The additional information provided by the X-Parameters can be used to improve filter and multiplexer design in their nonlinear behavior [6].

References

[1] Jan Verspecht, David E. Root, “Polyharmonic Distortion Modeling”, IEEE Microwave Magazine, Vol. 7, 2006.

[2] Farhad Baytpur, Siamak Fouladi, Jong-Hoon Lee, Dong Shim, John Larson, David Feld, “Vectorial Measurement of the 2nd Harmonic Response of an FBAR Resonator”, IEEE International Ultrasonics Symposium Proceedings, 2013.

[3] Keysight Technologies, “High Power Amplifier Measurements Using Agilent’s Nonlinear Vector Network Analyzer, Application Note 1408-19, 5990-5039EN, 2010.

[4] Keysight Technologies, “Keysight U9391C/F/G Comb Generator – Technical Overview”, 5989-7619EN, 2014.

[5] Keysight Technologies, “Agilent De-embedding and Embedding S-Parameter Networks Using a Vector Network Analyzer”, Application Note 1364-1, 5980-2784EN, 2004.

[6] A. Tag, W. Akstaller, C. Musolff, B. Bader, M. Pitschi, R. Weigel, A. Hagelauer, “Polyharmonic Distortion Modeling of RF BAW Components“, International Microwave Symposium, 2015.

Effects of the effective efficiency of the thermistor mount with WR-22(33 to 50 GHz) microcalorimeter

Chao Ma, Xiaohai Cui, Wenze Yuan, and Yong Li

National Institute of Metrology, China, e-mail: machao@nim.ac.cn, cuixh@nim.ac.cn

***Abstract*—In this paper, the effective efficiency of the thermistor mount was evaluated by three WR-22 (33–50 GHz) rectangular waveguide microcalorimeters. Three sets of microcalorimeter were made from the same design drawing. The only difference among them was some key parts (thermal conductive plate and heat isolation section) coming from different manufactures. The relative deviation of measurement results of each microcalorimeter was within one percent. However, the evaluated effective efficiencies of same DUT were highly inconsistent for different microcalorimeters in some frequency points. The preliminary conclusion was that manufacturing process of microcalorimeter would be likely to affect the effective efficiency evaluation of the thermistor mount, and some necessary improvement works have been planned in near future.**

***Index Terms*—microcalorimeter, power measurement, thermistor mount, effective efficiency.**

I. Introduction

Microcalorimeters are used as the national primary standards for microwave and millimeter-wave power in many National Metrology Institutes (NMIs) [1][2]. A series of rectangular waveguide microcalorimeters, such as WR-28, WR-22, WR-15, WR-10, were developed by the National Institute of Metrology (NIM) of China, enhancing Chinese radio frequency power measurement capability up to 110 GHz[3]. And the WR-22 (33 to 50 GHz) rectangular waveguide microcalorimeter was taken part into international key comparison in 2012[4].

In order to further study for reducing the uncertainty, an additional couple of WR-22 rectangular waveguide microcalorimeters were manufactured in 2014, according to the previous design drawing.

For the comparison among the WR-22 microcalorimeters, the experiments were performed base on the same commercially thermistor mount (Hughes 45774H-1100), using the three WR-22 rectangular waveguide microcalorimeters respectively. However, the measurement results were highly inconsistent in some frequency points. In this paper, the experimental results from evaluation and validation will be discussed and presented.

This work was supported by National Science and Technology Supportting Program "Wireless Communication Power Measurement Standard and Traceability Technology Research" (2014BAK02B02).

II. Measurement Methodologies

The microcalorimeter is used to measure the effective efficiency of the thermistor mount. The effective efficiency is the ratio of the change in direct current (DC) power (or DC substitution power) to the absorbed millimeter-wave power. Any thermistor mount mentioned in this paper is a commercial thermistor sensor or "mount" and will be referred to as a device under test (DUT)[5].

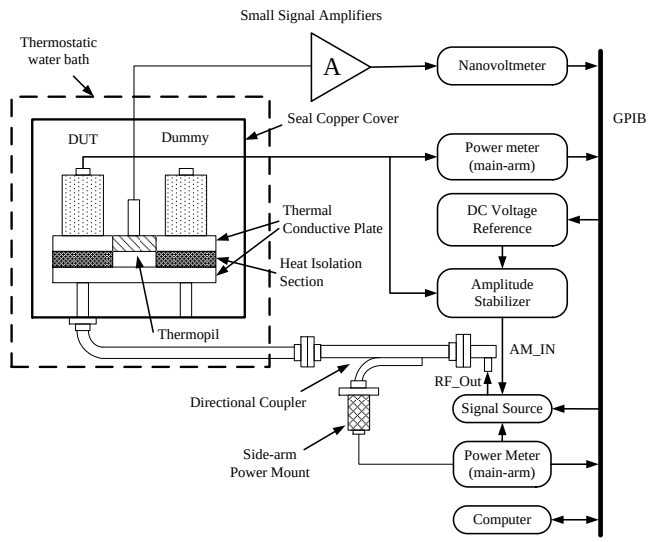

Fig. 1. Schematic diagram of the WR-22 (33 to 50 GHz) microcalorimeter at NIM

As introduced in [5], the effective efficiency at each frequency of interest can be calculated by the equation

$$\eta_e = g\frac{1-(\frac{V_2}{V_1})^2}{\frac{e_2}{e_1}-(\frac{V_2}{V_1})^2} = g\eta_{un} \tag{1}$$

Where η_e is the effective efficiency of the thermistor mount, g is the correction factor of the microcalorimeter, the V_1 and e_1 are the output voltages of the power meter and thermopile with only the DC applied to the mount, and V_2 and e_2 are the same voltages with both the RF and DC applied. The η_{un} is described as uncorrected effective efficiency, which can be directly measured by microcalorimeter's calibration mode.

As discussed in [2][10], the g in eq. (1) can be measured and evaluated using the flat short or back-to back method[6].

$$g = 1 + cs = 1 + c\frac{p_i}{p_{rf}} \tag{2}$$

978-1-4799-8887-7/15/$31.00 ©2015 IEEE

Here, c is the constant that describes the relative sensitivity of the thermopile voltage to heat dissipated at calorimeter transmission line, p_i is the absorbed millimeterwave power in the microcalorimeter, and p_{rf} is the power absorbed by the DUT. The detailed derivation of eq. (1) can be obtained in [5].

The main uncertainty source of the effective efficiency is coming from correction factor g, it contributes about 70 percent or more of the total uncertainty.

III. Measurement Results

In this paper, three microcalorimeters were fabricated to evaluate the Hughes thermistor mount 45772H-1100, and they were made according to an identical plan. The only difference between them was manufacture error of thermal conductive plate and heat isolation section, as shown in Fig. 1. The first one, labeled as Core1, was produced at Xi'an. The remaining two, labeled as Core2 and Core3, were manufactured by one company at Chengdu together. In order to maintain consistency of experiment condition, the relative humidity and temperature in the lab were controlled within a certain range of ±10% and ±1 degrees, and the three microcalorimeters were alternately used for experiment.

Firstly, the uncorrected effective η_{un} in eq. (1) was obtained using microcalorimeter's calibration mode. In order to verify repeatability, each microcalorimeter was taken to measure the same thermistor mount three times.

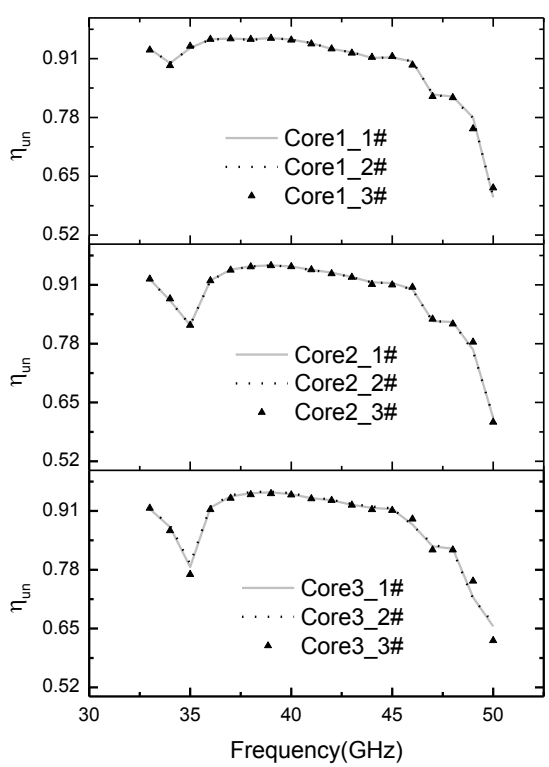

Fig. 2. The uncorrected effective efficiency η_{un} among the three microcalorimeters. The Core1_1# indicates the first time measure with the Core1. The Core1_2# indicates the second time measure with the Core1.

Finally, the correction factor of the microcalorimeter g was acquired by the flat short model, and the effective efficiency of the thermistor mount η_e was evaluated by eq. (1).

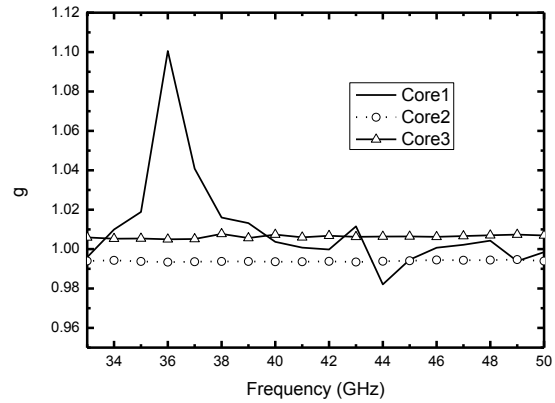

Fig. 3. The correction factor g among the three microcalorimeters.

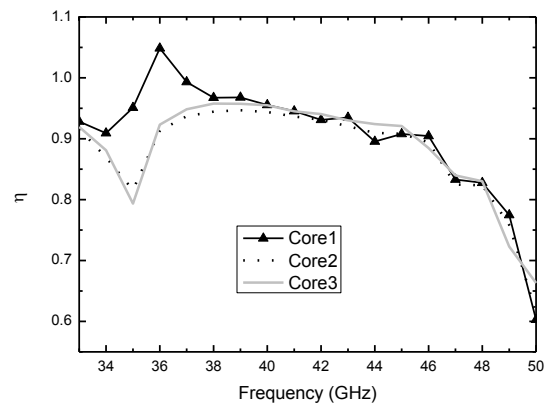

Fig. 4. The effective efficiency η_e among the three microcalorimeters.

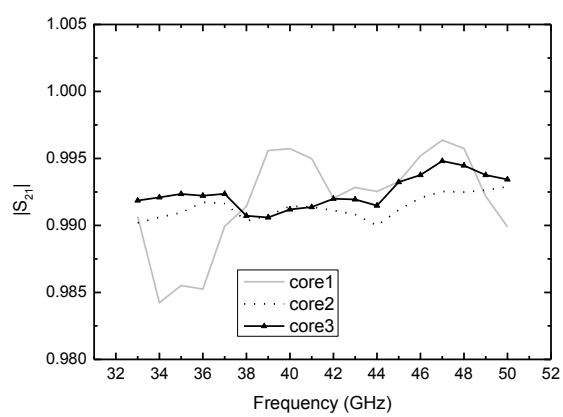

Fig. 5. The scattering parameter $|S_{21}|$ of thermal conductive plate and heat isolation section among the three microcalorimeters.

Table 1. The parameter comparison among the three microcalorimeters at 35GHz.

microcalorimeter	η_{un}	g	η_e	$\lvert S_{21} \rvert$
Core1	0.9333	1.0032	0.9509	0.9855
Core2	0.8211	0.9937	0.8159	0.9910
Core3	0.7925	1.0053	0.7935	0.9924

From above experiments, there are no great differences results between Core2 and Core3. However, the experiment results clearly demonstrates that the differences between Core1 and the remaining two cores were unacceptable. We have attempted to find out the reason, and some preliminary conclusion is that the manufacturing process may affect the results. In the near step, the thermistor mount will be replaced as another one to verify the phenomenon, and the more detailed experimental data could be obtained, such as the physical size of the key parts (thermal conductive plate and heat isolation section), more sampling points over a range of frequencies (34.5GHz to 35.5GHz) , and so on.

IV. Discussion

In this paper, three sets of the WR-22 (33 to 50 GHz) microcalorimeters were used to evaluate the effective efficiency of the sole thermistor mount. They are exactly the same, except of the manufacture error of thermal conductive plate and heat isolation section. However, the evaluated effective efficiencies weren't completely consistent among the three microcalorimeters in some frequency points. Some preliminary results for evaluating microcalorimeter were reported, and quantitative relation between manufacturing process and effective efficiency of the thermistor mount will be study in the near future.

References

[1] R. Judaschke and J. Ruhaak, “Determination of the correction factor of waveguide microcalorimeters in the millimeter-wave range,” *IEEE Trans. Instrum. Meas.*, vol. 58, no. 4, pp. 1104–1108, Apr. 2009.

[2] T. P. Crowley and X. H. Cui, “Design and evaluation of a WR-15 (50 to 75 GHz) microcalorimeter,” in *2008 Conference on Precision Electromagnetic Measurements*, Broomfield, CO, Jun. 2008, pp. 420-421.

[3] X. H. Cui and T. P. Crowley, “Comparison of experimental techniques for evaluating the correction factor of a rectangular waveguide microcalorimeter,” *IEEE Trans. Instrum. Meas*., vol. 60, no. 7, pp. 2690-2695, Jul. 2011.

[4] Cui Xiaohai, Li Yong, and Gao Xiaoxun, “A new design and evaluation technique of a microcalorimeter,” in *2012 Conference on Precision Electromagnetic Measurements (CPEM)*, pp. 736-738.

[5] J. W. Allen, F. R. Clague, N. T. Larsen, and M. P. Weidman, “NIST microwave power standards in waveguide,” *NIST Technical Note 1511*, Feb. 1999.

[6] X. H. Cui, Y. Li, X. Gao, Z. Song, and W. Sun, “Correction factor evaluation technique for a rectangular waveguide microcalorimeter,” in *2013 82nd ARFTG Microwave Measurement Conference*, Columbus, OH, Dec. 2013.

Microstrip Open - Problematic Calibration Standard

Martin HAASE, Karel HOFFMANN, Zbynek SKVOR

Czech Technical University in Prague, Faculty of Electrical Engineering, Dept. of Electromagnetic Field, Technicka 2, 166 27, Prague, Czech Republic, haasema1@fel.cvut.cz, hoffmann@fel.cvut.cz, skvor@fel.cvut.cz

Abstract — Microstrip open end (Open) applied as a calibration standard in frequency band up to 26 GHz was analyzed using CST Microwave Studio (CST). Arlon CuClad 233 with thickness 0.508mm was used for simulations. Different lengths of the microstrip lines in front of the Open were considered. Significant influence of the radiated field and the length of the microstrip line on the reflection coefficient magnitude of the standard in the order 0.01 was discovered. Physical explanation of the phenomenon is given.

Index Terms — Calibration standards, electromagnetic radiation, measurement, microwave propagation, offset reflects.

I. Introduction

A lot of different calibration techniques for precise s-parameter measurements using vector network analyzers (VNA) have been developed in recent four decades. Some of them need full knowledge of parameters of calibration standards [1], another have differently limited demands on calibration standards [2], [3], [4] using somehow simplified the error model with some terms neglected. Some of calibration methods use open end as a calibration standard. Namely on planar lines like the microstrip line it is very advantageous due to technology simplicity. It is even possible to use three Opens in a different reference planes for reflection calibration. It is a well known fact that Open radiates. A launcher connecting a coaxial line of the VNA port and a microstrip line also radiates. Studies of this problem and certain recommendation suppressing the influence of the launcher radiation can be found in [5] and [6]. Radiation of the launcher also means that it can also work as a receiving antenna. To the best knowledge of the authors, any interaction of the Open radiation and the launcher working as a receiving antenna has not been analyzed yet. The purpose of this paper is to present first qualitative results of such an analysis performed on CST simulator. The launcher as a receiving antenna was substituted in this analysis by the waveguide port in CST for simplicity.

II. Simulations

50Ω microstrip line designed on common Arlon CuClad 233 0.508mm thick substrate was used for all simulations, see Fig. 1.

Open radiation has only moderate effect on properties of the standard. Therefore it is very important to properly set the

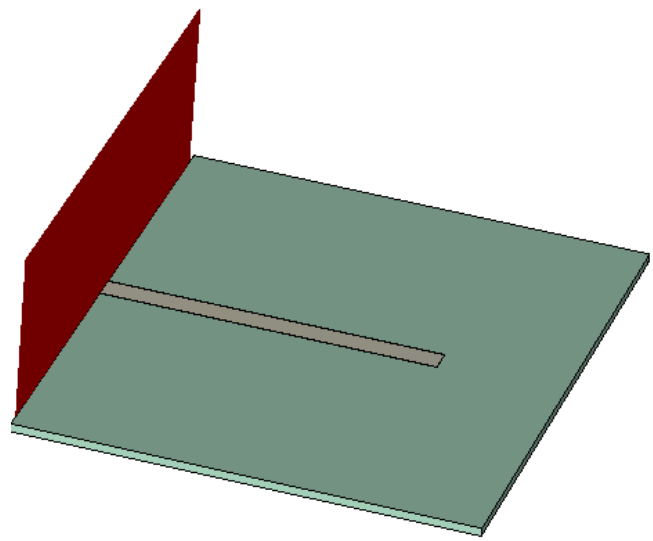

Fig. 1. Studied structure of the calibration standard Open.

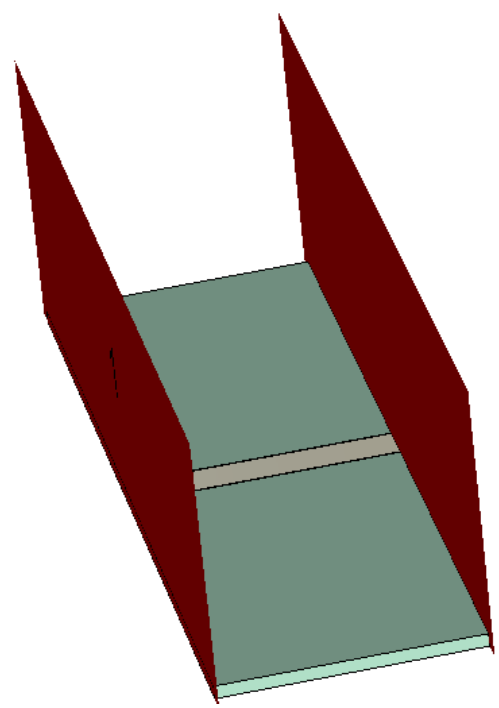

Fig. 2. Two port structure used for the port settings.

978-1-4799-8887-7/15/$31.00 ©2015 IEEE

simulator so that it was possible to distinguish the searched phenomenon from uncertainties of the simulator itself.

In the first step properties of the waveguide port in CST were tested. Fig. 2 shows the applied structure. The length of the microstrip line was set to 10mm, the width of the waveguide port was 21 times the width of the microstrip and its height was 20 times the thickness of the substrate.

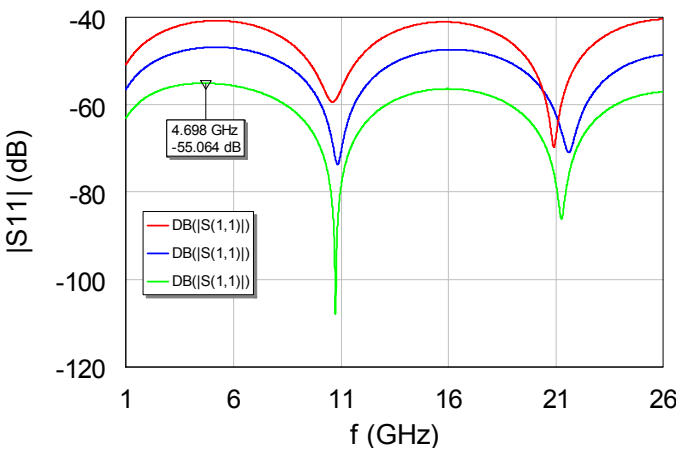

Fig. 3. Reflections of the structure of Fig. 2 with respect to Δs settings in CST.

Fig. 3 shows traces of the input reflection coefficient with respect to Δs settings of CST. Reflection coefficient -55dB of the cascade corresponding to -61dB reflection coefficient of the individual port was considered as sufficient with respect to studied problem.

The structure shown in Fig. 1 was analyzed in a box with perfect matched layer boundary condition on its surface, see Fig. 4.

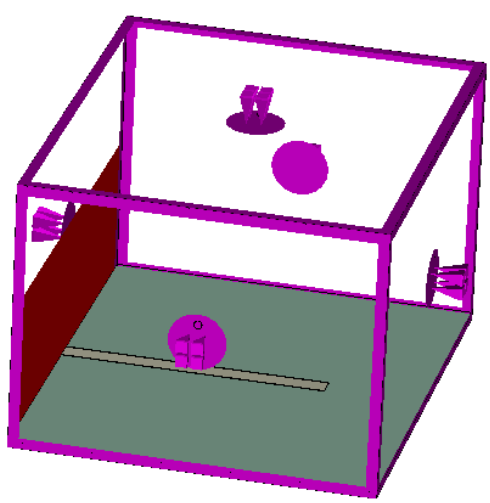

Fig. 4. Boundaries of the analyzed volume.

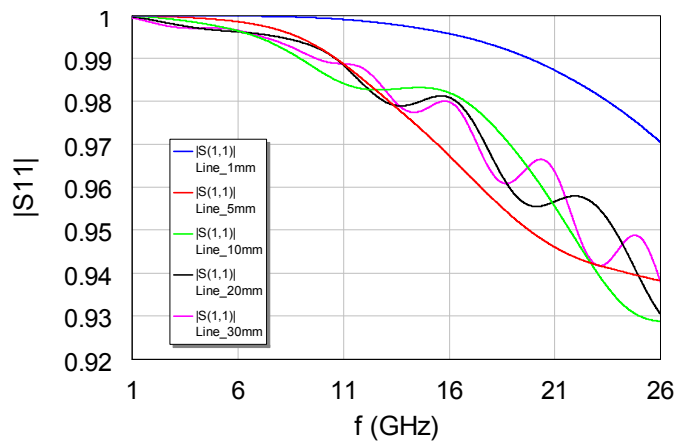

Fig. 5. Frequency dependence of reflection coefficient of Open.

Dimensions of the box were set so that their further increase had an effect less than 0.001 in magnitude of the simulated reflection coefficient.

The length of the microstrip in the analyzed structure was varied at the beginning from 1mm up to 30mm. The waveguide port was set to work with only quasi TEM mode. Corresponding simulated reflection coefficients are displayed in Fig. 5. It can be seen that starting from the length of 1mm of the microstrip the reflection coefficient monotonously decreases with increasing frequency. It is natural and expectable because of increasing radiation of the Open. However, for longer microstrips some strange wave disturbances of the traces with amplitude about 0.01 can be observed. Periods of this waves decrease with increasing length of the microstrip. Physical explanation of the phenomenon is problematic. Therefore further simulations for 20mm long microstrip with a metal short at the end (Short) were performed, see Fig. 6 and Fig. 7.

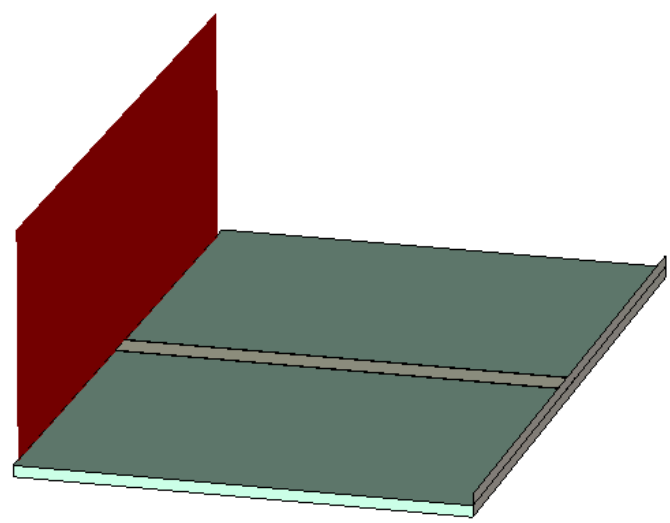

Fig. 6. Structure with short at the end of the microstrip.

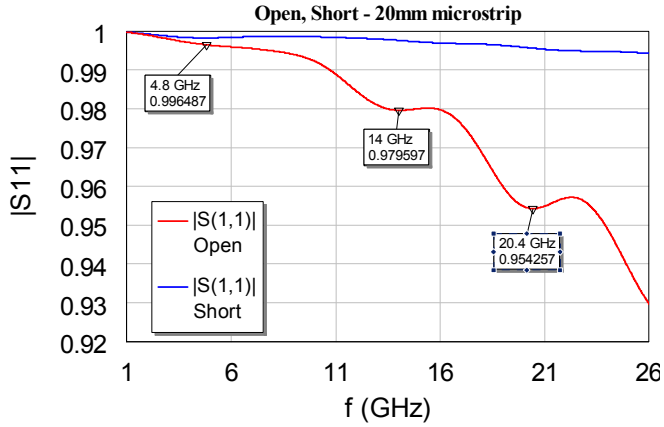

Fig. 7. Reflection coefficients of Open and Short for 20mm long microstrip.

It can be seen that the wave character of the trace is practically negligible for the Short. It guided us to an assumption that the wave character of the Open trace has something common with radiation of the Open as radiation of the Short was found out very small. Therefore animations of space distribution of electrical intensity in the studied structure with 20mm long microstrip were simulated for better understanding to the effect, see Fig. 8 and Fig. 9. A complex field distribution was obtained with two basic observable components. One corresponds to the expectable standing wave of the quasi TEM mode on the microstrip. The second one corresponds to a space wave radiated from the Open.

Significant facts can be observed on these two figures.

- The space wave reaches the waveguide port.
- The wavelength of the quasi TEM mode and the space wave are different. The electrical length between the end of microstrip and the waveguide port is about $2\lambda_g$ for quasi TEM wave and about $1¼\ \lambda_g$ for the space wave.

The field space distributions indicated that both the space wave and quasi TEM mode may interfere in the waveguide port. In some frequencies they are in phase and in some frequencies they are out of phase. The in phase case results in a greater amplitude of the resultant reflected wave entering the waveguide port yielding a greater reflection coefficient and vice versa for the out of phase case. However, three interfering minima on frequencies 4.8GHz, 14GHz and 20.4GHz displayed in Fig. 7 do not correspond to the difference of electrical length $2\ \lambda_g$ and $1¼\ \lambda_g$. Simulations in AWR Microwave Office proved only one minimum in the frequency band up to 26 GHz. Therefore interference of quasi TEM mode and radiated wave from Open as nature of wave traces in Fig. 5 and 7 is not physically provable. It probably results from rather unclear properties of the waveguide port set to work only with quasi TEM mode with respect to the incident radiated wave.

To get physically robust explanation of the phenomenon simulations were repeated for structures with 20mm and

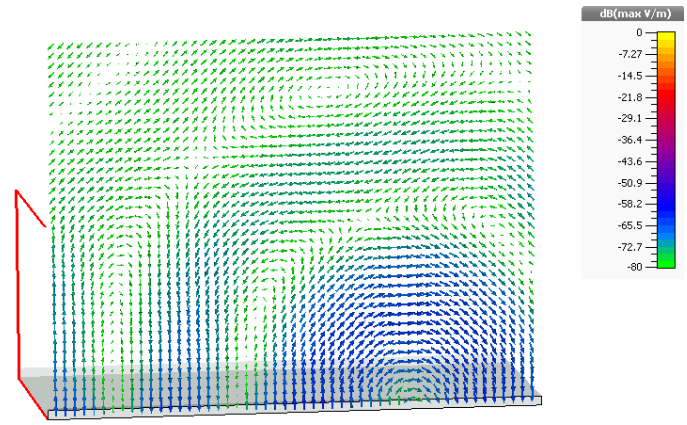

Fig. 8. Space wave in the moment when the standing wave equals to zero, f=20GHz.

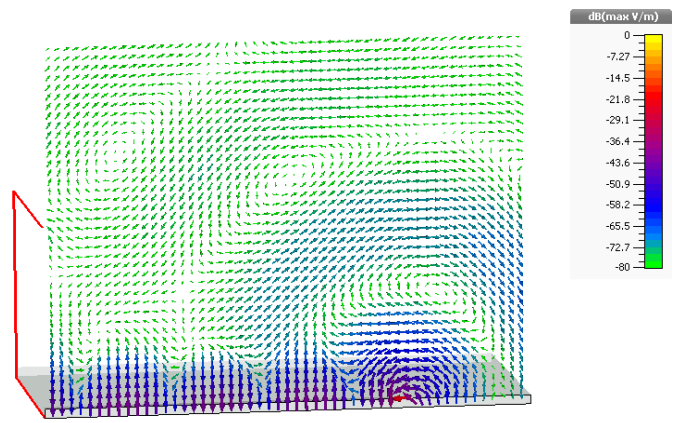

Fig. 9. Space wave and standing wave at the moment of the maximum of the standing wave, f=20GHz.

60mm long microstrip line with the waveguide port set to work also with higher order modes. The obtained reflection coefficients for individual modes are in fact conversion transmission coefficients between the exciting quasi TEM mode and modes entering the port after reflection or radiation from the Open. These coefficients were renormalized to 50Ω and added including their phase shifts. It approximates properties of a launcher converting received modes into TEM mode in the coaxial line. Fig. 10 and 11 display reflection coefficient for quasi TEM mode and sum of quasi TEM mode and renormalized the 1st and 2nd higher order mode. Both figures confirm the interference effect of quasi TEM mode and the higher order modes. The influence of the radiated field can change the reflection coefficient of the standard at the waveguide port of more than 0.05 in amplitude.

Standard calibration methods using microstrip Open calibration standards suppose quasi TEM mode in the reference plane. Simulations proved that it is not true in the distance of several wave-lengths from the Open what corresponds to current experimental arrangements. Even

60mm distance from the microstrip Open is not enough far to insure only quasi TEM mode propagation on the microstrip. It

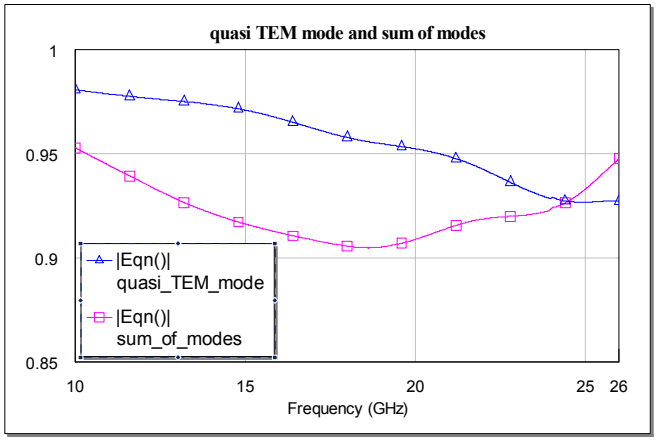

Fig. 10. Reflection coefficients of 20mm long microstrip line with Open. Quasi TEM mode and quasi TEM mode plus two higher order modes considered.

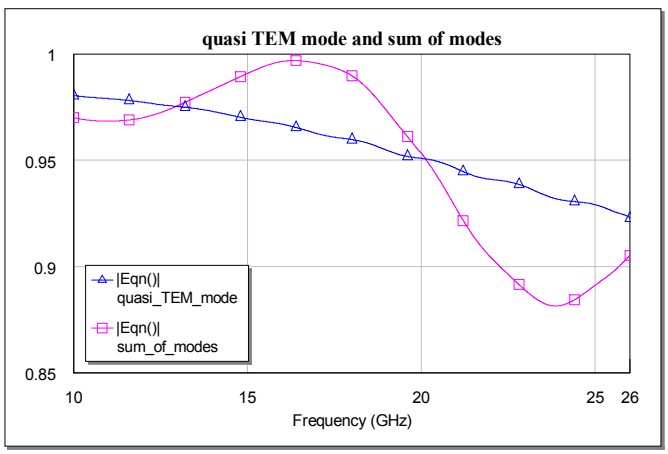

Fig. 11. Reflection coefficients of 60mm long microstrip line with Open. Quasi TEM mode and quasi TEM mode plus two higher order modes considered.

may result in increase of calibration measurement uncertainty in case of the waveguide port in the order of several units of 10^{-2} in amplitude. In a real case with a real launcher the effect will depend also on radiation properties of the launcher.

III. Conclusion

Microstrip Open calibration standard was analyzed in frequency band up to 26 GHz using CST microwave Studio simulator. A current launcher was replaced in the analysis for simplicity by the waveguide port as a partially receiving antenna. A new interference phenomenon resulting from the radiation of the Open and resulting in disturbances of frequency dependence of reflection coefficient of the standard was observed. Qualitative physical explanation of the disturbances was given. The effect may occur in current microstrip measurement test fixture arrangements. Further analysis including a real launcher making possible to get quantitative results is under way.

Acknowledgement

This work was funded through the European Metrology Research Programme (EMRP) Project SIB62 'Metrology for New Electrical Measurement Quantities in High-frequency Circuits'. The EMRP is jointly funded by the EMRP participating countries within EURAMET and the European Union.

The authors would like also to express their thanks to V. Sokol (CST) and O. Moravek (CTU Prague) for their valuable comments and advices.

References

[1] Rehnmark S., “On the Calibration Process of Automatic Network Analyzer System,” *IEEE Trans. on MTT*, Vol. 22, No. 4, Apr. 1974, pp. 457-458.

[2] Ferrero A. , Pisani U., “Two-Port Network Analyzer Calibration Using an Unknown “Thru“,” *IEEE Microwave and Guided Wave Letters*, Vol. 2, No.12, Dec. 1992, pp. 505-507.

[3] Eul H. J., Schiek B., “A Generalized Theory and New Calibration Procedures for Network Analyzer Self-Calibration,” *IEEE Trans. on MTT*, Vol. 39, No. 4, Apr. 1991, pp. 724-731.

[4] Engen G., Hoer C., ““Thru-Reflect-Line”-An Improved Technique for Calibrating the Dual Six-Port Automatic Network Analyzer,” *IEEE Trans. on MTT*, Vol. 27, No.12, Dec. 1979, pp. 987-993.

[5] K. Hoffmann and J. Raboch. “Hidden problems in precise calibration on microstrip II explanation and solution,” In: *Microwave Measurement Symposium (ARFTG), 2011 78th ARFTG*. Dec. 2011, pp. 1–5.

[6] O. Moravek, K. Hoffmann, M. Polivka, and L. Jelinek, “Precise Measurement Using Coaxial-to-Microstrip Transition Through Radiation Suppression,” *IEEE Trans. on MTT,* Vol. 61, No. 8, Aug. 2013, pp. 2956–2965.

Consideration of Error Model with Cable Flexure Influences on Waveguide Vector Network Analyzers at submillimeter-wave frequency

Masahiro Horibe[1)], Ryoko Kishikawa[1)], Yuto Kato[1)] and Yuta Tsukahara[2)]
[1)]National Metrology Institute of Japan, National Institute of Advanced Industrial Science and Technology,
[2)] Junkosha Inc.
[1)]1-1-1 Umezono, Tsukuba Ibaraki, 305-8563, Japan, [2)] 961-20 Fukuda, Kasama, Ibaraki, 309-1603, Japan

***Abstract* –In microwave and millimeter wave frequency region, systematic error terms, i.e. directivity, matching and tracking, in vector network Analyzer (VNA) can be corrected by a calibration process. However, it is difficult to correct the other random error terms, i.e. connection repeatability and flexure influences of cables attached to test ports, etc.. In the waveguide VNA using frequency extension modules, fortunately, it is unnecessary to consider cable flexure influences of test ports in the measurement uncertainty due to no test port cables being used. However, LO and RF cables making connection from frequency extension modules to microwave VNA have a large impact on the uncertainty in the transmission phase measurements. This paper proposes and demonstrates an evaluation technique of cable flexure influences of RF and LO cables in the millimeter and submillimeter wave VNA using frequency extension modules. Then, new VNA error model considering the LO and RF cable flexure influences are discussed.**

***Index terms* – Cable flexure influences, Waveguide VNA, LO signal cable, RF signal cable, Transmission characteristics, Phase measurements**

I. Introduction

The use of electronic applications and instruments at millimeter- and sub-millimeter-wave frequencies has demanded in recent years and commercial waveguide vector network analyzers (VNA) are now widely used. Furthermore, operation frequency reaches up to 1100 GHz. The national metrology institutes (NMIs) are mainly developing S-parameter national standards and measurement systems with uncertainty analysis [4-8]. Many research groups have already proposed new and modified designs of waveguide flanges to improve connection repeatability [9-12] as a major source of measurement uncertainty in waveguide VNA measurements at submillimeter wave frequency. New flange designs have already developed to improve connection repeatability to less than -50 dB of standard deviation at 330 GHz and -34 dB at 1 THz [13]. In the uncertainty analysis evaluation in waveguide VNA at submillimeter frequency, published papers have already discussed connection repeatability, system performance, noise and linearity, and uncertainty from calibration standards. However, a discrepancy between the phase measurement results of S_{12} and S_{12} can be found in passive device measurements by VNA with frequency extension modules (Fig. 1). Unfortunately, the issue have not been taken into account to the uncertainty analysis in waveguide VNA measurements.

In this paper, evaluation methods of flexure influences

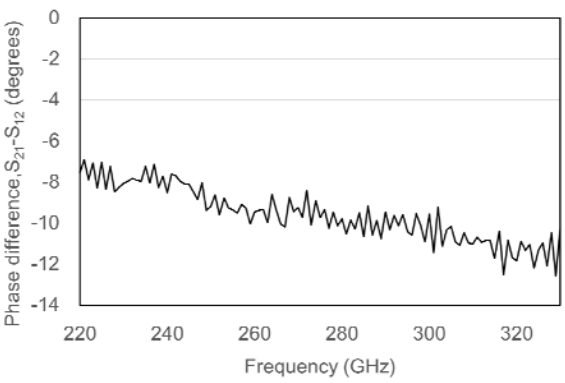

Fig. 1 A discrepancy between the phase measurement results of S_{12} and S_{12} for MW-864 waveguide straight line (Length is applox. 100 mm).

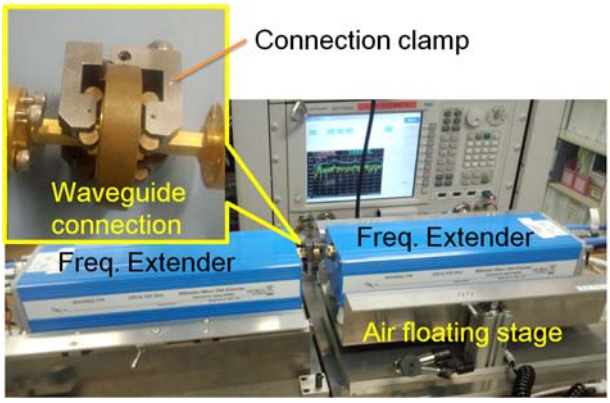

Fig. 2 Measurement system constructed by WR-3 frequency extension modules and air floating stage.

978-1-4799-8887-7/15/$31.00 ©2015 IEEE

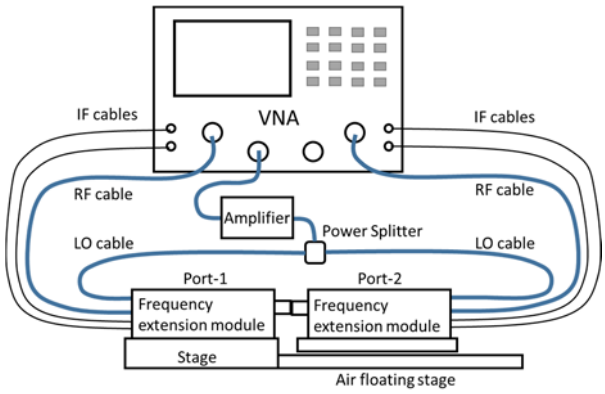

Fig. 3 Schematic views of our measurement system for waveguide device

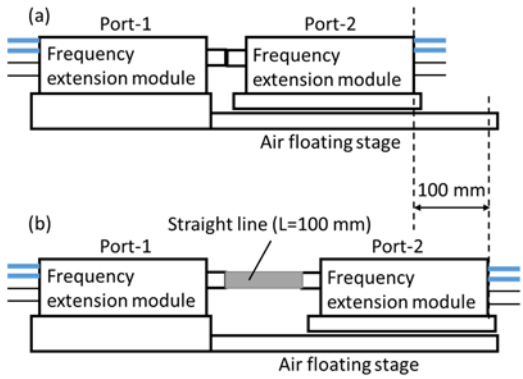

Fig. 4 Schematic views of measurement overviews for waveguide straight line.

of LO and RF cables is demonstrated in VNA measurement in the WM-864 waveguide frequency band. We then discuss new VNA error model taking in to account cable flexure influences of LO and RF cables.

II. Measurement System

Measurement system were constructed by a PNA Vector Network Analyzer from Keysight Technologies and WR-3 (WM-864) frequency extension modules from Oleson Microwave Inc. (OML) (Fig.2 and 3). All results presented in this paper have been taken with IF bandwidth 100 Hz. One frequency extension module is connected to VNA by two 3.5 mm coaxial cables, *JUNFLON® MWX Cable Assembly*, used as LO and RF cables and two IF cables. Power level and frequency range of LO and RF signals are approximately 10 dBm at the cable end and 10 GHz to 20 GHz, respectively.

For these evaluations the VNA was first calibrated by TRL calibration. The advantage in our measurement system is the connection platform "air floating stage" as

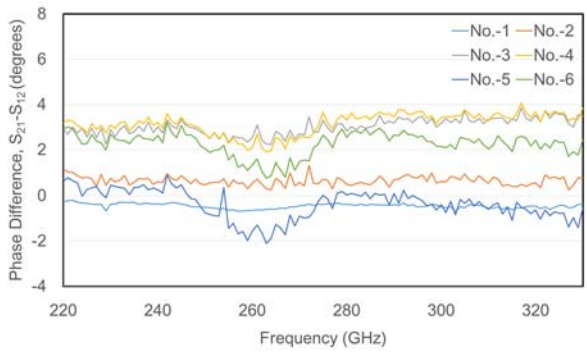

(a)

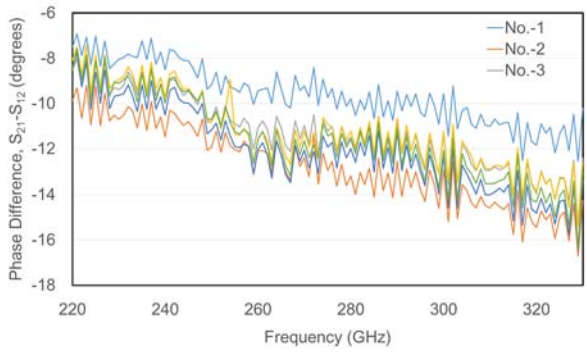

(b)

Fig. 5 Measurement results of phase difference between S_{12} and S_{12} for MW-864 waveguide straight line (Length is applox. 100 mm) (N=6). (a) Through connection and (b) straight line. Six measurements were made.

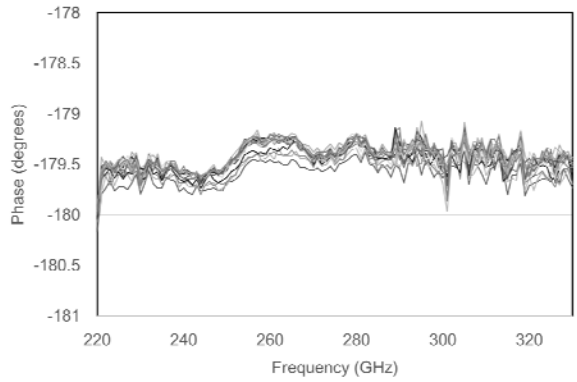

Fig. 6 Results of phase measurement, S_{22}, of flash short device.

shown in Fig. 2. Since frequency extension modules are generally heavy and hard to handle making precise alignments difficult, our connection platform eliminates the distorting effect of gravity force on the extension module by orienting them vertically. Precision waveguide flange [13] and connection clump are also used in the measurement

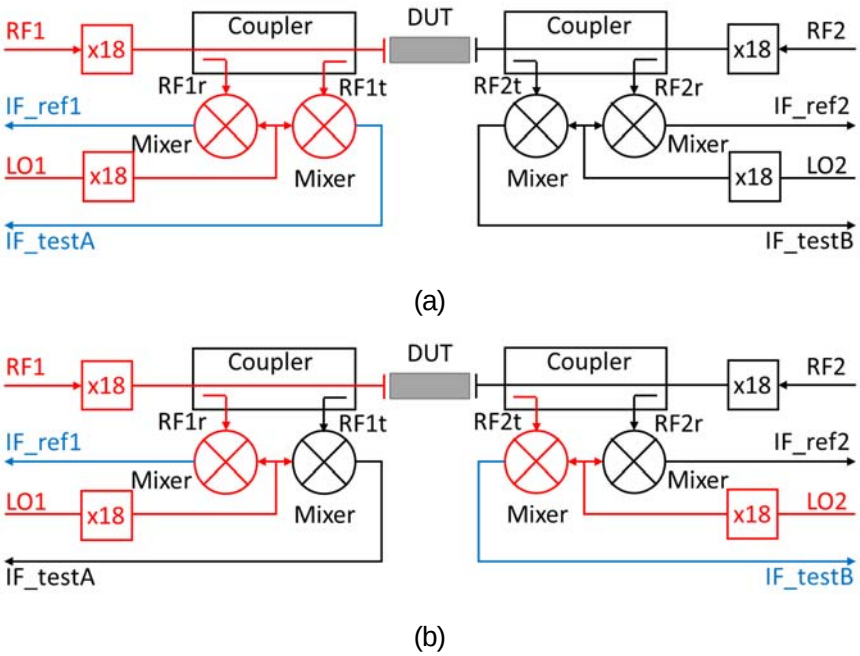

Fig. 7 Simplified block diagram of frequency extender modules (OML, V03VNA-T/R modules [14]), (a) S_{11} measurement and (b) S_{21} measurement. Blue lines and characters indicate IF signals used in the analysis, red lines indicates microwave signals to generate the IF signals indicated as blue lines.

system. As the clamp is tightened with a torque wrench the test port aperture and a device under test (DUT) aperture are mated under no gravity force so that the connection repeatability is dramatically improved [3]. Furthermore, clamp and air floating stage provide quick connection rather than the usual screw connection. It is possibly establish at least 60 disconnection/reconnection cycles for 1 hour in the measurement system. This is benefit to make stable measurements.

III. Measurements Results of Transmission Phase

Due to investigation a cable flexure influences in VNA measurement, MW-864 waveguide straight line (L=100 mm) have been measured. Six independent through/line cycle were made just after VNA calibration. Frequency extension module for port-1 side was fixed and module of port-2 was only moved for the line measurement (Fig.4). Movement distance was at least 120 mm. After measurement of straight line, port-2 module went back to initial position to make a direct through connection.

After obtaining full two port scattering parameter, the phase difference between S_{21} and S_{12} of each measurement were calculated. Figure 5 shows results of phase difference between S_{21} and S_{12} for line and through measurements, respectively. In the results, deviation of six traces indicates

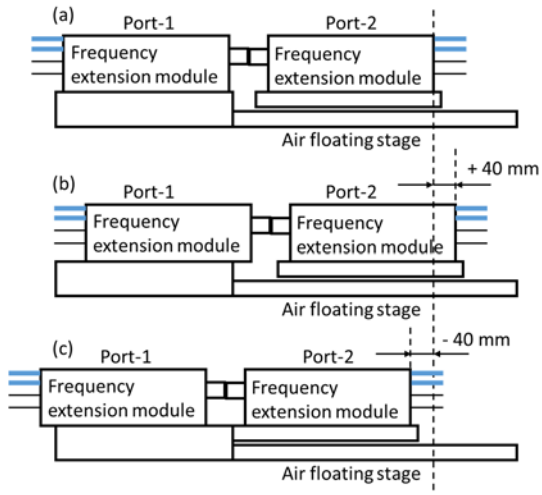

Fig. 8 Schematic views of evaluation for cable flexure influence (no disconnection/reconnection cycle).(a) initial position (40 mm), (b) right end position(80 mm) and (c) left end position(0 mm).

the measurement repeatability from cable flexure influence.

Figure 5(a) shows the repeatability of through measurements can be estimated and distribution of phase is up to a maximum of 6 degrees in the six independent measurements. In addition, phase difference of S_{21} and S_{12} is almost

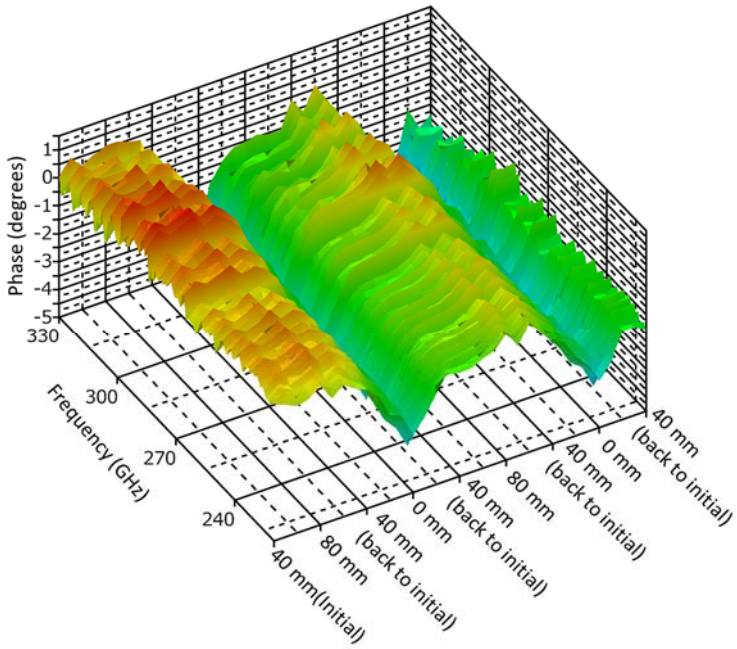

(a)

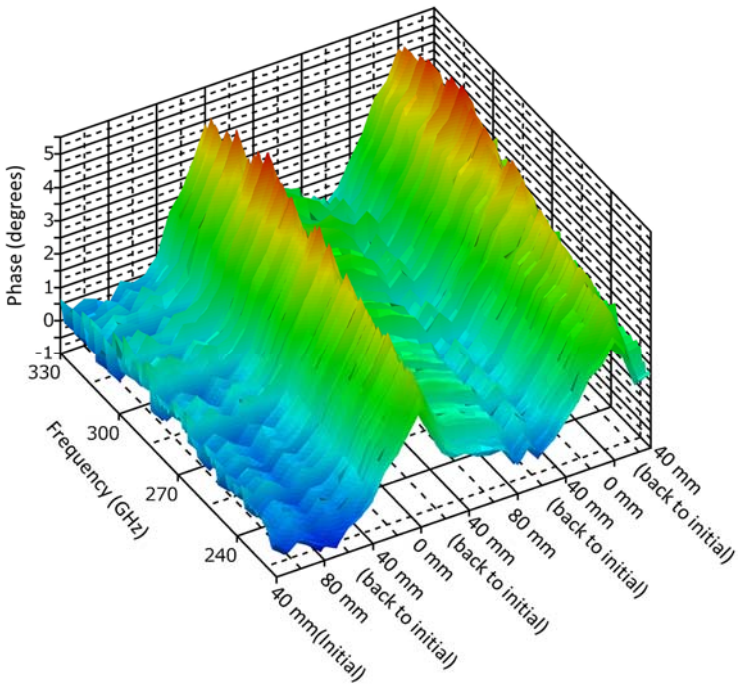

(b)

Fig. 9 Evaluation results of cable flexure influence for through connection (no disconnection/reconnection cycle). (a) S_{21} and (b) S_{12}. Vertical axis indicate position of frequency extension module and horizontal axis means operation frequency. Color means phase measurement results. Measurement value of phase at the initial position (40 mm) is typically zero.

independent of operation frequency. This means that positional repeatability of frequency extension module provides phase offset in the S_{21} and S_{12} measurement.

Figure 5(b) shows the repeatability of long straight line measurements can be estimated and distribution of phase is from 7 degrees to 17 degrees in the six independent measurements. In addition, phase difference of S_{21} and S_{12} was 5 degrees variation in the six independent measurements. This means that movement of frequency extension module provides the both phase change and phase offset in the S_{21} and S_{12} measurement.

Cable flexure influence in reflection phase measurement, S_{22}, was also investigated for flush short device. 20 measurands of S_{22} phase were drawn in Fig. 6. In this case, movement distance of port-2 module was 120 mm. However, phase measurements are stable in the measurement operations even if frequency extension module was moved over a long distance, i.e. 120 mm.

Thus, movement of frequency extension modules are providing cable flexure, and then making an impact on only transmission, S_{ij}, phase measurements.

IV. Understanding Cable Flexure Influence in waveguide VNA

Simplified block diagram of frequency extension modules, OML V03VNA-T/R module [13], are shown in Figs. 7. Frequency expansion in the modules are typically established by frequency multipliers and harmonic mixers and using RF and LO signals from VNA. In the case of WR-3 modules, submillimeter wave signal are generated by multiplying RF and LO signals by 18 times, then IF signals are obtained by harmonic mixing using multiplied LO signals. At first, characteristics of all component, mixers and RF/LO cables, etc., in the VNA system can be corrected by a calibration. Thus, measured value of phase is zero with no frequency dependence for S_{21} and S_{12} of direct thru connection just after calibration.

If the modules are moved, it is experience changes in flexure conditions of RF/LO cable depending on moving module to different position after calibration. This thus produces the change of phase of RF and LO signals in the cables. Then phase change at submillimeter wave frequency is magnified by multiplying signal in the module.

In the measurement, S_{11} characteristics of DUT is analyzed by dividing "IF_testA" signal by "IF_ref1" signal;

$$S_{11} = \frac{\mathrm{RF1t}}{\mathrm{RF1r}} \equiv \frac{\mathrm{IF\_testA}}{\mathrm{IF\_ref1}} \qquad (1),$$

$$S_{22} = \frac{\mathrm{RF2t}}{\mathrm{RF2r}} \equiv \frac{\mathrm{IF\_testB}}{\mathrm{IF\_ref2}} \qquad (2).$$

Then, S_{21} characteristics of DUT can be obtained by dividing "IF_testB" signal by "IF_ref1" signal. IF signals of "IF_testA", "IF_testB" and "IF_ref1" are generated by mixing RF1t, RF2t and RF1r signals, respectively. In this case, all three signal, RF1t, RF2t and RF1r, are initially generated by RF1 signals. Then, there is no cable flexure influence in the RF cables. (If phase characteristics is changed in the RF cables, change of phase characteristics of all three signals at submillimeter wave frequency is no difference.);

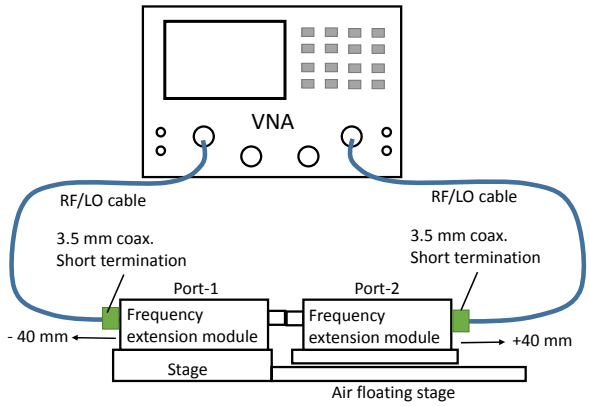

Fig. 10 Schematic views of evaluation for LO cable flexure influence at microwave frequency.

$$S_{21} = \frac{\mathrm{RF2t}}{\mathrm{RF1r}} \equiv \frac{\mathrm{IF\_refB}}{\mathrm{IF\_ref1}} \qquad (3).$$

Then, S_{12} is also analyzed by

$$S_{12} = \frac{\mathrm{RF1t}}{\mathrm{RF2r}} \equiv \frac{\mathrm{IF\_refA}}{\mathrm{IF\_ref2}} \qquad (4).$$

In the case of LO signals, "IF_ref1" and "IF_testA" signals are originally generated by mixing by LO1 signal, but "IF_testB" is obtained by mixing by LO2 signal. Thus, "IF_testB" signals have different phase information due to different phase behavior between LO1 and LO2 cables. As the results, S_{11} phase characteristics is still stable (no influence of cable flexure) even if module movement due to use of same LO signal to obtain two IF signals, "IF_testA" and "IF_ref1". However, S_{21} phases characteristics is affected by influence of cable flexure due to use of different LO signals to obtain two IF signals, "IF_testB" and "IF_ref1". At the same time, S_{12} phase is also affected by cable flexure, then, S_{21} and S_{12} is not same in the phase measurement of thru connection;

$$S_{21} \neq S_{12}, \qquad \frac{\mathrm{IF\_refA}}{\mathrm{IF\_ref2}} \neq \frac{\mathrm{IF\_refB}}{\mathrm{IF\_ref1}} \qquad (5).$$

V. Evaluation of Cable Flexure Influence

A. *Cable Flexure Influence for waveguide VNA*

Figures 8 show evaluation configuration for cable flexure influence for waveguide VNA. VNA calibration was performed by Thru-Reflect-Line (TRL) method at 40 mm

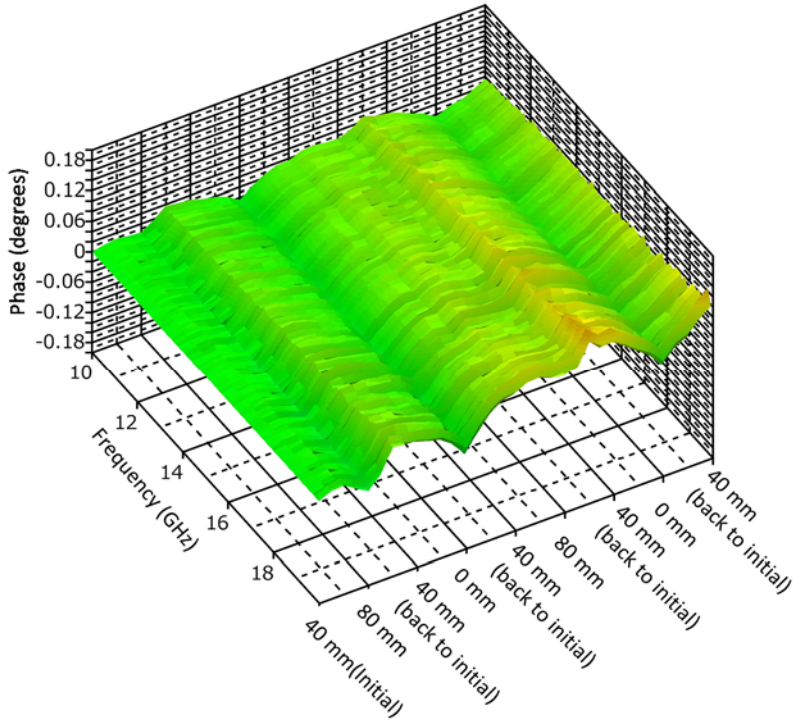

(a)

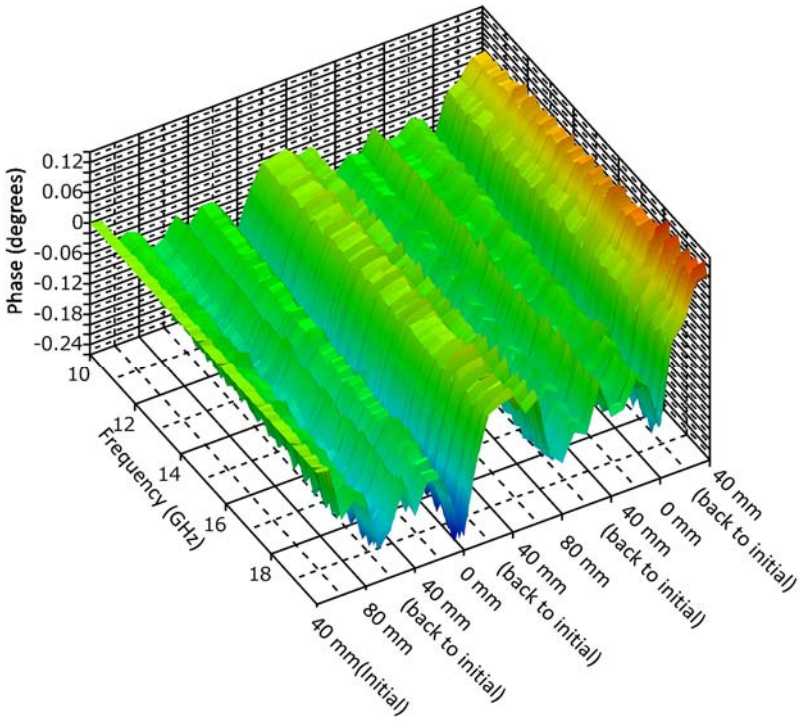

(b)

Fig. 11 Evaluation results of cable flexure influence at microwave frequency. (a) port-1 LO cable and (b) port-2 LO cables.

as the initial position, in this study. Thru connection was made at the final calibration process, then S_{21} and S_{12} phase characteristics was measured without disconnection. After first measurement was done, frequency extension modules was moved to right hand side and measured the S_{21} and S_{12} phase characteristics by 10 mm step. After measurement

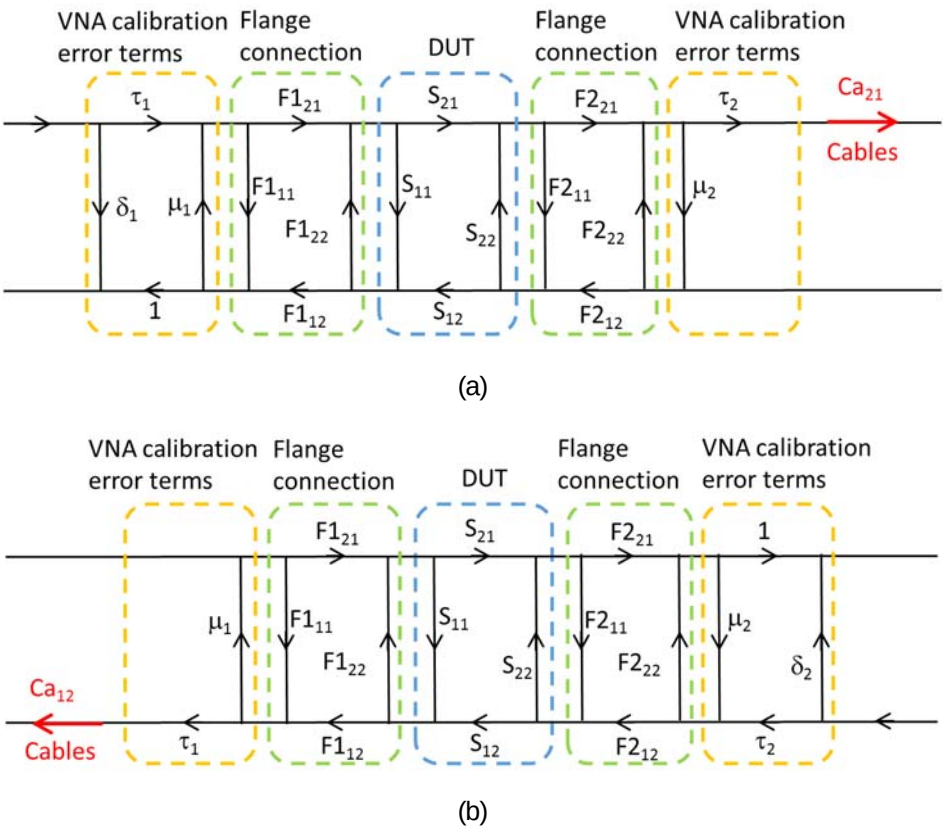

Fig. 12 waveguide VNA error model (a) Forward transmission, S_{11} and S_{21}, and (b) Revers transmission, S_{22} and S_{12}.

at 80 mm position, the modules went back to initial position by 10 mm and measured phase at each position. Then, modules was moved to 0 mm position and went back to initial position. Furthermore, same cycle was performed. (40 mm (initial position) →80 mm →40 mm →0 mm →40 mm →80 mm →40 mm →0 mm →40 mm).

Figures 9 show evaluation results of cable flexure influence for waveguide VNA measurement. For the both S_{21} and S_{12}, values of phase measured at 0 mm are dramatically changed from those at initial position (40 mm). Over 300 GHz, phase value of S_{21} is approximately +5 degrees, however, S_{12} phase is -5 degrees. Entire frequency range and movement range, S_{12} phase change is definitely at the opposite end of the scale from S_{21} phase change.

B. Cable Flexure Influence for LO signal

Due to investigation a relationship between cable flexure and change of measured phase in waveguide VNA, cable phase change was evaluated under the system described in figure 10. Tow cables were connected to VNA test port and other ends were terminated by 3.5 mm coaxial short circuits. After calibration for each cable end by 1 port open-short-load calibration, S_{11} and S_{22} phase characteristics were measured. Then cables were moved and measured phase at each position under the same procedure in the above subsection.

Figure 11s show measurement results of phase change (for one way) of two LO cables. Plotted data was normalized by the phase values measured at the initial position. For port-1 LO cable, cable flexure contributes little to phase change in the coaxial cable, i.e. phase change from 0.0 degrees to 0.15 degrees entire movement range and operation frequency range. However, at the port-2 side, phase was changed from -0.26 degrees to 0.14 degrees by cable flexure. Phase change of LO cable at port-2 side was affected by cable flexure.

As the result of this evaluation, phase changes of the LO cables are typically ±0.2 degrees ~ ±0.3 degrees. Thus, phase difference is possibly ±3.6 degrees ~ ±5.4 degrees due to 18 multiplying rate in WR-3 frequency extension modules we used. This estimation is agreed to the phase change in the waveguide VNA shown in Fig. 9.

In addition, phase difference of port-2 LO cable is much large at 0 mm compared to phase measured at the initial position. This positional behavior of phase change is the same as that in the waveguide VNA shown in Fig. 9.

VI. Waveguide VNA Error Model

As the results of above evaluation and analysis, LO cable flexure have an impact on S_{21} and S_{12} phase measurements in the waveguide VNA. (There is no impact to S_{11} and S_{22} measurements.) We can, thus, propose the calibration error model of waveguide VNA shown in Fig. 12. In figure 12, τ_i, δ_i, μ_i (i=1,2) indicate VNA calibration error terms, $F1_{ij}$ and $F2_{ij}$ indicate flange connection repeatability, then Ca_{21} and Ca_{12} means cable flexure errors and just make an impact to phase measurands of S_{21} and S_{12} . The phase change of forward and reverse from cable flexure errors are antiphase relationship, i.e. $\Delta\theta(S_{12}) = -\Delta\theta(S_{21})$, in the waveguide VNA. Thus, uncertainty element coming from cable flexure influence must be added to total uncertainty of S_{21} and S_{12}.

VII. Summary

This paper has investigated the influence of cable flexure on transmission phase measurements in waveguide VNA. The cable flexure has an impact to phase change in the coaxial cable used for LO cable to connect to frequency extension modules. Phase change was typically ±0.2 degrees ~ ±0.3 degrees, as the results, phase change was approximately 5 degrees at submillimeter wave frequency. The both results was agreed with each other due to taking into account multiplying rate of frequency extension modules. And phase change depending on the measurement positions was also agreed with cable flexure.

It is worth noting that, to the best of the authors' knowledge, this is the first time that a cable flexure influence on waveguide VNA measurement uncertainty has been demonstrated in a quantitative way. This type of evaluation provides very valuable underpinning measurement quality assurance not only for calibration method, but also for hardware optimization, which are fundamental to establishing accurate measurements made at submillimeter wave frequencies in waveguide VNA.

Acknowledgement

The work described in this paper was supported by Junkosha Inc. as a provider of coaxial cables, *JUNFLON® MWX Cable Assembly*, used for RF and LO cables to connect to the frequency extension modules.

References

[1] M. Horibe, and K. Noda, "Modification of Waveguide Flange Design for Millimeter and Sub-millimeter-wave measurements," *77th ARFTG Conference Digest*, pp. 1-7, June. 2011.

[2] M. Horibe, and R. Kishikawa, "Performance of New Design of Waveguide Flange for Measurements at Frequencies from 800 GHz to 1.05 THz," *81th ARFTG Conference Digest*, pp. 1-6, June. 2013.

[3] D.J Bannister, E. J. Griffin and T. E. Hodg etts, "On the dimensional tolerances of rectangular waveguide for reflectmetry at millimetric wavelengths ", NPL Report DES 95, National Physical Laboratory, UK September, 1989.

[4] D. F. Williams, "500 GHz – 750 GHz Rectangular-Waveguide Vector-Network-Analyzer Calibrations," IEEE Trans. THz Sci. Technol., vol. 1, no. 2, pp. 364-377, Nov 2011.

[5] D. F. Williams, "Comparison of Sub-Millimeter-Wave Scattering-Parameter Calibrations with Imperfect Electrical Ports," IEEE Trans. THz Sci. Technol., vol. 2 no. 1, pp. 144-152, Jan 2012.

[6] N. M. Ridler, R. G. Clarke, M. J. Salter, and A. Wilson, "Traceability to National Standards for Sparameter Measurements in Waveguide at Frequencies from 140 GHz to 220 GHz," Proc. 76th ARFTG Microw. Meas. Conf., Clearwater Beach, FL, Dec. 2010.

[7] T. Schrader, K. Kuhlmann, R. Dickhoff, J. Dittmer, and M. Heibel, "Verification of scattering parameter measurements in waveguides up to 325 GHz including highly-reflecting devices, Adv. Radio Sci., vol. 9, pp. 9-17, 2011.

[8] M Horibe, R Kishikawa and M Shida, "Complete characterization of rectangular waveguide measurement standards for vector network analyzer in the range of millimeter and sub-millimeter wave frequencies", 76th ARFTG Microwave Measurement Conference digest, pp 1-15, Marriott Suites on Sand Key, Clearwater Beach, FL, 2-3 December 2010.

[9] M. Horibe, and K. Noda, "Modification of Waveguide Flange Design for Millimeter and Sub-millimeter-wave measurements," 77th ARFTG Conference Digest, pp. 1-7, June. 2011.

[10] H. Lil, An. R. Keit J. L. Hesler, H. Xu and R. M. Weikle, "A Ring-Centered Waveguide Flange for Millimeter- and Submillimeter-Wave Applications," International Microwave Conference (IMS) 2010, Digt, pp. 604-607, 2010

[11] Nick Ridler, Ron Ginley, "IEEE P1785: A New Standard for Waveguide Above 110 GHz", Microwave Journal, Vol 54, No 3, Cables & Connectors Supplement, pp 20-24, March 2011.

[12] Lau, Y.S. , D. J. Vondran, "An Innovative Waveguide Interface and Quarter-Wavelength Shim for the 220-325 GHz Band," 80th ARFTG Conference Digest, pp. 1-4, Nov. 2012.

[13] M. Horibe, and R. Kishikawa, "Performance of New Design of Waveguide Flange for Measurements at Frequencies from 800 GHz to 1.05 THz" 81th ARFTG Conference Digest, pp. 1-6, June. 2013.

[14] "220 to 325 GHz Vector Network Analysis, Introduction to a new air of vector network analyzer frequency extension modules covering 220 to 325 GHz," Microwave Journal, September 1, 2001.

Investigating Scattering Parameters Measurements for 50GHz High-speed Printed Circuit Boards (PCBs)

Hui Huang[1] Di Liu[2] Tao Guan[3] Xinmeng Liu[1]

[1]National Institute of Metrology, China; [2]Keysight Technologies Co., China;

[3]Huawei Technologies Co., China;

Abstract — This paper describes some investigations, made using coaxial launch connectors and microwave probes, into the scattering parameters (S-parameters) measurements for a high-speed Printed Circuit Boards (PCBs) by using Vector Network Analyzers (VNAs) operating at microwave frequency up to 50GHz. The grounded Coplanar Waveguide (GCPW) transmission line with Electromagnetic Band Gap (EBG) in ground planes as one reference standard for S-parameters of the general high-speed PCBs, of which characteristic impedance is 50 ohm, is predicted and analyzed from electromagnetic theory. The paper describes the impedance standard in detail and compares experimental results, obtained using a VNA operating in the 10MHz to 50GHz band, with values predicted by electromagnetic modeling software. The measurement is implemented after using Multiline Thru-Reflect-Line (Multi-TRL) algorithm by Wincal XE4.5. The impedance mismatch is analyzed by Time-domain Reflection (TDR) method.

Index Terms — S-parameters, High-speed PCBs, GCPW, EBG, Multi-TRL, TDR.

I. Introduction

Due to the rapid growth in the use of internet and mobile communications, the high-speed transmission capacity requirements have been increasing at a high rate. As a result of this, the high-speed **Printed Circuit Boards (PCBs)** have seen significant advances as high-speed interconnects for 10 Gb/s even higher speed signals in the modern communication systems, especial for the next generation mobile communications, like 5G techniques.

The grounded coplanar waveguides (GCPW) is regarded as one of the best transmission line structure for the Signal Integrity (SI) and electromagnetic radiation, as the interconnect for the transportation of 10 Gb/s or faster electrical signals on digital high-speed PCBs and in high-speed connectors. [1][2] The microwave properties, including impedance match, reflection coefficient, transmission loss, and etc., must be considered when the GCPW is used at microwave frequency up to 50GHz. [3][4]

In order to minimize the discontinuity, impedance control is facilitated by controlling the spacing and width of the ground traces on either sides of the signal trace without changing the width of the signal trace or its height above the ground plane which are constrained. In the meantime, the Electromagnetic Band Gap (EBG) is implemented using the array hole in the ground planes, in order to suppress dispersive loss, the resonances, and other higher modes. [5][6][7]

This paper presents a complete analysis for the new design GCPW with EBG in the ground plane. The new structure is as the one reference standard for the general high-speed PCBs, of which characteristic impedance is 50 ohm. The **scattering parameters (S-parameters)** for the new standard is predicted from electromagnetic theory by electromagnetic modeling software and measured using a VNA operating in the 10MHz to 50GHz band. The measurement is implemented after using Multiline Thru-Reflect-Line (Multi-TRL) algorithm by Wincal XE4.5. In the meantime, the impedance mismatch is analyzed by Time-domain Reflection (TDR) method.

II. Reference Impedance Standards for High-speed PCBs

The new GCPW with EBG is used as the reference impedance standard for S-parameters at microwave frequency up to 50GHz, which is near to 50ohm. The simulation for structure is shown in Fig.1, and the fabrication sample is shown in Fig.2. The especial EBG is implemented using the two arrays holes both in the ground planes, in order to suppress dispersive loss, the resonances, and other higher modes.

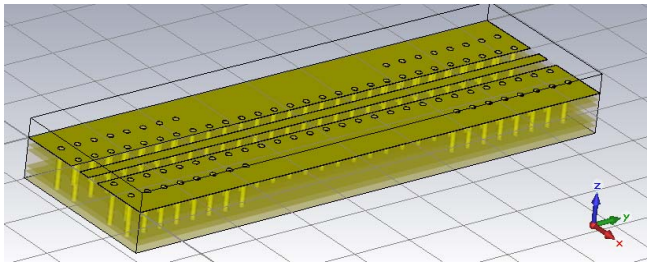

Fig.1 The GCPW transmission line as reference impedance standard for high-speed PCBs

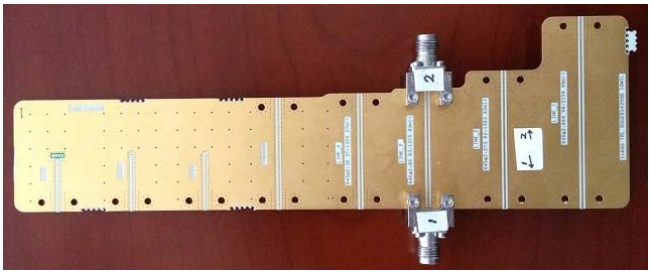

Fig.2 The sample for GCPW transmission line as reference impedance standard for high-speed PCBs

978-1-4799-8887-7/15/$31.00 ©2015 IEEE

This standard GCPW **transmission line** should be the match characteristic, of which return loss is near to -40dB, shown in Fig.3. Additionally, the insertion loss is less than -0.6dB, shown in Fig.4. The length is 853mil for GCPW **transmission line in the simulation.**

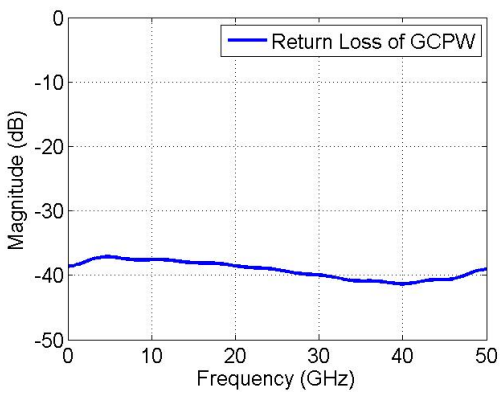

Fig.3 The return loss of GCPW transmission line as reference impedance standards for high-speed PCBs

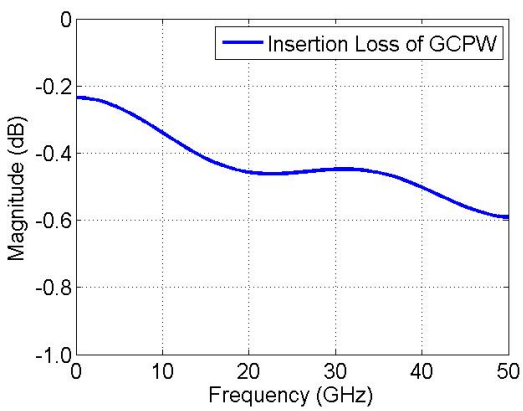

Fig.4 The insertion loss of GCPW transmission line as reference impedance standards for high-speed PCBs

III. MEASUREMENT VERIFICATIONS

The **S-parameters** of this new standard are measured using VNA with 50GHz end launch connectors and microwave GSG probes, operating in the 10MHz to 50GHz frequency band. The measurement setups are shown in Fig.5 and Fig.6. The measurement is implemented after using Multi-TRL algorithm by WinCal XE 4.5. The Multi-TRL calibration kits include five different length lines and the shortest line uses as the through line. The reference plane is on the center of the through line. In the calibration kit, also include two reflection standards, are open and short. Additionally, one matched load as impedance reference kit is used in the lower frequency band. The calibration kit is shown in Fig2.

The different length lines with adaptors and probes are measured after calibration as the same setup. All the results, including return loss and insertion loss, are shown in Fig.7 and Fig.8. From measurement results, the true values are measured with probes.

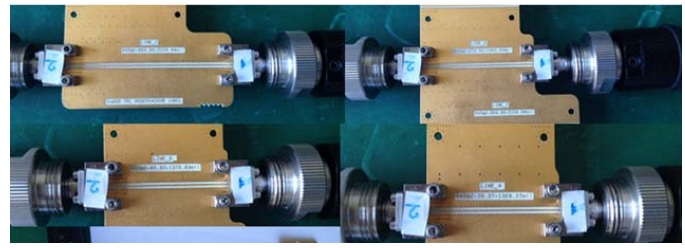

Fig.5 The measurement setup with 50GHz end launch connectors

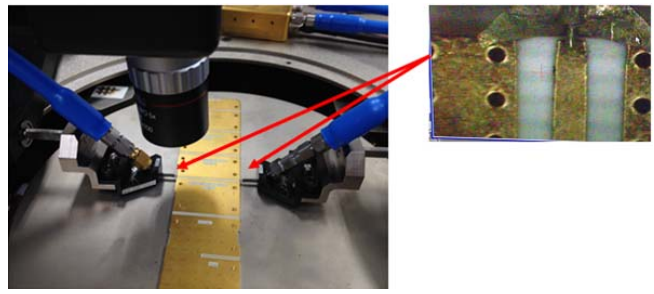

Fig.6 The measurement setup with microwave GSG probes

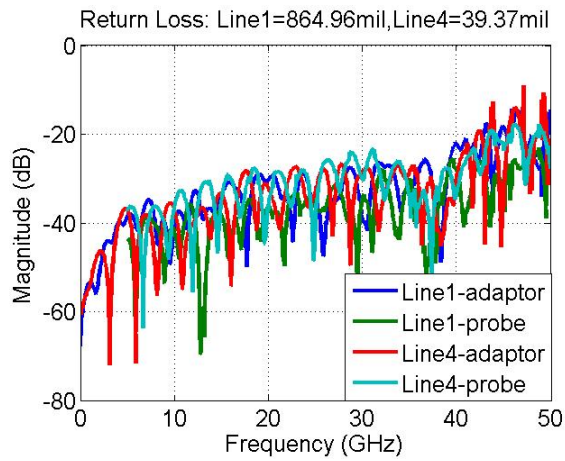

Fig.7 The return loss measurement results for two different length GCPW lines with adaptors and probes

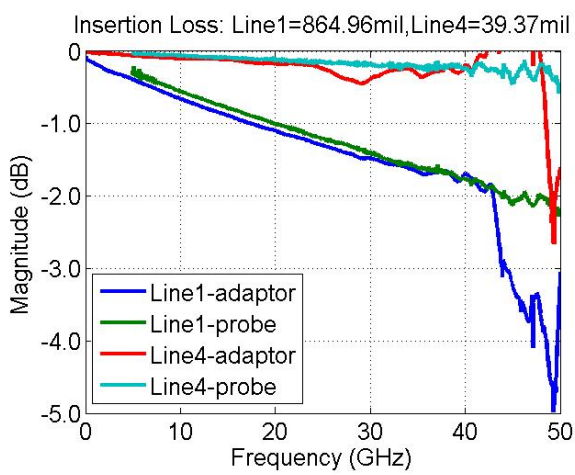

Fig.8 The insertion loss measurement results for two different length GCPW lines with adaptors and probes

IV. ANALYSIS AND OBSERVATIONS

From the results, the measured S-parameters of the GCPW with commercial probes are much ideal than with commercial 50GHz end launch connectors due to the probe's matches are better than the adaptors'. There is the obvious mismatch for the connection between the GCPW transmission line and 50GHz end launch connectors. The mismatch is still different within the different transmission line.

The impedance mismatch is analyzed by using Keysight Signal Integrity (SI) tool, Physical Layer Test System (PLTS) software as TDR. As shown in Fig.9, the 50 GHz end launch connectors and the high-speed **PCBs** are relatively good in terms of coaxial connectors repeatability and characteristics impedance variation, with less than 0.2 ohm difference for four end launch connectors and less than 0.5 ohm variation for the characteristics impedance of four line standards. However, there is a big mismatch from the coaxial plane to the GCPW transmission line, with worst value peaking to almost 58 ohm, which was introduced by a significant inductive effect.

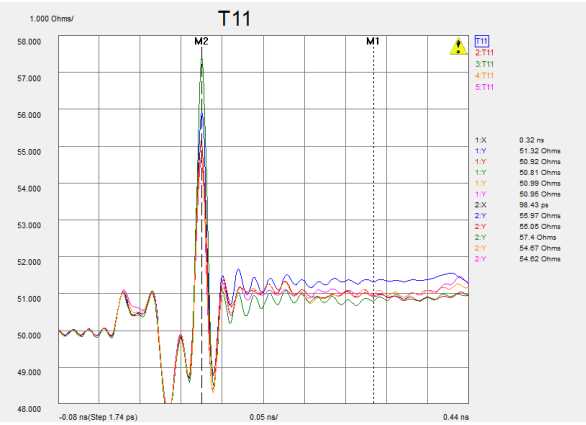

Fig.9 TDR analysis for impedance mismatch of GCPW with 50GHz end launch connectors

V. CONCLUSION

This paper has presented the new GCPW impedance standards for S-parameters measurement of the high-speed PCBs transmission media. The GCPW impedance standard is predicted by electromagnetic theory. The comparison for S-parameters of the GCPW transmission line shows the better matches of commercial probes than commercial 50GHz end launch connectors. The mismatch for 50GHz end launch connectors can be analyzed by TDR techniques. This is analogous to the use of commercial probe to measure high-speed PCBs that operate at frequencies up to 110 GHz, and there is a need to design and fabricate special adaptors with customized end launch to improve the mismatch.

ACKNOWLEDGEMENT

This work was funded through the Chinese Special Fund for Scientific Research in the Public Interest Project 201410010 'Research on time domain impedance metrology'.

Di Liu's involvement with this work was funded by Keysight Technologies Co., China.

Tao Guan's involvement with this work was funded by Huawei Technologies Co., China.

REFERENCES

[1] Syed Bokhari, Hassan Ali, "On grounded co-planar waveguides as interconnects for 10Gb/s signals", Electromagnetic Compatibility, 2003 IEEE International Symposium, 607 - 609 vol.2, 18-22 Aug. 2003.

[2] Lyons et al, "Connector interconnections to transmission lines for 40 Gb/s broadband applications", Proc. Electronic components and technology conference, pp, 1021-1026,2002.

[3] "High-Speed PCB Design Considerations", Lattice Semiconductor Corp, TN1033, April 2011.

[4] S. A. Bokhari, "Radiation from printed differential traces", Proc. IEEE EMC Symp., 2001, pp. 552-554.

[5] "Optimizing Test Boards for 50 GHz End Launch Connectors: Grounded Coplanar Launches and Through Lines on 30 mil Rogers 4350 with Comparision to Microstrip", Southwest Microwave, Inc.,

[6] "The Design and Test of Broadband Launches up to 50 GHz on Thin and Thick Substrates", Southwest Microwave, Inc.,

[7] www.southwestmicrowave.com.

A simplified calibration procedure for on-wafer power levelled S-parameter measurements at mm-wave

S. Galbano, L. Galatro and M. Spirito

Electronics Research Laboratory, Delft University of Technology

Mekelweg 4, 2628CD Delft, Netherlands

Abstract — In this paper, we present a simplified calibration procedure to obtain on-wafer power levelled s-parameters when employing VNA extender modules. The approach presented removes the required calibration at the module interface (i.e., waveguide), by assuming symmetry in the tracking terms of the error coefficient and only requiring an on-wafer calibration and the knowledge of the two port s-parameters of the wafer probe.

The calibration procedure with its mathematical approximation is then validated and compared to a conventional absolute power calibration using an equivalent model of the VNA front-end realized in a circuit simulator environment.

The calibration technique is then implemented in a WR10 system employing OML inc. modules. The experimental results, demonstrating an error lower than 0.5dB in the entire waveguide band, are reported.

I. Introduction

Millimeter-wave (mm-wave) on-wafer measurements are becoming increasingly more common in high frequency laboratories due to wide availability of VNA extenders. Such network analyzer add-ons are today available from various vendors and allow to characterize components, devices and building blocks operating in the entire millimeter and sub-millimeter waveguide bands.

The various VNA extenders available in commerce share all the basic approach of covering higher frequency bands by multiplying the RF and LO signals provided by the network analyzer. Due to the absence of an amplitude level control (ALC) within the extenders, the power available from the source can vary significantly within the waveguide band [1].

Fig. 1 shows the power fluctuation within the WR10 band due to the non-idealities present in the multiplication chain of the VNA extender. As can be noticed from the plot, variation up to 9dB can be seen, leading to an incorrect signal amplitude when measurement are performed on active device for model extraction.

Note, that if the minimum value of Fig. 1 (i.e., 85.5GHz) is set as the correct stimulus level for the DUT, the excess power at other frequencies can violate the small-signal requirement condition, necessary for model extraction. On other hand, if the maximum value (i.e., 75GHz) is set as the correct level, then a loss of dynamic range is experienced for the other frequencies.

The above considerations justify the need of power calibration to provide a software-based amplitude level control.

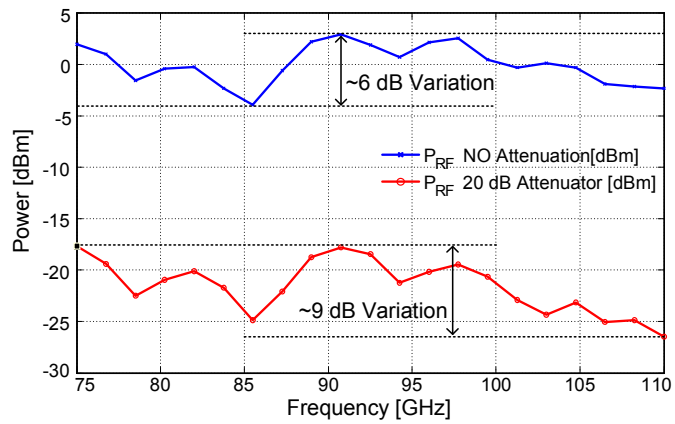

Fig. 1: Calibrated output power versus frequency of a mm-wave extender module in the WR-10 range, at different value of external attenuation.

The control of the available power enables to minimize the power fluctuation in s-parameter measurement at every frequency covered by VNA extenders.

In this contribution we describe the hardware setup employed by the test-bench, present the simplified calibration algorithm, which is validated by means of circuit level simulations and conclude with the measurement data comparing the proposed and a conventional power calibration in the frequency range from 75 to 110 GHz.

II. System Architecture

Fig. 2 presents the simplified block scheme of the proposed test-bench. In this setup, the test-set is provided by two VNA extender modules, to enable full two-port calibrated s-parameters. The generation of the RF signals providing the feed to the mm-wave extenders is performed using the internal source of the VNA, while the LO signals needed for the down-conversion of the scattered waves, are provided using an external low phase noise signal generator with sub-Hz resolution for highly accurate IF frequency control. The acquisition of the coupled waves is performed using the internal VNA mixers and receivers. To achieve absolute power control a power meter is employed during the calibration process. In this setup a dry calorimeter power meter (PM5) from VDI [2] has been used.

978-1-4799-8887-7/15/$31.00 ©2015 IEEE

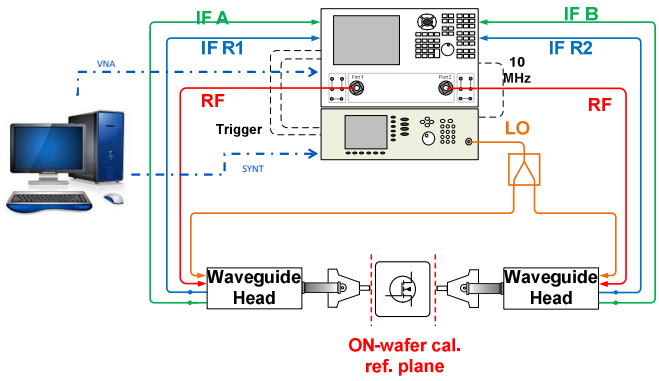

Fig. 2: Simplified schematic for the proposed measurement setup.

To provide the signal to the on-wafer environment Infinity probes from Cascade Microtech are considered in the simulation environment.

III. The Proposed Method

Power calibration in an on-wafer environment was first presented in [3] employing a secondary calibration plane and de-embedding process to shift the reference plane of the power measurement at the probe tips. A similar concept can be employed in frequency extended VNA test-benches, and was presented in [1] and is summarized in Fig. 3.

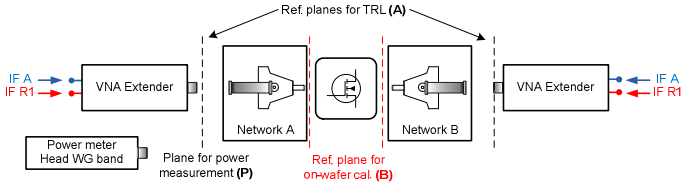

Fig. 3: Reference plane for s-parameter calibration at the module interface (A), plane for the power calibration (P), calibration plane for the on-wafer measurements (B).

The calibration at reference plane A (see Fig. 3) is required to account for the power meter input reflection coefficient and to provide the first-tier calibration to extract network A and B.

When the network A is known from vendor data or from a previous two-tier calibration and the calibration at plane A is unfeasible (i.e., no waveguide calibration kit), the simplified approach proposed here can be employed.

The simplified approach is based on the following procedure:

- symmetry in the two terms composing the tracking error term [4], can be imposed,
- the input port error box, composed of the conventional three terms is spilt in 4 term by applying a square root and phase control on the transmission term (see Appendix),
- the calibration reference plane is shifted from B (actual cal plane) to A employing ABCD matrix de-embedding,
- the $|I_{10}|^2$ of [3] is then achieved at plane A,
- the final term required for the absolute power knowledge at plane B is then achieved by embedding the $|I_{10}|^2$ with the s-parameters of the probe.

IV. Method Analysis

In order to validate the proposed approach a simplified model of the VNA front-end was implemented in Keysight ADS, see Fig. 4. All the mathematical framework to compute the error coefficient required for a one port calibration were defined in the ADS data display.

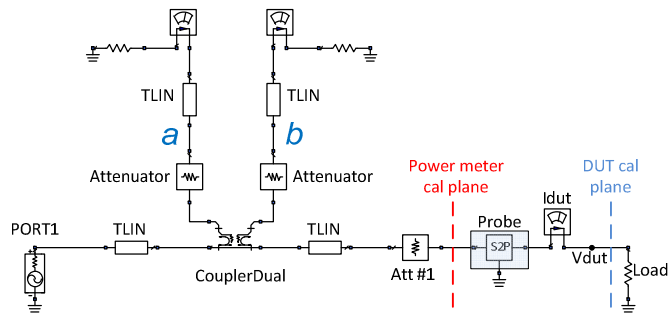

Fig. 4: ADS schematic representing the VNA RF front end, incorporating the coupler, non-ideal transmission lines and different delays, a variable attenuator and the two-port data element representing a W-band infinity probe.

The various components of Fig. 4 (i.e., transmission lines, attenuators, couplers) are introduced with a VSWR higher than one, and asymmetries are introduced in the amplitude and phase of the *a* and *b* signal paths.

The results obtained by the simplified procedure described in the previous section is then compared with the exact power input to the DUT (computed using a voltage and current probe in the simulation environment, see Fig. 4). We observe no loss of accuracy, even when the losses of the attenuator *Att #1* component are increased from 0 to 10dB, see Fig. 5.

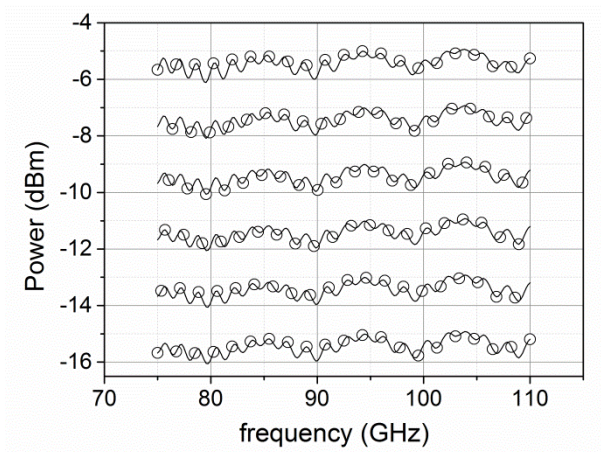

Fig. 5: Comparison of power input in the DUT (i.e., load of 25Ohm) for different level of the *Att #1* settings (0-10dB). Where the continuous line is the proposed method, and the black dots is the exact power computed by the current and voltage probe.

V. Experimental Results

The proposed method was implemented in a WR10 test-bench employing an Agilent PNA and OML inc., VNA extender. The simplified method was compared with the accurate method, where a first calibration at reference plane A was performed, the results are shown in Fig. 6.

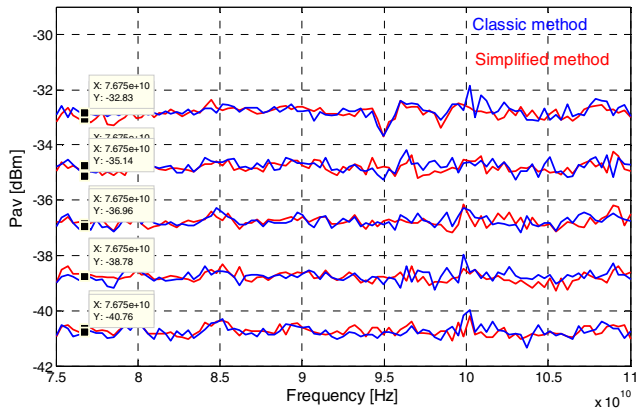

Fig. 6: Absolute power measured at wafer tip, applying error correction based on the conventional method (i.e., using TRL cal at plane A) shown in blue, and the proposed simplified method, shown in red, for different controlled power levels.

VI. Conclusions

In this contribution we presented a simplified method to obtain power levelled s-parameters on-wafer in mm-wave test benches employing VNA extenders. The simplified method does not require a TRL calibration at the module interface (i.e., waveguide) and achieves an error of less than 0.5dB in a practical setup within the entire WR10 band.

Appendix

The simplified method is based on the following procedure:

1. The input error box is split in the 2 by 2 s-parameter matrix shown below:

$$E_{term} = \begin{pmatrix} Ed_1 & \sqrt{i_{10}i_{01}} \\ \sqrt{i_{10}i_{01}} & Es_1 \end{pmatrix}$$

2. The error box at plane A is obtained by the de-embedding the probe contribution:

$$A_{term_x} = A_{term} * (A_{Probe})^{-1}$$

$$E_{term_x} = ABCDtoS(A_{term_x})$$

3. The $|I_{10}|^2$ is shifted from plane A to B using the probe data and the terms from the error box at plane A:

$$\left|I_{10plane\ B}\right|^2 = \left|I_{10\ plane\ A}\right|^2 * \frac{\left|S_{21_{Probe}}\right|^2}{\left|1 - E_{Splane\ A} * S_{11_{Probe}}\right|^2}$$

References

[1] L. Galatro, S. Galbano, A. Santaniello, M. Spirito; "Power Control for S-parameters and Large Signal Characterization at (sub)-mmWave frequencies", 85th ARFTG Conf. Dig., May, 22nd, 2015.

[2] Virginia Diodes [Online], available: www.vadiodes.com

[3] A. Ferrero, U. Pisani, "An Improved Calibration Technique for On-Wafer Large Signal Transistor Characterization", IEEE Trans. Instrum. Meas., vol. IM-47, pp.260-364, Apr. 1993.

[4] Douglas K. Rytting, "Network Analyzer Error Models and Calibration Methods," 62nd ARFTG Conference Short Course Notes, December 2-5, 2003, Boulder, CO.

Repeatability Performance of Non-Contact Probes in the 500-750 GHz Band

Cosan Caglayan*, Georgios C. Trichopoulos, and Kubilay Sertel
The ElectroScience Laboratory, The Ohio State University
1330 Kinnear Rd, Columbus, OH 43212
E-mail: {caglayan.1, trichopoulos.1, sertel.1}@osu.edu

***Abstract*—We present the repeatability performance of an automated non-contact probe system for on-wafer device and integrated circuit characterization in the 500-750 GHz band. Unlike conventional contact-probe systems, a computer controlled x-y translation stage is employed to realize a completely automated non-contact probe setup. Thanks to this simplicity, far superior repeatability performance can be achieved with great ease. We present the repeatability study specifically for the 500-750 GHz band utilizing a precision servo system with 1 micron translation accuracy. At 625 GHz, our setup achieves 2.2° deviation in phase and 4.4% deviation in magnitude for 25 successive measurements spanning over 1.5 hours. This fully computerized non-contact probe system also facilitates intermittent re-calibrations that are normally needed for reliable sub-mmW measurements.**

I. Introduction

Aggresively scaled contact probes attached to waveguide outputs of frequency multiplier modules are currently the standard for mmW and sub-mmW on-wafer measurements. However, these probes are typically rather fragile, particularly in the higher sub-mmW frequency bands, requiring a precise control of the contact force between the probe tip and test wafer. Thus, manual operation of such probes often result in poor repeatability and fast deterioration of the probe tips [1]. Even for automated systems, the usual wear and tear of the contact probes may lead to repeatability problems in large-scale wafer measurements (e.g. over 10000 contacts).

To address the current challenges associated with the scaling requirements of the contact-based test probes, we recently developed a cost-effective non-contact device characterization approach for wafer-scale testing that eliminates the wear/tear and automation issues associated with contact probes in [2]. This novel approach is based on radiative coupling of standard network analyzer test ports onto the coplanar waveguide (CPW) environment of typical monolithic THz devices, through the use of planar on-chip antennas integrated with the device under test.

In this summary, we describe the operation of the semi-automated non-contact probe setup and present its repeatability performance for the WR 1.5 band.

II. Automated Non-Contact Probes

Non-contact probes testing of on-wafer active and passive devices as well as integrated circuits can be realized with the aid of an external quasi-optical sub-system finely tuned to couple the incident energy onto specially designed planar antennas integrated onto the test chip. That is, the incident beam launched from the horn antenna attached to a THz VNA extender module is coupled onto a planar antenna using a hemispherical lens focused on the antenna. A typical test device connected to CPW transmission line is excited with the aid of the planar antenna integrated onto the same CPW environment. The signal reflected from the device arrives back by the incident antenna which subsequently re-radiates the reflected energy back to the horn antenna of Port 1 of the VNA enabling reflection S-parameter measurements (S_{11} and S_{22}). Part of the incident signal transmitted through the test device arrives at a secondary antenna (on the output port of the CPW environment), which is subsequently coupled to the second VNA port, enabling transmission measurements (S_{12}, S_{21}). The prototype of the non-contact measurement setup is shown in Fig. 1 and a detailed description of the non-contact

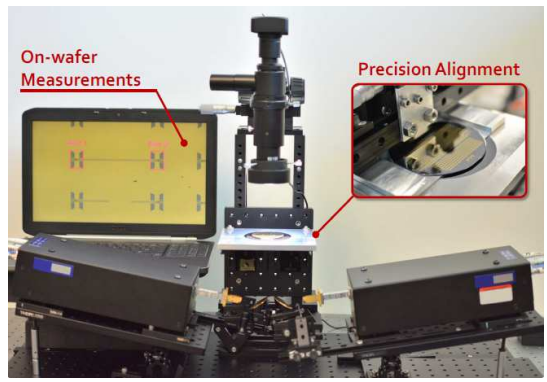

Fig. 1. Photograph of the non-contact probe setup prototype

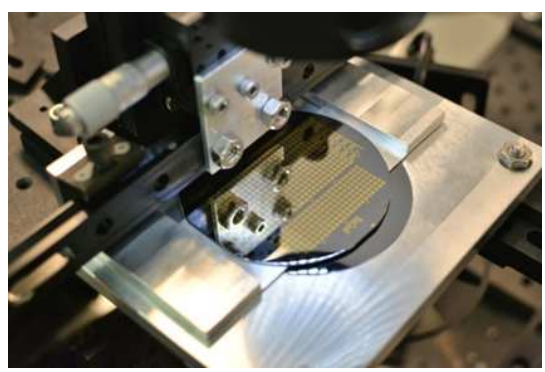

Fig. 2. Custom-made wafer handler for non-contact measurement setup. The handler can either be attached to an automated 2-axis precision controller or to manual micromanipulators for precise non-contact measurements

978-1-4799-8887-7/15/$31.00 ©2015 IEEE

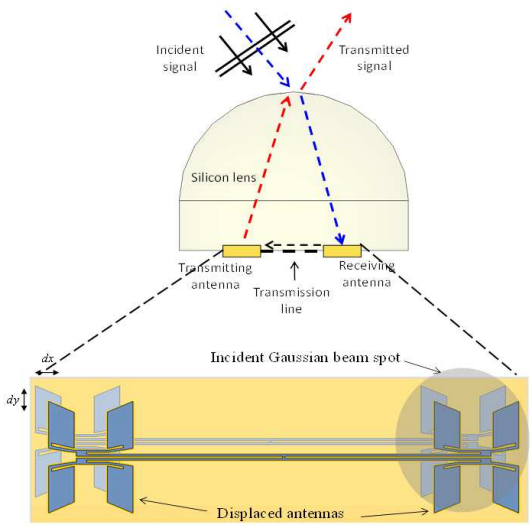

Fig. 3. Illustration of virtual probe tip placement error for the non-contact probe testbed

probe setup as well as calibration procedure can be found in [2].

Non-contact characterization of on-wafer devices is simply performed by placing the respective test structure over the fixed quasi-optical beam spots on the hemispherical lens. As such, only the position of the test wafer is adjusted with the aid of a microscope to collect the calibration and measurement data, whereas the quasi-optical alignment of the system is kept unchanged. In order to implement this process in a completely automated manner, we fabricated a custom wafer handler as shown in Fig. 2. This handler is attached to a 2-axis micromanipulator x-y stage. As such, the non-contact test-bed can be conveniently automated. Full automation is also possible by employing a straightforward pattern recognitions software in conjunction with software-controlled, commercially-available servos. Based on the above setup, below we investigate the repeatability of the non-contact test bed operated with servo-controlled manipulators and demonstrate the performance of fully-automated, on-wafer sub-mmW measurements for the first time.

III. Repeatability Performance of Non-Contact Probes

Here, we first focus on identifying and quantifying the main sources of non-repeatable errors in the non-contact probing process. The instrument drift is the other source of measurement error. Due to temperature sensitivity of the electronic components used in multipliers and mixers in VNA frequency extenders, they exhibit varying degrees of magnitude and phase drift over time, mainly due to fluctuations in the environment. For our current 2-port configuration in the WR 1.5 band, 12% of magnitude drift and $\pm 10^\circ$ phase drift over 1 hour time span is specified according to the manufacturer (Virginia Diodes Inc.). In addition, it is expected that the virtual probe tip placement under the beam spot will be slightly different for each of the calibration, as well as test device measurements.

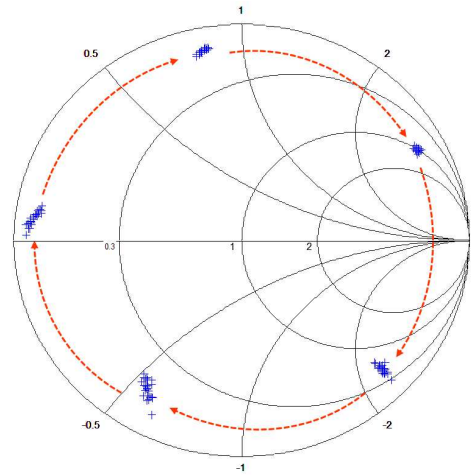

(a)

Standards	Phase Dev (deg)	σ_{mag}/μ_{mag} (%)
Short(ref)	2.1992	1.96
Short+18um	1.0813	0.87
Short+36um	0.6053	0.74
Short+54um	0.5936	2.79
Short+72um	2.0388	4.41

(b)

Fig. 4. 1-port repeatability of semi-automatic non-contact probe test bed in WR 1.5: (a) Smith Chart scatter plot of re-measured standards (b) Midband (625 GHz) phase and magnitude deviations tabulated for each standard.

The placement under the optimal beam spot location relies on the precision of the alignment of the virtual probe tip under the microscope. Manipulating precision is another limitation to this placement. Typically, manual placement of the virtual probe tip under the marked beam spot better than 1 micron is not possible in both of the manipulation axes. However, this precision can be significantly improved using a software-controlled automated test-bed.

We performed the following experimental procedure similar to the one presented in [3] to study the 1-port repeatability of our non-contact probe system: After an initial on-wafer calibration, the calibration feature set, which consists of 5 offset short CPW lines and a through standard, was measured 25 times over a time span of 1.5 hours in typical laboratory conditions. The Smith Chart representation of the collected 25 measurements is shown in Fig. 4(a) as a scatter plot. As seen in Fig. 4(b), the worst case phase deviation in the midband (625 GHz) is about 2.2° and the magnitude deviation is 4.4%. According to manufacturer specifications, 1-port stability of the frequency extenders is expected to be 5 times better than the 2-port configuration. As seen in this experiment, the measured repeatability of the non-contact probes is indeed very close to the instrument limitations. Considering this is the combined effect two factors discussed above, non-contact probes show excellent repeatability with this semi-automated

setup. In a fully automated test-bed, repeatability is expected to further improve compared to semi-automatic version presented here.

IV. Conclusion

An initial study of the 1-port repeatability performance of non-contact probes in the 500-750 GHz band is presented. Measured repeatability performance was shown to be close to instrument drift, demonstrating the effectiveness and ease of use of the non-contact probes. Due to relatively simple and quasi-optical nature of this new approach, the non-contact probe system is cost-effective and free from fragility and wear/tear issues of traditional contact-based probes. More importantly, the non-contact setup can be easily automated to enable large-scale wafer-level multi-port characterization of on-chip devices and ICs in the mmW and sub-mmW frequencies.

References

[1] T. Reck, L. Chen, C. Zhang, A. Arsenovic, C. Groppi, A. Lichtenberger, R. Weikle, and N. Barker, "Micromachined probes for submillimeter-wave on-wafer measurements part I: Mechanical design and characterization," *IEEE Transactions on Terahertz Science and Technology*, vol. 1, no. 2, pp. 349–356, November 2011.

[2] C. Caglayan, G. Trichopoulos, and K. Sertel, "Non-contact probes for on-wafer characterization of sub-millimeter-wave devices and integrated circuits," *IEEE Transactions on Microwave Theory and Techniques*, vol. 62, no. 11, pp. 2791–2801, September 2014.

[3] L. Chen, C. Zhang, T. Reck, A. Arsenovic, M. Bauwens, C. Groppi, A. Lichtenberger, R. Weikle, and N. Barker, "Terahertz micromachined on-wafer probes: Repeatability and reliability," *IEEE Transactions on Microwave Theory and Techniques*, vol. 60, no. 9, pp. 2894–2902, July 2012.

Impedance Renormalization in CMOS-based Single-Element Electronic De-embedding

Jun-Chau Chien and Ali M. Niknejad

Department of Electrical Engineering and Computer Science, University of California, Berkeley, CA

Abstract — In this work, an impedance renormalization technique dedicated for single-element de-embedding algorithm is proposed. By performing impedance modulation using CMOS transistors, reflection measurements with both ideal shorts and opens are generated from the measured two-port S-parameters. Such measurements with known terminations are further utilized for finding the solution to the test fixture and the characteristic impedance of the on-chip transmission line. As a single structure is sufficient, considerable savings in silicon area and improved accuracy due to reduced number of probing is achievable. Experimental results up to 65 GHz have validated the proposed single-element approach.

Index Terms — electronic calibration, de-embedding, thru-reflect-line, TRL, CMOS, impedance modulation, T-matrix.

I. Introduction

On-wafer S-parameter calibration suffers from increasing error due to probe re-positioning as measurement frequency enters millimeter-wave and sub-THz [1]. For example, a probe skating difference of 5 μm results in 3.6º phase shift at 300 GHz on silicon. In addition, contact resistance, in particular when interfacing aluminum pads on CMOS, suffers from considerable variation [2]. In [3], we propose a CMOS-based single-element de-embedding technique aiming to minimize accuracy degradation caused by the probing uncertainty. The idea is to utilize the versatility and reciprocity of CMOS transistors to solve for the unknowns of the test fixture error boxes, often consisting of pads and interconnection leads, through impedance modulation. More importantly, such an algorithm makes no approximation in the modeling and hence TRL level of accuracy is preserved. However, the results are being normalized to the transmission-line (t-line) characteristic impedance (Z_0) inserted in the calibration structure; therefore, it is essential to renormalize the measurement impedance to some known value such as 50 Ω.

In TRL, such impedance renormalization is achieved through a two-tier calibration by referencing the unknown line impedance to a known one from another set of TRL lines fabricated on non-dispersive substrates such as GaAs [4]-[5]. Such *calibration comparison method* estimates the line impedance by modeling the contact pad with single shunt admittance in the equivalent circuit model.

In this work, we present an impedance renormalization technique applied to the proposed single-element electronic de-embedding by self-referencing using on-chip terminations. We will first review the concept and the mathematical details of the electronic de-embedding algorithm in [3]. Next, we will discuss how the renormalization is achieved followed by experimental results.

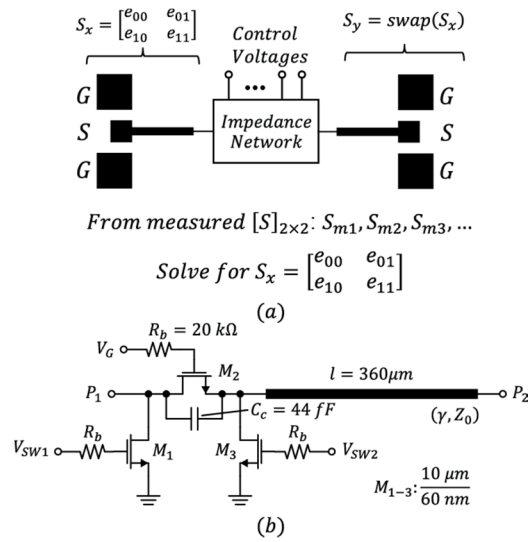

Fig. 1. (a) General concept of the single-element electronic calibration. (b) Implemented impedance network.

II. Single-Element Electronic De-embedding

Fig. 1 illustrates the motivation and the concept of the proposed technique where the problem has been tailored for de-embedding in order to preserve the clarity of the equations and to arrive at fair comparison to on-wafer TRL. In this problem, the test fixtures to be de-embedded are the two probing pads plus the interconnections (S_x and S_y). To solve for the unknowns, we perform S-parameter measurement on a single calibration structure, which comprises three NMOS transistors and a t-line with known length but unknown propagation constant (γ) (Fig. 1(b)). The impedance of each device can be modulated through individual gate bias. The goal is to find the exact solutions for four unknowns (e_{00}, e_{11}, $e_{01} = e_{10}$, and γ) without any prior impedance information.

A. Reflection Measurements with Known Termination

The first step in the algorithm is to convert the measured $[S]_{2\times2}$ into one-port reflection measurements (Γ) with *known* termination. To achieve this, two $[S]_{2\times2}$ measurements, differing only in the impedance state of one of the shunt NMOS transistors, are collected. As shown in Fig. 2(a), these measured $[S]_{2\times2}$ are described using T-matrices:

$$T_{m1} = T_x T_{Y_1} T_{Z_2} T_{Y_3} T_l T_y, \quad (1)$$

978-1-4799-8887-7/15/$31.00 ©2015 IEEE

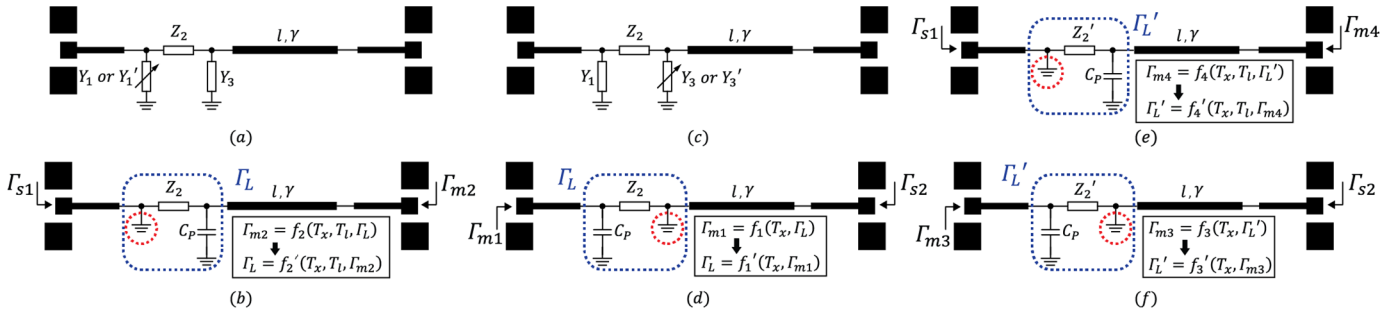

Fig. 2. Derived reflection measurements when modulating (a) and (b) Y_1; (c) and (d) Y_3. (e)(f) Reflection measurements at different Z_2.

$$T_{m2} = T_x T_{Y_1}{}' T_{Z_2} T_{Y_3} T_l T_y, \tag{2}$$

where T_x and T_y represents the test fixtures on both sides, T_{Y1} and $T_{Y1'}$ are the T-matrices of the modulated impedance from M_1, and T_{Z2}, T_{Y3}, and T_l are the T-matrices of M_2, M_3, and the inserted t-line, respectively. Multiplying T_{m2} with the inverse of T_{m1}, we arrive at

$$T_m = T_{m2}(T_{m1})^{-1} = T_x T_{Y_1}{}'(T_{Y_1})^{-1}(T_x)^{-1}. \tag{3}$$

Note that the T-matrix of shunt admittance exhibits the following property:

$$T_{Y_1}(T_{Y_2})^{-1} = T_{Y_1-Y_2} = T_{\Delta Y} = I_{2\times 2} + \frac{\Delta Y Z_0}{2}\begin{bmatrix} -1 & -1 \\ 1 & 1 \end{bmatrix}, \tag{4}$$

where $I_{2\times 2}$ is the identity matrix. Consequently, (3) can be grouped as

$$(T_m - I_{2\times 2})T_x = T_m{}' T_x = T_x \cdot \frac{\Delta Y Z_0}{2}\begin{bmatrix} -1 & -1 \\ 1 & 1 \end{bmatrix}. \tag{5}$$

By expanding (5), the following equality is derived:

$$\frac{x_{11} - x_{12}}{x_{21} - x_{22}} = -\frac{m_{12}}{m_{11}}. \tag{6}$$

Here m_{11} and m_{12} are the elements in the T_m' and x_{11}, x_{12}, x_{21}, and x_{22} are the elements in T_x. Note that the left side of (6) is equivalent to the reflection coefficient (Γ_{s1}) with an *ideal short* terminating Y_1, i.e. the position of modulation. In short, a measurement with *known* termination is extracted without any knowledge of the actual Y_1, which formulates the core of the proposed algorithm. Finally, by reversing T_{m1} and T_{m2} and repeating (3) – (6), Γ_{m2}, the reflection coefficient of the test fixture loaded with t-line and Z_2 in parallel with Y_3 (now C_p), is also derived (Fig. 2(b)). The same procedure is applied when modulating Y_3 (Fig. 2(c) and (d)).

B. Shared Termination

From Fig. 2(b) and 2(d), it is observed that Γ_{m1} and Γ_{m2} both shares Z_2; in other words, both measurements are loaded with identical termination. This leads to the merging of Γ_{m1} and Γ_{m2} by first inverting the expressions for each measurement to isolate the common term Γ_L and then equating the two. Such a single expression is free of the unknown Γ_L but relates all the unknowns of interest and therefore is considered as a useful measurement in the solution finding. It is worth mentioning that this is the same technique in LRRM [6].

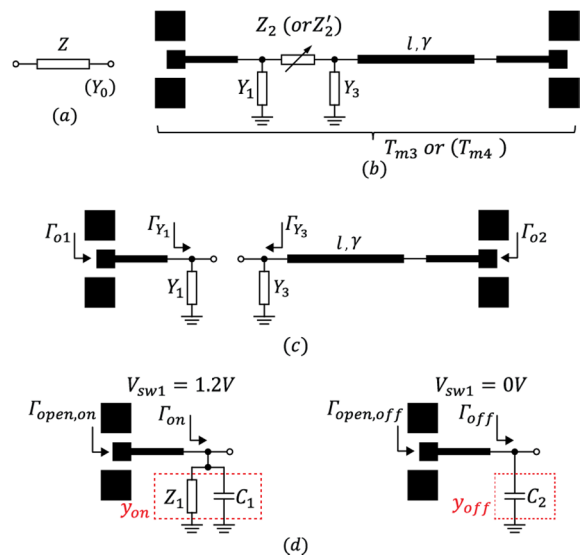

Fig. 3. (a) Series impedance. (b) $[S]_{2\times 2}$ when modulation Z_2. (c) Reflection measurements with open termination. (d) Equivalent circuit models of M_1 in its on (left) and off (right) states.

Lastly, the same procedure is repeated with a different value of Z_2 (Fig. 2(e) and 2(f)). This leads to the collection of another pair of reflection coefficients (Γ_{m3} and Γ_{m4}), which is then merged through sharing of the termination, Γ_L'.

C. Equation Solving

With a total of six reflection measurements, we arrive at the following four nonlinear equations:

$$xz(1-w) - xy(\Gamma_{m1} - \Gamma_{m2}w) - z(\Gamma_{m2} - \Gamma_{m1}w) + \Gamma_{m1}\Gamma_{m2}y(1-w) = 0 \tag{7}$$

$$xz(1-w) - xy(\Gamma_{m3} - \Gamma_{m4}w) - z(\Gamma_{m4} - \Gamma_{m3}w) + \Gamma_{m3}\Gamma_{m4}y(1-w) = 0 \tag{8}$$

$$x + z - \Gamma_{s1} - \Gamma_{s1}y = 0 \tag{9}$$

$$x + zw - \Gamma_{s2} - \Gamma_{s2}yw = 0 \tag{10}$$

where $x = e_{00}$, $y = e_{11}$, $z = e_{00}e_{11} - e_{01}e_{10}$ ($= \Delta_x$) and $w = e^{-2\gamma l}$. Combining (7) – (10) leads to a 5th-order polynomial equation; the solutions can be found using *solve* in Matlab.

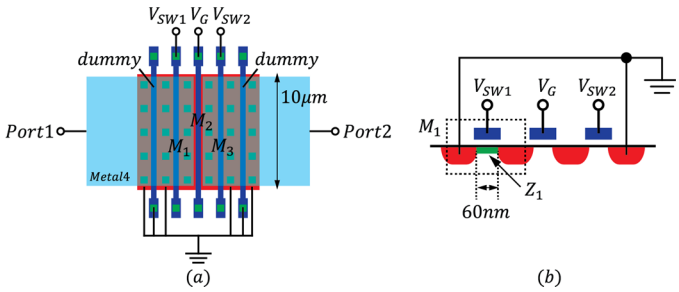

Fig. 4. (a) Layout and (b) cross-section of the π-network

III. Impedance Renormalization

Up to this point, the extracted S_x is normalized to the Z_0 of the on-chip t-line. To solve for unknown Z_0, we take advantage of the shunt switches (M_1 and M_3) in the π-network, which will serve as an on-chip *calibration* standard.

From section II.A, we have shown how reflection measurement terminated with an ideal short can be derived mathematically. On the other hand, network duality tells us that reflection measurements terminated with an *ideal open* can also be extracted in a similar way. To see this, we notice that the T-matrix of any arbitrary series impedance Z reference to Y_0 is described by (Fig. 3(a))

$$T_Z = I_{2x2} + \frac{ZY_0}{2}\begin{bmatrix}-1 & 1\\ -1 & 1\end{bmatrix}. \quad (11)$$

Applying the procedure of (1) – (3) with two measured $[S]_{2\times2}$ differing only in Z_2 (T_{m3} and T_{m4} in Fig. 3(b)) leads to the following expression similar to (5):

$$(T_{m4}(T_{m3})^{-1} - I_{2\times2})T_xT_{Y1} = T_xT_{Y1}\cdot\frac{\Delta ZY_0}{2}\begin{bmatrix}-1 & 1\\ -1 & 1\end{bmatrix}. \quad (12)$$

The following equality is derived after some algebra:

$$\frac{x_{11}' + x_{12}'}{x_{21}' + x_{22}'} = -\frac{m_{12}'}{m_{11}'}. \quad (13)$$

Here m_{11}' and m_{12}' are the elements in $T_{m4}(T_{m3})^{-1}$ and x_{11}', x_{12}', x_{21}', and x_{22}' are the elements of T_xT_{Y1}. Note that the left side of (13) is now equivalent to the reflection coefficient (Γ_{o1}) with an open termination. As S_x is known, Γ_{Y1} is found:

$$\Gamma_{Y_1} = \frac{e_{00} - \Gamma_{o1}}{\Delta_x - e_{11}\Gamma_{o1}}. \quad (14)$$

The procedure is repeated twice with M_1 turned on and off, leading to two expressions of the normalized admittance at different biasing:

$$y_{on} = \frac{Z_0}{Z_1} + j\omega Z_0 C_1, \quad (14)$$

$$y_{off} = j\omega Z_0 C_2. \quad (15)$$

Here Z_1 represents the on-state impedance of M_1 and C_1 and C_2 model the corresponding capacitance loading.

Before moving on, let's study Z_1 in regard to its physical location and geometry. Fig. 4 shows the layout and the cross-section of the π-network. It is observed that the modulation of impedance occurs within the transistor channel having a value on the order of tens of nm in deep sub-micron CMOS. Such fine length allows us to approximate Z_1 with a frequency independent resistance as the phase shift is negligible even at sub-THz frequencies. By modeling Z_1 with a constant resistance R_1 whose value can be measured at DC, Z_0 is found assuming $C_1 \approx C_2$:

$$Z_0 = R_1 \cdot (y_{on} - y_{off}). \quad (16)$$

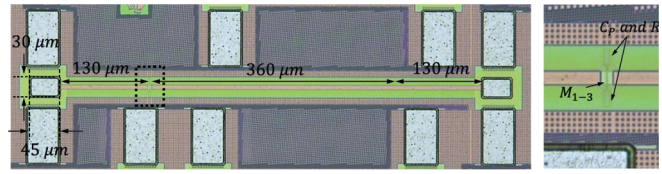

Fig. 5. Calibration structure micrograph.

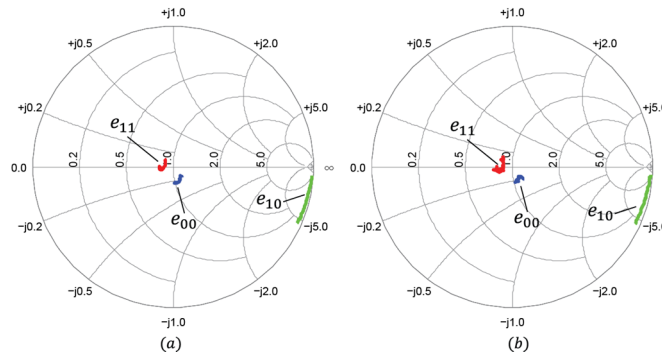

Fig. 6. Extracted S_x: (a) TRL and (b) proposed algorithm

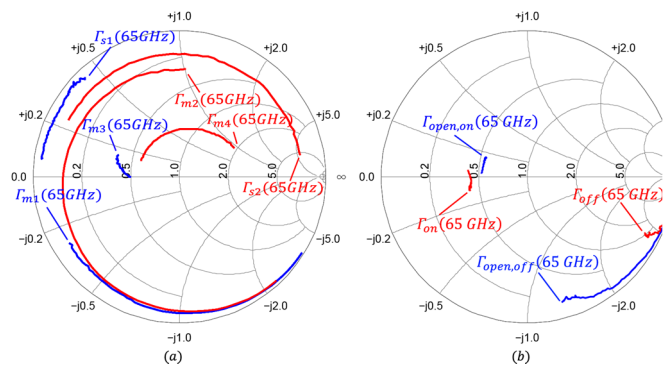

Fig. 7. Reflection measurements with (a) short terminations and (b) open terminations.

IV. Design

Fig. 5 shows the micrograph of the de-embedding structure fabricated in 65-nm CMOS. Microstrip t-lines with 6-μm signal width at M9 on top of a ground plane constructed with a mesh of M1 and M2 is implemented to sustain single-mode propagation. The length of the inserted t-line is 360 μm, equivalent to 45° phase shift at 50 GHz. The schematic of the π-network is shown in Fig. 1(c). To minimize the impact of the capacitive loading, both the NMOS gates and bodies are floated with 20 kΩ poly-resistors and undoped silicon, respectively. A 44-fF MOM capacitor (C_c) is used to lower the

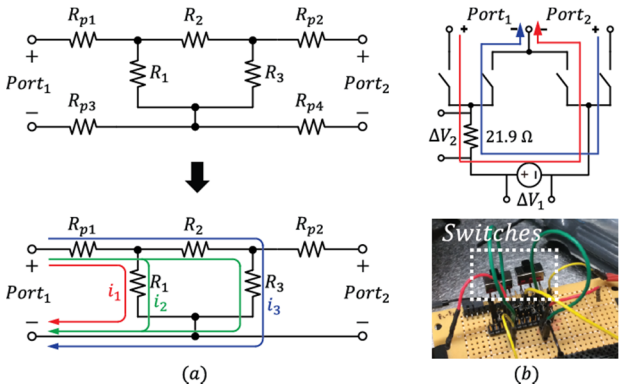

Fig. 8. (a) DC equivalent circuit and (b) customed switch network.

series impedance (Z_2) when M_2 is completely off to keep S_{21} higher than -12 dB above 10 GHz.

V. Experimental Results

First, SLOT calibration is performed at the probe tips using ISS from Cascade Microtech with R&S ZVA-67 VNA. The output power at VNA ports is kept below -10 dBm to avoid measurement error induced by transistor non-linearity. Fig. 6 compares the extracted S_x with TRL, validating our single-element approach. Different reflection coefficients derived in the algorithm are plotted in Fig. 7. Each of them shows the expected behavior.

Fig. 8(a) shows the DC equivalent circuit of the de-embedding structure in the measurement setup taking into account the wiring resistance $R_{p1} - R_{p4}$. The network can be further simplified to five unknowns by ensuring the current returns from the same port. These unknown resistances are found through different combination of impedance states in $M_{1\text{-}3}$. In order to maintain consistent R_{p1} and R_{p2}, a customed switching network is soldered on a PCB (Fig. 8(b)).

Fig. 9 shows the calculated Z_0 and the equivalent t-line circuit elements, exhibiting the expected frequency de-pendency. Comparing to TRL calibration comparison method, our single-element approach captures the increase of the line conductance ($G_{p.u.l.}$) surprisingly well but suffers from higher error in the line resistance ($R_{p.u.l.}$). The accuracy could be limited by the deviation of C_1 and C_2 at different transistor biasing. Such effect is still under investigation.

VI. Conclusion

A CMOS-based electronic calibration technique is presented requiring only a single calibration structure. The technique uses CMOS transistors as impedance modulators to generate reflection measurements with known termination. TRL comparable accuracy is achieved in the experiments up to 65 GHz. In addition, a self-reference impedance renormalization approach is introduced by taking advantage of the fine channel length offered by deep sub-micron CMOS for modeling simplification. Such an approach shows great

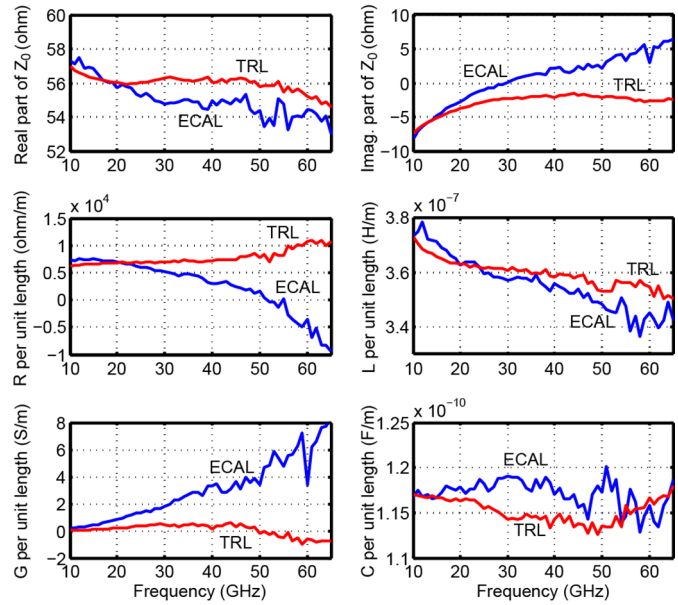

Fig. 9. Extracted Z_0 and the t-line circuit parameters with TRL and the proposed electronic calibration (ECAL).

potential in eliminating the probing error and is therefore beneficial for high frequency measurements. Optimization is applicable to further enhance the accuracy.

Acknowledgement

We would like to acknowledge TSMC University shuttle program and Professor Amin Arbabian, Nemat Dolatsha, and Nicholas Saiz of Stanford University for measurement support.

References

[1] K. Eriksson, V. Vassilev, and H. Zirath, "H-band MMIC amplifier in 250 nm InP DHBT," in *International Conf. on Microwaves, Radar and Wireless Communication*, May. 2012, pp. 744 – 747.

[2] D. F. William, et. al., "Calibration-kit design for millimeter-wave silicon integrated circuits," *IEEE Trans. Microw. Theory Tech.*, vol. 61, no. 7, pp. 2685– 2694, Jul. 2013.

[3] J.-C. Chien and A. M. Niknejad, "A single-element CMOS-based electronic de-embedding technique with TRL level of accuracy," submitted to *IEEE MTT-S Int. Microw. Symp.*, 2015.

[4] D. F. Williams, "Accurate characteristic impedance measurement on silicon," in *IEEE MTT-S Int. Microw. Symp.*, Jun. 1998, pp. 1917 – 1920.

[5] D. F. Williams, U. Arz, and H. Grabinski, "Characteristic-impedance measurement error on lossy substrates," *IEEE Microwave Wireless Compon. Lett.*, vol. 11, no. 7, pp. 299 – 301, Jul. 2001.

[6] L. Hayden, "An enhanced line-reflect-reflect-match calibration," *67th ARFTG Conf. Dig.*, Jun., 2006, pp. 143-149.

V- and W-band Waveguide Microcalorimeters for Millimeter-wave Power Standards

Jae-Yong Kwon[1,2], Young-Pyo Hong[1], Dong-Joon Lee[1], and Tae-Weon Kang[1,2]

[1]Center for Electromagnetic Wave, Korea Research Institute of Standards and Science, 267 Gajeong-ro, Yuseong-gu, Daejeon 305-340, Korea

[2]University of Science and Technology, 217 Gajeong-ro, Yuseong-gu, Daejeon 305-350, Korea

E-mail: jykwon@kriss.re.kr

Abstract — This paper introduces a recently constructed V-band and an under development W-band waveguide microcalorimeters that will serve as primary power standards in KRISS. The design scheme of the V- and W-band microcalorimeters is briefly presented, and their basic performance was checked. We propose a thermoelectric reference standard that will cover V- and W- bands. We also propose an in-house V-band source signal module for high RF power and low signal impurity output.

Index Terms — Calorimetry, waveguide, thermistor, electromagnetic measurements, measurement standards, measurement uncertainty.

I. Introduction

We have developed coaxial microcalorimeters that will become power standards up to 50 GHz [1, 2, 3] and have studied on the V- and W-band waveguide microcalorimeters and power standard calibration systems for up to 110 GHz [4]. In Korea, the communication industry already demonstrated 5G trial communications in 2013, and the government has plans to rollout a trial 5G service by 2017 and provide a commercial 5G service by 2020 [5]. To support the future demand on the millimeter-wave power standards service in Korea, KRISS has developed V- and W-band waveguide power standard calibration system. However, the transfer standards of the calibration system are traceable to a foreign national metrology institute, and it provides the service for a limited number of frequencies. We have sought to make our own microcalorimeters to replace the transfer standards with KRISS traceable ones. We will discuss the key components of V- and W-band waveguide microcalorimeters in detail.

II. Design and Implementation

A. Basic concept and structure of microcalorimeters

We developed three coaxial, Type-N, 3.5-mm, and 2.4-mm, microcalorimeters [1, 2, 3]. They have a dry-type triple metal shield thermostat, twin adiabatic lines, and a thin film thermopile module. Our basic concept was not changed, however we modified the structure of the microcalorimeter. Fig. 1 shows the structure of the V- and W-band waveguide microcalorimeters. We adopted an upright design for the core parts of the microcalorimeters to lessen torque from the attached reference standards. Fig. 2 shows the adiabatic lines, thermopile module, and reference standards of the V-band waveguide microcalorimeter. The adiabatic line has an electroformed thin wall that confines the heat from the reference standard. The thermopile module and the dry-type thermostat of the V-band microcalorimeter have the same basic structure as those of the 3.5 mm coaxial microcalorimeter at KRISS [1].

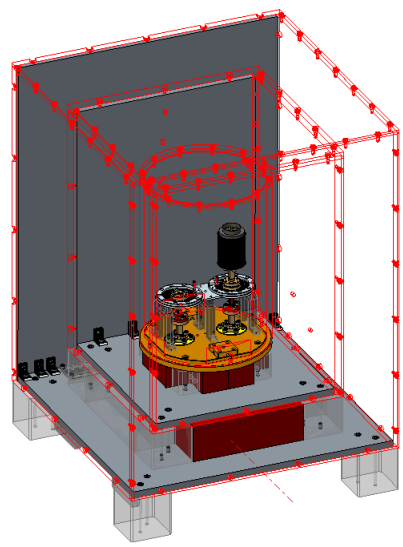

Fig. 1. Basic structure of the V- and W-band waveguide microcalorimeters at KRISS.

B. Reference standards

Conventionally many national metrology institutes (NMIs) adopt thermistor mounts as their reference standards for microcalorimeters. Thermistor mounts are applicable to the RF-DC power substitution method for effective efficiency evaluation, and they have very good linearity [6]. However, V- and W-band thermistor mounts are no longer available in the market. As latecomers on V- and W-band power standards research, it has been very hard for us to get appropriate

978-1-4799-8887-7/15/$31.00 ©2015 IEEE

reference standards. For the last 5 years, we have bought a small number of thermistor mounts in the used market around the World. To make a breakthrough, we started to develop thermoelectric-type waveguide reference standards in 2013, and Physikalisch-Technischen Bundesanstalt (PTB), Germany, presented some research result on a thermoelectric-type W-band waveguide reference standard [7]. To make the reference standard, we adopted a core part of 1.0 mm coaxial thermoelectric power sensor, Rohde & Schwarz NRP-Z58 thermal power sensor, and a V-band (or W-band) waveguide to coaxial adapter, Flann Microwave 25373-WF or 27373-WF waveguide to 1 mm coaxial end launch adapter.

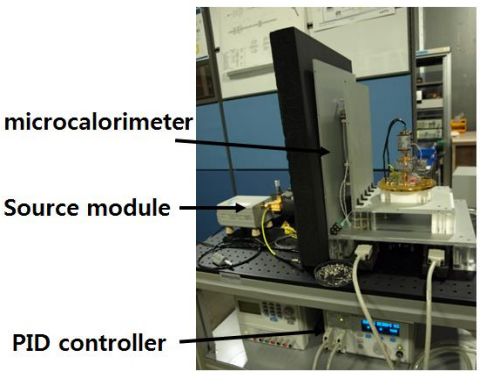

(a)

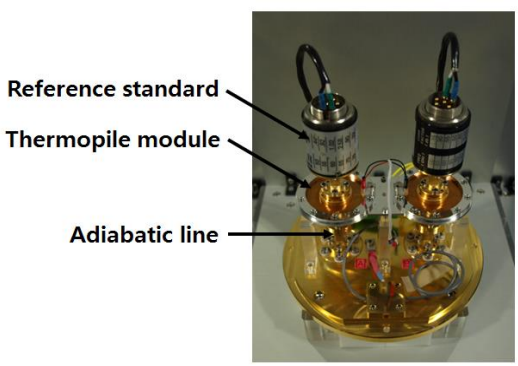

(b)

Fig. 2. The V-band waveguide microcalorimeter. (a) With a source module and a PID controller. (b) Core parts of the microcalorimeter.

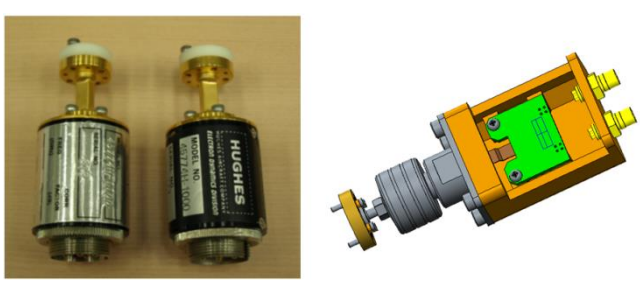

(a) (b)

Fig. 3. Reference standards for a microcalorimeter. (a) Conventional reference standards (V-band thermistor mounts). (b) Thermoelectric-type reference standard (V- and W-band).

C. Signal source module

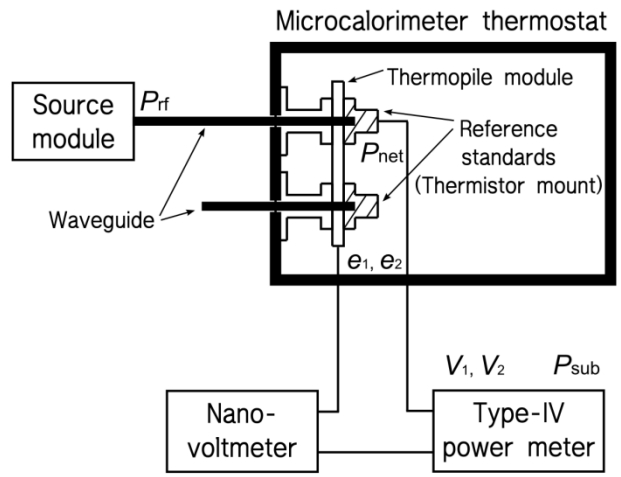

Fig. 4. Measurement system of the V-band waveguide microcalorimeter.

Fig. 4 shows the measurement setup of the V-band waveguide microcalorimeter. To perform a low uncertainty measurement, we should have to transmit an appropriate amount of RF power to the reference standard, substituted power P_{sub}, in the microcalorimeter. We usually apply $P_{sub} \approx$ 10 mW for the coaxial microcalorimeters.

Usually, the signal source modules in millimeter-wave adopt a frequency multiplier, and their RF outputs are limited [8-9]. Fig. 5 shows the structure of an in-house V-band signal source module for the KRISS V-band waveguide microcalorimeter. We doubled the frequency of a signal generator, Keysight E8257D PSG, to get a high power and low signal impurity RF output.

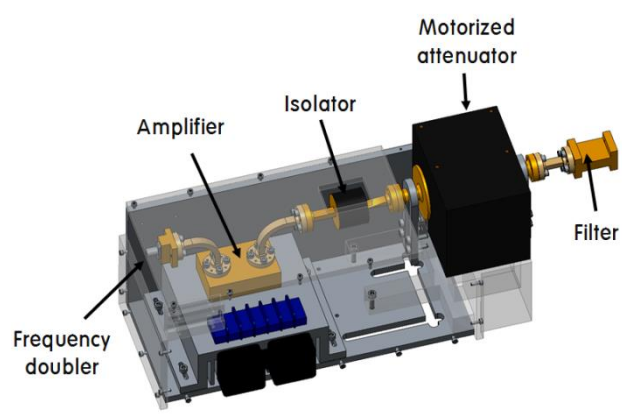

Fig. 5. The structure of the in-house V-band signal source module (KRISS-V) for the microcalorimeter.

In Fig. 6, we compared the RF output of the in-house V-band signal source module (blue dot) with an OML S15MS-AG frequency extension module (red dot).

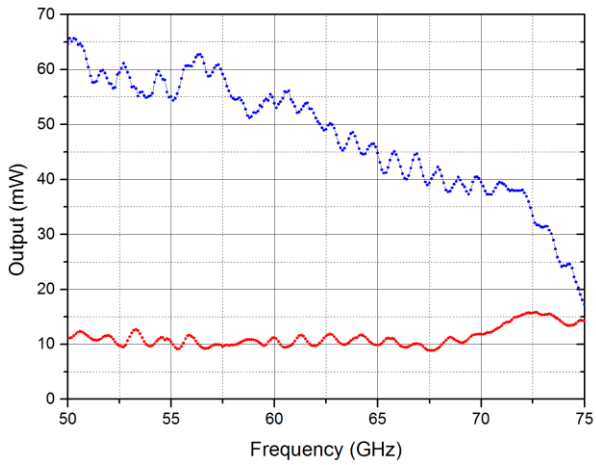

Fig. 6. The RF power output of the in-house V-band signal source module (KRISS-V) for the microcalorimeter.

III. Preliminary Measurement

Fig. 7 shows the preliminary measured data of the V-band waveguide microcalorimeter with the V-band thermistor mounts shown in Fig. 3(a) and the OML S15MS-AG signal source module. The voltage output of the thermopile module (red) is approximately 60% of the output of the KRISS type-N coaxial microcalorimeter [10]. A thermistor mount saver, one-inch V-band waveguide section, that increases heat volume and the limited RF power output of the signal source module, results in that reduction of the thermopile output. We will tune the level of the signal source module to apply uniform P_{sub} on the reference standards.

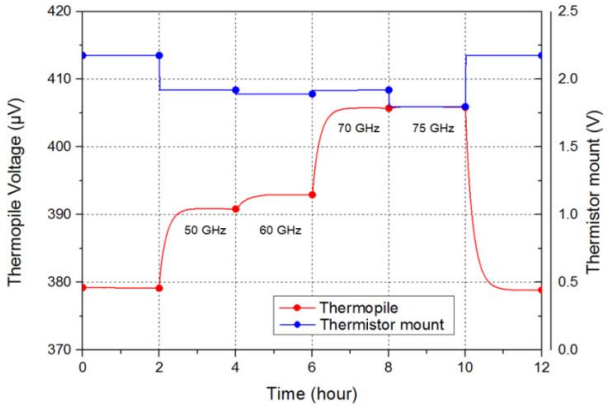

Fig. 7. Measured data of the microcalorimeter system for 50, 60, 70, and 75 GHz. Voltage outputs of the type-IV power meter (blue) and thermopile module (red).

IV. Conclusion

A V-band waveguide microcalorimeter has been developed and its preliminary performance has been evaluated to establish a KRISS traceable RF power standard. As a further work we will optimize an adiabatic structure for the transmission line that connects the signal source module and the waveguide microcalorimeter for the minimum thermal fluctuation.

Acknowledgement

This work was supported by the Korea Research Institute of Standards and Science under the project "Development of Technologies for Next-Generation Electromagnetic Wave Measurement Standards," through grant 15011014.

References

[1] J.-Y. Kwon, T.W. Kang, J.H. Kim, and J.S. Kang, "Development of a 3.5-mm coaxial microcalorimeter for RF and microwave power standards at KRISS," *IEEE Trans. Instrum. Meas.*, Vol. 60, No. 7, pp. 2609-2614, July 2011.

[2] J.-Y. Kwon, T.W. Kang, J.H. Kim, and T. Crowley, "Development of a 2.4-mm coaxial microcalorimeter for RF and microwave power standards at KRISS," *CPEM 2012 Digest*, pp. 734-735, July 2012.

[3] J.-Y. Kwon, T.-W. Kang, J.-H. Kim, and N.-W. Kang, "Development of a Type-N coaxial microcalorimeter for RF and microwave power standards at KRISS," *CPEM 2014 Digest*, pp. 350-351, Aug. 2014.

[4] J.-Y. Kwon, T.-W. Kang, J.-S. Kang, and D.-J. Lee, "A W-band millimeter-wave power standard transfer system using the direct comparison method," *The Journal of Korean Institute of Electromagnetic Engineering and Science*, pp. 47-54, Jan. 2013.

[5] http://spectrum.ieee.org/telecom/wireless/millimeter-waves-may-be-the-future-of-5g-phones

[6] A. Fantom, *Radio frequency & Microwave Power Measurement*, Peter Peregrinus Ltd., England, 1990.

[7] R. H. Judaschke, K. Kuhlmann, T. Reichel, and W. Perndl, "A W-band thermoelectric power transfer standard," *CPEM 2014 Digest*, pp. 756-757, Aug. 2014.

[8] Rohde & Schwarz, *R&S SMZ Frequency Multiplier Data Sheet*, Ver. 03.00, Sep. 2013.

[9] Keysight Technologies, *mm-wave Source Modules from OML, Inc. for PSG Signal Generators*, Technical Overview, Aug. 2014.

[10] J.-Y. Kwon, T.-W. Kang, J.-H. Kim, and N.-W. Kang, "Development of a Type-N coaxial microcalorimeter for RF and microwave power standards at KRISS," *IEEE Trans. Instrum. Meas.*,Vol. 64, 2015. DOI 10.1109/TIM.2015.2408802

A 500 MHz Portable Evaluation Platform for Digital Pre-Distortion and Envelope Tracking Power Amplifiers

Jonmei J. Yan, Toshifumi Nakatani, Paul Theilmann, and Donald F. Kimball

MaXentric Technologies, LLC. La Jolla, CA 92037.

Abstract — Efficiency and linearity are important design criteria for power amplifier (PA) designers. These two constraints usually contradict each other in the realm of PAs. However, with many recent efforts, various architectures such as envelope tracking, when used in conjunction with digital pre-distortion, allow the system to achieve both efficiency and linearity simultaneously. Many of the available evaluation platform/testbeds today are limited in bandwidth to ~200 MHz. This limits the bandwidth of the supported signal to ~40 MHz. As talk of future 5G LTE systems call for signal bandwidths of greater than 100 MHz, the need for an evaluation platform with 500 MHz is crucial. In this work, a 500 MHz bandwidth evaluation platform for DPD development and envelope tracking design will be presented.

Index Terms — Power amplifier, envelope tracking, bandwidth, digital pre-distortion, portability, testbed.

I. Introduction

The increasing demand for higher data rates and larger signal bandwidth, while maintaining signal integrity, has led to the use of high spectral efficiency signals with non-constant envelope and high peak-to-average power ratio (PAPR). In conventional fixed bias power amplifiers (PAs), the maximum efficiency occurs at saturation, with a single-tone signal. As the PA operates at power levels away from saturation, the efficiency degrades. This creates a challenge in the presence of high PAPR signals (such as OFDM), where the average power is well below saturation.

Various techniques have been explored to increase the efficiency of power amplifiers for high PAPR signals [1] while maintaining adequate linearity. One technique with much recent interest is the envelope tracking (ET) [2]. The drain voltage of the RF PA is varied dynamically to track the envelope of the signal, providing the appropriate DC supply signal and keeping the RF transistor operating continuously at saturation region where the efficiency is highest. As a result, no extra DC power is consumed, resulting in a dramatic increase in PA average efficiency in the presence of high PAPR signals.

The platform development of the ET PA is very important because the ETPA transmitter architecture is different from the conventional transmitter. Fig. 1 shows block diagrams of (a) conventional transmitter and (b) ETPA transmitter. In Fig. 1(a), the baseband data is converted to the modulated RF signal through DAC and up-converter. The bandwidth of the forward (TX) path, including the DAC and up-converter, is

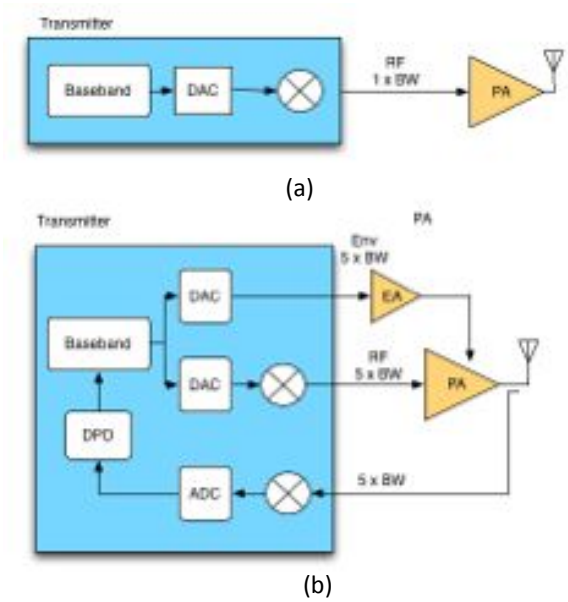

Fig. 1 Simplified block diagram of (a) conventional PA platform and (b) ETPA platform

the same as the signal bandwidth of the modulated signal. In Fig. 1(b), in contrast to the conventional transmitter, the ETPA transmitter requires an additional envelope signal to be generated. In the conventional transmitter, digital pre-distortion (DPD) is assumed absent. Under the ETPA transmitter, in order to simultaneously achieve high efficiency and high linearity, digital pre-distortion is used. In order to cancel out or pre-distort the input signal to the ETPA, a much wider bandwidth in the forward TX path is needed. The typical rule of thumb is to use five times to signal bandwidth in order to pre-distort the 3rd and 5th order IMDs. For DPD to be possible, a feedback RX path is also needed. Despite the added complexity introduced to the transmitter as a result of using envelope tracking, the various attributes, such as high efficiency and carrier frequency independence, make the technique a worthwhile effort. The amount of savings one can potentially achieve from higher efficiency, lower DC power consumption, and less thermal management accessories can offset the added cost of an extra DAC and feedback path. Such reasons have motivated the research in ETPA development and hence, it is important to establish the ETPA platform for designing, testing, and optimizing.

978-1-4799-8887-7/15/$31.00 ©2015 IEEE

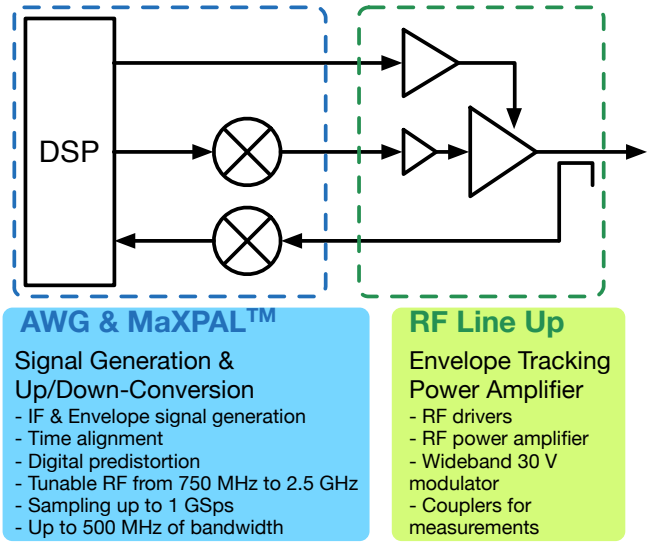

Fig. 2. Structure of portable ETPA platform (Bento Box 3.0).

Several evaluation platforms for the ETPA have been proposed. In [3], Keysight Technologies, formerly Agilent Technologies, introduced a solution using vector signal generator, arbitrary waveform generator and vector signal analyzer. However, complicated time-alignment mechanism between RF and envelope paths is required since each signal is generated from two separate signal generators. The maximum bandwidth of the RF signal generation instrument is 160 MHz, where is equivalent to a RF signal with only 32 MHz bandwidth. In [4], Rohde & Schwarz provided a 160 MHz solution, where only vector signal generator and vector signal analyzer are used. The solution provides a real-time DPD function without downloading data to a PC. However, the use of multiple instruments is relatively large and heavy for demonstration. National Instruments has also provided a solution with 200 MHz of bandwidth, supporting a 40 MHz signal, in a single PXI-E chassis. Each of these solutions is viable solution for today's market where 40 MHz is desired. However, for future market development, such as 5G LTE, the community has expressed interest in developing solutions for signals with >100 MHz of bandwidth.

In this work, a 500 MHz DPD and ET platform, named BentoBox 3.0, is proposed for supporting signals with bandwidth of 100 MHz. Signal generation, up-/down-conversion and DPD analysis functions are integrated into the "AWG & MaXPAL™" box and an RF pre-drivers, drivers, and ETPA (RF PA and envelope modulator) are accommodated into the "RF Line Up" box. The maximum bandwidth of the forward TX path and the feedback RX path is 500 MHz. Additionally, real-time DPD functionalities have been implemented into the signal processing and can be toggled off and on to see the improvements.

II. Hardware Design of ETPA Platform

The block diagram is depicted in Fig. 2. The first layer is the "AWG & MaXPAL™" that consists of the signal generation and pre-distortion, as well as the up- and down-conversion for the forward and feedback path respectively. The second layer is the "RF Line Up", which consists of the RF drivers and envelope tracking power amplifier (RFPA in conjunction with the envelope modulator/amplifier). The first layer supports upconversion from 750 MHz to 2.5 GHz. Other functions of the "AWG & MaXPAL™" layer include time alignments of both the reference/feedback and the envelope/RF, as well as envelope shaping specifically for ET operation. However, the RF Line Up essentially houses the ETPA, the DUT, and the necessary RF drivers to drive the ETPA. In this setup, we will be looking at the 2.14 GHz RF Line (LTE Band 1). The BentoBox 3.0 is designed to be a rackmount unit (19" wide x 14.5" depth). The "AWG & MaXPAL™" is 2U in height (3") and the "RF Line Up" is 3U (4.5") in height, limited by the heatsink height.

Fig. 3 (a) shows the circuit schematic of the RF PA tuned to the frequency of 2.14 GHz. A commercial GaN FET is used for the demonstration with peak output power of 30W at 48V and the peak efficiency of 65% under single-tone excitation. The small signal gain is 14 dB. For the envelope tracking operation, bias capacitors at the drain of the PA were removed to allow for envelope modulation to occur. A series RC snubber was placed at the drain of the PA. The output matching network was modified to achieve higher PAE under the envelope tracking operation.

The envelope amplifier (EA), sometimes called envelope modulator, developed in this work uses the architecture shown in Fig. 3 (b). A wideband, high-speed linear stage is coupled with a high efficiency low bandwidth switcher stage through a hysteretic feedback path. The switcher stage provides the bulk of the low frequency power while the linear stage provides the remaining signal components. The linear stage consists of a folded-cascode input stage and Class AB output stage. Linear stage current is sensed by a current mirror and used to control the switcher stage via an anti-shoot through driver path. The design was integrated in a BCD high voltage CMOS process that co-integrates low voltage 0.18μm devices with high voltage (30V) FET devices. The design targets a 5W average output power ET system with peak drain voltages of up to 30V and peak envelope powers up to 35W. This modulator has nearly double to voltage of recently published integrated micro-basestation EAs [3]. These features allow the EA to couple with high voltage, high efficiency GaN and LDMOS RF PAs.

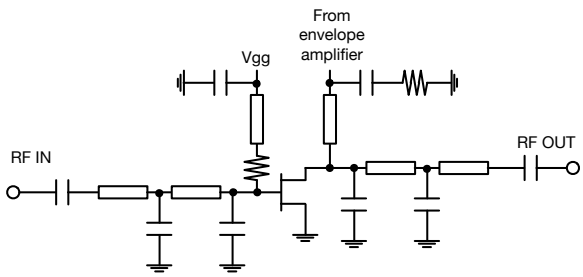

(a)

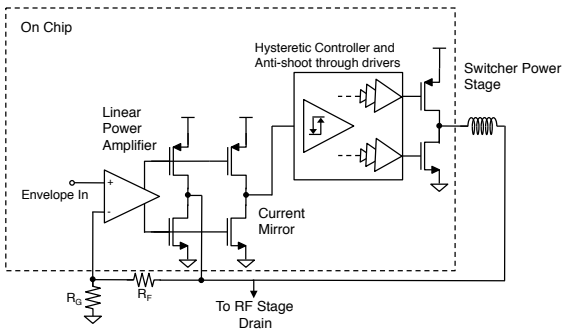

(b)

Fig. 3 Block diagrams of (a) RF PA and (b) envelope amplifier for envelope tracking operation.

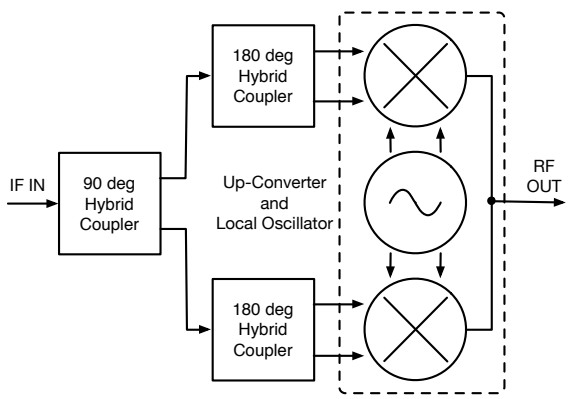

(a)

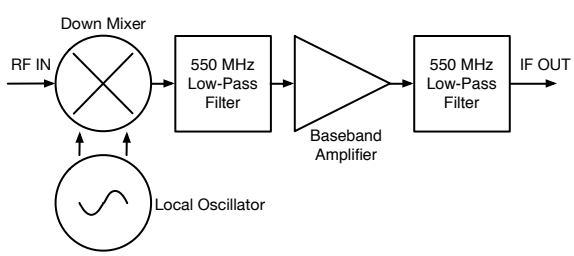

(b)

Fig. 4 Block diagram of (a) up-converter and (b) down-converter.

Fig. 4 (a) shows the block diagram of the up-converter. The up-converter has an image rejection configuration in order to reduce the need or the requirements of the RF band-pass filter. To realize the configuration, the single-end IF signal is split to two signals with 90-degree phase difference and each signal is split to two signals with 180-degree phase difference. Finally, these four signals with different phases are up-converted at the quadrature modulator, resulting in higher image rejection. Fig. 4 (b) shows the block diagram of the down-converter, where RF signal is converted to an IF signal at 250 MHz. The undesired high frequency components of the IF signal are filtered by two low-pass filters in order to prevent the aliasing of the ADC on this feedback path. To maintain sufficient SNR and maximum ADC resolution, a baseband amplifier is inserted between two filters to keep the output voltage swing high enough.

Fig. 5 (a) shows the measured RF output power over frequency of the up-converter when the frequency at the IF IN port is swept. The quadrature phase splitter is configured to be the low side injection (the LO frequency is lower than the frequency at the RF OUT port). The LO frequency is 1.75 GHz and the IF input power is 8 dBm. The output power is almost flat in the range from 1.8 GHz to 2.25 GHz. More than 20 dBc image-rejection ratio is obtained in the range from 1.7 GHz to 2.25 GHz.

Fig. 5 (b) shows the measured conversion gain over frequency when only the LO frequency is swept. The blue diamond symbols are the results when the RF is 1 GHz and the LO frequency is varied from 1 GHz to 1.5 GHz (upper local). The red square symbols are the results when the RF is 2 GHz and the LO frequency is varied from 1.5 GHz to 2 GHz (lower local). The RF input power is -22 dBm. The roll-off of the conversion gain at the 500 MHz is approximately 2 dB.

III. DSP Algorithms of ETPA Platform

The forward path for digital pre-distortion (DPD) was coded in VHDL for implementation in FPGA hardware. The DPD accepts complex inputs split into real and imaginary parts with each input as 16-bit signed number. The DPD outputs a 16-bit unsigned envelope and a 16-bit signed pre-distorted digitally up-converted IF signal. The DPD has a latency (time between valid input and valid output) of 50 clock cycles and can generate an output on every clock. Fig. 6 shows the diagram for FPGA implementation.

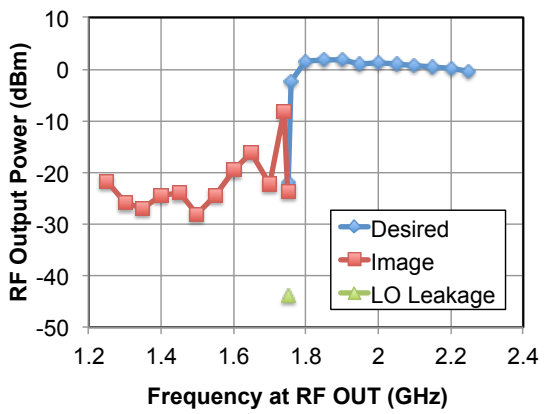

(a)

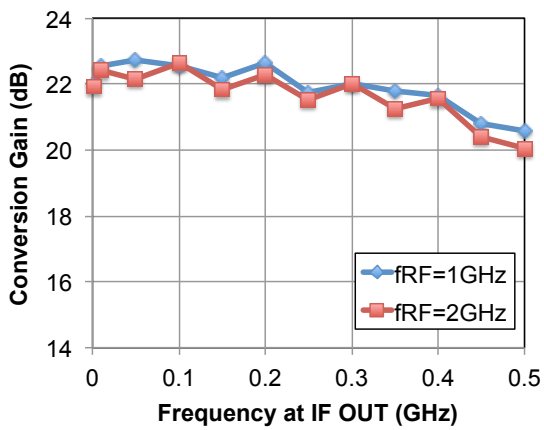

(b)

Fig. 5 (a) RF output power vs frequency of up-converter and (b) conversion gain vs frequency of down-converter.

The input converter uses a CORDIC core to convert complex data to polar form. The pre-distorter comprises the amplitude and phase correction. Amplitude distortion correction maps the input amplitude to its distorted value. Phase correction maps the input amplitude to the phase delta. The delta output is then added to the input phase to come up with the corrected phase. Interpolation is used to work within the constraints of memory resources. The output converter comprises two parts – envelope shaping or detroughing and digital IF upconverting. The envelope shaping gives the designer a tradeoff knob for efficiency and linearity by choosing different trajectories and relationships between the true envelope of the RF signal and the actual drain supplied by the modulator. Delays are added to the envelope signal to ensure that the envelope path and the RF path arrive at the drain of the RFPA at the same time for best performance. In this design, IF generation was chosen to mitigate the complexities added from IQ imbalances and impairments. To maximize use of the Nyquist bandwidth, digital up-conversion is performance such that the IF output centers at one-fourth of the clock rate.

The feedback path is composed of the feedback converter, aligner, and predistortion engine. The reference signal is a capture of the input baseband signal. The feedback signal is the RF-downconverted output of the PA fed back in to the FPGA and then down-converted to baseband. The feedback converter is broken down into three separate modules – a down-converter, a low pass filter, and a complex to polar converter. The delay between the two signals is determined to align the signals in the reference/feedback alignment block. A second time alignment calculation is performed, specific to envelope tracking. This alignment calculates the envelope/IF time delay to determine how well the two paths are aligned at the drain of the RFPA. The linearizer engine performs the analysis and calculations to determine the necessary modifications to achieve a linear RFPA output.

A 100 MHz 16-QAM signal with 6.6 dB PAPR was generated and analyzed in MATLAB for its linearity on a straight-through measurement. Fig. 7 illustrates the AMAM, AMPM, and spectrum of the 100 MHz signal generated from the "AWG & MaXPAL™" layer. Results demonstrated a linear behavior. Additionally a decent amount of spread was observed. This is due to the fundamental frequency dependence response of the filters, DAC sinc response, and other system components when operating over such a wide bandwidth. The frequency response variation can be compensated for with a system calibration/equalization.

IV. Demonstrations

Fig. 8 shows the BentoBox 3.0 with the assembled "AWG & MaXPAL™" layer (bottom) and assembled "RF Line Up" layer (top). There are two outputs: fully modulated RF signal at 2.14 GHz for the RF path and the envelope signal for the envelope modulator. The third main SMA connector is the RF feedback signal. To configuration the up- and down-conversion LO, the user uses a GUI interface to specify the desired RF frequency and the computer programs the LOs associated to it. The USB connection under "FPGA Program" allows the user to program a new FPGA source file. The "FPGA Control" ethernet connection allows the user to interface with the FPGA to send/retrieve signals, as well as control other components such as DAC gain, envelope floor, etc. Additionally, the platform operates like envelope tracking "adaptor", allowing one to stream-in a real-time signal from the outside world via the "analog streaming input". The signal needs to be an IF signal with 1V pk-pk centered at 250 MHz. A10 MHz reference is used to lock the clock of the FPGA to the signal source. Connections at "IF sample" allows the user to tap the signal before the up-conversion and after the feedback down-conversion.

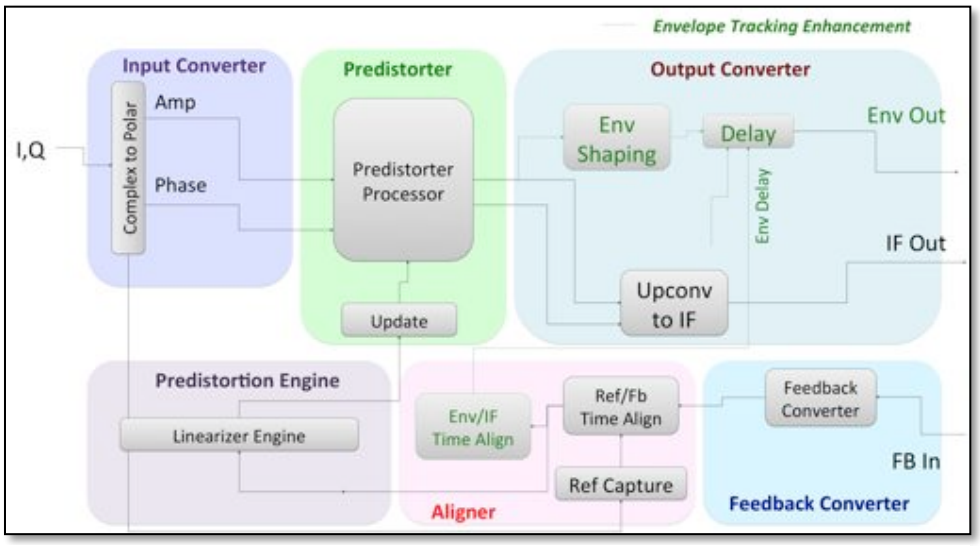

Fig. 6 Block diagram of FPGA forward and feedback path implementation.

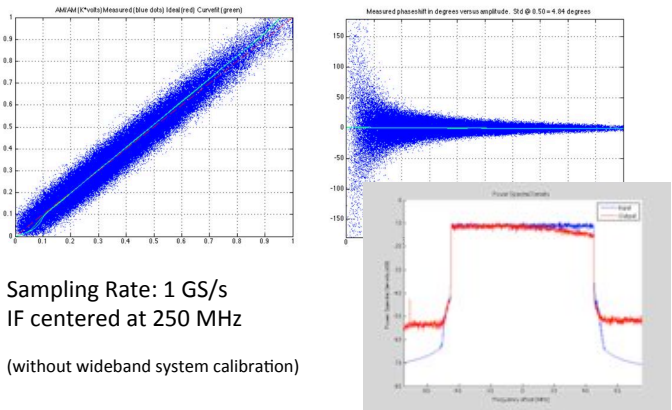

Fig. 7 AMAM, AMPM, and spectrum of the captured 100 MHz 16-QAM signal from the Kansei ADC, as analyzed in MATLAB.

In the "RF Line Up" layer, the top three SMA connections are the main signals. "RF Input" drives the RF driver. "Envelope Input" drives the envelope modulator. "RF Output" is the output of the PA after an isolator. To measure the input and output power of the ETPA for efficiency measurement, "PA Input Sample" and "PA Output Sample" allows the user to tap the input to the RFPA and the output of the RFPA respectively. To ensure the safety operation of these depletion-mode GaN power amplifiers, a push button PSU sequencer is used to ensure that the proper gate voltage is applied prior to supplying the drain voltage. DC power consumption for efficiency measurements is made by measuring the DC voltage and current by a supply circuit break on the front panel.

Fig. 8 BentoBox 3.0 "RF Line UP" assembly on the top and "AWG & MaXPAL™" assembly on the bottom.

Using the pre-distortion implemented in the FPGA, measurements under envelope tracking was performed with a 5 MHz 6.6 dB PAPR WCDMA signal. The envelope modulator was the MaXEA1.0 and the RFPA was a commercially available RF3931 PA retuned for ET operation. The RF output before and after DPD was captured and plots were generated in MATLAB. Fig. 9 illustrates the measured AM-AM, AM-PM and spectrum of the ETPA under test. The measured average ETPA efficiency of this particular setup was 43%, with efficiency split of 73% for the envelope modulator and 59% for the RFPA. The output power of the WCDMA signal was 4.2 W with 10 dB of RFPA gain.

To demonstrate the bandwidth capability of the evaluation platform, digital predistortion, which imposes this bandwidth requirement, was applied to various constant drain power amplifiers. Fig. 10 illustrates the measured AM-AM, AM-PM and spectrum of the constant drain power amplifier under the excitation of an 60 MHz 16-QAM LTE signal. The system also lends itself to mm-wave testing with a simple direct

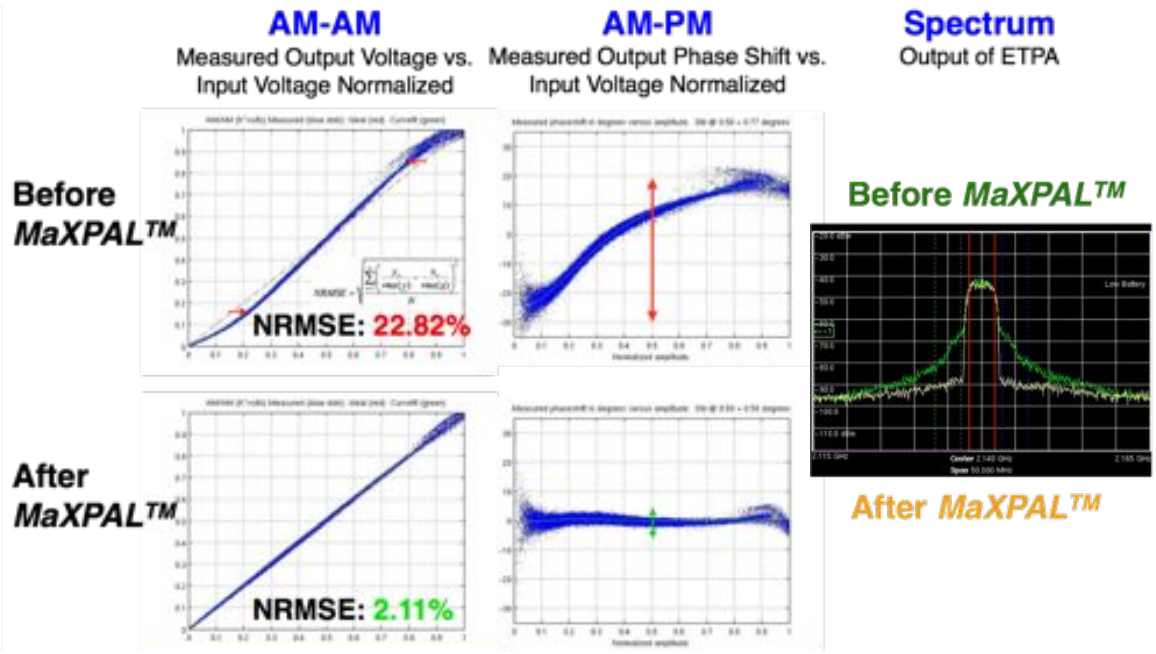

Fig. 9 Measured AM-AM, AM-PM, and spectrum before DPD and after DPD under envelope tracking at 2.14 GHz with a 5 MHz WCDMA downlink signal.

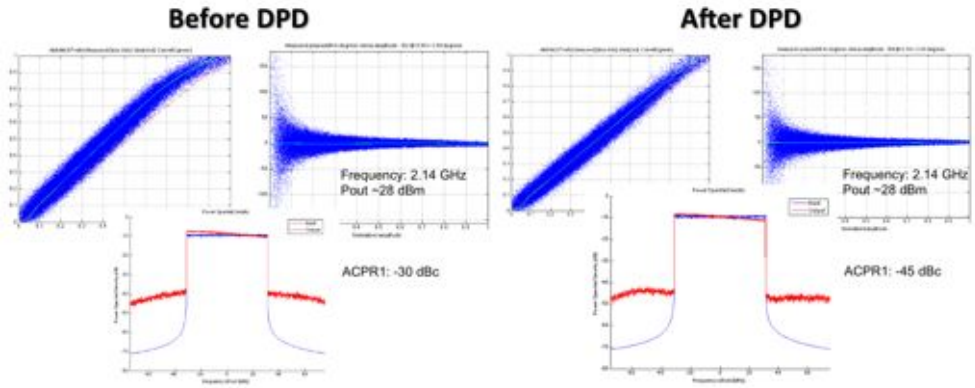

Fig. 10 Measured AM-AM, AM-PM, and spectrum before DPD and after DPD under constant drain at 2.14 GHz with an 60 MHz 16-QAM LTE signal

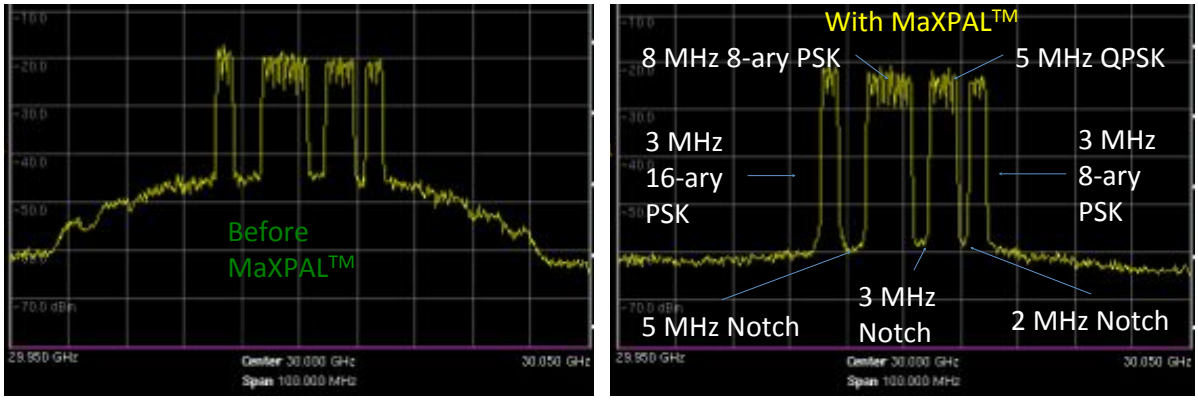

Fig. 11 Measured spectrum before DPD (left) and after DPD (right) under constant drain at 30 GHz with an 30 MHz multi-carrier signal

up/down-conversion addition. DPD sees the entire system as a black box and hence is not susceptible to carrier frequency changes, similar to ET. Fig. 11 shows the spectral results of using the platform with an additional L-band to Ka-band converter on a constant drain power amplifier with and without DPD. The signal is a 30 MHz multi-carrier signal with different modulation, bandwidths, and center notches.

V. Conclusion

A portable evaluation platform for digital pre-distortion and envelope tracking has been developed. Using image-rejection up-converter and digital compensation algorithm, a 100 MHz modulated signal was generated and its straight-through linearity was shown. Measurements under envelope tracking operation were performed using the MaX1.0 modulator with a 5 MHz WCDMA signal. To demonstrate the wide bandwidth capability of the platform, linearity under constant drain with an 60 MHz signal were measured. Additionally, carrier frequency flexible to support other systems was demonstrated using direct up-/down-conversion to 30 GHz using a multi-carrier 30 MHz signal. The proposed platform is useful for future wideband and high efficiency PAs, both envelope tracking and constant drain.

References

[1] S. C. Cripps, Advanced Technique in RF Power Amplifier Design, Norwood, MA: Artech House, 2002.

[2] J. J. Yan, P. Theilmann, and, D. F. Kimball, "A high efficiency 780 MHz GaN envelope tracking power amplifier," in Proc. CSICS, 2012.

[3] Envelope Tracking and Digital Pre-Distortion Power Amplifier Testing for LTE User Terminal Components, Agilent Technologies Application Note 5991-4069EN, March 2014.

[4] C. Troster-Schmid, Envelope Tracking and Digital Pre-Distortion Test Solution for RF Amplifiers, Rohde & Schwarz Application Note 1GP104-1E, Sept. 2014.